UNIVERSITY OF CALIFORNIA SAN DIEGO

Design and Applications of Immunoregulatory Biomaterials in Autoimmune Disease

A Dissertation submitted in partial satisfaction of the requirements
for the degree Doctor of Philosophy

in

Chemical Engineering

by

David A. McBride

Committee in charge:

Professor Nisarg Shah, Chair
Professor Nunzio Bottini
Professor Jesse Jokerst
Professor Liangfang Zhang

2023

The Dissertation of David A. McBride is approved, and it is acceptable in quality and form for publication on microfilm and electronically.

University of California San Diego

2023

DEDICATION

I dedicate my dissertation work to my family, friends and mentors. I would like to thank my family, my mom Karen, my dad Pete, and my brother Willie, for their support throughout my life. I can distinctly remember the time I spent studying with them growing up, going through essays with my mom, practicing vocabulary with my dad, and learning quadratics and calculus from my brother. My excitement to spend time with them fostered an excitement for learning that I continue to carry with me.

I would like to thank my grandma, Mary, for encouraging all of her grandchildren to explore, see the world, and pursue meaningful passions.

I would like to thank Eden Borsack, the love of my life, for all the understanding and support she has given to me during my program, and for the many more joyous years we will spend together. Eden, you are the most caring person, and I couldn't imagine a better partner-in-law-abiding. You are also the best dog (and chicken) mom in the world. I would also like to thank our dog, Hoodoo, whose sheer joy at seeing me come home at the end of each day helped motivate me throughout my program. I love you both more than anything in the world.

I would like to thank all my track coaches and teammates who helped me to develop a confidence in myself that extended beyond the races and repeats. Special thanks to Marilyn Hantgin, Anthony Garibay, Travis Anderson, and Elysia Hodges who all helped me become a better person, leader, teacher, and friend.

A big thanks to Dr. Royya Modir and her team, as well as Dr. Isac Thomas and Dr Victor Pretorious, and his team for their excellent care to get me back to health as if I never missed a beat.

A big thanks to Mike Lubliner and Pat Boyle for not just their excellent friendship but for allowing me to live a balanced life on a graduate student budget.

TABLE OF CONTENTS

LIST OF TABLES

LIST OF FIGURES

ACKNOWLEDGEMENTS

First and foremost, I would like to acknowledge my mentor and advisor Professor Nisarg Shah. Nisarg's dedication to my success, realized through countless hours spent on scientific and career discussions, the revising of manuscripts, grants and presentations, as well as supporting me during unexpected life events, has been critical to my development over the last five years. Thank you for everything.

I would also like to acknowledge Doctor Nunzio Bottini for the staggering amount of insights and feedback he provided when considering how my research might be directed to one-day benefit patients in the clinic.

I would like to acknowledge the rest of my committee, Professor Jesse Jokerst, Professor Liangfang Zhang, for their support and feedback on my research.

I would like to thank Professor Frank Doyle and John Abel for initially taking me in as an undergraduate at UCSB and showing me the ropes of research. I would like to thank Professor Linda Petzold for continuing to mentor me and develop my passion for research. My time spent in the Petzold lab was integral to my decision to pursue a PhD.

I would like to acknowledge the staff at UCSD's Institute for the Global Entrepreneur for their help considering how to translate science from the benchtop into the real world for the benefit of others, with special thanks to Todd Hylton.

Lastly, I would like to thank the other members of the Shah lab, Bottini lab, and countless technicians across many facilities who helped me complete my graduate work. I'd like to especially recognize Matt Kerr, Wade Johnson, and Martina Zoccheddu.

Chapter 2, in full, is adapted with modifications from "Characterization of regulatory T cell expansion for manufacturing cellular immunotherapies", Biomaterials Science 2020, 8,

4186 with authors David A. McBride, Matthew D. Kerr, Shinya L. Wai, Yvonne Y. Yee, Dora A. Ogbonna, and Nisarg J. Shah.

Chapter 3, in full, is adapted with modifications from "Short-chain fatty acid-mediated epigenetic modulation of inflammatory T cells in vitro", Drug Delivery and Translation Research 2022, 13, 1912-1924 with authors David A. McBride, Nicholas C. Dorn, Mina Yao, Wade T. Johnson, Wei Wang, Nunzio Bottini, and Nisarg J. Shah.

Chapter 4, in full, is adapted with modifications from "Immunomodulatory Microparticles Epigenetically Modulate T Cells and Systemically Ameliorate Autoimmune Arthritis", Advanced Science 2023, 10(11), 2202720 with authors David A. McBride, Matthew D. Kerr, Wade T. Johnson, Anders Nguyen, Martina Zoccheddu, Mina Yao, Edward B. Prideaux, Nicholas C. Dorn, Wei Wang, Mattias N.D. Svensson, Nunzio Bottini, and Nisarg J. Shah.

VITA

2016 Bachelor of Science in Chemical Engineering, University of California Santa Barbara

2020 Master of Science in Chemical Engineering, University of California San Diego

2023 Doctor of Philosophy in Chemical Engineering, University of California San Diego

PUBLICATIONS

McBride DA, Kerr MD, Johnson WT, Nguyen A, Zoccheddu M, Yao M, Prideaux EB, Dorn NC, Wang W, Svensson MND, Bottini N, Shah NJ. "Immunomodulatory Microparticles Epigenetically Modulate T Cells and Systemically Ameliorate Autoimmune Arthritis". Advanced Science. March 2023. https://doi.org/10.1002/advs.202202720.

McBride DA, Dorn NC, Yao M, Johnson WT, Wang W, Bottini N, Shah NJ. "Short-chain fatty acid-mediated epigenetic modulation of inflammatory T cells in vitro". Drug Delivery and Translational Research. December 2022. https://doi.org/10.1007/s13346-022-01284-6.

Kerr MD, **McBride DA**, Johnson WT, Chumber AK, Najibi AJ, Ri Seo B, Stafford AG, Scadden DT, Mooney DJ, Shah NJ. "Immune-responsive biodegradable scaffolds for enhancing neutrophil regeneration". Bioengineering and Translational Medicine. March 2022. https://doi:10.1002/btm2.10309. (research article)

Kerr MD, **McBride DA**, Chumber A, Shah NJ. "Combining therapeutic vaccines with chemo- and immunotherapies in the treatment of cancer". Expert Opinion on Drug Discovery. August 2020. https://doi.org/10.1080/17460441.2020.1811673 (review article)

McBride DA, Kerr MD, Wai SL, Yee YY, Ogbonna DO, Shah NJ. "Characterization of regulatory T cell expansion for manufacturing cellular immunotherapies". 2020; Biomater. Sci. 8(15), 4186-4198. https://doi.org/10.1039/D0BM00622J

Lopez-Ramirez MA, Soto F, Wang C, Rueda R, Shukla S, Silvia-Lopez C, Kupor D, **McBride DA**, Pokorski JK, Nourhani A, Steinmetz NF, Shah NJ, Wang J. "Built-in Active Microneedle Patch with Enhanced Autonomous Drug Delivery". 2020; Adv. Mater. 32(1), 1905740. https://doi.org/10.1002/adma.201905740

McBride DA, Kerr MD, Wai SL, Shah NJ. "Applications of molecular engineering in T-cell-based immunotherapies". 2019; WIREs Nanomed Nanobiotechnol. 11:e1557. https://doi.org/10.1002/wnan.1557

McBride DA, Petzold LR. "Model-based Inference of a Directed Network of Circadian Neurons". 2018; Journal of Biological Rhythms. 33(5), 515 – 522. https://doi.org/10.1177/0748730418790402

ABSTRACT OF THE DISSERTATION

Design and Applications of Immunoregulatory Biomaterials in Autoimmune Disease

by

David A. McBride

Doctor of Philosophy in Chemical Engineering

University of California San Diego, 2023

Chronic autoimmune disorders collectively affect 5-7% of the global population and are a major public health concern. The prevailing paradigm for autoimmune disease treatment relies on immunosuppression, which can be effective but leaves patients susceptible to opportunistic or serious infections and cancer. Moreover, these therapies are not designed to correct immune dysfunction that underlies autoimmunity. For those that continue to experience disease symptoms, there is an unmet need for therapies that operate via immunoregulation and avoid generalized immunosuppression. A key challenge is that unlike diseases with known etiology, the pathogenesis of autoimmune diseases can be complex. However, a common feature involves hyperactivated immune cells that, left unchecked, can lead to permanent damage of healthy tissue. To this end, a key defect arises from a loss in the number and function of autoimmune-protective

cells called regulatory T cells (T_{reg}) that normally prevent immune responses against one's own cells and tissues. The premise of this dissertation is that enhancing T_{reg} can be harnessed to promote disease-specific immunoregulation without causing generalized immunosuppression. To test the premise, the work reported herein describes the development and applications of biomaterial-based disease modifying agents. Three methods are described. The first method described used an immunomodulatory nanocomplex formulation that differentially modulated immune cell metabolism to enhance T_{reg} over inflammatory T cells. A kinetic model describing T_{reg} enhancement confirmed a strong dependence on the initial T cell population. The second and third methods described demonstrated that the epigenetic modulation of immune cells can strongly influenced the immunophenotypic trajectories of T cells that favor a T_{reg} phenotype. Further, the formulation of a novel sustained biomaterial designed to locally enhance T_{reg} via epigenetic modulation and its application in a model of inflammatory arthritis is reported. Overall, this work paves the way for the systematic design and validation of immunoregulatory biomaterials for the treatment of autoimmune disorders.

CHAPTER 1

Introduction

1.1 Background

1.1.1 Unmet needs in autoimmunity

The immune system is a complex network of cells and signaling molecules that normally work together for generating protection against harmful pathogens and cancerous cells throughout the lifetime of an individual. An important feature of protective immunity is the capacity to distinguish self from non-self through molecular and cellular recognition mechanisms[1-3]. A loss in this capacity can lead to autoimmune disorders which are characterized by pathogenic immune responses against one's own healthy cells and tissues. While the underlying causes are complex, most autoimmune conditions are chronic and are frequently associated with specific tissue or organ systems but have systemic consequences[4-7]. The collective spectrum of autoimmune disorders affects 5-7% of the population globally, and this number is thought to be increasing as the populations ages[8].

Current treatments for autoimmune diseases generally either focus on inhibiting inflammatory signaling mechanisms systemically to slow tissue destruction[9]. While strides have been made to improve treatments, for example using immunosuppressive disease-modifying agents, a large fraction of patients have inadequately controlled disease and respond poorly to existing medications. In part, the inadequate disease control arises from the inability of immunosuppression to address the underlying breakdown in immunological function that drives disease pathogenesis while inducing generalized immune suppression which leaves patients at higher risk for opportunistic or serious infections and cancers. Thus, there is a

critically unmet need for immunoregulatory strategies that seek to repair dysregulation and promote immune homeostasis.

1.1.2 T_{reg} in autoimmune disease

Regulatory T cells (T_{reg}) play a crucial role in maintaining immune homeostasis and preventing excessive immune responses that can lead to autoimmune disorders.[3,4] T_{reg}, characterized by the expression of the transcription factor Foxp3, regulate immune responses through a number of mechanisms, including by suppressing autoreactive T cells. Dysfunctional T_{reg} are well recognized to be key contributors in autoimmune diseases such as rheumatoid arthritis, multiple sclerosis, and systemic lupus erythematosus. On the other hand, enhancement of T_{reg} in disease models has been demonstrated to ameliorate disease.[6] However, cell therapies that involve extraction, expansion, and reinfusion of T_{reg} face challenges in translation to the clinic.[10] Moreover, T_{reg} may even exhibit immunological plasticity and convert to a pathogenic phenotype in some patients.[11] Therefore, improving strategies that focus on enhancing the number and function of T_{reg} are critically needed.

1.1.3 Epigenetic modifications to enhance T_{reg}

Epigenetic modifications, such as DNA methylation and histone methylation or acetylation, play a critical role in regulating gene expression.[12] Immunomodulators that make epigenetic changes in T_{reg} can confer enhanced stability and function in inflammatory settings.[13,14] These changes may operate on multiple downstream pathways to enhance numerous genes involved in T_{reg} function while suppressing genes associated with inflammatory T cell function. Additionally, because epigenetic changes are durable these

modifications can enable long-term immune regulation, even after a cell is no longer directly exposed to the immunomodulatory agent.[14] Therefore, epigenetic modification might promote durable disease-protective T_{reg} in autoimmune diseases.

1.1.4 Immunometabolism modulation to promote T_{reg}

Modulation of immunometabolism is an alternate strategy for promoting T_{reg} differentiation and suppressive activity. Promoting fatty acid oxidation and oxidative phosphorylation or redirecting glucose metabolism towards alternate pathways can skew T cells towards T_{reg} and inhibit inflammatory T cell responses.[15,16] Leveraging this difference, agents that modulate immunometabolic pathways can promote T_{reg} differentiation, expansion, and stability.[17] Therapeutic strategies to control immunometabolism might restore T_{reg} function and immunoregulation in autoimmune diseases.

1.1.5 Biomaterials strategies to control drug delivery

Biomaterials have been widely used to improve drug delivery by, for example, enhancing spatiotemporal control over therapeutic release to allow for precise modulation of immune response.[18-22] In autoimmune disease, nano- and microscale biomaterials, including liposomes and polymer-based particles, may be used to target therapeutics to specific tissues to influence T cell fate and activation. Biomaterials may be injected directly at the site of disease to provide sustained release of immunological cues in a disease-specific microenvironment. By directly targeting specific cells and tissues, biomaterials enable reduced systemic exposure, drug-sparing doses, improved treatment efficacy and sustained therapeutic concentrations at

site of disease. An ideal biomaterial-based immunoregulatory therapy would be able to durably promote disease-specific T_{reg} while maintaining a favorable safety profile.

1.2 Objective and Overview

1.2.1 Objective

The objective of this dissertation is to develop and test biomaterials-based technologies to enhance T_{reg} for developing immunoregulatory therapies for autoimmune diseases, with a specific focus on autoimmune arthropathies.

1.2.2 Overview

This dissertation reports three topics of research towards the aforementioned objective. Chapter 2 is focused on the preparation and characterization of a nanomaterial comprised of cyclodextrin and rapamycin for the enhancement of T_{reg} manufacturing. Chapter 3 is focused on the preparation and characterization of butyrate-loaded liposomes to epigenetically modify T cells to enhance T_{reg} development. Chapter 4 describes the formulation and characterization of all-trans retinoic acid containing biodegradable microparticles for epigenetic modification of T cells to promote T_{reg} in vivo.

1.3 Significance

The work reported herein contributes to the development of new biomaterials-based disease modifying agents that are based on promoting disease-protective T_{reg}. This work demonstrates that the encapsulation of immunomodulators into biomaterials can facilitate metabolic and epigenetic modulation that enhance T_{reg}. Furthermore, sustained local delivery

of a T_{reg}-enhancing epigenetic modifier can mediate a systemic but disease specific immunomodulation. The results support the possibility of generating disease-specific suppression without the need for prior knowledge of the initiating antigens, but instead by leveraging cells that infiltrate the local microenvironment. Overall, these methods may be used as a foundation for developing new biomaterial therapeutic agents for autoimmunity.

1.4 Chapter 1 References

1. Iberg, C. A. & Hawiger, D. Natural and Induced Tolerogenic Dendritic Cells. The Journal of Immunology 204, 733–744 (2020).

2. ElTanbouly, M. A. & Noelle, R. J. Rethinking peripheral T cell tolerance: checkpoints across a T cell's journey. Nat Rev Immunol 21, 257–267 (2021).

3. Klein, L., Robey, E. A. & Hsieh, C.-S. Central CD4+ T cell tolerance: deletion versus regulatory T cell differentiation. Nat Rev Immunol 19, 7–18 (2019).

4. Gravallese, E. M. & Firestein, G. S. Rheumatoid Arthritis — Common Origins, Divergent Mechanisms. N Engl J Med 388, 529–542 (2023).

5. Finckh, A. Gilbert B, Hodkinson B, Bae SC, Thomas R, Deane KD, Alpizar-Rodriguez D, Lauper K. Global epidemiology of rheumatoid arthritis. Nature Reviews Rheumatology 18, 591–602 (2022).

6. Wahren-Herlenius, M. & Dörner, T. Immunopathogenic mechanisms of systemic autoimmune disease. The Lancet 382, 819–831 (2013).

7. Rosetti, F., Madera-Salcedo, I. K., Rodríguez-Rodríguez, N. & Crispín, J. C. Regulation of activated T cell survival in rheumatic autoimmune diseases. Nat Rev Rheumatol 18, 232–244 (2022).

8. Roberts, M. H. & Erdei, E. Comparative United States autoimmune disease rates for 2010–2016 by sex, geographic region, and race. Autoimmunity Reviews 19, 102423 (2020).

9. McInnes, I. B. & Gravallese, E. M. Immune-mediated inflammatory disease therapeutics: past, present and future. Nat Rev Immunol 21, 680–686 (2021).

10. Raffin, C., Vo, L.T. & Bluestone, J.A. Treg cell-based therapies: challenges and perspectives. Nat Rev Immunol 20, 158–172 (2020).

11. Svensson, M.N., Doody, K.M., Schmiedel, B.J., Bhattacharyya, S., Panwar, B., Wiede, F., Yang, S., Santelli, E., Wu, D.J., Sacchetti, C. and Gujar, R., Reduced expression of phosphatase PTPN2 promotes pathogenic conversion of Tregs in autoimmunity. Journ Clin Immuno, 129(3), pp.1193-1210. (2019)

12. Allis, C., Jenuwein, T. The molecular hallmarks of epigenetic control. Nat Rev Genet 17, 487–500 (2016).

13. Huehn, J., Polansky, J. K., & Hamann, A. Epigenetic control of FOXP3 expression: the key to a stable regulatory T-cell lineage?. Nature Reviews Immunology, 9(2), 83-89. (2009)

14. Lu, L., Lan, Q., Li, Z., Zhou, X., Gu, J., Li, Q., Wang, J., Chen, M., Liu, Y., Shen, Y. and Brand, D.D.. Critical role of all-trans retinoic acid in stabilizing human natural regulatory T cells under inflammatory conditions. Proceedings of the National Academy of Sciences, 111(33), pp.E3432-E3440.(2014)

15. Mangal, J.L.; Basu, N.; Wu, H.J.; Acharya, A.P. Immunometabolism: An Emerging Target for Immunotherapies to Treat Rheumatoid Arthritis. Immunometabolism 3(4):e210032 (2021)

16. Newton R, Priyadharshini B, Turka LA. Immunometabolism of regulatory T cells. Nat Immunol. May 19;17(6):618-25. (2016

17. Shi H, Chi H. Metabolic Control of Treg Cell Stability, Plasticity, and Tissue-Specific Heterogeneity. Front Immunol. Dec 11;10:2716. (2019)

18. Dellacherie, M. O., Seo, B. R. & Mooney, D. J. Macroscale biomaterials strategies for local immunomodulation. Nature Reviews Materials 4, 379–397 (2019).

19. Schudel, A., Francis, D. M. & Thomas, S. N. Material design for lymph node drug delivery. Nat Rev Mater 4, 415–428 (2019).

20. Cifuentes-Rius, A., Desai, A., Yuen, D., Johnston, A. P. R. & Voelcker, N. H. Inducing immune tolerance with dendritic cell-targeting nanomedicines. Nat. Nanotechnol. 16, 37–46 (2021).

21. Stabler, C. L., Li, Y., Stewart, J. M. & Keselowsky, B. G. Engineering immunomodulatory biomaterials for type 1 diabetes. Nat Rev Mater 4, 429–450 (2019).

22. Gammon, J. M. & Jewell, C. M. Engineering Immune Tolerance with Biomaterials. Adv. Healthcare Mater. 8, 1801419 (2019).

CHAPTER 2

Characterization of regulatory T cell expansion for manufacturing cellular immunotherapies

2.1 Abstract

Regulatory T cells (T_{reg}) are critical mediators of peripheral immune tolerance. T_{reg} suppress immune activation against self-antigens and are the focus of cell-based therapies for autoimmune diseases. However, T_{reg} circulate at a very low frequency in blood, limiting the number of cells that can be isolated by leukapheresis. To effectively expand T_{reg} ex vivo for cell therapy, we report the metabolic modulation of T cells using mono-(6-amino-6-deoxy)-β-cyclodextrin (βCD-NH2) encapsulated rapamycin (Rapa). We used a computational model to qualitatively describe the kinetics of T_{reg} expansion. Encapsulating Rapa in β-cyclodextrin increased its aqueous solubility ~154-fold and maintained bioactivity for at least 30 days. βCD-NH2-Rapa complexes (CRCs) enriched the fraction of CD4+CD25+FoxP3+ mouse T (mT) cells and human T (hT) cells up to 6-fold and up to 2-fold respectively and suppressed the overall expansion of effector T cells by 5-fold in both species. Combining CRCs and transforming growth factor beta-1 (TGF-β1) synergistically promoted the expansion of CD4+CD25+FoxP3+ T cells. CRCs significantly reduced the fraction of pro-inflammatory interferon-gamma (IFN-γ) expressing CD4+ T cells, suppressing this Th1-associated cytokine while enhancing the fraction of IFN-γ- tumor necrosis factor-alpha (TNF-α) expressing CD4+ T cells. The computational model describes the influence of the composition of the initial cell population on the enrichment of T_{reg} in vitro and reveals how differences in the expansion kinetics of mT and hT cells result in differences in their susceptibility to immunophenotypic modulation. CRCs may be an effective and potent means for phenotypic modulation of T cells

and the enrichment of T_{reg} in vitro and our findings contribute to the development of experimental and analytical techniques for manufacturing T_{reg} cell-based immunotherapies.

2.2 Introduction

Regulatory T cells (T_{reg}) are a subset of T cells that suppress aberrant activation of self-reactive effector lymphocytes and are widely regarded as the primary mediators of peripheral tolerance[1]. Cell-based therapy using T_{reg} effectively treats autoimmune diseases such as arthritis and type 1 diabetes in animal models and at least one clinical trial (NCT02772679) is underway to evaluate efficacy in humans[2-5]. However, sourcing T_{reg} from leukapheresis is inefficient as they circulate at a low frequency (3-5%) in the blood and therefore ex vivo expansion is required to enhance their numbers. Current expansion methods, which use natural or artificial antigen-presenting cells and interleukin-2 (IL-2), induce the activation of not only T_{reg} but also conventional T cells[6,7]. Because T_{reg} divide more slowly than effector T cells, the latter may significantly outgrow T_{reg}[8]. Therefore, T_{reg} must be highly purified and sorted to avoid transfusion of T effector cells, which can be challenging[9]. Furthermore, T_{reg}-mediated suppression could diminish after repetitive stimulation[10]. These requirements for expanding and isolating T_{reg} ex vivo limit their use for cell therapy.

One method to efficiently enhance T_{reg} is by expanding T cells in medium containing rapamycin (Rapa), a carboxylic lactone–lactam triene macrolide with antifungal, antitumor, anti-inflammatory properties[11]. Rapa is administered orally or intravenously for systemic immunosuppression to prevent organ transplant rejection[12,13]. Rapa inhibits the serine/threonine protein kinase called mammalian target of rapamycin (mTOR), which is involved in a broad range of physiological processes linked to the control of cell cycle[14]. Consistent with this

mechanism, Rapa locks T cell-cycle progression from G1 to S phase after activation, enhances T_{reg} number and maintains their function by preferentially reducing proliferation of effector T cells, while minimally affecting the regulatory T cell subset[15-18]. Rapa induces operational tolerance and suppresses the proliferation of effector T cells and decreases the production of proinflammatory cytokines by T cells in vivo and in vitro[19-22]. However, the poor aqueous solubility of Rapa, low stability in serum and short half-life (~10 hours at 37C) limits bioavailability and uptake by T cells[23,24].

Cyclodextrin monomers are well characterized cyclic oligosaccharides that form complexes with drug molecules via secondary hydrophobic interactions[25]. The formation of inclusion complexes with small molecule drugs delays the rate of drug release beyond that of diffusion alone[26]. The most common pharmaceutical applications of beta-cyclodextrin (βCD) derivatives are as excipients in clinical drug formulations to enhance the aqueous solubility of the complexed species, to improve the aqueous stability, photostability, and bioavailability of complexed drugs[27]. In vivo, βCDs have been shown to enhance drug absorption and oral bioavailability as well as facilitate drug transport across physiologic barriers and biological membranes. Complexes of Rapa with βCD derivatives improve solubility and stability of Rapa, while preserving bioactivity[28,29]. Prior experiments have quantified a K_d between Rapa and βCD derivatives in the micromolar range[30]. The high supramolecular affinity prolongs its bioavailability and therefore is an attractive choice for formulations to promote enhancements of the half-life of Rapa in vitro. The extended half-life of Rapa could synergize with other potent inducers of T_{reg}, including transforming growth factor-beta (TGF-β1), which mediates the transition of naïve T cells toward a regulatory phenotype with potent immunosuppressive potential[31].

To promote the enrichment of T_{reg} in vitro, we encapsulated and characterized the function of Rapa encapsulated in mono-(6-amino-6-deoxy)-β-cyclodextrin (βCD-NH2) forming cyclodextrin-Rapa complexes (CRCs). CRCs enhanced the solubility of Rapa in water 154 -fold and maintained bioactivity of Rapa for at least 30 days in solution. CRCs enriched the fraction by 5-fold of T_{reg} in vitro from both PBMC-isolated human T (hT) cells and splenocyte-isolated mouse T (mT) cells. CRCs synergize with TGF-β1 to enhance the enrichment of murine T_{reg}. The combination also enhanced the fraction of human T_{reg} over single factor treatments. CRCs reduced interferon-gamma (IFN-γ) expression by T cells and increased the fraction of T cells that expressed tumor necrosis factor-α (TNF-α) without IFN-γ. In hT cells, combining CRC and TGF-β1 further enhanced the enrichment of IFN-γ- TNF-α+ T cells, while in mT cells the addition of TGF-β1 increased the fraction of IFN-γ+ T cells, both alone and in combination with CRCs.

We developed a computational model to describe the expansion kinetics of T_{reg} enrichment. The model recapitulated key features associated with CRCs and TGF-β1 individually and in combination on T_{reg} expansion. A sensitivity analysis demonstrated that the initial fraction of naïve T cells is critical for ensuring a high fraction of T_{reg}. CRCs are a potent delivery system for Rapa to enhance the preferential expansion of T_{reg} and inhibiting inflammatory T cells, and the model may serve to predict T_{reg} expansion in manufacturing practice.

2.3 Results

2.3.1 Mono-(6-amino-6-deoxy)-beta-cyclodextrin increases aqueous solubility of Rapa

To test the encapsulation of Rapa and improve the aqueous solubility, we used the βCD Mono-(6-amino-6-deoxy)-beta-cyclodextrin (βCD-NH_2), forming βCD-NH_2-Rapa inclusion complexes (Figure 2.1a, b). We first measured loading of Rapa in 0-4 % (w/v) βCD-NH_2 in deionized water (Figure 2.1c). The loading of Rapa in the inclusion complexes was quantified using a standard curve (Figure 2.9a). The amount of Rapa in solution was proportional to the βCD-NH_2 concentration and achieved a maximum loading of 4.02 ± 0.52 mg/mL in a 4 wt% solution of βCD-NH_2 on day 7 (Figure 2.1d). The supernatant of the solution prepared without βCD-NH_2 did not have a detectable amount of Rapa. To test the stability of the inclusion complex, CRC containing supernatant was transferred to new tubes that were incubated at room temperature over 30 days. In all samples, the amount of Rapa initially decreased and equilibrated after 7 days at 82.5% ± 1.7% of the initial concentration (Figure 2.1e).

2.3.2 Rapa preferentially expands T_{reg}

To test the suppressive activity of Rapa on T cell proliferation and enriching regulatory T cells (T_{reg}), we measured its dose-dependent effect in vitro. mT cells were isolated from splenocytes using magnetic bead-based depletion. Approximately 90% of the cells were either $CD4^+$ or $CD8^+$ T cells post-enrichment (Figure 2.9b.). We tested a broad range of Rapa concentrations (1 μM, 100 nM, 10 nM) (Figure 2.2a) and measured fold-expansion and the frequency of $CD4^+CD25^+FoxP3^+$ T cells relative to the total number of $CD4^+$ T cells seven days post-activation. T cell expansion in 1 μM Rapa (5.26 ± 0.15) was comparable to 10 nM (6.13 ± 0.96) and 100 nM concentration (4.65 ± 0.63 -fold expansion) (Figure 2.2b), and were significantly lower compared to the Dynabead-only (25.8 ± 1.2) and DMSO controls (20.7 ± 1.2 -fold expansion). The fraction of $CD4^+$ T cells that were also $CD25^+FoxP3^+$ was similar at

10 nM (10.3% ± 1.3%), 100 nM (10.3% ± 1.6%), and 1 μM (12.2% ± 0.7%) and significantly higher compared with the Dynabead-only (2.96% ± 1.51%) and DMSO controls (1.54% ± 0.78%) (Figure 2.2c). To examine the effects of DMSO-solubilized Rapa on expansion of $CD25^{hi}$ and $CD25^{lo}$ $CD4^{+}$ T cell subsets, we conducted a proliferation assay using carboxyfluorescein succinimidyl ester (CFSE). In the absence of Rapa, $CD25^{lo}$ T cells proliferated more than $CD25^{hi}$ T cells. When 100 nM Rapa was added, both $CD25^{hi}$ and $CD25^{lo}$ T cells proliferated a similar amount, with both groups expanding less than controls (Figure 2.10a).

2.3.3 Cyclodextrin-Rapa complexes potently suppress T cell proliferation

To test the bioactivity of Rapa encapsulated in CRCs, we compared the phenotypic modulation of murine T cells mediated by CRCs and Rapa solubilized in a DMSO carrier (Figure 2.2d). In contrast to DMSO-solubilized Rapa, T cell expansion was strongly dependent on the concentration of CRCs, but unaffected by βCD-NH_2 alone (Figure 2.2e). 10 nM CRCs did not substantially affect T cell expansion (21.4 ± 2.1-fold) compared to the Dynabead-only control (24.2 ± 1.2 -fold). T cell expansion with 100 nM CRCs (14.4 ± 1.7 -fold) and 1μM CRCs (6.93 ± 0.91 -fold) was significantly lower than the Dynabead-only and βCD-NH_2 (24.1 ± 1.6-fold) controls. In addition, the suppression of T cell expansion mediated by 1μM CRCs was comparable to 100 nM DMSO-solubilized Rapa (7.81 ± 1.75 -fold expansion). Similarly, the enrichment of $CD4^{+}CD25^{+}FoxP3^{+}$ murine T cells was comparable between the 10 nM CRC (1.46% ± 0.10%), Dynabead-only control (1.57% ± 0.25%), and βCD-NH_2 control (1.21% ± 0.21%) (Figure 2.2f). These cells were significantly enriched with 100 nM CRC (2.29% ± 0.26%) and 1 μM CRC (5.86% ± 0.28%).

2.3.4 TGF-β1 and CRCs promote T_{reg} enrichment through distinct mechanisms

To test if combinations of immunomodulatory factors might further enrich $CD4^+CD25^+FoxP3^+$ T_{reg}, we tested transforming growth factor-beta (TGF-β1) in combination with Rapa. Murine T cells were cultured in media containing either 5 ng/mL TGF-β1, 1 μM CRCs or both factors and quantified the expansion of T cells as well as the fraction of $CD25^+FoxP3^+CD4^+$ T cells (Figure 2.3a). TGF-β1 alone did not suppress the expansion of T cells (26.8 ± 3.2 -fold) relative to the Dynabead-only control (24.2 ± 1.2 -fold). However, TGF-β1 in combination with 1 μM CRCs suppressed T cell expansion (6.73 ± 0.82 -fold expansion) which was comparable to 1 μM CRCs alone (6.93 ± 0.91 -fold expansion) (Figure 2.3b). TGF-β1 in combination with 1 μM CRCs (21.1% ± 0.46%) increased the fraction of T_{reg} more than TGF-β1 (10.8% ± 0.46%) or 1 μM CRCs (5.86% ± 0.28%) alone (Figure 2.3c). Strikingly, this enrichment was greater than the sum of the enhancement mediated by either CRCs or TGF-β1 alone (Figure 2.3d). We compared $CD4^+FoxP3^+$ T_{reg} and the $CD4^+FoxP3^-$ T cell counts between the test groups (Figure 2.3e). 100 nM and 1 μM CRCs reduced the number of total $CD4^+FoxP3^-$ cells compared with the Dynabead-only control but did not affect the number of T_{reg}. In contrast, TGF-β1 increased the number of T_{reg} relative to control but did not significantly affect proliferation of $CD4^+FoxP3^-$ T cells. In combination, TGF-β1 and 1 μM CRC increased T_{reg} and decreased $CD4^+FoxP3^-$ T cells.

2.3.5 CRCs and TGF-β1 have opposing effects on IFNγ expression in murine T cells

As the immunophenotype of T cells is associated with its cytokine profile, we next measured the difference in production of pro-inflammatory cytokines in mT cells with

combination of single factor CRCs and TGF-β1 (Figure 2.4a,b). The fraction of $CD4^+$ IFN-γ^+ T cells was significantly depleted in CRC-treated cells (10.0% ± 0.6%) relative to Dynabead-only control (30.6% ± 2.9%). $CD4^+$ IFN-γ^+ T cells were enriched in the presence of TGF-β1 alone (44.6% ± 1.0%) (Figure 2.4c). The combination of CRCs and TGF-β1 (28.9% ± 2.7%) was lower than TGF-β1 alone, but similar to the Dynabead-only and DMSO controls.

2.3.6 CRCs preferentially enrich $CD4^+CD25^+FoxP3^+$ primary human T cells

We next tested the Rapa concentration-dependent enrichment of $CD4^+CD25^+FoxP3^+$ human T_{reg} with DMSO-solubilized Rapa. T cells were enriched from donor derived PBMCs using magnetic depletion to a purity of approximately 85% $CD8^+$ and $CD4^+$ T cells (Figure 2.9c) and subsequently activated using Dynabeads. The suppression in hT cell expansion was similar at 1 μM (8.84 ± 0.62 -fold), 100 nM (8.88 ± 2.72 -fold), and 10 nM (8.92 ± 1.41 -fold) DMSO-solubilized Rapa, relative to the Dynabead-only control (24.5 ± 3.8 -fold) (Figure 2.5a,b). The enrichment in $CD4^+CD25^+FoxP3^+$ human T_{reg} at 1 μM (22.1% ± 1.7%), 100 nM (22.2% ± 0.81%), and 10 nM Rapa (21.3% ± 1.3%) was similar and greater than the Dynabead-only control (12.0% ± 2.2%) (Figure 2.5c).

To test the bioactivity of CRCs with hT cells, we measured CRC-mediated suppression on hT cell expansion with 1 μM, 100 nM, and 10 nM CRCs (Figure 2.5d). At 10 nM, T cell expansion was comparable to the Dynabead-only control (23.8 ± 2.5 -fold expansion) as well as the βCD-NH_2 control (25.0 ± 2.7 -fold expansion). However, at 100 nM (8.7 ± 1.2 -fold) and 1 μM CRC (7.7 ± 0.6 -fold), suppression in T cell expansion was comparable to DMSO-solubilized 100 nM Rapa (9.0 ± 0.6 -fold) (Figure 2.5e). Similarly, the enrichment of $CD4^+CD25^+FoxP3^+$ T_{reg} at 10 nM CRCs (12.0% ± 1.2%) was comparable to the Dynabead-

control (14.1% ± 1.6%) and βCD-NH_2 control (14.5% ± 1.5%). Enrichment at 100 nM (21.8% ± 1.2%) and 1 μM (21.4% ± 1.4%) CRCs was higher than the Dynabead-control and comparable to 100 nM DMSO-solubilized Rapa (22.3% ± 1.9%) (Figure 2.5f).

2.3.7 Expansion with TGF-β1 and CRCs results in high fraction of $CD4^+CD25^+FoxP3^+$ hT cells

To test the effect of TGF-β1 in combination with CRCs on T_{reg} enrichment we cultured PBMC-derived hT cells with the same single-factor and combination treatments previously described for murine T cells (Figure 2.6a). CRCs in combination with TGF-β1 (3.2 ± 0.4 -fold expansion) suppressed hT cell proliferation more than CRCs (5.3 ± 1.2 -fold expansion) or TGF-β1 (22.3 ± 0.4 -fold expansion) alone (Figure 2.6b). The fraction of $CD25^+FoxP3^+$ T cells among $CD4^+$ T cells was highest in the combination group (63.5% ± 7.4%), though the enrichment was not greater than the single treatment CRCs (58.1% ± 2.7%) and TGF-β1 (32.9% ± 0.6%) combined (Figure 2.6c).

2.3.8 TGF-β1 and CRCs reduce IFNγ expression, enrich $IFN\gamma^-TNF\alpha^+$ human T cells

To characterize the effect of CRCs on cytokine expression in hT cells alone and in combination with TGF-β1, we expanded T cells as previously described. After 7 days of expansion, the cells were re-stimulated with phorbol 12-myristate 13-acetate (PMA) and ionomycin and analyzed for interferon-γ (IFNγ) and tumor necrosis factor-α (TNFα) expression (Figure 2.7a,b). DMSO-solubilized 100 nM Rapa (8.1% ± 0.4%) and 1 μM CRCs (8.6% ± 0.5%) reduced IFNγ expression of $CD4^+$ hT cells relative to a DMSO-treated control (14.7% ± 1.1%) and untreated control (12.4% ± 1.1%) (Figure 2.7c). TGF-β1 alone (11.3% ± 0.4%) did

not reduce IFNγ relative to controls. However, TGF-β1 in combination with 1 μM CRCs (5.2% ± 0.3%) decreased IFNγ more than TGF-β1 or 1 μM CRCs alone. TGF-β1 (49.5% ± 1.6%) increased the fraction of $IFN\gamma^{-}TNF\alpha^{+}$ more than the combination of 1 μM CRCs and TGF-β1 (46.0% ± 0.7%) relative to untreated control (31.5% ± 4.8%) (Figure 2.7d). DMSO-solubilized 100 nM Rapa (34.6% ± 4.3%) did not increase the $IFN\gamma^{-}TNF\alpha^{+}$ fraction relative to DMSO containing controls (31.9% ± 1.5%), while 1 μM CRCs (39.6% ± 2.9%) enhanced the fraction relative to control.

2.3.9 Computational model characterizes the dependence of T_{reg} enrichment to initial cell population

To explain how culture conditions and starting cell populations contribute to experimental outcomes and variance, we developed and optimized a model describing the kinetics of differentiation and expansion of model naïve (T_n), regulatory (T_r) and effector (T_e) $CD4^{+}$ T cells (Figure 2.8a). Details of the model and parameter fitting may be found in the Supplementary Information. First, we looked at the sensitivity to the initial T_r population over a range of commonly reported T_{reg} splenocyte fractions. We initialized the model with 1%, 2%, and 3% T_r with a fixed T_e (36.5%) fraction and variable T_n (62.5%, 61.5% and 60.5%) fraction that correspond to the averages of values from isolated murine splenocytes analyzed via flow cytometry (Figure 2.9d). This revealed that the post-expansion T_r fraction was most sensitive to the initial T_r fraction in the 1 μM CRC condition with a range of 4.9% - 13.8%, while outcomes for control (3.0% - 8.7%), TGF-β1 (39.7% - 42.2%), and combination (53.1% - 55.6%) conditions are tightly grouped and independent of the initial T_r fraction (Figure 2.8b). The results from the model were consistent with experimental data for control (5.80% ± 1.66% vs 2.61% ± 1.03%), 1 μM CRC (9.38% ± 2.58% vs 12.6% ± 5.9%), and TGF-β1 (39.1% ±

6.1% vs 34.6% ± 6.3%), and slightly underestimated T_r enrichment by the combination of CRC/TGF-β1 (52.2% ± 6.5% vs 62.7% ± 4.2%), but still demonstrated a synergistic effect (Figure 2.8c). Due to the high variability in naïve T cell fraction in human peripheral blood samples, we next analyzed the sensitivity of final T_r fraction to the initial naïve-to-effector T cell ratio. We quantified the effect of changing the initial T_e fraction between 18.2%, 36.5% and 54.7% while fixing the T_r fraction at 2%. The range of values for the initial T_e fraction was chosen to cover the range of observed fractions of effector T cells seen in human and mouse samples. The impact of variance in initial T_e fraction on the final T_r fraction was significantly higher with TGF-β1 (27.4% - 47.3%) and combination of CRC/TGF-β1 (39.4% - 60.5%), and minimal in the control (5.5% - 6.1%) and with CRCs only (9.0% - 9.7%) (Figure 2.8d). Finally, to characterize the role that the delay in hT cell expansion kinetics relative to mT cells plays in abrogating the synergistic effect of combination CRC/TGF-β1, a modified model was used in which expansion did not begin until 48 hours after differentiation. Results from the modified model revealed that the additive T_{reg} enrichment observed with 1 μM CRCs (7.86% ± 2.35%) or TGF-β1 (36.8% ± 5.3%) alone was not significantly different than the combination of both factors (45.6% ± 5.6%) (Figure 2.8e).

2.4 Discussion

Here we demonstrate T_{reg} are enriched up to 5-fold in vitro in which β-cyclodextrin encapsulated Rapa complex (CRC) plays a key role in the differential modulation of proliferating T cell subsets. The encapsulation of Rapa in the CRC enhanced its activity in vitro

and delivery to T cells, synergizing with TGF-β1 to efficiently produce mouse and human T_{reg}. Encapsulation of Rapa in the CRC by equilibrium mixing was directly proportional to the concentration of the βCD-NH_2 concentration, up to the limit of solubility of βCD-NH2. The CRC complex significantly improved the aqueous solubility of Rapa by over 2 orders of magnitude and was stable in solution for at least one month. The addition of CRCs in T cell growth medium selectively suppressed the expansion of $CD4^+FoxP3^-$ T cells in a dose-dependent manner and enhanced the fraction of $CD4^+FoxP3^+$ T_{reg} with both mT and hT cells. The coadministration of the T cell modulating factor TGF-β1 and CRC enriched mouse and human T_{reg} through the expansion of $CD4^+FoxP3^+$ T_{reg} and suppression of $CD4^+FoxP3^-$ T cells respectively, with evidence of synergism in mouse T_{reg} expansion. The findings are consistent with the observations of CRC-mediated reduction in the expression of the inflammatory mediator, IFN-γ, in both mT and hT cells.

Mono-(6-amino-6-deoxy)-beta-cyclodextrin enhances the aqueous solubility of Rapa over 100-fold and is a stable carrier for Rapa. Mono-(6-amino-6-deoxy)-beta-cyclodextrin was chosen as it has significantly enhanced solubility compared to unmodified beta-cyclodextrin and previous reports found that hydroxypropyl-beta-cyclodextrin minimally improved Rapa solubility [32]. The ~1:100 ratio of solubilized Rapa to βCD-NH_2s is comparable to Rapa encapsulation with other βCD molecules. After an initial decrease in concentration βCD-NH_2-Rapa complexes maintained a stable concentration in solution and retained their bioactivity for up to one month (Figure 2.11). The initial drop in concentration is likely due to the small fraction that dissociates to establish equilibrium.

The CRCs potently modulated both mT and hT cells, supporting the relevance of this delivery strategy for Rapa in generating T_{reg} in vitro. In prior work, particle systems composed

of poly(lactide-co-glycolide) (PLGA), poly(d,l-lactide) (PDLLA), poly(ε-caprolactone) (PCL), and poly(alkyl cyanoacrylates) (PACs) have been used to improve the bioavailability of Rapa in vivo and improved its delivery to target tissues before release [12, 33, 34]. However, in contrast to in vivo delivery, particle-based Rapa delivery systems are unsuitable for in vitro expansion as their uptake by activated T cells is highly inefficient. Moreover, the high concentration of degradable synthetic polymers in vitro would likely be cytotoxic. The introduction of synthetic polymers would also increase the complexity of manufacturing in vitro generated T_{reg}.

The apparent effect of Rapa in the CRC was diminished by approximately 100-fold in mT cells and 10-fold in hT cells compared to DMSO-solubilized Rapa. In contrast to cyclodextrins, DMSO is a cell membrane permeabilizing agent that directly inserts and disrupts the cell membrane and thereby facilitates intracellular drug delivery. However, the use of DMSO for intracellular delivery is not a scalable strategy for T cell manufacturing in vitro. Consistent with prior results, we observe that $CD4^+$ T cells are highly sensitive to the concentration of DMSO and even low doses potently suppresses their expansion [35]. Moreover, DMSO are potentially toxic at the high concentrations that are often used to manufacture cells, which complicates direct use in patients, and its removal is a complex processes associated with a detrimental osmotic shock to the cells [36]. In contrast, and consistent with prior reports, we observe that T cell growth, function and phenotype is not affected by βCD-NH_2 alone.

The difference in the intracellular concentration of Rapa may have a considerable effect on the enrichment of T_{reg} because of the concentration-dependent effect on mTOR complex formation (mTORC1 and mTORC2). We observed that the suppression in mT cell expansion was dose dependent for 10 nm, 100 nm, and 1 μM CRC, while enrichment in T_{reg} was observed for 1 μM CRC. These findings are consistent with previous reports, which have established that

mTORC1 is more sensitive to Rapa-mediated inhibition than mTORC2 [37]. Inhibition of mTORC1 prevents the differentiation of T helper (Th) 1 $CD4^+$ T cells, consistent with the reduction of IFN-γ expression of T cells expanded with CRCs, and is an important step for enriching T_{reg}[38] On the other hand, the inhibition of mTORC2 enhances the suppressive capacity of T_{reg}[39]. Robust mTORC2 inhibition requires sustained exposure to higher concentrations of Rapa, and therefore CRCs are preferred over DMSO as they are an inert carrier and preserve bioactivity of Rapa, and thereby sustain presentation to T cells[40].

The enhancement in murine T_{reg} with CRCs together with TGF-β1 was greater than the sum of T_{reg} when either factor was applied individually. CRCs increased the fraction T_{reg} primarily via suppression of $CD4^+CD25^+FoxP3^-$ T cell expansion whereas TGF-β1 increased the fraction of T_{reg} by increasing the absolute number of $CD4^+CD25^+FoxP3^+$ T cells. This observation is supported by prior observations of the synergistic effect of Rapa and TGF-β1 for the in vitro induction of T_{reg} from naïve $CD4^+$ T cells. The in vitro enhancement of human T_{reg} from naïve T cells by TGF-β1 alone is consistent with prior reports. However, in contrast to splenocyte-isolated mT cells, naïve $CD4^+$ T cells must be isolated from human blood and only make up 1-10% of leukocytes, with significant variation between donors. This variability supports the combined use of both Rapa and TGF-β1 to generate human T_{reg}. Here, we confirmed that the immunomodulation by Rapa and TGF-β1 extends to polyclonal T cells, consisting of both mature and naïve T cells (Figure 2.9d). The enhancement of the T_{reg} from heterogenous T cell subsets is clinically relevant as PBMC-isolated T cells are often a combination of memory T cells and recently activated naïve T cells.

The reduction in IFNγ expression and enrichment of $IFN\gamma^-TNF\alpha^+$ mediated by CRCs was consistently observed in both mT and hT cells. In mT cells, TGF-β1 enhanced the

expression of both IFNγ and TNFα. This is consistent with prior reports characterizing the inhibition of naïve murine T cell activation and enhancement of Th1 cells in a mixed T cell population by TGF-β1 [41]. Because the initially isolated T cells contained a mixed population of T cell subsets, the TGF-β1 likely enhanced activation of pre-existing Th1 T cells. In contrast, with hT cells, the combination of TGF-β1 and CRCs decreased the fraction of IFNγ$^+$ T cells more than either factor individually. The difference in cytokine expression between mT and hT cells suggests that the source of T cells for T_{reg} enrichment is important. Furthermore, TGF-β1 did not enhance IFN-γ expression in hT cells and supports the translation of this approach for T_{reg} expansion in the clinic, where it will likely be difficult to enrich high numbers of naïve autologous T cells. CRCs enhanced the fraction of IFN-γ$^-$TNF-α$^+$ T cells. This observation is consistent with prior reports that have demonstrated that T_{reg} priming via the TNFRII receptor enhances T_{reg} function and TNFRII marks a highly immunosuppressive T_{reg} subset [42].

The kinetic growth model describing T_{reg} expansion and differentiation supported the role of CRCs in mediating T_{reg} enrichment primarily through suppression of effector T cell expansion, and that of TGF-β1 through the differentiation of naïve T cells into T_{reg}. Strikingly, the model accurately recapitulates the synergistic effect of CRCs and TGF-β1 in murine T cells, and the incorporation of a delay in T cell expansion abrogates this effect, providing a possible explanation for why synergism is not observed under the same conditions with hT cells. However, the model under-represents the fraction of T_{reg} in the murine combination condition, and in human control and CRC only conditions. CRCs inhibit IFN-γ, a key driver of Th1 differentiation. Thus, in the combination conditions the rate of differentiation into effector CD4 T cells is likely lower than predicted by the model, and a larger fraction differentiates into T_{reg}. The model is also useful for evaluating the distribution of final T cell subsets based on the initial

fractions and suggests that a high naïve-to-effector ratio improves the enrichment of T_{reg}, confirming the importance of pre-sorting for naïve T cells before expansion and phenotypic modulation in clinical applications [43]. As quality control guidelines for ACT based T_{reg} therapies are established, this model may serve as the basis for a tool to determine product sensitivity to key input parameters and apply process controls to minimize variance in T_{reg} manufacturing, a necessary step in developing good manufacturing practice protocols [44].

Our findings collectively suggest that the βCD-NH2 encapsulated Rapa enhances T_{reg} in vitro. CRCs increase the bioavailability of Rapa due to strong hydrophobic interactions with βCD-NH2, and the stability of the inclusion complex was confirmed via spectrophotometry. Compared with DMSO, the CRCs (i) improve the solubility of Rapa without inducing T cell toxicity, (ii) shield Rapa from degradation, thereby increasing half-life and uptake by T cells, (iii) synergize with TGF-β1 to enhance preferential expansion of Treg. Additionally, CRCs significantly decrease the production of IFN-γ by effector T cells and thereby reduces naïve T cells differentiation into a Th1 phenotype. The enhancement in TNF-α expression may act to prime the T_{reg} and enhance functionality. The kinetic model recapitulates the synergism between the CRCs and TGF-β1 in modulating the kinetics of T_{reg} expansion in vitro and evaluates parameters for scalable manufacturing methods for immune cell therapies with T_{reg}.

2.5 Materials and Methods

2.5.1 Materials

Basal T cell culture media was prepared from RPMI medium 1640 powder (Gibco) supplemented with 10% HI-FBS, 1% penicillin-streptomycin, 1 mM sodium pyruvate, 50 μM β-mercaptoethanol and 0.1 mM non-essential amino acids. Primary mT and hT cell media used

for expansion was further supplemented with 50 IU/mL murine recombinant IL-2 (Peprotech) and 50 IU/mL human recombinant IL-2 (Biolegend), respectively. Rapa was purchased from LC Laboratories. Mono-(6-amino-6-deoxy)-β-cyclodextrin, with an upper solubility limit of 4.2 wt% in water, was purchased from Cavcon (CAS#: 29390-67-8). Dimethylsulfoxide (DMSO) was purchased from Sigma-Aldrich.

2.5.2 Generation and Characterization of CRCs

CRCs were prepared by first creating 0%, 1%, 2%, 3%, and 4% (wt/v) solutions of βCD-NH2 in DI water. 500 μL of each solution was added to 1 mg of Rapa and vortexed at 3200 rpm for 5 minutes, and then agitation was maintained at 1500 rpm until sampling. The inclusion complexes were equilibrated over 7 days as previously reported. Subsequently, the solution was spun down (21000 rcf, 5 min) and the supernatant was collected and analyzed on day 7. The amount of Rapa in the supernatant was analyzed using UV-vis spectrophotometry ($\lambda = 278$ nm) (Figure 2.9a).

2.5.3 Primary T cell Isolation

All animal procedures were approved by the Institutional Animal Care and Use Committee at UC San Diego. Primary murine T cells were freshly isolated from C57BL/6J mice. A single cell suspension of splenocytes was created and T cells were isolated via magnetic depletion using CD4+ or pan-T cell isolation kits (Miltenyi Biotec) according to the manufacturer's recommendations. Murine T cells were not cryopreserved as the cells were found to be sensitive to DMSO at concentrations greater than 1 %(v/v) and reconstituted murine T cells expanded less than freshly isolated cells (data not shown).

Primary hT cells were isolated from anonymous donor blood concentrate enriched in the buffy coat (Stanford Blood Bank and San Diego Blood Bank). PBMCs were enriched from buffy coat within 24 hours of collection using density separation in a Ficoll gradient (Lymphopure). PBMCs were then transferred to serum-free cell freezing media (Bambanker) and frozen overnight at -80 °C. Aliquots were then stored in liquid nitrogen and used within 6 months. Pan T cells were isolated from thawed PBMC aliquots using magnetic depletion (Dynabeads Untouched Human T cells, Invitrogen) according to the manufacturer's recommendations.

2.5.4 In vitro T cell expansion assays

Primary mT and hT cells were isolated as previously described and resuspended in T cell culture media without IL-2. Mouse or human αCD3/αCD28 activator Dynabeads (Invitrogen) were added to mT and hT cells, respectively, according to manufacturer recommendations and cells were plated in 96 well plates. After one day of culture, recombinant murine or human IL-2 was added to cultures at a concentration of 50 IU/mL along with any factors being tested. On the seventh day of culture cells were enumerated with cell counting using a hemocytometer and analyzed with flow cytometry. In cultures testing the suppressive effects of DMSO- or βCD-NH2-solubilized Rapa, Rapa was added at concentrations of 10, 100 or 1000 nM and TGF-β1 was used at 5 ng/mL. DMSO concentration was maintained across groups at a concentration of 0.1% (v/v). For CFSE analysis, cells were stained prior to activation with Dynabeads with CFSE (CFSE Cell Division Tracker Kit, Biolegend) according to manufacturer's instructions. Cells stained with CFSE were analyzed after 72 hours with flow cytometry.

2.5.5 Cytokine Assay

Primary mT and hT cells were cultured as previously detailed. 5 days post activation with Dynabeads, the cells were restimulated with PMA and ionomycin and blocked with Brefeldin A (Cell Activation Kit with Brefeldin A, Biolegend) for 5 hours according to manufacturer's instructions. Cells were then washed, stained, and analyzed with flow cytometry.

2.5.6 Flow Cytometry

Antibodies for anti-mouse CD25 (PC61), CD8α (53-6.7), CD4 (GK1.5), CD45 (30-F11), TNF-α (MP6-XT22), IFN-γ (XMG1.2), and anti-human CD8α (RPA-T8), CD4 (SK3), CD25 (M-A251), CD45 (HI30), TNF-α (Mab11), and IFN-γ (B27) were purchased from Biolegend. Antibodies for anti-mouse FoxP3 (FJK-16s) and anti-human FoxP3 (236A/E7), were purchased from eBioscience. Samples analyzed for FoxP3 expression were fixed and permeabilized using the FoxP3/Transcription Factor Staining Buffer Set (eBioscience) according to manufacturer supplies protocols. Samples analyzed for TNF-α and IFN-γ expression but not FoxP3 were fixed using the IC Fixation Buffer (eBioscience) and permeabilized using Permeabilization Buffer (eBioscience) according to manufacturer supplied protocols. All cells were gated based on forward and side scatter characteristics to limit debris. Gating for surface markers, cytokines, and FoxP3 were determined using fluorescence-minus-one controls.

2.5.7 Computational Modeling and Parameter Analysis

To calculate the parameter values in the model we used data sets from our experiments. To determine the sensitivity of the model outputs to initial model regulatory T cell (Tr) fraction the model was initialized with 1%, 2%, and 3% Tr with a fixed model effector T cell (Te) (36.5%) fraction and variable model naïve T cell (Tn) (62.5%, 61.5% and 60.5%.The range of initial Tr values examined, as well as the starting Te and Tn values, were informed by analysis of T cell isolations and naïve T cell staining for CD62L and CD44. To determine the sensitivity of the model to initial Te fraction the model was initialized with 18.2%, 36.5% and 54.7% Te, with a fixed Tr (2%) and variable Tn (79.8%, 61.5%, 43.3%). An Excel sheet detailing parameter calculation and all code used to generate the model may be found at https://github.com/Shah-Lab-UCSD/Treg_Enrichement_Model_In_Vitro. All code was written to be compatible with Python 3.7.6.

2.6 Chapter 2 Acknowledgements

Chapter 2, in full, is adapted with modifications from "Characterization of regulatory T cell expansion for manufacturing cellular immunotherapies", Biomaterials Science 2020, 8, 4186 with authors David A. McBride, Matthew D. Kerr, Shinya L. Wai, Yvonne Y. Yee, Dora A. Ogbonna, and Nisarg J. Shah.

2.7 Chapter 2 Model Details Appendix

2.7.1 Model Background

In the present study, we developed a deterministic kinetic model of CD4 T cell expansion and differentiation to provide insight into the observed synergistic effects of CRCs and TGF-β1 on T_{reg} enrichment and account for differences between observed effects on hT

and mT cell differentiation. The model includes three cell populations, namely naïve CD4 T cells (T_n), effector CD4 T cells (T_e), and regulatory T cells (T_r), and the interactions between these populations are depicted in Figure 2.8a.

2.7.2 Model Governing Equations

In this model, we aimed to describe T cell developmental kinetics as simply as possible to provide a basis for treating T_{reg} manufacturing as a bioreactor and allow for direct fitting of relevant differentiation and expansion parameters based on observed phenotypic and cell expansion data. Thus, the model does not directly consider intracellular processes and broadly classifies mature non-T_{regs} as effector T cells. The differential changes in populations due to differentiation and expansion are and the resultant governing equations, as well as their analytical solutions, are summarized in Table S1.

To describe differentiation kinetics, we set up the model such that T_n cells differentiate into T_r and T_e according to the equations

$$\frac{dT_r}{dt}_{diff} = k_r T_n \tag{1}$$

$$\frac{dT_e}{dt}_{diff} = k_e T_n \tag{2}$$

$$\frac{dT_n}{dt}_{diff} = (-k_r - k_e)T_n \tag{3}$$

where T_n, T_r, and T_e are the number of naïve, regulatory, and effector CD4 T cells respectively, and k_r and k_e are kinetic parameters that determine the rate of differentiation of T_n into T_r and T_e. To capture expansion kinetics, we use the terms

$$\frac{dT_r}{dt}_{expans} = \frac{T_r}{t_r} \tag{4}$$

$$\frac{dT_e}{dt}_{expans} = \frac{T_e}{t_e} \tag{5}$$

$$\frac{dT_n}{dt}_{expans} = 0 \tag{6}$$

where t_r and t_e represent timescales for the expansion of T_r and T_e respectively. We assumed that T_n do not undergo expansion upon stimulation and serve only as a pool for T_r and T_e differentiation.

The addition of the expansion and differentiation differential terms gives the overall rate of population change for each cell type. The governing differential equations for cell growth are then

$$\frac{dT_r}{dt} = k_r T_n + \frac{T_r}{t_r} \tag{7}$$

$$\frac{dT_e}{dt} = k_e T_n + \frac{T_e}{t_e} \tag{8}$$

$$\frac{dT_n}{dt} = (-k_r - k_e)T_n. \tag{9}$$

This system of first order linear differential equations is solvable, and results in the analytical solutions

$$T_r = -\frac{k_r T_{n0}}{k_e + k_r + \frac{1}{t_r}} e^{-(k_e+k_r)t} + \left(T_{r0} + \frac{k_r T_{n0}}{k_e + k_r + \frac{1}{t_r}} \right) e^{\frac{t}{t_r}} \tag{10}$$

$$T_e = -\frac{k_e T_{n0}}{k_e + k_r + \frac{1}{t_r}} e^{-(k_e+k_r)t} + \left(T_{e0} + \frac{k_e T_{n0}}{k_e + k_r + \frac{1}{t_r}} \right) e^{\frac{t}{t_e}} \tag{11}$$

$$T_n = T_{n0} e^{-(k_e+k_r)t}. \tag{12}$$

To examine the role that the delay in hT cell expansion kinetics relative to mT cells plays in determining T_{reg} enrichment a modified version of the model was used in which (4) and (5) were changed to

$$\frac{dT_r}{dt}_{expa} = 0, \quad t < 48; \quad \frac{dT_r}{dt}_{expans} = \frac{T_r}{t_r}, \quad t \geq 48 \tag{13}$$

$$\frac{dT_r}{dt}_{expans} = 0, \quad t < 48; \frac{dT_e}{dt}_{expans} = \frac{T_e}{t_e}, \quad t \geq 48 \tag{14}$$

Table 1 Model governing equations and analytical solutions.

CD4 T Cell Type	Rate of differentiation (cells/hr)	Rate of expansion (cells/hr)	Rate of population growth (cells/hr)	Population size as a function of time (cells)
Regulatory (T_r)	$k_r T_n$	$\frac{T_r}{t_r}$	$k_r T_n + \frac{T_r}{t_r}$	$-\frac{k_r T_{n0}}{k_e + k_r + \frac{1}{t_r}} e^{-(k_e+k_r)t} + \left(T_{r0} + \frac{k_r T_{n0}}{k_e + k_r + \frac{1}{t_r}} \right) e^{\frac{t}{t_r}}$
Effector (T_e)	$k_e T_n$	$\frac{T_e}{t_e}$	$k_e T_n + \frac{T_e}{t_e}$	$-\frac{k_e T_{n0}}{k_e + k_r + \frac{1}{t_r}} e^{-(k_e+k_r)t} + \left(T_{e0} + \frac{k_e T_{n0}}{k_e + k_r + \frac{1}{t_r}} \right) e^{\frac{t}{t_e}}$
Naïve (T_n)	$(-k_r - k_e)T_n$	0	$(-k_r - k_e)T_n$	$T_{n0} e^{-(k_e+k_r)t}$

2.7.3 Parameter Fitting

We used the analytical solutions from Table S1 along with key assumptions to directly solve parameter values using experimental data. A summary of the parameter values in different experimental conditions may be found in Table S2.

To determine the differentiation parameter k_e, we first assumed that the factors necessary for T_e differentiation are established over the course of the first day of stimulation prior to the addition of exogenous IL-2 and any additional factors, and that T_e differentiation factors are maintained in all conditions over the course of the experiment. Thus, k_e is assumed to be constant regardless of culture conditions. Additionally, we assumed that the majority (>99.0%) of differentiation has occurred by day 4 in culture. In the absence of TGF-β1, we

assume that there is no T_r differentiation and that k_r is negligible. Combined, this results in the simplification of (12) to

$$T_n = T_{n0} e^{-(k_e)t} \tag{15}$$

in control conditions which allows for the direct solving of k_e. The resulting k_e value may be used in conjunction with (12) to find k_r using data from TGF-β1 only data.

To determine the expansion timescale parameters t_r and t_e we assume that (i) the rate of expansion is dependent directly on the number of cells of the population and (ii) is zero on the first day prior to factor addition and constant for each subsequent day. Due to lack of differentiation of T_r in the control condition, (10) simplifies to

$$T_r = T_{r0} e^{\frac{t}{t_r}} \tag{16}$$

and we can directly solve for t_r using control condition experimental data. Additionally, we can solve for the value of t_e in the presence and absence of CRCs using (11) in combination with data from control and CRC only experiments. An Excel sheet with example calculations may be found at https://github.com/Shah-Lab-UCSD/Treg_Enrichement_Model_In_Vitro.

Table 2 Experimentally determined model parameter values.

Parameter	Control	1 µM CRCs	TGF-β1	1 µM CRCs + TGF-β1
k_e (1/hr)	0.06396	0.06396	0.06396	0.06396
k_r (1/hr)	0	0	0.05638	0.05638
t_e (hr)	49.59	61.23	49.59	61.23
t_r (hr)	44.75	44.75	44.75	44.75

2.7.4 Comparison to Similar Models

This model of expansion is comparable to a previously proposed model proposed in Mayer et al. in which T cell expansion is governed according to the equation

$$\frac{dT}{dt}_{expans} = \alpha \frac{TC}{K + T + C} \tag{17}$$

in which α is the maximal rate of expansion, and K, T, and C are values determined by the antigen affinity, T cell number, and concentration of cognate antigen [45]. Relative to this model, the present model value of C, determined by the concentration of Dynabeads, is assumed to be much larger than K or T, so (17) simplifies to

$$\frac{dT}{dt}_{expans} = \alpha T \tag{18}$$

where the rate of expansion is determined to only be dependent on the T cell number and the maximal rate of expansion α, which is analogous to the reciprocal of t_r or t_e in the current model depending on the cell type. It should be noted that the characteristic doubling times reported here are slower than reported literature values (36 hr ± 7.2 hr) for T cells undergoing peak expansion in comparable studies. This may be due to the use of Dynabeads over a TCR specific cognate antigen, but also likely arises as a result of the assumption of a constant rate of

expansion in the present model. However, from a manufacturing perspective, it is more convenient to deal with a time averaged expansion rate than consider instantaneous expansion rate, and as all experiments were conducted over a 7-day period with the same amount of stimulation, the value still allows for comparison between groups.

2.8 Chapter 2 Figure Appendix

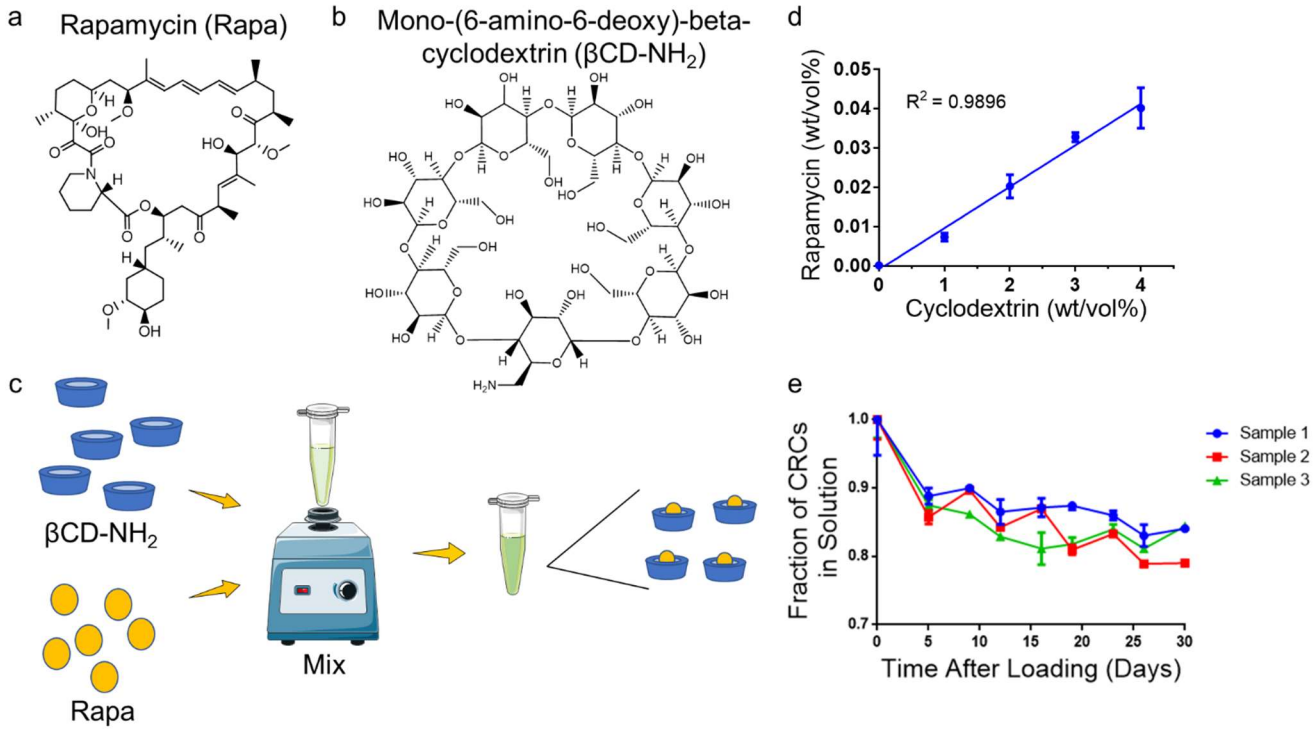

Figure 2.1 Complexation with mono-(6-amino-6-deoxy)-beta-cyclodextrin enhances the aqueous solubility of rapamycin.
Chemical structure of (a) rapamycin (Rapa) and (b) Mono-(6-amino-deoxy)-beta-cyclodextrin (βCD-NH_2) (c) Schematic for βCD-Rapa complexes (CRC). (d) Quantification of the Rapa loading in βCD-NH_2. (e) Stability of CRC in solution over 30 days. Data in (d) represent the mean ± s.d. for n=3 independent experiments. Data in e represent the mean mean ± s.d. for n=3 technical replicates.

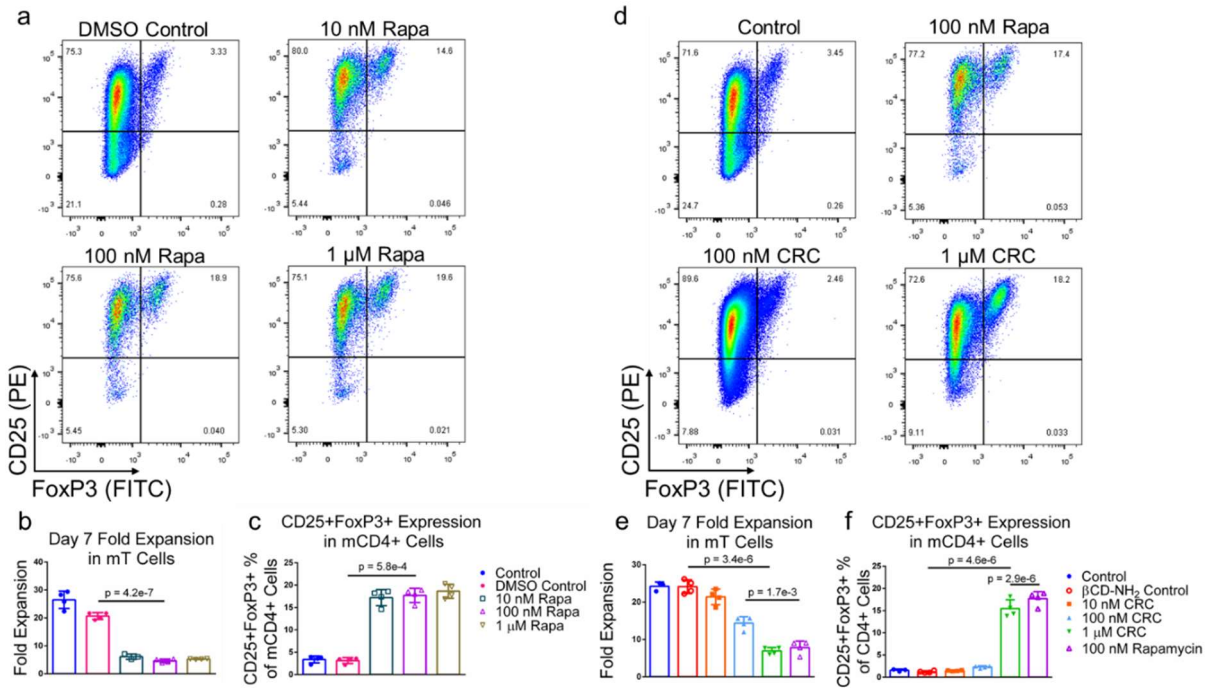

Figure 2.2 Rapa and CRCs suppress mouse T cell expansion and enhance T_{regs}.
(a) Representative flow cytometry plots of $CD25^{+}FoxP3^{+}$ $CD4^{+}$ mouse T (mT) cells. Quantification of the fold expansion of $CD4^{+}$ and $CD8^{+}$ T cells (b) and the fraction of $CD4^{+}CD25^{+}FoxP3^{+}$ T cells (c) after 7 days of expansion at a range of Rapa concentrations. (d) Representative flow cytometry plots of $CD4^{+}CD25^{+}FoxP3^{+}$ T cells. Quantification of the fold expansion of $CD4^{+}$ and $CD8^{+}$ T cells (e) and the fraction of $CD25^{+}FoxP3^{+}$ $CD4^{+}$ T cells (f) after 7 days of expansion at a range of CRC concentrations. Data represents the mean ± s.d. (n=4). Experiments were repeated at least three times.

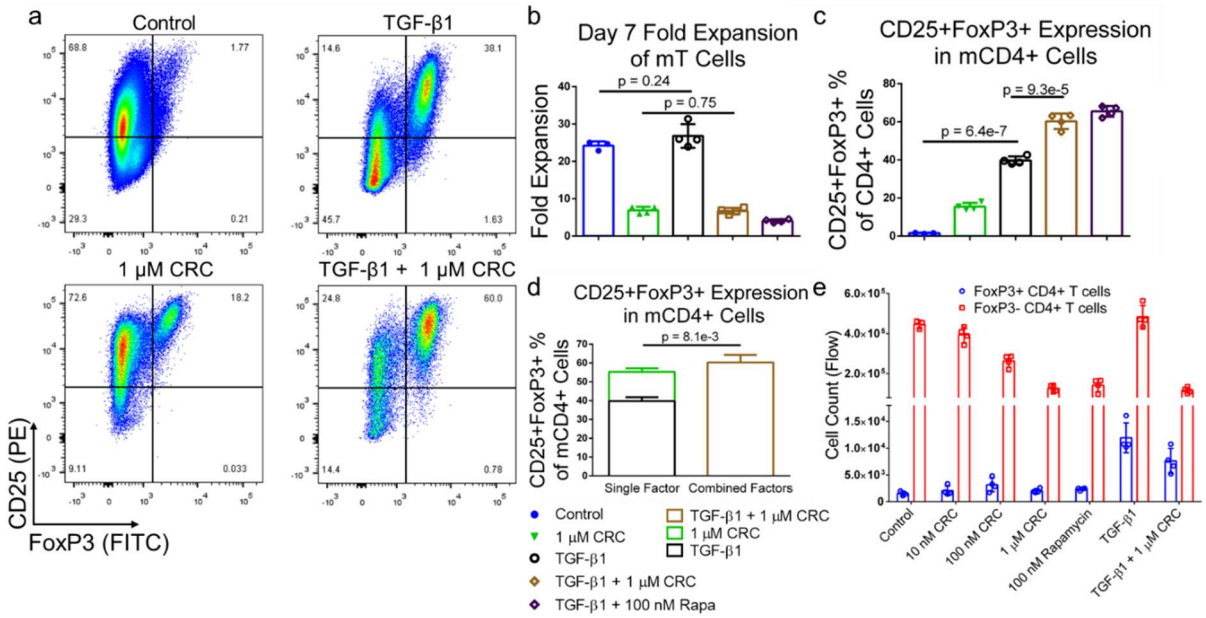

Figure 2.3 Mouse T_{regs} are enriched with combination of TGF-β1 and CRCs.
(a) Representative flow cytometry plots gated on $CD4^+CD25^+FoxP3^+$ mT cells with TGF-β1, CRCs or both. Quantification of the fold expansion of splenic $CD4^+$ and $CD8^+$ T cells (b) and the fraction of $CD25^+FoxP3^+$ $CD4^+$ T cells (c) after 7 days of expansion. (d) Stacked columns representative of the additive enrichment in the fraction of $CD25^+FoxP3^+$ $CD4^+$ T cells mediated with single-factor TGF-β1 (black) and CRCs (green) compared to the enrichment with combination TGF-β1 and CRCs (brown). (e) Quantification of $CD4^+FoxP3^+$ and $CD4^+FoxP3^-$ T cells with CRCs and TGF-β1. In a-e, untreated, TGF-β1, CRCs, TGF-β1 and CRCs, and TGF-β1 and Rapa were compared. Data represents the mean ± s.d. (n=4). Experiments were repeated at least two times.

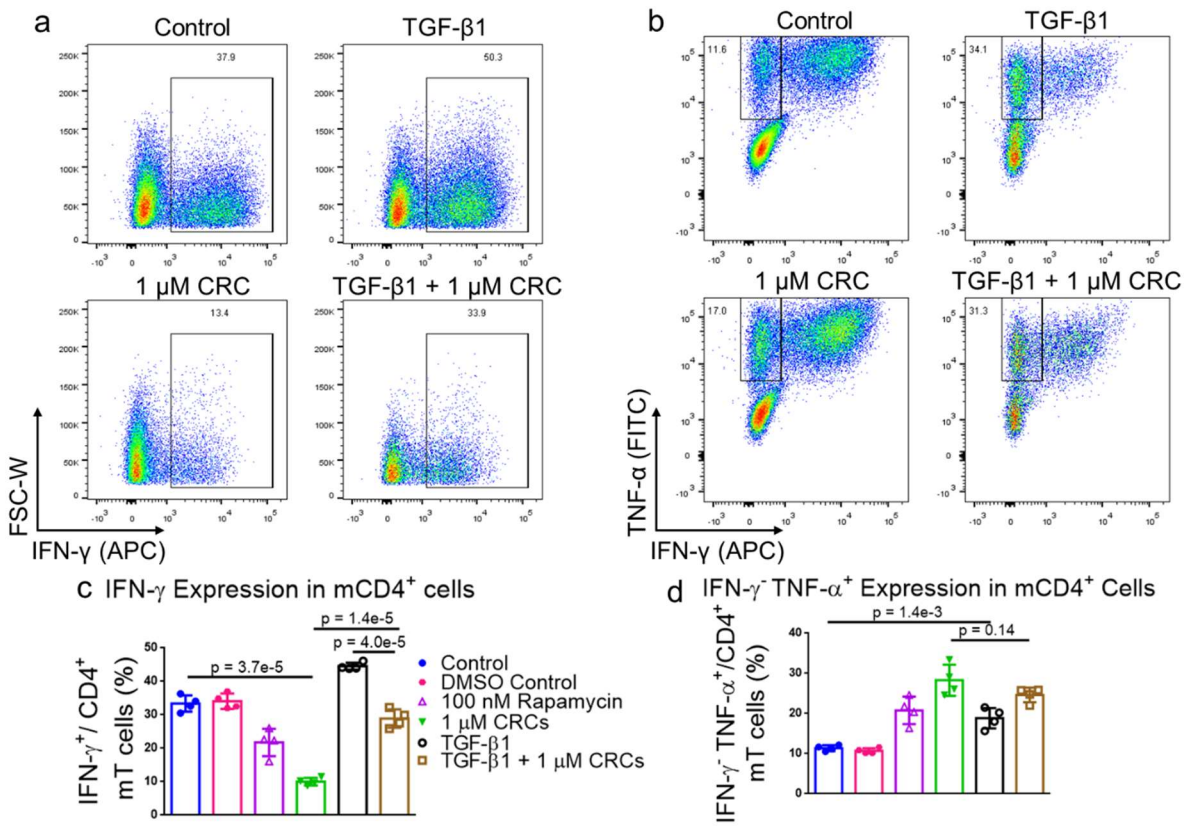

Figure 2.4 CRCs and TGF-β1 modulate cytokine expression in CD4$^+$ murine T cells.
Representative flow cytometry plots showing the fraction of IFN-γ$^+$ (a) and INF-γ$^-$TNF-α$^+$ (b) CD4$^+$ mT cells when TGF-β1, CRCs or both are included in culture medium. Flow cytometry of IFN-γ$^+$ (c) and INF-γ$^-$TNF-α$^+$ (d) CD4$^+$ T cells after 7 days of expansion. In a-d, untreated cells, TGF-β1, CRCs, TGF-β1 and CRCs, and TGF-β1 and Rapa were compared. Data represents the mean ± s.d. (n=4). Experiments were repeated at least two times.

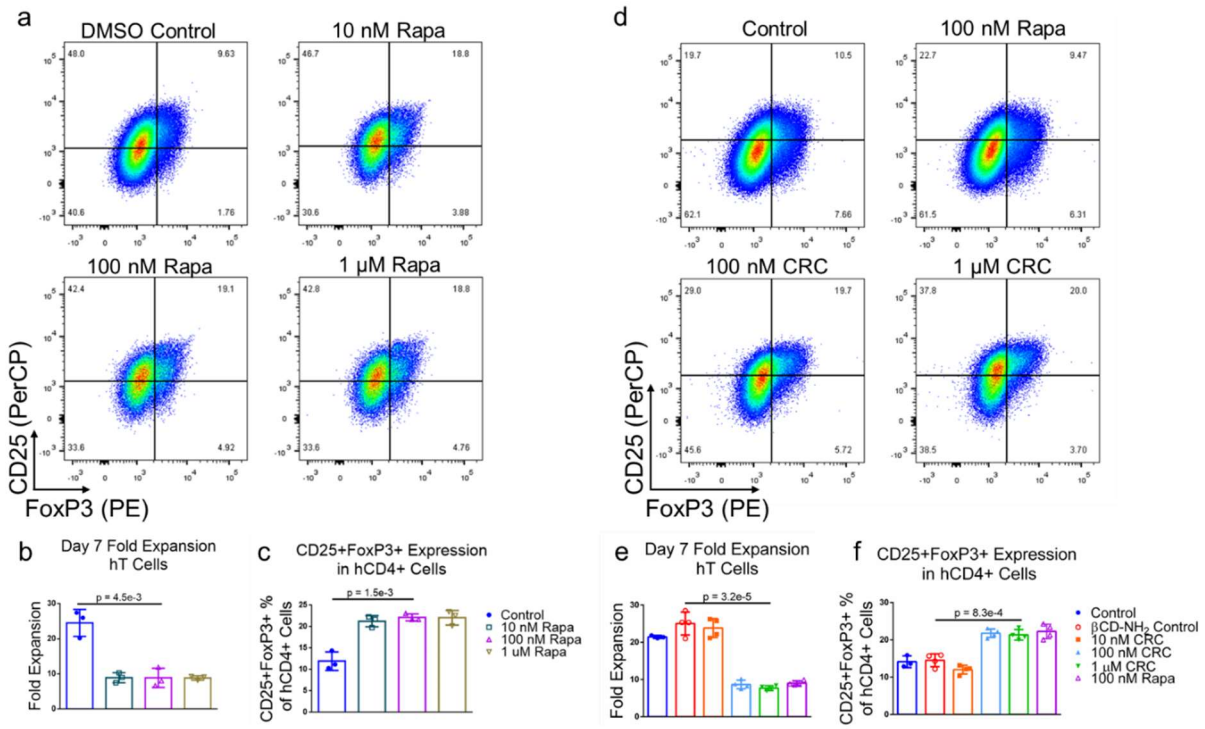

Figure 2.5 Rapa and CRCs suppress human T cell expansion and enhances human T_{reg}.
(a) Representative flow cytometry of $CD4^+CD25^+FoxP3^+$ human T (hT) cells when Rapa is include in the culture medium. Quantification of the fold expansion of $CD4^+$ and $CD8^+$ T cells (b) and the fraction of $CD4^+CD25^+FoxP3^+$ T cells (c) after 7 days of expansion with varying concentrations of Rapa. (d) Representative flow cytometry of $CD4^+$ $CD25^+FoxP3^+$ T cells when CRCs are included in culture medium. Quantification of the fold expansion of $CD4^+$ and $CD8^+$ T cells (e) and the fraction of $CD25^+FoxP3^+$ $CD4^+$ T cells (f) after 7 days of expansion with multiple concentrations of CRCs. Data represents the mean ± s.d. (n=4). Experiments were repeated at least three times.

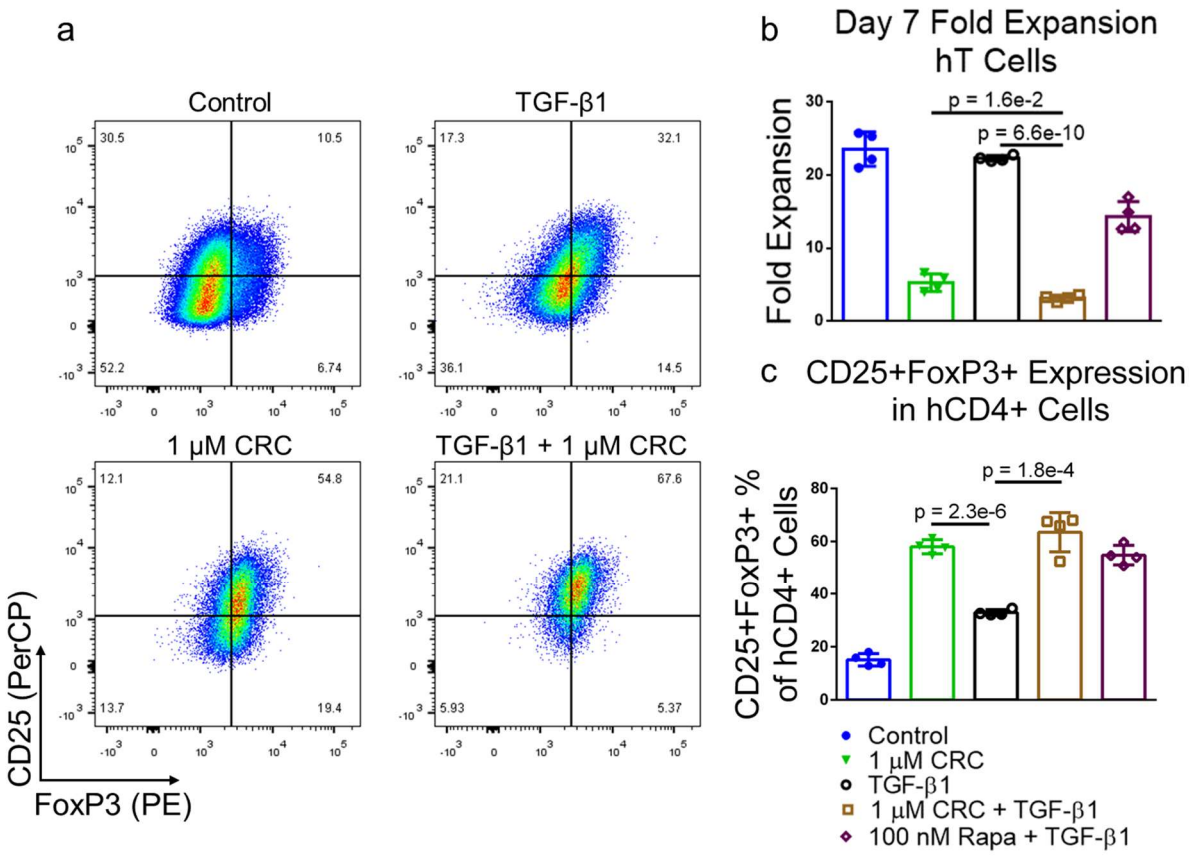

Figure 2.6 Human T_{regs} are enriched with the combination of TGF-β1 and CRCs.
(a) Representative flow cytometry of $CD25^{+}FoxP3^{+}$ $CD4^{+}$ T cells when TGF-β1, CRCs or both are included in culture media. Quantification of the fold expansion of splenic $CD4^{+}$ and $CD8^{+}$ T cells (b) and the fraction of $CD4^{+}CD25^{+}FoxP3^{+}$ T cells (c) after 7 days of expansion. In a-c, untreated cells, TGF-β1, CRCs, TGF-β1 and CRCs, and TGF-β1 and Rapa were analyzed. Data represents the mean ± s.d. (n=4). Experiments were repeated at least two times.

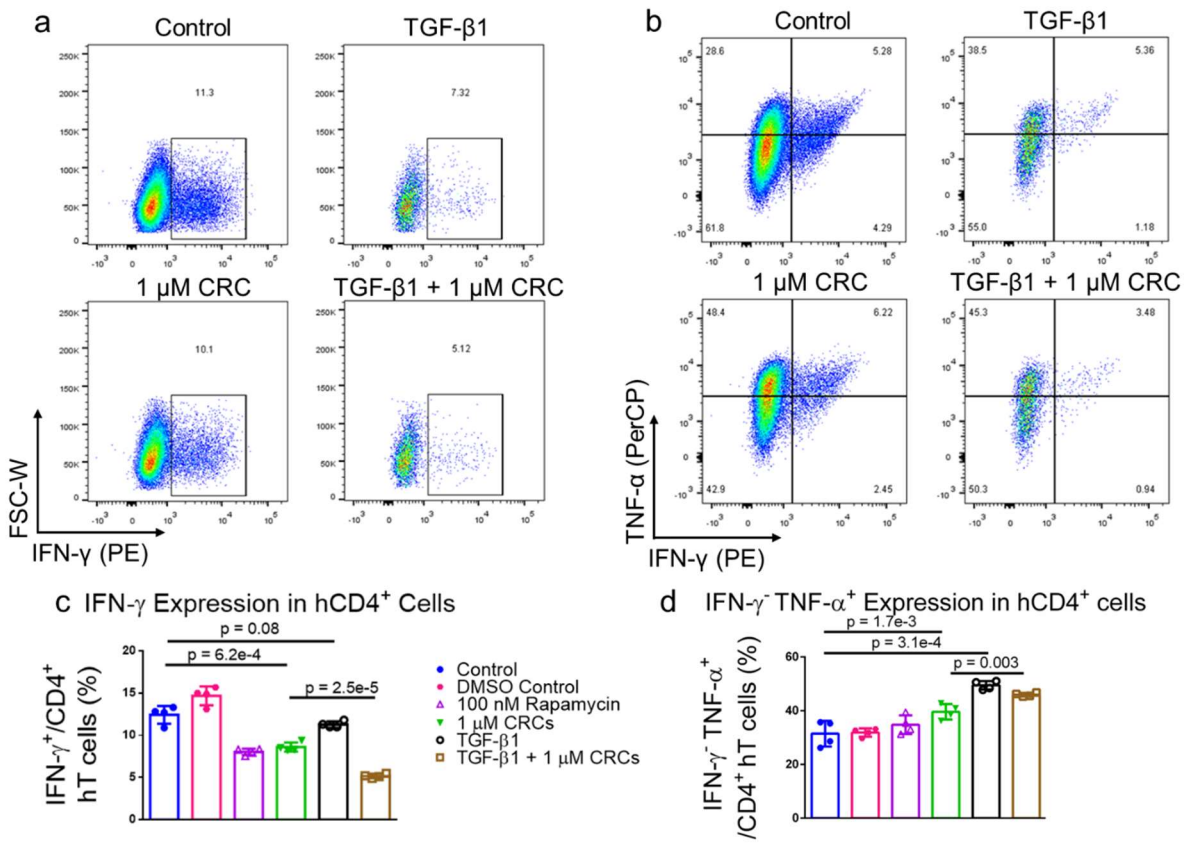

Figure 2.7 CRCs and TGF-β1 modulate cytokine expression in CD4+ human T cells.
Representative flow cytometry of IFN-γ+ (a) and INF-γ-TNF-α+ (b) CD4+ T cells when TGF-β1, CRCs or both are included in culture media. Flow cytometry of IFN-γ+ (c) and INF-γ-TNF-α+ (d) CD4+ T cells after 7 days of expansion. In a-d, untreated cells, TGF-β1, CRCs, TGF-β1 and CRCs, and TGF-β1 and Rapa were compared. Data represents the mean ± s.d. (n=4). Experiments were repeated at least two times.

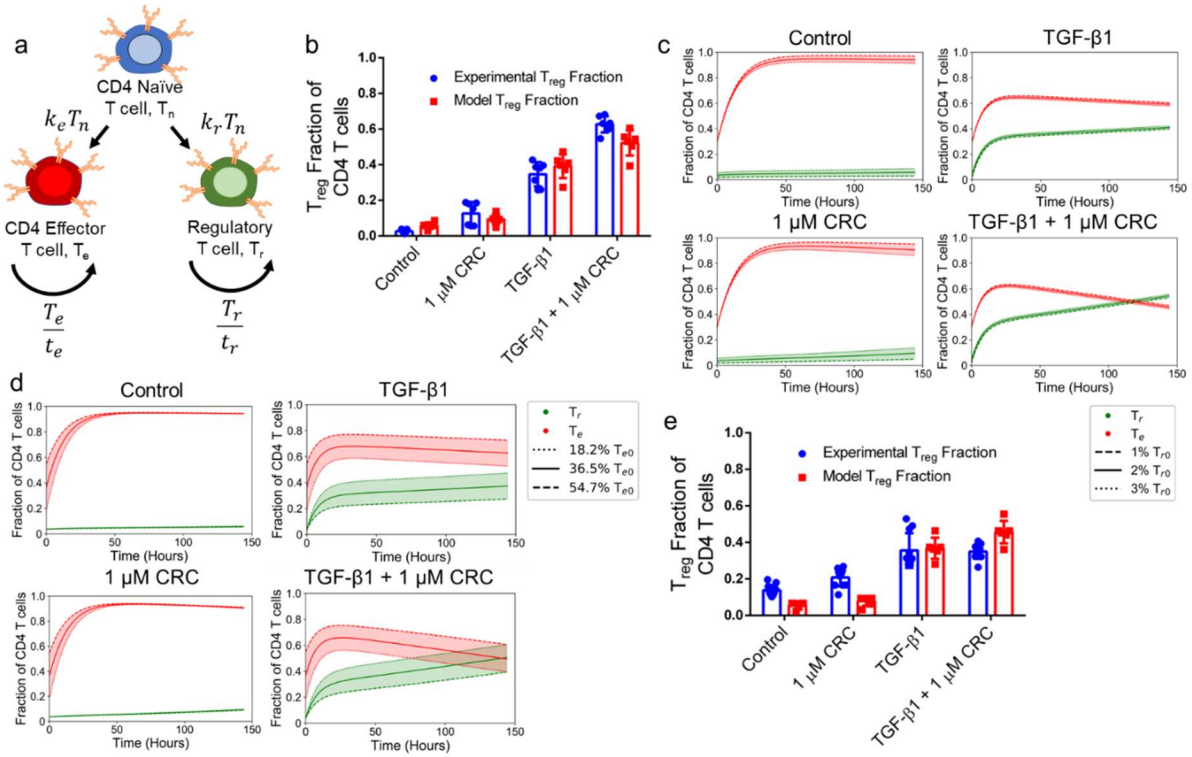

Figure 2.8 Enrichment of Treg in vitro is enhanced with a high initial naïve-to-effector T cell ratio. **(**a,b). Schematic depicting the interactions between T cells in a model of T cell expansion (a) and side-by-side comparison of experimental data (red) and model predictions (blue) when of TGF-β1, CRCs, both, or neither (Control) are included in culture media (b). (c) Model predictions for the fraction of effector (red) and regulatory (green) T cells when simulations are initialized with 1%, 2% or 3% Treg in the starting population corresponding to the dashed, solid, and dotted lines respectively. (d) Model predictions for the fraction of effector (red) and regulatory (green) T cells when simulations are initialized with 54.7%, 36.5% or 18.2% effector T cells in the starting population corresponding to the dashed, solid, and dotted lines respectively. (e) Predictions for effector and regulatory T cell fractions when a two day delay is placed on T cell expansion to mimic hT cell expansion dynamics. In b, experimental data represents the mean ± s.d. (n=7) and model data represents the final values for the three simulations depicted in (c).

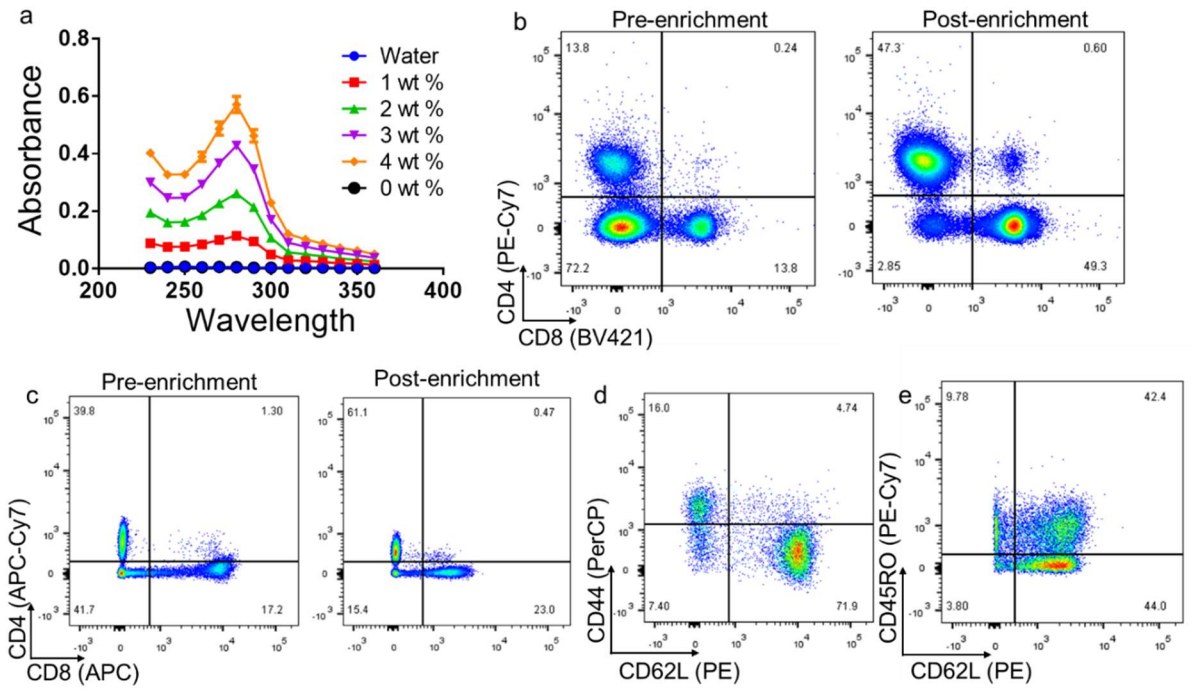

Figure 2.9 Extended characterization of CRCs and freshly isolated T cells.
(a) Representative absorbance curves from spectrophotometric analysis of CRCs made with increasing concentrations of □CD. (b) Representative flow cytometry plots of murine splenocytes pre- and post-enrichment for T cells. (c) Representative flow cytometry plots of human PBMCs pre- and post-enrichment. (d) Representative flow cytometry plot for CD4+CD62L+CD44- naïve mT cells. (e) Representative flow cytometry for CD4+CD62L+CD45RO- naïve hT cells. In a, data represents mean ± s.d. (n=3) of technical replicates.

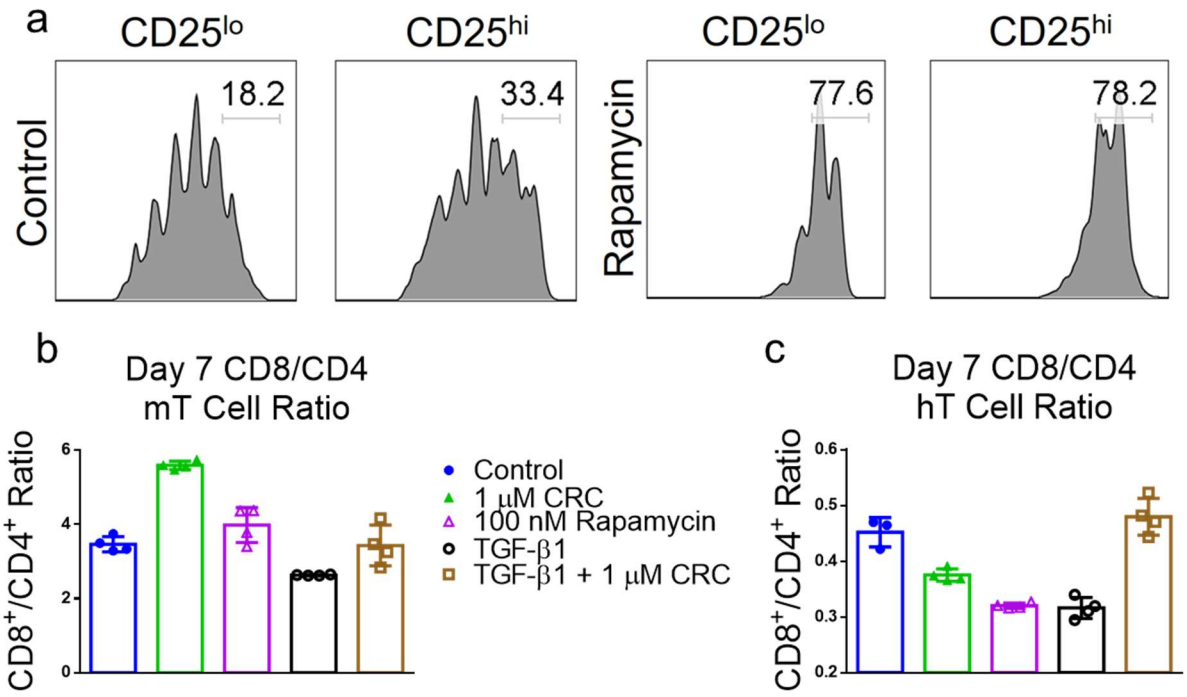

Figure 2.10 Extended characterization of T cell expansion.
(a) Representative CFSE plots gated on CD4+ CD25lo and CD4+CD25hi T cells. (b) CD8+/CD4+ ratio in murine T cells after 7 days of expansion. (c) CD8+/CD4+ ratio in hT cells after 7 days of expansion.

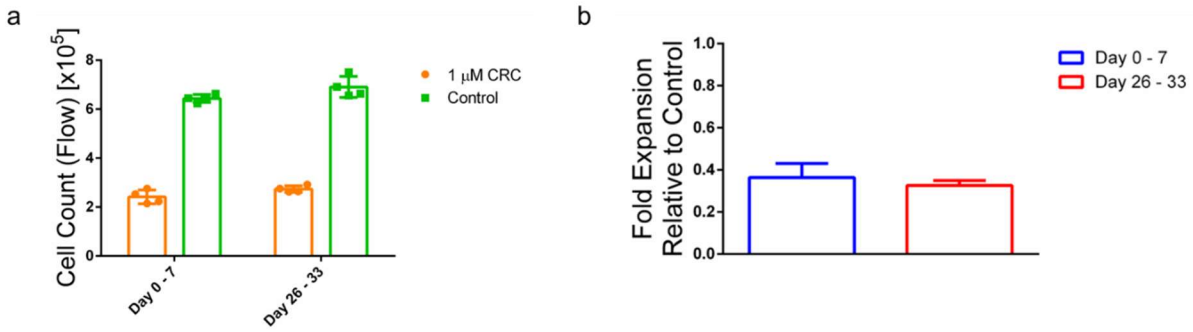

Figure 2.11 Extended characterization of CRC bioactivity.
Quantification of 1μM CRC-mediated suppression of hT cell expansion relative to proliferation of Dynabead-only controls of experiments starting at 0 and 26 days after initial preparation of CRCs. Data is represented as (a) total flow cytometry counts and (b) fold-expansion of CRC treated groups relative to controls. CRCs were stored at 4oC and warmed to room temperature and vortexed before addition to culture media. Data represent the mean ± s.d. (n = 4).

2.9 Chapter 2 References

1. S. Sakaguchi, R. Setoguchi, H. Yagi and T. Nomura, Current topics in microbiology and immunology, 305, 51-66. (2006)

2. J. A. Bluestone and Q. Tang, Science, 362, 154-155. (2018)

3. N. Marek-Trzonkowska, M. Mysliwiec, A. Dobyszuk, M. Grabowska, I. Derkowska, J. Juscinska, R. Owczuk, A. Szadkowska, P. Witkowski, W. Mlynarski, P. Jarosz-Chobot, A. Bossowski, J. Siebert and P. Trzonkowski, Clin Immunol 153, 23-30. (2014)

4. G. P. Wright, C. A. Notley, S. A. Xue, G. M. Bendle, A. Holler, T. N. Schumacher, M. R. Ehrenstein and H. J. Stauss, Proceedings of the National Academy of Sciences of the United States of America 106, 19078-19083. (2009)

5. N. J. Shah, A. S. Mao, T. Y. Shih, M. D. Kerr, A. Sharda, T. M. Raimondo, J. C. Weaver, V. D. Vrbanac, M. Deruaz, A. M. Tager, D. J. Mooney and D. T. Scadden, Nature biotechnology, 37, 293-302. (2019)

6. B. R. Olden, C. R. Perez, A. L. Wilson, Cardle, II, Y. S. Lin, B. Kaehr, J. A. Gustafson, M. C. Jensen and S. H. Pun, Advanced healthcare materials, 8, e1801188. (2019)

7. C. S. Verbeke, S. Gordo, D. A. Schubert, S. A. Lewin, R. M. Desai, J. Dobbins, K. W. Wucherpfennig and D. J. Mooney, Advanced healthcare materials , 6. (2017)

8. Q. Tang, K. J. Henriksen, M. Bi, E. B. Finger, G. Szot, J. Ye, E. L. Masteller, H. McDevitt, M. Bonyhadi and J. A. Bluestone, Journal of Experimental Medicine, 199, 1455-1465. (2004)

9. A. L. Putnam, T. M. Brusko, M. R. Lee, W. Liu, G. L. Szot, T. Ghosh, M. A. Atkinson and J. A. Bluestone, Diabetes, 58, 652-662. (2009)

10. S. Sakaguchi, K. Wing, Y. Onishi, P. Prieto-Martin and T. Yamaguchi, International immunology, 21, 1105-1111. (2009)

11. J. Li, S. G. Kim and J. Blenis, Cell metabolism, 19, 373-379. (2014)

12. A. Haeri, M. Osouli, F. Bayat, S. Alavi and S. Dadashzadeh, Artificial cells, nanomedicine, and biotechnology, 46, 1-14. (2018)

13. N. Saber-Moghaddam, H. Nomani, A. Sahebkar, T. P. Johnston and A. H. Mohammadpour, International immunopharmacology, 69, 150-158. (2019)

14. Y. Dobashi, Y. Watanabe, C. Miwa, S. Suzuki and S. Koyama, International journal of clinical and experimental pathology, 4, 476. (2011)

15. M. Battaglia, A. Stabilini, B. Migliavacca, J. Horejs-Hoeck, T. Kaupper and M. G. Roncarolo, J Immunol, 177, 8338-8347. (2006)

16. P. Monti, M. Scirpoli, P. Maffi, L. Piemonti, A. Secchi, E. Bonifacio, M. G. Roncarolo and M. Battaglia, Diabetes, 57, 2341-2347. (2008)

17. H. Q. Niu, Z. H. Li, W. P. Zhao, X. C. Zhao, C. Zhang, J. Luo, X. C. Lu, C. Gao, C. H. Wang and X. F. Li, Clinical and experimental rheumatology, 38, 58-66. (2019)

18. A. Schmidt, M. Eriksson, M. M. Shang, H. Weyd and J. Tegner, PloS one, 11, e0148474. (2016)

19. M. Esposito, F. Ruffini, M. Bellone, N. Gagliani, M. Battaglia, G. Martino and R. Furlan, Journal of neuroimmunology, 220, 52-63. (2010)

20. H.-J. Shin, J. Baker, D. B. Leveson-Gower, A. T. Smith, E. I. Sega and R. S. Negrin, Blood, 118, 2342-2350. (2011)

21. K. Wieder, W. Hancock, G. Schmidbauer, C. Corpier, I. Wieder, L. Kobzik, T. Strom and J. Kupiec-Weglinski, The Journal of Immunology, 151, 1158-1166. (1993)

22. R. Setoguchi, Y. Matsui and K. Mouri, European journal of immunology, 45, 893-902. (2015)

23. K. Mahalati and B. D. Kahan, Clinical pharmacokinetics, 40, 573-585. (2001)

24. P. Simamora, J. M. Alvarez and S. H. Yalkowsky, International journal of pharmaceutics, 213, 25-29. (2001)

25. M. E. Davis and M. E. Brewster, Nature reviews Drug discovery, 3, 1023. (2014)

26. F. Hirayama and K. Uekama, Advanced drug delivery reviews, 36, 125-141. (1999)

27. V. J. Stella and Q. He, Toxicologic pathology, 36, 30-42. (2008)

28. M. A. Rouf, I. Vural, E. Bilensoy, A. Hincal and D. D. Erol, J Incl Phenom Macro, 70, 167-175. (2011)

29. Y. Dou, J. W. Guo, Y. Chen, S. L. Han, X. Q. Xu, Q. Shi, Y. Jia, Y. Liu, Y. C. Deng, R. B. Wang, X. H. Li and J. X. Zhang, J Control Release, 235, 48-62. (2016)

30. N. A. Rohner, S. J. Schomisch, J. M. Marks and H. A. von Recum, Mol Pharmaceut, 16, 1766-1774. (2019)

31. S. Yamagiwa, J. D. Gray, S. Hashimoto and D. A. Horwitz, J Immunol, 166, 7282-7289. (2001)

32. M.-s. Kim, J.-s. Kim, H. J. Park, W. K. Cho, K.-H. Cha and S.-J. Hwang, International journal of nanomedicine, 6, 2997. (2011)

33. J. Zhao, Z. Mo, F. Guo, D. Shi, Q. Q. Han and Q. Liu, Journal of biomedical materials research. Part B, Applied biomaterials, 106, 88-95. (2018)

34. S. Jhunjhunwala, S. C. Balmert, G. Raimondi, E. Dons, E. E. Nichols, A. W. Thomson and S. R. Little, Journal of controlled release : official journal of the Controlled Release Society, 159, 78-84. (2012)

35. L. Holthaus, D. Lamp, A. Gavrisan, V. Sharma, A.-G. Ziegler, M. Jastroch and E. Bonifacio, Journal of immunological methods, 463, 54-60. (2018)

36. S. Thirumala, W. S. Goebel and E. J. Woods, Organogenesis, 5, 143-154. (2009)

37. A. Toschi, E. Lee, L. Xu, A. Garcia, N. Gadir and D. A. Foster, Molecular and cellular biology, 29, 1411-1420. (2009)

38. G. M. Delgoffe, K. N. Pollizzi, A. T. Waickman, E. Heikamp, D. J. Meyers, M. R. Horton, B. Xiao, P. F. Worley and J. D. Powell, Nature immunology, 12, 295-303. (2011)

39. L. M. Charbonnier, Y. Cui, E. Stephen-Victor, H. Harb, D. Lopez, J. J. Bleesing, M. I. Garcia-Lloret, K. Chen, A. Ozen, P. Carmeliet, M. O. Li, M. Pellegrini and T. A. Chatila, Nature immunology, 20, 1208-1219. (2019)

40. D. D. Sarbassov, S. M. Ali, S. Sengupta, J. H. Sheen, P. P. Hsu, A. F. Bagley, A. L. Markhard and D. M. Sabatini, Molecular cell, 22, 159-168. (2006)

41. D. J. Huss, R. C. Winger, H. Peng, Y. Yang, M. K. Racke and A. E. Lovett-Racke, The Journal of Immunology, 184, 5628-5636. (2010)

42. X. Chen, J. J. Subleski, H. Kopf, O. Z. Howard, D. N. Männel and J. J. Oppenheim, The Journal of Immunology, 180, 6467-6471. (2008)

43. J. M. Marin Morales, N. Munch, K. Peter, D. Freund, U. Oelschlagel, K. Holig, T. Bohm, A. C. Flach, J. Kessler, E. Bonifacio, M. Bornhauser and A. Fuchs, Frontiers in immunology, 10, 38. (2019)

44. S. Eaker, M. Armant, H. Brandwein, S. Burger, A. Campbell, C. Carpenito, D. Clarke, T. Fong, O. Karnieli, K. Niss, W. Van't Hof and R. Wagey, Stem cells translational medicine, 2, 871-883. (2013)

45. A. Mayer, Y. Zhang, A. S. Perelson and N. S. Wingreen, Proceedings of the National Academy of Sciences of the United States of America, 116, 5914-5919. (2019)

CHAPTER 3

Short chain fatty acid-mediated epigenetic modulation of inflammatory T cells in vitro

3.1 Abstract

Short chain fatty acids (SCFAs) are major metabolic products of indigestible polysaccharides in the gut and mediate the function of immune cells to facilitate homeostasis. The immunomodulatory effect of SCFAs has been attributed, at least in part, to the epigenetic modulation of immune cells through the inhibition the nucleus-resident enzyme histone deacetylase (HDAC). Among the downstream effects, SCFAs enhance regulatory T cells (T_{reg}) over inflammatory T helper (Th) cells, including Th17 cells, which can be pathogenic. Here, we characterize the potential of two common SCFAs – butyrate and pentanoate – in modulating differentiation of T cells in vitro. We show that butyrate but not pentanoate exerts a concentration dependent effect on T_{reg} and Th17 differentiation. Increasing the concentration of butyrate suppresses the Th17-associated RORgt and IL-17 and increases the expression of T_{reg}-associated FoxP3. To effectively deliver butyrate, encapsulation of butyrate in a liposomal carrier, termed BLIPs, reduced cytotoxicity while maintaining the immunomodulatory effect on T cells. Consistent with these results, butyrate and BLIPs inhibit HDAC and promote a unique chromatin landscape in T cells under conditions that otherwise promote conversion into a pro-inflammatory phenotype. Motif enrichment analysis revealed that butyrate and BLIP mediated suppression of Th17 associated chromatin accessibility corresponded with a marked decrease in bZIP family transcription factor binding sites. These results support the utility and further evaluation of BLIPs as an immunomodulatory agent for autoimmune disorders that are characterized by chronic inflammation and pathogenic inflammatory T cells.

3.2 Introduction

T cells are an important immune cell subset that are normally protective, prevent disease and destroy pathogens. However, T cells can contribute to autoimmune disease by causing or exacerbating inflammation[1,2]. While the disease etiology can be complex, an imbalance between effector and regulatory T cell function is a major contributor to pathogenic inflammation[3,4]. Among T cell subsets that have been associated with inflammatory disease are T helper (Th)-17 T cells expressing retinoic acid-related orphan receptor gamma t (RORgt)[5]. On the other hand, regulatory T cells (T_{reg}), characterized by their expression of forkhead box P3 (FoxP3), are widely recognized as important inhibitors of autoimmunity[6]. However, T_{reg} can be insufficiently effective in autoimmune disorders[7].

Suppressing inflammation by inhibiting immune cell activation or neutralizing select pro-inflammatory cytokines can be effective. However, immunosuppression also increases the risk of infections and immunosurveillance disorders, including cancer[8,9]. Therefore, therapies that restore immunoregulation could augment the existing standard-of-care without increasing the associated iatrogenic risk[10]. Among the endogenous regulators of immune function, short chain fatty acids (SCFAs) are metabolic products of gut microbiota and important immunomodulators that promote T_{reg}[11–13]. Butyrate, a 4 carbon SCFA, and pentanoate, a 5 carbon SCFA, are anti-inflammatory immunomodulators which are among the major SCFA products of anaerobic fermentation of polysaccharide-based fibers in the gut[14–16]. Recent studies have demonstrated that SCFAs modulate gene expression in immune cells, including T cells, by inhibition of nucleus-resident enzyme histone deacetylase (HDAC) and binding to G-protein coupled receptors (GPCR) associated with cells in the gut[14,17]. By inhibiting HDAC, butyrate and pentanoate increase acetylation of lysine residues on histone proteins, thereby loosening

the chromatin structure and facilitating access of certain transcription factors[18]. Both HDAC inhibition and GPCR binding promote the differentiation of $CD4^+$ T cells towards T_{reg} over Th17[19]. Under homeostatic conditions, SCFAs can promote T_{reg} and have the potential to potently enhance T_{reg} while suppressing Th17. These characteristics support the use of SCFAs as potential therapies in inflammatory disorders. However, the oral administration of free SCFAs is limited by the need for frequent dosing and potential challenges with patient compliance. To this end, a formulation for enhancing SCFA delivery could facilitate control over the timing, location, and specificity of immunomodulation.

Seeking to harness the therapeutic potential of SCFAs for immunomodulation, we first assessed the potential of butyrate and pentanoate to enhance T_{reg} using SKG mice, a model which recapitulates key features of human inflammatory arthritis arising from pathogenic imbalance between T_{reg} and Th17[20–22]. We show that butyrate, but not pentanoate, has a concentration-dependent effect on enhancing T_{reg} and suppressing Th17 cell differentiation and secretion of associated cytokines. Encapsulation of butyrate in a liposomal carrier, termed butyrate liposomes (BLIPs), permitted effective cellular uptake with minimal toxicity, while retaining T_{reg} upregulation and inflammatory Th17 suppression compared to butyrate. ATACseq revealed that both butyrate and BLIPs modulated the accessibility of Th17 associated loci and diminished basic leucine zipper (bZIP) binding motifs relative to cells exposed to Th17-inducing conditions alone, confirmed epigenetic modulation as a potential mechanism of action. The results support the utility of butyrate as an immunomodulatory agent in the treatment of inflammatory disease.

3.3 Results

3.3.1 Butyrate suppresses induction of Th17 and enhances T_{reg} in inflammatory conditions

To test the effect of butyrate on enhancing T_{reg}, we used an ex vivo polarization assay in which SKG $CD4^+$ T cells were subject to Th17 polarizing conditions using cytokine supplementation (**Fig. 3.1a**). $CD4^+$ splenocytes were stimulated and plated with Th17 polarizing cytokines IL-6, TGF-β1, IL-1β, and IL-23, and immunophenotypes were analyzed after four days, as described in the materials and methods section. We found that IL-17A expression, referred to henceforth just as IL-17, was increased 15-fold in when compared to expanding $CD4^+$ T cells using IL-2 alone (**Fig. 3.6a,b**). In a subset of conditions, butyrate was added to the T cell culture medium, ranging from 0.5 mM to 3 mM.

1 mM butyrate did not suppress expansion in Th17 polarizing conditions, however reduced mean viability from 84% to 71% [p = 0.004]. The highest concentration of butyrate, 3 mM, reduced mean viability to 46% [p < 0.0001]. Expansion was reduced but not statistically significant (**Figs. 3.1b, c, d**). 1 mM Butyrate increased FoxP3 expression to 23% compared to 10% in the control [p=0.003] (**Figs. 3.1e, f**). Additional butyrate supplementation did not have a significant additional effect on FoxP3 or CD4 expression. Distinct populations of $RORgt^+$ and $IL\text{-}17^+$ cells were observed by flow cytometry (**Fig. 3.1g**). RORgt was suppressed in a concentration dependent manner, with mean expression of 69% in the control (0 mM butyrate), 50% at 0.5 mM [p = 0.003], 43% at 1 mM [p = 0.002] and 21% at 3 mM [p = 0.0008] butyrate (**Fig. 3.1h**). 0.5 mM butyrate and 1 mM butyrate did not significantly reduce IL-17 expression compared to the control. However, addition of 3 mM butyrate reduced IL-17 expression from 18% to 10% [p = 0.03] (**Fig. 3.1i**).

3.3.2 Pentanoate modulates FoxP3 and IL-17 expression in $CD4^+$ T cells

To test the effect of pentanoate on T cell expansion and differentiation we cultured $CD4^+$ splenocytes in Th17-inducing conditions and concentrations of pentanoate from 0.5 mM to 3 mM for 4 days, and quantified immunophenotypes by flow cytometry on day 4 (**Fig. 3.2a**). Pentanoate reduced $CD4^+$ T cell expansion across all conditions and reduced cell viability at concentrations of 1 mM and greater (**Figs. 3.2b-d**). Pentanoate reduced FoxP3 at all concentrations (**Figs. 3.2e, f**). Pentanoate at 1mM reduced RORgt expression to 57% [$p < 0.0001$], similar to pentanoate at 3 mM where expression was reduced to 55% [$p < 0.0001$], compared to 82% in Th17 polarizing conditions alone (**Fig. 3.2g, h**). IL-17 expression was reduced in all pentanoate conditions, with 15% of cells expressing IL-17 in the 0.5 mM pentanoate condition and 11% in the 1 mM pentanoate condition, compared to 18% in Th17 polarizing conditions alone (**Fig. 3.2i**).

3.3.3 Butyrate modulates $CD4^+$ T cell cytokine secretion in *in vitro* inflammatory conditions

We selected butyrate for further characterization of T_{reg} enhancement and assessed the effect on cytokine production by $CD4^+$ T cells in Th17 polarizing conditions (**Fig. 3.3a**). We collected cell culture supernatant from the experiment described above and analyzed cytokine concentration using a Multiplex Cytokine Bead Array. We found that there was an optimal concentration of butyrate that enhanced IL-10, a cytokine associated with anti-inflammatory effects. 0.5 mM and 1 mM butyrate increased IL-10 concentration to ~6000 [$p = 0.07$] and ~6600 pg/mL [$p = 0.02$] respectively, compared to ~3700 pg/mL in the untreated group (**Fig. 3b**). Consistent with the results from intracellular staining, butyrate suppressed IL-17 most effectively at 2 and 3 mM, reducing the concentration to 1400 [$p = 0.004$] and 700 pg/mL [$p <$

0.002] respectively, compared to 7800 pg/mL in the control group (**Fig. 3.3c**). To characterize whether butyrate affected production of other cytokines, we quantified IFN-g, a Th1-associated cytokine and IL-4, a Th2-associated cytokine. Butyrate induced IFN-g secretion of 327 pg/mL in the control, and upregulated IFN-g secretion to 1404 pg/mL at 0.5 mM [$p = 0.003$] and 2228 pg/mL at 1 mM [$p < 0.0001$] (**Fig. 3.3d**). No effect was observed in IL-4, IL-2, and TNF secretion (**Fig. 3.3e-g**).

3.3.4 Butyrate-loaded liposomes maintain T_{reg} immunomodulatory effects while improving viability

To facilitate delivery of butyrate, we synthesized butyrate-loaded PEGylated liposomes (BLIPs) using a thin film hydration method. We selected a water-soluble phospholipid – 1, 2-distearoyl-sn-glycero-3-phosphoethanolamine-poly(ethylene glycol) (DSPE-PEG) and 1-palmitoyl-2-oleoyl-glycero-3-phosphocholine (POPC), commonly used materials in liposome formulations[32–34](**Fig. 3.4a, b**). After dissolving the lipids in chloroform, the solvent was allowed evaporate and generate a lipid film which was hydrated with 1M sodium butyrate. The hydrated lipid film was then sonicated to generate liposomal particles, which were dialyzed to remove unencapsulated butyrate, and the final solution was stored at 4ºC (**Fig. 3.4c**). The z-average of the BLIP diameter was determined by dynamic light scattering to be ~230 nm with a polydispersity index (PDI) of 0.236. To determine if the liposomal formulation improved uptake, Cyanine 5 (Cy5) was encapsulated into BLIPs to create fluorescent BLIPs (Fluo-BLIPs. Fluo-BLIPs or free Cy5 solubilized via sonication without lipids was cultured with splenocytes. After 5 hours, $CD4^+$ T cells were analyzed using flow cytometry to examine Cy5 uptake (**Figure 3.7a**). $CD4^+$ T cells from splenocytes cultured with Fluo-BLIPs exhibited a higher

mean fluorescent intensity on the Cy5 channel and a greater fraction of $Cy5^+$ $CD4^+$ T cells (68 ± 5%) compared to free Cy5 (53 ± 1%) (**Fig. 3.7b,c**).

To assess whether BLIPs enhance T_{reg} and suppress Th17, we tested concentrations between 0.05 mg/mL to 500 mg/mL in Th17-polarizing $CD4^+$ cell cultures (**Fig. 3.4d**). BLIPs reduced expansion of $CD4^+$ T cells in a concentration dependent manner, similar to butyrate. At 500 μg/mL, expansion was reduced to 3.6 fold, compared to 7.1 fold in the control [$p = 0.005$]. 500 μg/mL marginally reduced viability, to 73%, compared to 78% in the BLIP-free control [$p = 0.002$] (**Figs. 3.4e, f, g**). A distinct population of $FoxP3^+$ cells was observed by flow cytometry (**Fig. 3.4h**). FoxP3 expression was upregulated in a concentration dependent manner, with 500 μg/mL BLIP resulting in mean expression of 22%, compared to 14% in the control group [$p = 0.003$] (**Fig. 3.4i**). Both RORγt and IL-17 were suppressed in a concentration dependent manner by BLIPs, with RORγt reducing from 60% in the control to 50% at 50 μg/mL [$p = 0.0004$] and 29% at 500 μg/mL [$p < 0.0001$] (**Figs. 3.4j, k**). IL-17 was reduced from 23% in the control to 17% at 5 ug/mL [$p < 0.0001$] and 9.4% at 500 ug/mL [$p < 0.0001$] (**Fig. 3.4l**).

As phosphatidylcholines are known to have immunomodulatory properties, we sought to determine if the liposome formulation itself contributed to the immunomodulatory activity of the BLIPs. We conducted the Th17 polarization assay and treated cells with blank liposomes, 0.5 mM butyrate, or BLIPs. Blank liposomes alone at 500 mg/ml suppressed IL-17 expression (**Fig. 3.4m-o**). However, only BLIPs enhanced FoxP3 expression significantly over Th17 only conditions.

3.3.5 Butyrate reduces HDAC activity and alters chromatin accessibility of Th17-associated genes

To evaluate the effect of different treatments on HDAC inhibition, we performed HDAC activity assays comparing butyrate, BLIPs and blank liposomes. T cells were differentiated in Th17 inducing conditions alone, or in combination with either 0.5 mM butyrate, 500 μg/mL BLIPs, or 500 μg/mL blank liposomes. Whole nuclear proteins were isolated and assayed for HDAC activity. HDAC activity was comparable between T cells in the Th17 polarizing conditions and T cells treated with blank liposomes (**Fig. 3.5a,b**). 0.5 mM butyrate reduced HDAC activity compared to Th17 inducing conditions alone. HDAC activity in T cells treated with 500 μg/mL BLIP was the lowest among the tested groups. We also confirmed the effects in another cell type by testing supplier provided HDAC isolated from HeLa cells. HDAC inhibition by 500 μg/mL BLIP and 0.5 mM butyrate was comparable to Trichostatin A (TSA), a known pan-HDAC inhibitor, while blank liposomes did not inhibit HDAC activity (**Fig. 3.8a**).

As histone modifications play important roles in determining chromatin accessibility, we next sought to assess whether butyrate and BLIP epigenetically modified the chromatin landscape of $CD4^+$ T cells in Th17-polarizing conditions, we performed the assay for transposable-accessible chromatin with high-throughput sequencing (ATAC-Seq). Differences in chromatin accessibility between cells treated with 0.5 mM butyrate, BLIPs, and Th17 polarization only were observed at several regions, including T_{reg} and Th17 associated loci such as *Foxp3*, *Rorc*, and *Il17a* (**Fig. 3.5c**). When comparing 0.5 mM butyrate to the untreated Th17-polarizing control, we found 26000+ differentially accessible regions (DARs), 13000+ associated with Th17 polarization alone and 12000+ with 0.5 mM butyrate (**Fig. 3.5d, e**). Chromatin accessibility was downregulated by 0.5 mM butyrate at the *Il17*, *Il21* and *Rorc* gene loci, which are associated for Th17 differentiation (**Fig. 3.5f**). Downregulation by 0.5 mM

butyrate was also observed at the T_{reg}-associated *Foxp3* and *Il10* gene loci. When comparing chromatin accessibility between BLIPs and Th17-polarizing conditions alone, 9000+ DARs were found, with 4728 regions more accessible in the BLIP condition and 4635 regions more accessible in the Th17-polarizing condition alone (**Fig. 3.5g, h**). Chromatin accessibility to the Th17-associated gene loci for *Il17*, *Il21* and *Rorc* as well as the T_{reg}- associated gene loci for *Foxp3* and *Il10* were downregulated by BLIPs compared to Th17-inducing conditions alone (**Fig. 3.5i**). Direct comparison of the BLIPs to the 0.5 mM butyrate revealed that the chromatin accessibility was similar between the two conditions, with only 943 DARs. BLIPs increased accessibility at 737 of those regions while 0.5 mM butyrate increased accessibility at 206 regions (**Fig. 3.5j, k**). 0.5 mM butyrate marginally downregulated gene accessibility to *Il17*, *Il21*, *Rorc*, *Foxp3* and *Il10* (**Fig. 3.5l**). However, when compared across all treatment groups and including Th1 associated markers *Tbet* and *Ifng*, samples from the BLIPs and 0.5 mM butyrate groups were much more similar than Th17-polarizing conditions alone (**Fig. 3.9a**). To determine if the changes in chromatin accessibility were dose dependent, we compared 0.5 mM butyrate to 1 mM butyrate, but found no significant differences between the groups (**Fig. 3.9b, c**). Motif enrichment analysis comparing cells treated with Th17 polarization alone to 0.5 mM butyrate revealed a striking reduction in bZIP family binding motifs in the 0.5 mM butyrate condition (**Fig. 3.5m**). Comparison of BLIPs to Th17 polarization alone showed a similar trend.

3.4 Discussion

The regulation of the immune response by endogenously produced immunoregulators is important in maintaining health and preventing inflammatory disorders. Here, we demonstrated the immunoregulatory effect of SCFAs in modulating the differentiation of T

cells into T_{reg} in conditions that otherwise favor Th17. We show that butyrate upregulates FoxP3$^+$ T_{reg} and suppresses IL-17$^+$/RORgt$^+$ Th17 cells in inflammatory conditions that promote Th17 polarization in naïve SKG CD4+ T cells. Butyrate exerted a concentration-dependent effect on transcription factor and intracellular protein expression and cytokine secretion. Pentanoate downregulated RORgt and IL-17 expression in a concentration dependent manner in the same *in vitro* conditions, however the effect was less pronounced than that of butyrate. We demonstrate that encapsulating butyrate within POPC/DSPE-PEG-Mal liposomes maintains cell viability while retaining preferential modulation of T_{reg}/Th17 ratio. Both butyrate and BLIPs modulated chromatin accessibility in Th17-polarizing conditions, supporting the idea that butyrate can epigenetically modulate T cell differentiation in inflammatory conditions.

Butyrate upregulated T_{reg} and downregulated Th17 in a concentration dependent manner. At the upper limit of concentrations tested, 2 mM and 3 mM, butyrate was cytotoxic, reducing cell viability by half. While RORgt was more effectively suppressed at these higher concentrations, significant differences in IL-17+ or FoxP3+ proportions were not observed compared to 0.5 and 1 mM. The concentration of butyrate which suppressed IL-17 and RORgt while upregulating FoxP3 and retaining cell viability appears to be 1 mM. Prior work has shown the effect of butyrate on T cell differentiation at lower concentrations, up to 1 mM[35]. Concentrations above 1 mM were not investigated, and T_{reg} and Th17 differentiation was observed in their respective polarizing conditions. Cell viability was not quantified in this study. SCFA-mediated T_{reg} modulation in inflammatory Th17-inducing conditions has not been characterized. Our results point towards potent effects of SCFAs in inflammatory environments, and a significant impact on cell viability by butyrate. On the other hand, the suppression of Th17 and upregulation of T_{reg} by pentanoate was less pronounced compared to

butyrate. In contrast to butyrate, pentanoate did not reduce cell viability, and did not enhance FoxP3. These data are consistent with the literature, in which pentanoate has been shown to primarily modulate metabolic function in T cells[16] . Moreover, pentanoate has been shown to increase $CD4^+$ T cell proliferation in the absence of inflammatory cytokines. Therefore, based on the results of this work, we selected butyrate over pentanoate for further evaluation.

Butyrate at 1 mM and 0.5 mM enhanced the production of the immunoregulatory cytokine IL-10, which is associated with T_{reg} function. 1 mM butyrate maximized IL-10 production, suggesting that there could be an optimal concentration for T_{reg} enhancement and suppression of Th17 differentiation. The differential effect of butyrate is further supported by the observation that higher concentration reduced IL-10 and IL-17, whereas 0.5 mM and 1 mM butyrate did not significantly reduce IL-17. Therefore, harnessing the anti-inflammatory properties of butyrate will likely be context dependent, as higher concentrations of butyrate suppress Th17 activity while lower concentrations enhance T_{reg} activity. Furthermore, IFN-g, which was upregulated at all concentrations of butyrate, has been shown to have a context-dependent effect on autoimmune inflammation[36]. IFN-γ can have both immunostimulatory and immunoregulatory effects[37]. It is associated with a helper 1 (Th1)-driven immune response which mediates protection against pathogens. IFN-γ has also been demonstrated to play a protective role in autoimmune disease models while enabling induced T_{reg} cells to control immune responses in others. For example, ablation of IFN-γ signaling exacerbates autoimmune arthritis in mouse models of autoimmune arthritis, including SKG mice [38–40]. IFN-γ has been shown to be essential for the conversion of $CD4^+$ T cells to $CD4^+$ T_{reg} in inflammatory conditions in experimental autoimmune encephalomyelitis [41]. In graft-versus-host disease IFN-

γ expressing T_{reg} have been demonstrated to be essential for preventing disease [42]. Our results support that the delivery of butyrate would benefit from a disease-specific evaluation.

To assess whether encapsulating butyrate for effective delivery would preserve the modulation Th17/T_{reg} *in* vitro, we encapsulated butyrate in a liposomal formulation, termed BLIPs. Liposomes have been extensively studied as drug delivery vehicles[43,44]. Here, for the first time, we have assessed the liposomal delivery of butyrate to modulate T cells. To formulate BLIPs, we used DSPE-PEG-Mal, a common PEGylated phospholipid widely used in various preparations, including in clinically approved drug formulations. While we assessed their effect in vitro, DSPE-PEG has been demonstrated to increase bioavailability of encapsulated drugs molecules over non-PEGylated formulations[33]. The mean size of BLIPs (~230 nm) is consistent with prior reports of similar liposomal formulations[45]. Due to challenges regarding detection of butyrate in vitro, we examined liposomal delivery of the model dye Cy5 and found that liposomal encapsulation improved delivery of the Cy5 relative to free dye solubilized via sonication without lipids. Additionally, the results from the HDAC activity and inhibition assays support the notion of enhanced delivery of butyrate as T cell isolated HDACs of T cells treated with BLIPs displayed enhanced inhibition relative to HDAC from T cells treated with 0.5 mM butyrate, while both BLIPs and 0.5 mM butyrate displayed similar capacities for HDAC inhibition when tested on HeLa isolated HDACs. This suggests that differences in the activity of HDAC isolated from treated T cells represents the ability of butyrate to access HDAC in cells rather than added inhibition due to the activity of liposomal compounds.

Phenotypic modulation by BLIPs was observed to be concentration dependent. BLIPs attain similar upregulation of FoxP3 and downregulation of IL-17 to butyrate, while maintaining cell viability. While the blank liposomal formulation, which consists of

phosphatidylcholines POPC and DSPE-PEG, inhibited IL-17 expression, it did not increase FoxP3 expression to the same extent as BLIPs or demonstrate HDAC inhibitory activity. The observation of reduced IL-17 expression is consistent with prior work demonstrating the phosphatidylcholines are associated with immunoregulatory effects in animals and humans[46–48]. These results support that BLIPs are suitable for butyrate delivery.

BLIPs maintain the immunomodulatory activity butyrate while maintaining high viability of T cells compared to free butyrate. A possible reason is that exogenous butyrate can also induce signaling via G-protein-coupled receptors (GPCRs), such as GPR43, which has been demonstrated to have a potent anti-proliferative effect on $CD4^+$ T cells which affects viability in vitro[49]. In contrast, internalized butyrate, delivered via BLIPs, could reduce GPCR signaling while potentially enhancing HDAC inhibition compared to free butyrate and thereby avoid a reduction in cell viability.

ATAC-seq analysis revealed that butyrate and BLIPs comparably modulated the chromatin accessibility of loci associated with both T_{reg} and Th17 function, with only a small number of DARs arising between the two groups, but a significant number of DARs when either 0.5 mM butyrate or BLIP-treated cells were compared to Th17-inducing conditions alone. These observations are consistent with prior work that has demonstrated that butyrate promotes epigenetic changes via HDAC inhibition to induce a T_{reg} phenotype[50–52]. Most changes we observed were reductions in the accessibility of Th17 associated loci. While chromatin accessibility at the *Foxp3* and *Il10* loci was unaffected by addition of butyrate, the expression of FoxP3 and IL-10, as analyzed by flow cytometry and multiplex analysis respectively, increased. The apparent difference between the enhancement of gene products without a change in chromatin accessibility at these loci suggests that the mechanism of butyrate-mediated

upregulation of FoxP3 and IL-10 protein expression is not only due to changes in chromatin accessibility at the specific gene loci. We further assessed the effect of butyrate by conducting a motif enrichment analysis. Both butyrate and BLIPs significantly reduced the prevalence of several bZIP class motifs. Of these, it is notable that the AP-1 family transcription factors Basic leucine zipper transcription factor, ATF-like (BATF) and JunB, whose binding motifs were significantly downregulated by butyrate, have been demonstrated to play important roles in Th17 differentiation[53–56].

Our work suggests that BLIPs could be an effective agent for therapeutic delivery of butyrate. In addition to selection of the SCFA, an important consideration is that there is an optimal concentration range for butyrate for enhancing immunomodulation while avoiding cytotoxicity. Therefore, achieving target dose in affected tissue via systemic administration, for example via oral administration, could be challenging. Instead, local delivery of SCFAs via BLIPs is likely to result in therapeutically relevant immunomodulation. Therefore, future work should focus on characterizing the local and systemic effects of BLIP administration *in vivo* in an inflammatory disease context.

3.5 Materials and Methods

3.5.1 In vitro murine Th17 differentiation assay

Murine pan $CD4^+$ T cells were isolated from 8-14 week old male or female SKG mice via magnetic depletion using the mouse $CD4^+$ T cell Isolation kit (Miltenyi Biotech ref: 130-104-454) according to the manufacturer's instructions. Isolated $CD4^+$ T cells were plated in 96 well plates coated with anti-mouse anti-CD3 and anti-CD28 antibodies at 100,000 cells/well in RPMI 1640 (Gibco ref: 31800-022, lot: 2338416) supplemented with non-essential amino acids

(Gibco ref: 11140-050, lot: 2188976), sodium pyruvate (Corning ref: 25-000-CI, lot: 08620003), and beta-mercaptoethanol (Gibco ref: 21985-023, lot: 2060762). To induce Th17 differentiation $CD4^+$ T cells were stimulated with αCD3 and αCD28 (adsorbed at 5 µg/mL each in PBS at 37º C for 3 hours) and IL-6 (50 ng/mL) (ref: 200-06, lot: 031916-1 B2321), TGF-β1 (5 ng/mL) (100-21, lot: 1218209 H1919), IL-23 (5 ng/mL) (200-23, lot: 0712S227 K1119) and IL-1β (20 ng/mL) (200-01B, lot: 0606B95 B2421) were added at the time of plating with butyrate, pentanoate, BLIPs, or blank liposomes. Assays with blank liposomes were conducted using splenocytes from male SKG mice. All cytokines were recombinant human cytokines purchased from Peprotech.

3.5.2 Flow cytometry analysis

The cells were stimulated with PMA and Ionomycin (Cell Stimulation Cocktail, Invitrogen, Cat. No. 00-4970-03, lot: 2430454) for 4 hours. Cytokine transport was blocked with Brefeldin A (Invitrogen, Cat. No. 00-4506-51). After staining using a Fixable Viability Kit (Biolegend, lot: B333785) and for the CD4 marker (cat:1540-26, lot:F2212-T406C), the cells were fixed and permeabilized (Invitrogen ref: 00-5523-00 , lot: 2333698) followed by staining with fluorochrome-conjugated anti-mouse antibodies against RORgt (clone:B2D, lot: 2304447), IL-17 (clone:eBio17B7, lot: 2142931), IFN-g (clone: XMG1.2, lot: 2289505), and Foxp3 (clone:FJK-16s, lot: 2199652) at 1:800 dilution. IL-17, FoxP3, RORgt and IFN-g expression was quantified using an Attune NxT flow cytometer. Data was analyzed using FlowJo software.

3.5.3 Multiplex cytokine analysis

Cells were centrifuged for 5 min at 350 rcf, and 150 uL media was removed from each well for multiplex cytokine analysis. IL-10, TNF, IFN-g, IL-4, IL-2 and IL-17 expression were quantified using a BD Mouse Th1/Th2/Th17 Cytometric Bead Array (CBA) kit (BD ref: 560485, lot: 1229218) according to manufacturer's instructions. After preparation of the CBA samples, protein concentrations were quantified using an Attune NxT flow cytometer.

3.5.4 Butyrate liposome (BLIP) preparation

BLIP were synthesized by a thin film hydration method. 1-palmitoyl-2-oleoyl-glycero-3-phosphocholine (POPC) (Avanti ref: 870273C-25mg, lot: 870273C-25MG-A-064) and DSPE-PEG-Mal (MW: 2000) (Laysan Bio, lot: 165-07) were dissolved in 500z µL chloroform at 12.5 mg/mL. The chloroform was evaporated off by rotary evaporation, leaving a thin lipid film. The film was then hydrated by 3 mL of 1M butyrate in PBS for BLIPs, and PBS for blank liposomes. The solution was sonicated using a probe sonicator (Fisher Scientific, FB120) for 5 minutes at 80% amplitude with 1 second on and 2 seconds off. BLIP diameter and PDI was characterized by dynamic light scattering with a Malvern Zetasizer (ZEN3600).

Fluorescent BLIPs were synthesized as described above with the addition of 5 uL of Cy5 acid dissolved in DMSO at 10 mg/mL (Broad Pharm, BP-22274,lot CY5-1G-1) to chloroform solution prior to rotary evaporation. Control free Cy5 was prepared by evaporating off DMSO from the same amount of Cy5 acid and solubilizing the thin film via sonication in 3 mL of PBS.

3.5.5 HDAC Activity Assays

HDAC activity was quantified using a Flurorometric HDAC Activity Assay Kit (Abcam, ab156064). For assays assessing HDAC activity of HDACs extracted from cultured T cells, T cells were cultured as previously described in Th17 conditions with the addition of either nothing, blank liposomes (500 μg/mL), BLIPs (500 μg/mL) or butyrate (0.5 mM). Nuclear proteins were extracted after 4 days of culture by pooling 2 million cells together per treatment condition and using the Nuclear Extraction Kit (Abcam, ab113474) according to manufacturer's instructions with the omission of the peptidase inhibition cocktail (PIC) to prevent downstream inhibition of HDAC activity in the HDAC Activity Assay. Whole protein concentration of nuclear extracts were determined via absorbance on a Nanodrop at 280 nm, and samples were normalized for total protein concentration. Samples were then used in the HDAC Activity Assay according to manufacturer's instructions.

For HDAC inhibition assay, manufacturer supplied HeLa cell HDAC extract was used, and the assay was run according to manufacturer's protocol. Inhibitory function of BLIPs (500 μg/mL), blank liposomes (500 μg/mL) and butyrate (0.5 mM) were assayed. Manufacturer supplied Trichostatin A was used as a known HDAC inhibitor control.

3.5.6 ATAC-Seq Preparation and Sequencing

Cells used in ATAC-Seq experiments were subjected to the same procedure as described in the "In vitro mouse Th17 differentiation assay" above. On day 3, 10^5 cells were removed from media and prepared for ATAC-Seq using the Active Motif ATAC-Seq kit (Active Motif, Cat No. 53150) according to manufacturer instructions. Briefly, isolated cells were washed once with ice-cold PBS and subsequently resuspended in ATAC Lysis Buffer on ice to isolate the nuclei. The lysis buffer was removed, cells were washed, and nuclei were incubated with

tagmentation mix at 37ºC for 30 minutes, after which DNA was isolated and purified. DNA was then amplified via PCR using the[i] provided indexed primers according to manufacturer's instructions. SPRI cleanup beads were then used to purify the amplified DNA prior to sequencing. Samples were sequenced at the La Jolla Institute for Allergy and Immunology using an Illumina NovaSeq sequencer (NovaSeq 6000 S10OD025052).

3.5.7 ATAC-Seq Analysis

Analysis of raw reads from sequencing of ATAC-seq prepared libraries was performed as follows: FASTQ files were trimmed using NGmerge[23], and then aligned to mm10 reference genome using bowtie2[24] with the parameters (*-k 4 -X 2000 –very sensitive*). Reads corresponding to ENCODE blacklisted regions[25], mitochondrial genome, and chrY were removed. Reads were then filtered for uniquely mappable reads with mapping quality >= 30 using SAMtools[26], and duplicate reads were removed using MarkDuplicates from Picard tools. Peaks were then called using MACS2[27] with the parameters (*-g mm -q 0.05 –nomodel –nolambda –keep-dup all –call-summits –shift -100 –extsize 200*). Summits of all peaks were then extended to regions of 500 bp, and the 500 bp peaks from the groups being compared were merged to get consensus peaks via BEDtools[28] slop and merge routines. BAM files following removal of PCR duplicates were then converted to bed files and the reads for each region of the consensus peaks were counted using BEDtools coverage. Normalized coverage tracks for each group were created by merging BAM files of replicates withing each group, then running deeptools[29] bamCoverage with the parameters (*-bs 10 –effectiveGenomeSize 2652783500 –normalizeUsing RPKM -e 200).* Counts were normalized and differential ATAC-seq analysis was performed using DESeq2[30]. Differentially accessible regions (DARs) were filtered using

FDR-adjusted p-values <= 0.05 and fold-change >=2. For each pairwise comparison, motif enrichment analysis was performed by inputting all DARs into HOMER to identify known motifs for transcription factor binding sites enriched in peaks[31]. These results were filtered for known motifs with log p-value <= -35, with coverage >= 10% and fold increase of at least 1.5 over background coverage.

3.6 Chapter 3 Acknowledgements

Chapter 3, in full, is adapted with modifications from "Short-chain fatty acid-mediated epigenetic modulation of inflammatory T cells in vitro", Drug Delivery and Translation Research 2022, 13, 1912-1924 with authors David A. McBride, Nicholas C. Dorn, Mina Yao, Wade T. Johnson, Wei Wang, Nunzio Bottini, and Nisarg J. Shah.

3.7 Chapter 3 Figure Appendix

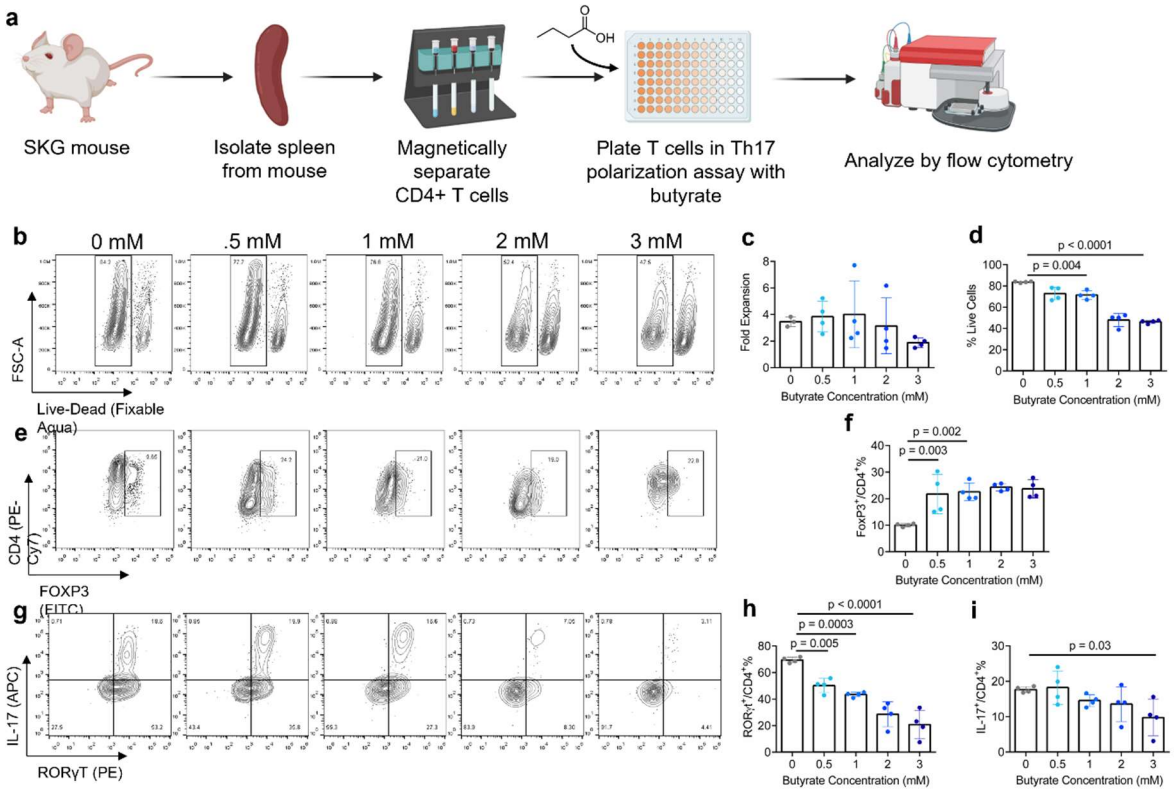

Figure 3.12 Butyrate suppresses induction of Th17 and enhances Treg in inflammatory conditions
a) Schematic of in vitro cell culture assessing effects of butyrate concentration on Th17 and Treg differentiation from CD4+ mouse T (mT) cells. b) Representative flow plot of cell viability of CD4+ mT cells in Th17 inducing conditions. (c-d) quantification of c) fold expansion d) % live CD4+ mT cells in Th17 inducing conditions. e) representative flow plot and f) quantification of FoxP3 expression in CD4+ mT cells in inflammatory conditions. (g-i) g) representative flow plot and quantification of h) ROR□t and i) IL-17 expression in CD4+ mT cells in the aforementioned culture conditions. Data in c,d,f,h,i are the mean ± S.D. of representative experiments. Statistical analyses in c,d,f,h,i were performed using one-way ANOVA with a post-hoc Dunnet's multiple comparison test.

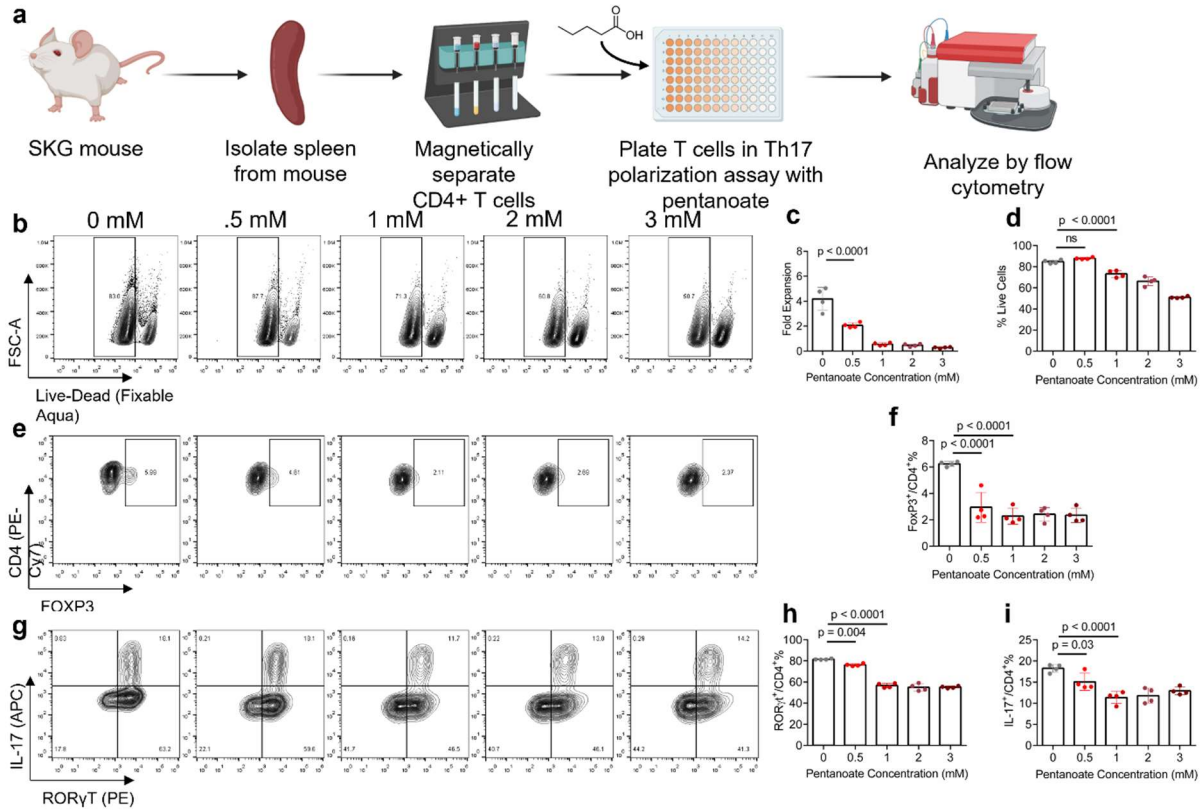

Figure 13.2 Pentanoate modulates FoxP3 and IL-17 expression in CD4+ T cells

a) Schematic of in vitro cell culture assessing effects of pentanoate concentration on Th17 and Treg differentiation from CD4+ mT cells. b) Representative flow plot of cell viability of CD4+ mT cells in Th17 inducing conditions. (c-d) quantification of c) fold expansion d) % live CD4+ mT cells in Th17 inducing conditions. e) representative flow plot and f) quantification of FoxP3 expression in CD4+ mT cells in inflammatory conditions. (g-i) g) representative flow plot and quantification of h) RORt and i) IL-17 expression in CD4+ mT cells in the aforementioned culture conditions. Data in c,d,f,h,I are the mean ± S.D. of representative experiments. Statistical analyses in c,d,f,h,I were performed using one-way ANOVA with a post-hoc Dunnet's multiple comparison test.

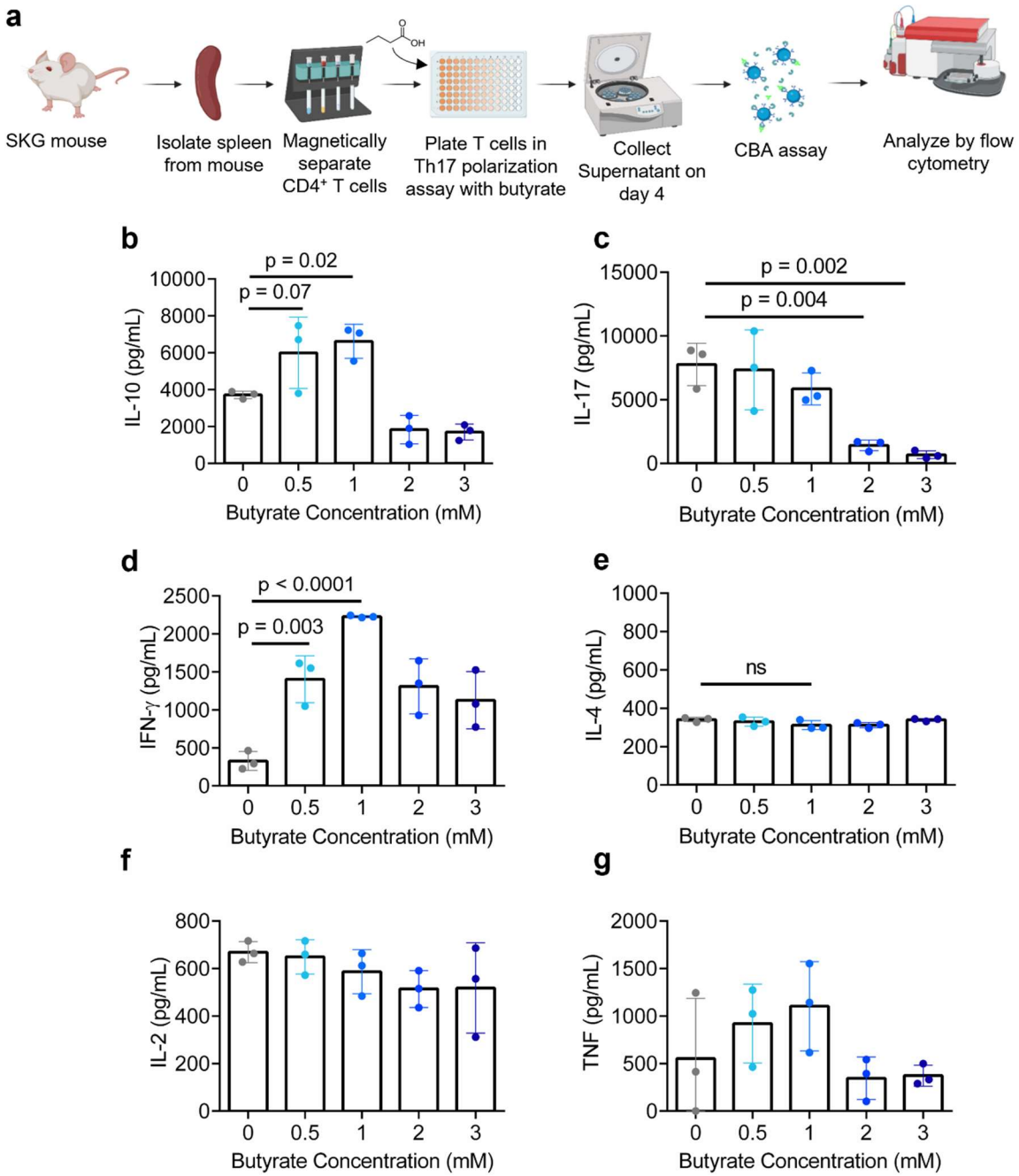

Figure 14 Butyrate modulates CD4+ T cell cytokine secretion in in vitro inflammatory conditions
a) Schematic of in vitro cell culture assessing effects of butyrate on CD4+ mT cell cytokine secretion in inflammatory conditions. (b-g) Quantification of b) IL-10, c) IL-17, d) IFN-□□ e) IL-4, f) IL-2 and g) TNF cytokine secretion as analyzed by multiplex assay in vitro. Data in b-g represented as the mean ± S.D. of representative experiments. Statistical analyses in b-g were performed using one-way ANOVA with a post-hoc Dunnet's multiple comparison test.

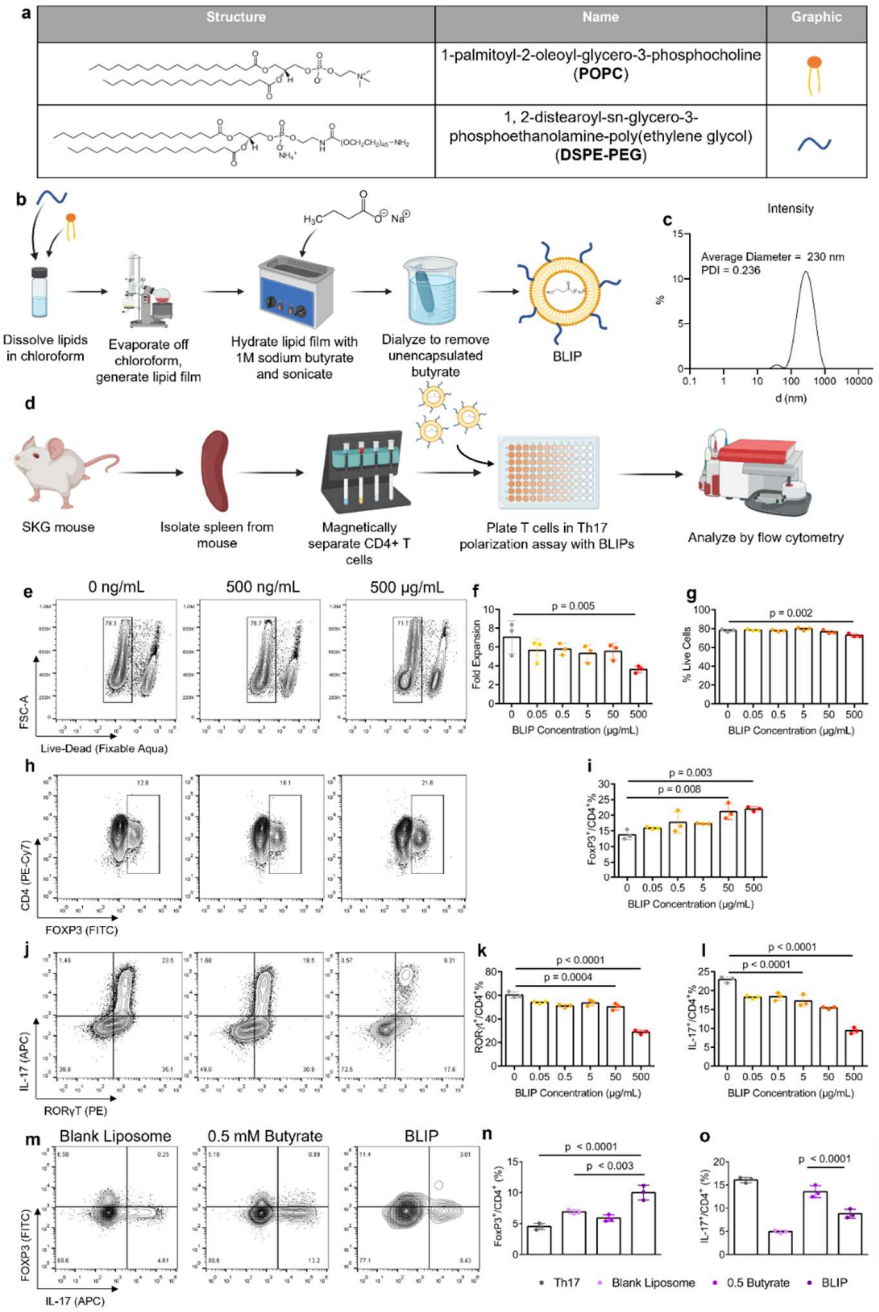

Figure 15 Butyrate-loaded liposomes maintain Treg immunomodulatory effects while improving viability a) Chemical structure of components of PEGylated Butyrate Liposome (BLIP) formulation. b) Schematic of BLIP synthesis. c) Intensity of BLIP particles as measured by dynamic light scattering. d) Schematic of in vitro cell culture assessing effects of BLIP concentration on Th17 and Treg differentiation from CD4+ mT cells. e) Representative flow plot of cell viability of CD4+ mT cells in Th17 inducing conditions. (f-g) quantification of f) fold expansion and g) % live CD4+ mT cells in Th17 inducing conditions. h) representative flow plot and i) quantification of FoxP3 expression in CD4+ mT cells in inflammatory conditions. (j-l) j) Representative flow plot and quantification of k) ROR□t and l) IL-17 expression in CD4+ mT cells in the aforementioned culture conditions. (m-o) m) Representative flow plot and quantification of n) FoxP3 and o) IL-17 expression in mT cells from male mice differentiated in Th17-polarizing conditions treated as indicated. Data in f,g,i,k,l,n,o are the mean ± S.D. of representative experiments. Statistical analyses in f,g,I,k,l were performed using one-way ANOVA with a post-hoc Dunnet's multiple comparison test. Statistical analysis in n, o were performed using one-way ANOVA with post-hoc Tukey test for multiple comparison.

Figure 16 Butyrate affects chromatin accessibility of Th17-associated genes
(a,b) HDAC activity readouts from nuclear protein extracts from groups of mT cells treated as indicated represented as a) standardized absorbance values over time after addition of nuclear extracts and b) average rate of reaction between 39-76 minutes, after reaction rate stabilized. c) Normalized ATAC-seq coverage at the Foxp3, Rorc, and Il17a loci in average representations of the 0.5 mM butyrate (B0.5, red), 500 μg/mL BLIPs (BLIPs, purple), and Th17 polarization only conditions (Th17, blue). d) Scatter plots of ATAC-seq counts per peak comparing cells from the B0.5 condition to the Th17 condition. Red corresponds to differentially accessible regions (DARs) enriched in the B0.5 condition, blue corresponds to DARs enriched in the Th17 condition, and grey corresponds to regions that are accessible in both conditions, but not significantly different. e) Boxplots of ATAC-Seq counts per peak from B0.5 and Th17 conditions at common (grey) or differentially accessible regions enriched in either the B0.5 (red) or the Th17 group (blue) from the comparison in Fig. 5b. f) Heatmap of select Th17 and Treg associated genes in B0.5 and Th17 conditions with dendrograms showing relatedness of samples (columns) and individual genes (rows). (g-i) g) Scatter plots of ATAC-seq counts per peak, h) boxplots of ATAC-seq counts per peak, and i) heatmap of select Th17 and Treg associated genes comparing cells from the BLIPs (purple) and Th17 (blue) conditions. (j-l) j) Scatter plots of ATAC-seq counts per peak, k) boxplots of ATAC-seq counts per peak, and l) heatmap of select Th17 and Treg associated genes comparing cells from the BLIPs (purple) and B0.5 (red) conditions. m) Motif enrichment analysis comparing peaks pairwise between cells treated with BLIPs, B0.5, and Th17, with enrichment of motifs quantified as -log(P) value. Data in a are the mean ± S.D. of n = 2 absorbance values per group standardized by subtracting the average absorbance value of the no enzyme control from the sample absorbance value. Data in b represent mean ± S.D.. Scales in c are as follows: Foxp3 [0-200], Rorc [0-400], Il17a [0-130]; data in f, i, l represent the integrated ATAC signal across each known gene promoter region ranked as z-scores using data across each row; data in m represent motifs with an enrichment log p-value less than -35 found in 10% or more regions with coverage showing a fold increase of at least 1.5 over background coverage in at least one pairwise comparison. Statistical analysis in a was performed using one-way ANOVA with post-hoc Tukey test for multiple comparisons on area under the curve.

a

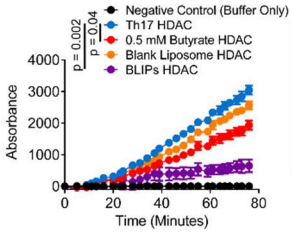

b

Condition	Negative Control	Th17 HDAC	0.5 mM Butyrate HDAC	Blank Liposome HDAC	BLIP HDAC
Reaction Rate ($\frac{\Delta Abs}{min}$)	0 ± 0.4	47.8 ± 3.1	32.5 ± 2.5	44.1 ± 1.8	7.1 ± 0.7

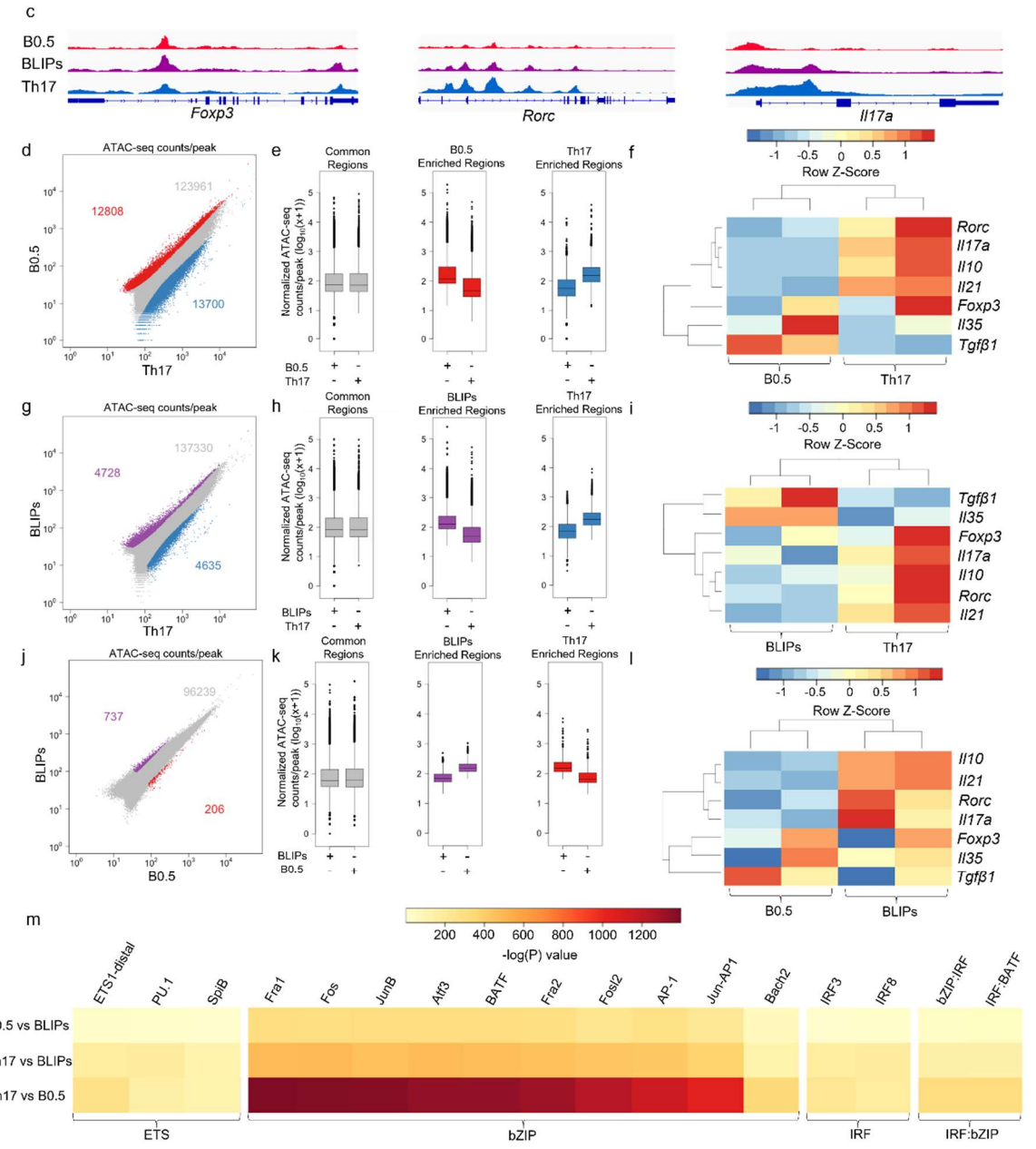

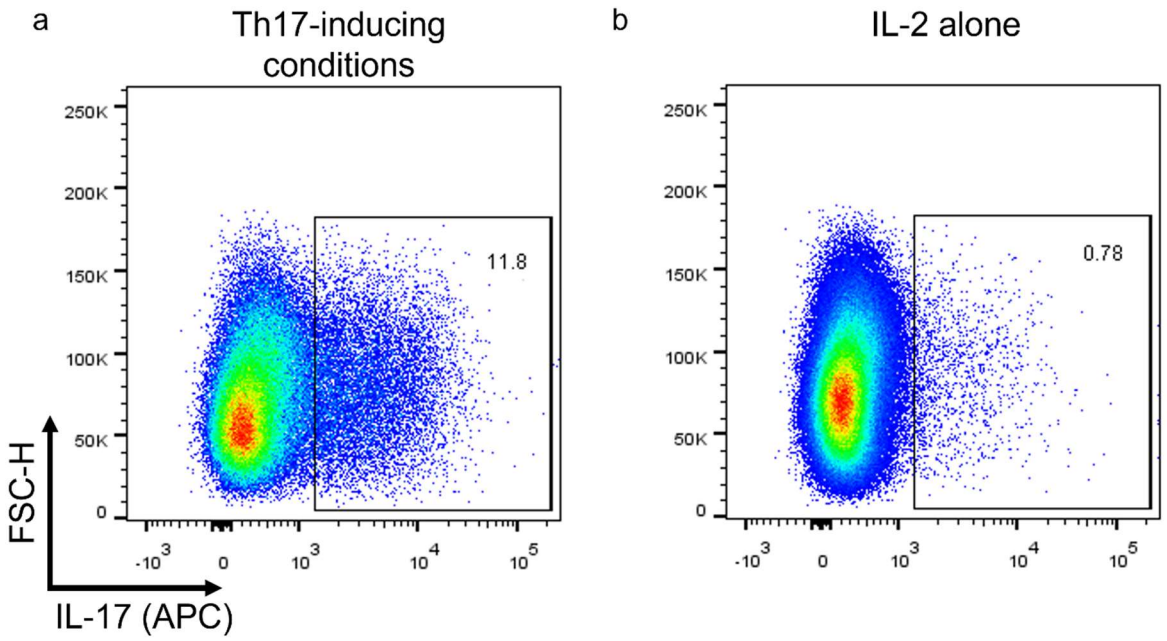

Figure 17 Representative Th17 differentiation
Representative flow cytometry plots depicting IL-17 expression in pan CD4+ mT cells exposed to either a) Th17 inducing conditions as described in Methods and Materials or b) IL-2 and platebound anti-CD3 and anti-CD28.

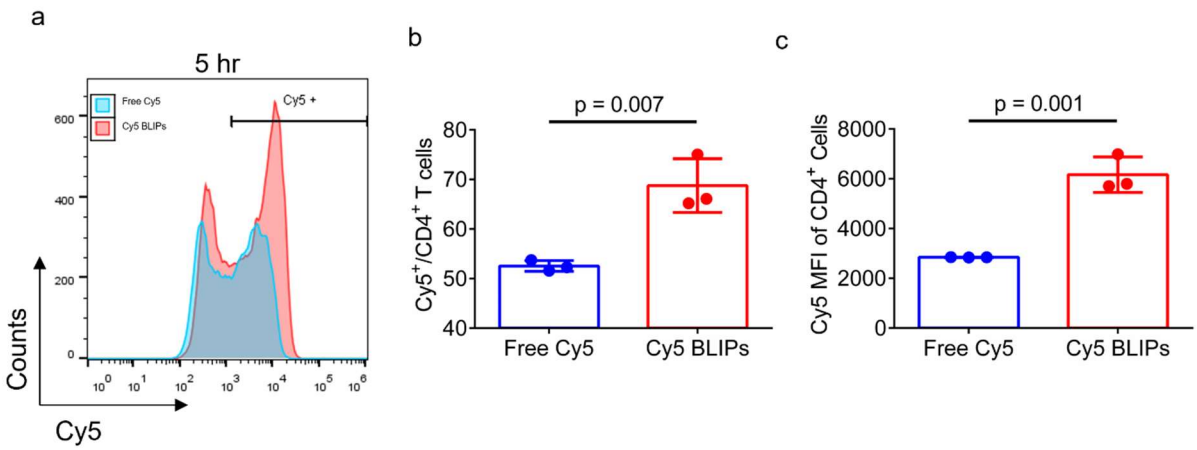

Figure 18 Liposome uptake quantification via Cy5

a) Representative flow cytometry histograms for uptake of Cy5 at 5 in CD4+ mT cells from splenocytes cultured with free Cy5 or Cy5 BLIPs. (b,c) Quantification of Cy5+ uptake by CD4+ T cells at 5 hours as b) Cy5+ fraction of CD4+ mT cells and c) MFI of CD4+ mT cells on the Cy5 channel. Data represent mean ± S.D. Statistical analysis were performed using Student's t-test.

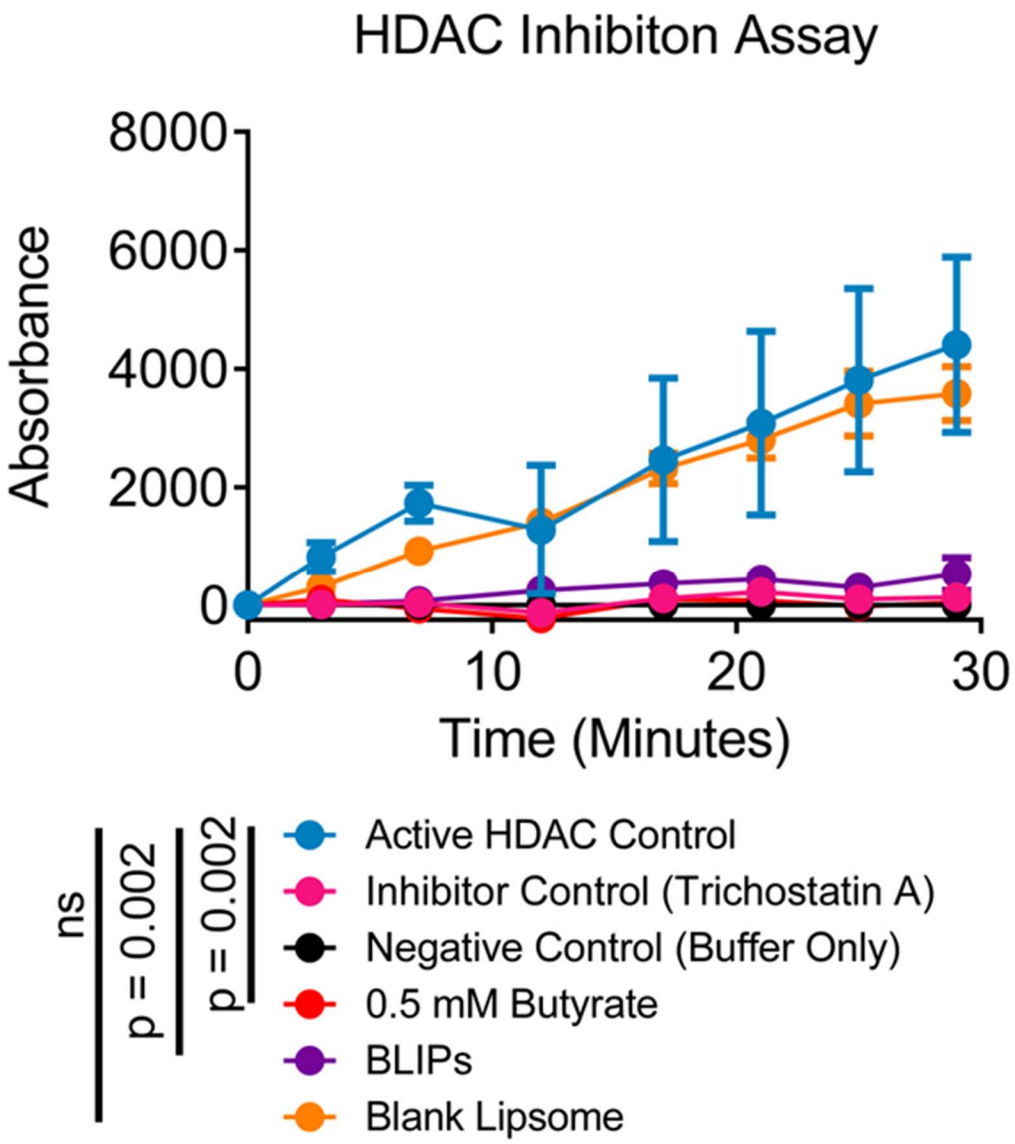

Figure 19 Butyrate and BLIPs have comparable inhibitory effect on HDAC extract
a) HDAC inhibition assay of agents acting on HDAC extract from manufacturer provided HeLa cells demonstrating inhibitory effect of blank liposomes, BLIPs and 0.5 mM butyrate relative to buffer only control (no HDACs), active HDAC control, and known HDAC inhibitor Trichostatin A. Data in a represent mean ± S.D. Statistical analysis was performed using one-way ANOVA with post-hoc Tukey test for multiple comparisons on area under the curve.

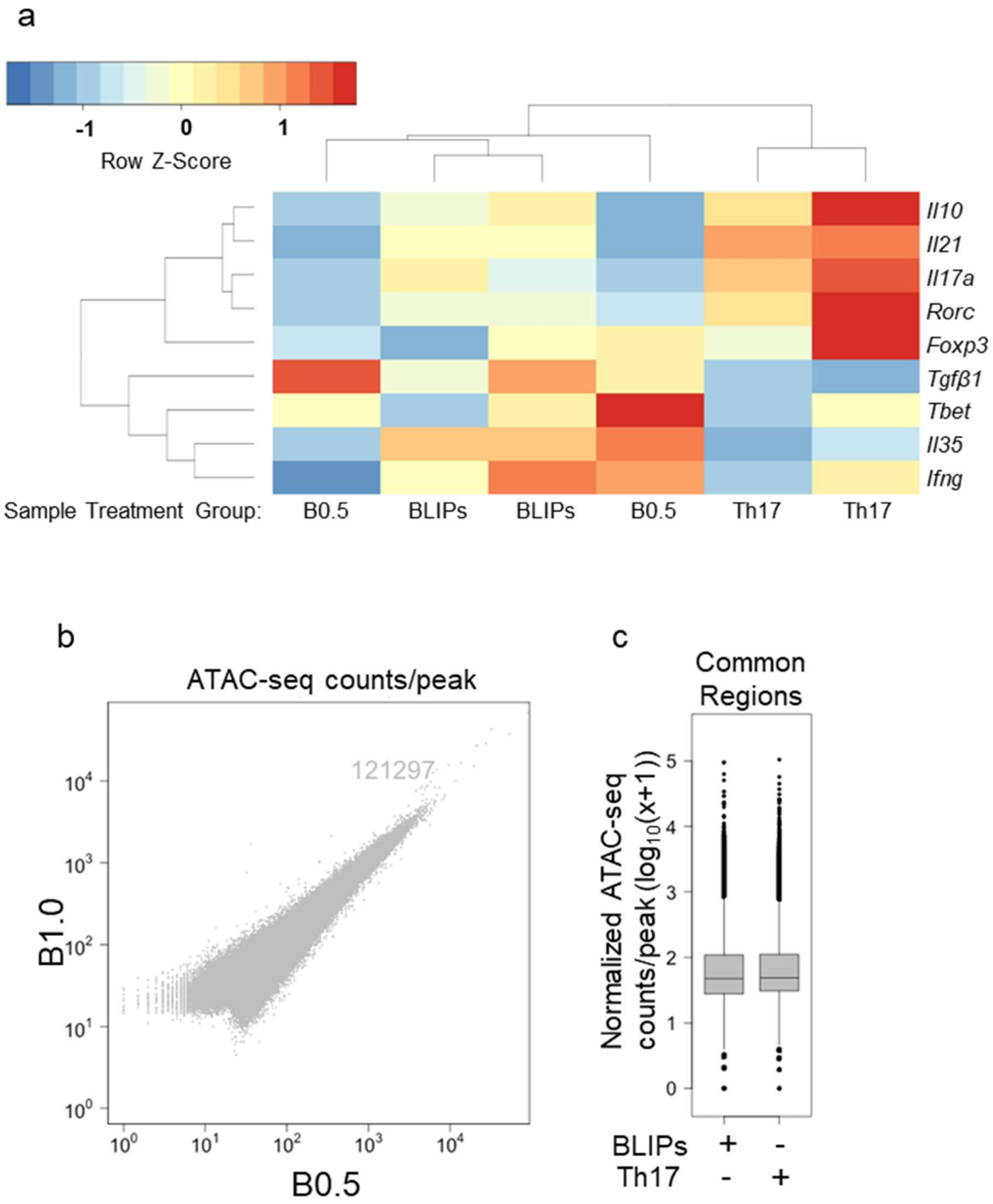

Figure 20 Additional ATAC-seq comparisons of treatment groups and 0.5 mM butyrate and 1 mM butyrate treated cells

a) Heatmap of select Th17, Treg and Th1 associated genes across B0.5, Th17, and BLIPs treatment groups with dendrograms showing similarity of samples (columns) and individual genes (rows). (b,c) ATAC-seq data comparing CD4+ T cells exposed to Th17 inducing conditions in combination with either 0.5 mM butyrate (B0.5) or 1 mM butyrate (B1.0) visualized as b) Scatter plot depicting common (grey) peaks. No peaks were found to be differentially accessible between the groups, so all points are grey. c) Box and whisker plots of common peaks in the B0.5 and B1.0 samples.

3.8 Chapter 3 References

1. Workman, C. J., Szymczak-Workman, A. L., Collison, L. W., Pillai, M. R. & Vignali, D. A. A. The development and function of regulatory T cells. Cellular and Molecular Life Sciences 66, 2603–2622 (2009).

2. Paust, S. & Cantor, H. Regulatory T cells and autoimmune disease. Immunol Rev 204, 195–207 (2005).

3. Ohl, K. & Tenbrock, K. Regulatory T cells in systemic lupus erythematosus. Eur J Immunol 45, 344–355 (2015).

4. Littman, D. R. & Rudensky, A. Y. Th17 and Regulatory T Cells in Mediating and Restraining Inflammation. Cell 140, 845–858 (2010).

5. Park, H. Park H, Li Z, Yang XO, Chang SH, Nurieva R, Wang YH, Wang Y, Hood L, Zhu Z, Tian Q, Dong C. A distinct lineage of CD4 T cells regulates tissue inflammation by producing interleukin 17. Nat Immunol 6, 1133–1141 (2005).

6. Sakaguchi, S. Ono M, Setoguchi R, Yagi H, Hori S, Fehervari Z, Shimizu J, Takahashi T, Nomura T. Foxp3 + CD25 + CD4 + natural regulatory T cells in dominant self-tolerance and autoimmune disease. (2006)

7. Pan, W. Zhu S, Dai D, Liu Z, Li D, Li B, Gagliani N, Zheng Y, Tang Y, Weirauch MT, Chen X, Zhu W, Wang Y, Chen B, Qian Y, Chen Y, Fang J, Herbst R, Richman L, Jallal B, Harley JB, Flavell RA, Yao Y, Shen N. MiR-125a targets effector programs to stabilize Treg-mediated immune homeostasis. Nat Commun 6, 7096 (2015).

8. Mortaz, E. Tabarsi P, Mansouri D, Khosravi A, Garssen J, Velayati A, Adcock IM. Cancers Related to Immunodeficiencies: Update and Perspectives. Front Immunol 7, (2016).

9. Vial, T. Immunosuppressive drugs and cancer. Toxicology 185, 229–240 (2003).

10. Tabas, I. & Glass, C. K. Anti-Inflammatory Therapy in Chronic Disease: Challenges and Opportunities. Science (1979) 339, 166–172 (2013).

11. Vinolo, M. A. R., Rodrigues, H. G., Nachbar, R. T. & Curi, R. Regulation of Inflammation by Short Chain Fatty Acids. Nutrients 3, 858–876 (2011).

12. Cummings, J. H., Pomare, E. W., Branch, W. J., Naylor, C. P. & Macfarlane, G. T. Short chain fatty acids in human large intestine, portal, hepatic and venous blood. Gut 28, 1221–1227 (1987).

13. Johnson, W. T., Dorn, N. C., Ogbonna, D. A., Bottini, N. & Shah, N. J. Lipid-based regulators of immunity. Bioeng Transl Med 7, (2022).

14. Dass, N. B. John AK, Bassil AK, Crumbley CW, Shehee WR, Maurio FP, Moore GB, Taylor CM, Sanger GJ. The relationship between the effects of short-chain fatty acids on

intestinal motility in vitro and GPR43 receptor activation. Neurogastroenterology & Motility 19, 66–74 (2007).

15. Hamer HM, Jonkers D, Venema K, Vanhoutvin S, Troost FJ, Brummer RJ. Review article: the role of butyrate on colonic function. Aliment Pharmacol Ther 27, 104–119 (2007).

16. Luu, M. Pautz S, Kohl V, Singh R, Romero R, Lucas S, Hofmann J, Raifer H, Vachharajani N, Carrascosa LC, Lamp B, Nist A, Stiewe T, Shaul Y, Adhikary T, Zaiss MM, Lauth M, Steinhoff U, Visekruna A. The short-chain fatty acid pentanoate suppresses autoimmunity by modulating the metabolic-epigenetic crosstalk in lymphocytes. Nat Commun 10, (2019).

17. Park, J. Kim M, Kang SG, Jannasch AH, Cooper B, Patterson J, Kim CH. Short-chain fatty acids induce both effector and regulatory T cells by suppression of histone deacetylases and regulation of the mTOR-S6K pathway. Mucosal Immunol 8, 80–93 (2015).

18. Xu, W. S., Parmigiani, R. B. & Marks, P. A. Histone deacetylase inhibitors: Molecular mechanisms of action. Oncogene vol. 26 5541–5552 Preprint at https://doi.org/10.1038/sj.onc.1210620 (2007).

19. Wawman, R. E., Bartlett, H. & Oo, Y. H. Regulatory T Cell Metabolism in the Hepatic Microenvironment. Front Immunol 8, (2018).

20. Sakaguchi, S., Takahashi, T., Hata, H., Nomura, T. & Sakaguchi, N. SKG mice, a new genetic model of rheumatoid arthritis. Arthritis Res Ther 5, 10 (2003).

21. Hsieh, W.-C. Svensson MN, Zoccheddu M, Tremblay ML, Sakaguchi S, Stanford SM, Bottini N. PTPN2 links colonic and joint inflammation in experimental autoimmune arthritis. JCI Insight 5, (2020).

22. Svensson, MND. Doody KM, Schmiedel BJ, Bhattacharyya S, Panwar B, Wiede F, Yang S, Santelli E, Wu DJ, Sacchetti C, Gujar R, Seumois G, Kiosses WB, Aubry I, Kim G, Mydel P, Sakaguchi S, Kronenberg M, Tiganis T, Tremblay ML, Ay F, Vijayanand P, Bottini N. Reduced expression of phosphatase PTPN2 promotes pathogenic conversion of Tregs in autoimmunity. Journal of Clinical Investigation 129, 1193–1210 (2019).

23. Gaspar, J. M. NGmerge: merging paired-end reads via novel empirically-derived models of sequencing errors. BMC Bioinformatics 19, 536 (2018).

24. Langmead, B. & Salzberg, S. L. Fast gapped-read alignment with Bowtie 2. Nat Methods 9, 357–359 (2012).

25. Amemiya, H. M., Kundaje, A. & Boyle, A. P. The ENCODE Blacklist: Identification of Problematic Regions of the Genome. Sci Rep 9, 9354 (2019).

26. Li, H. Handsaker B, Wysoker A, Fennell T, Ruan J, Homer N, Marth G, Abecasis G, Durbin R. The Sequence Alignment/Map format and SAMtools. Bioinformatics 25, 2078–2079 (2009).

27. Zhang Y, Liu T, Meyer CA, Eeckhoute J, Johnson DS, Bernstein BE, Nusbaum C, Myers RM, Brown M, Li W, Liu XS. Model-based Analysis of ChIP-Seq (MACS). Genome Biol 9, R137 (2008).

28. Quinlan, A. R. & Hall, I. M. BEDTools: a flexible suite of utilities for comparing genomic features. Bioinformatics 26, 841–842 (2010).

29. Ramírez, F. Ryan DP, Grüning B, Bhardwaj V, Kilpert F, Richter AS, Heyne S, Dündar F, Manke T. deepTools2: a next generation web server for deep-sequencing data analysis. Nucleic Acids Res 44, (2016).

30. Love, M. I., Huber, W. & Anders, S. Moderated estimation of fold change and dispersion for RNA-seq data with DESeq2. Genome Biol 15, (2014).

31. Heinz, S. Benner C, Spann N, Bertolino E, Lin YC, Laslo P, Cheng JX, Murre C, Singh H, Glass CK. Simple Combinations of Lineage-Determining Transcription Factors Prime cis-Regulatory Elements Required for Macrophage and B Cell Identities. Mol Cell 38, (2010).

32. Che, J., Okeke, C., Hu, Z.-B. & Xu, J. DSPE-PEG: A Distinctive Component in Drug Delivery System. Curr Pharm Des 21, 1598–1605 (2015).

33. Gabizon, A. & Martin, F. Polyethylene Glycol-Coated (Pegylated) Liposomal Doxorubicin Rationale for Use in Solid Tumours. Drugs vol. 54 (1997).

34. Oberholzer, T., Albrizio, M. & Luisi, P. L. Polymerase chain reaction in liposomes. Chem Biol 2, 677–682 (1995).

35. Kespohl, M. Vachharajani N, Luu M, Harb H, Pautz S, Wolff S, Sillner N, Walker A, Schmitt-Kopplin P, Boettger T, Renz H, Offermanns S, Steinhoff U, Visekruna A. The microbial metabolite butyrate induces expression of Th1- associated factors in cD4+ T cells. Front Immunol 8, (2017).

36. Ivashkiv, L. B. IFNγ: signalling, epigenetics and roles in immunity, metabolism, disease and cancer immunotherapy. Nature Reviews Immunology vol. 18 545–558 Preprint at https://doi.org/10.1038/s41577-018-0029-z (2018).

37. Wood, K. J. & Sawitzki, B. Interferon gamma: a crucial role in the function of induced regulatory T cells in vivo. Trends Immunol 27, (2006).

38. Ortmann, R. A. & Shevach, E. M. Susceptibility to Collagen-Induced Arthritis: Cytokine-Mediated Regulation. Clinical Immunology 98, (2001).

39. Hirota, K. Hashimoto M, Yoshitomi H, Tanaka S, Nomura T, Yamaguchi T, Iwakura Y, Sakaguchi N, Sakaguchi S. T cell self-reactivity forms a cytokine milieu for spontaneous development of IL-17+ Th cells that cause autoimmune arthritis. Journal of Experimental Medicine 204, (2007).

40. Lee, S. H., Kwon, J. Y., Kim, S.-Y., Jung, K. & Cho, M.-L. Interferon-gamma regulates inflammatory cell death by targeting necroptosis in experimental autoimmune arthritis. Sci Rep 7, (2017).

41. Wang, Z. Role of IFN-g in induction of Foxp3 and conversion of CD4+CD25- T cells to CD4+ Tregs. Journal of Clinical Investigation (2006) doi:10.1172/JCI25826.

42. Koenecke, C. Lee CW, Thamm K, Föhse L, Schafferus M, Mittrücker HW, Floess S, Huehn J, Ganser A, Förster R, Prinz I. IFN-γ Production by Allogeneic Foxp3 $^{+}$ Regulatory T Cells Is Essential for Preventing Experimental Graft-versus-Host Disease. The Journal of Immunology 189, (2012).

43. Shah, S., Dhawan, V., Holm, R., Nagarsenker, M. S. & Perrie, Y. Liposomes: Advancements and innovation in the manufacturing process. Adv Drug Deliv Rev 154–155, 102–122 (2020).

44. Antimisiaris, S. G. Marazioti A, Kannavou M, Natsaridis E, Gkartziou F, Kogkos G, Mourtas S. Overcoming barriers by local drug delivery with liposomes. Adv Drug Deliv Rev 174, 53–86 (2021).

45. Perez, R. Johnson J, Hubbard NE, Erickson K, Morgan M, Kim S, Rudich SM, Katznelson S, German JB. Selective targeting of Kupffer cells with liposomal butyrate augments portal venous transfusion-induced immunosuppression. Transplantation 65, 1294–1298 (1998).

46. Johnson, W. T., Dorn, N. C., Ogbonna, D. A., Bottini, N. & Shah, N. J. Lipid-based regulators of immunity. Bioeng Transl Med 7, (2022).

47. Broadhurst, M. J. Leung JM, Kashyap V, McCune JM, Mahadevan U, McKerrow JH, Loke P. IL-22 $^{+}$ CD4 $^{+}$ T Cells Are Associated with Therapeutic Trichuris trichiura Infection in an Ulcerative Colitis Patient. Sci Transl Med 2, (2010).

48. He, B. Wu L, Xie W, Shao Y, Jiang J, Zhao Z, Yan M, Chen Z, Cui D. The imbalance of Th17/Treg cells is involved in the progression of nonalcoholic fatty liver disease in mice. BMC Immunol 18, (2017).

49. Kibbie, J. J. Dillon SM, Thompson TA, Purba CM, McCarter MD, Wilson CC. Butyrate directly decreases human gut lamina propria CD4 T cell function through histone deacetylase (HDAC) inhibition and GPR43 signaling. Immunobiology 226, (2021).

50. Arpaia, N. Campbell C, Fan X, Dikiy S, van der Veeken J, deRoos P, Liu H, Cross JR, Pfeffer K, Coffer PJ, Rudensky AY. Metabolites produced by commensal bacteria promote peripheral regulatory T-cell generation. Nature 504, (2013).

51. Furusawa, Y. Obata Y, Fukuda S, Endo TA, Nakato G, Takahashi D, Nakanishi Y, Uetake C, Kato K, Kato T, Takahashi M, Fukuda NN, Murakami S, Miyauchi E, Hino S, Atarashi K, Onawa S, Fujimura Y, Lockett T, Clarke JM, Topping DL, Tomita M, Hori S,

Ohara O, Morita T, Koseki H, Kikuchi J, Honda K, Hase K, Ohno H. Commensal microbe-derived butyrate induces the differentiation of colonic regulatory T cells. Nature 504, (2013).

52. Arpaia, N. & Rudensky, A. Y. Microbial metabolites control gut inflammatory responses. Proceedings of the National Academy of Sciences 111, (2014).

53. Schraml, B. U. Hildner K, Ise W, Lee WL, Smith WA, Solomon B, Sahota G, Sim J, Mukasa R, Cemerski S, Hatton RD, Stormo GD, Weaver CT, Russell JH, Murphy TL, Murphy KM. The AP-1 transcription factor Batf controls TH17 differentiation. Nature 460, (2009).

54. Yamazaki, S. Tanaka Y, Araki H, Kohda A, Sanematsu F, Arasaki T, Duan X, Miura F, Katagiri T, Shindo R, Nakano H, Ito T, Fukui Y, Endo S, Sumimoto H. The AP-1 transcription factor JunB is required for Th17 cell differentiation. Sci Rep 7, (2017).

55. Pham, D., Silberger, D. J., Hatton, R. D. & Weaver, C. T. Batf promotes and stabilizes Th17 cell development by antagonizing the actions of STAT5. The Journal of Immunology 202, 124.10 (2019).

56. Carr, T. M., Wheaton, J. D., Houtz, G. M. & Ciofani, M. JunB promotes Th17 cell identity and restrains alternative CD4+ T-cell programs during inflammation. Nat Commun 8, (2017).

CHAPTER 4

Immunomodulatory Microparticles Epigenetically Modulate T Cells and Systemically Ameliorate Autoimmune Arthritis

4.1 Abstract

Disease modifying anti-rheumatic drugs (DMARDs) have improved the prognosis of autoimmune inflammatory arthritides but a large fraction of patients display partial or non-responsiveness to front-line DMARDs. Here we report an immunoregulatory approach based on sustained joint-localized release of all-trans retinoic acid (ATRA), which modulates local immune activation and enhances disease-protective T cells and leads to systemic disease control. ATRA imprints a unique chromatin landscape in T cells, which is associated with an enhancement in the differentiation of naïve T cells into anti-inflammatory regulatory T cells (T_{reg}) and suppression of T_{reg} destabilization. Sustained release poly-(lactic-co-glycolic) acid (PLGA)-based biodegradable microparticles encapsulating ATRA (PLGA-ATRA MP) were retained in arthritic mouse joints after intra-articular (IA) injection. IA PLGA-ATRA MP enhanced migratory T_{reg} which in turn reduced inflammation and modified disease in injected and uninjected joints, a phenotype that was also reproduced by IA injection of T_{reg}. PLGA-ATRA MP reduced proteoglycan loss and bone erosions in the SKG and collagen-induced arthritis (CIA) mouse models of autoimmune arthritis. Strikingly, systemic disease modulation by PLGA-ATRA MP was not associated with generalized immune suppression. PLGA-ATRA MP have the potential to be developed as a disease modifying agent for autoimmune arthritis.

4.2 Introduction

Inflammatory arthritides such as rheumatoid arthritis (RA) are systemic autoimmune inflammatory joint disorders that lead to chronic pain and disability. Disease modifying anti-

rheumatic drugs (DMARDs) that target cytokine signaling have greatly improved the prognosis of RA. However, a large fraction of patients display intolerance, partial or non-responsiveness towards frontline DMARDs and struggle to achieve disease control[1]. Moreover, DMARDs operate through generalized immunosuppression and increase the iatrogenic risk of opportunistic and serious infections and some DMARDs could impair immune responses to vaccines[2–4]. There is an unmet need for DMARDs that operate through immunoregulation to address pathogenic joint inflammation, rather than immunosuppression, for enhancing RA control in patients.

An emerging observation is that inflammatory changes in one RA-affected joint can enhance inflammation in other joints through systemic cell recirculation. For example, immune cells with unique transcriptomic profiles have been shown to circulate systemically and contribute to synovitis[5–14]. Importantly, T cells can migrate from the bloodstream to the synovial tissue where they play a key role in inducing local RA joint inflammation[15–18]. RA-affected joints are infiltrated with hyperactivated immune cells, including pathogenic $CD4^+$ T cells which produce pro-inflammatory mediators and have specificity to joint autoantigens[15]. Such $CD4^+$ T cells comprise pathogenic T helper (Th), which are pro-inflammatory, and disease protective T cells expressing FoxP3, called regulatory T cells (T_{reg}). T_{reg} generally suppress inflammatory T cells but a numerical imbalance between T_{reg} and autoreactive pro-inflammatory $CD4^+$ T cell subsets, including retinoic acid receptor-related orphan receptor gamma (RORγ)t-expressing Th17 cells, and impaired T_{reg} function in chronically inflamed joints and draining lymph nodes are major contributors to the pathogenesis of RA. In response to pathogenic inflammation, T_{reg} may lose immunoregulatory function and convert to an "ex-T_{reg}" phenotype which produce pro-inflammatory cytokines, such as interleukin (IL)-17[19–21].

Here we describe and validate an approach based on microparticles (MP) delivered via an IA injection which locally release an immunomodulatory agent that causes local enhancement of T_{reg} through epigenetic modulation. Since pathogenic T cells as well as protective T_{reg} are known to systemically recirculate throughout immune organs, our hypothesis is that locally enhanced T_{reg}, in turn, via systemic recirculation, can systemically suppress joint-specific autoimmunity, but without harming protective immune responses. The MP are composed of all-trans retinoic acid (ATRA) encapsulated in hydrolytically degradable poly-(lactic-co-glycolic) acid (PLGA) to generate PLGA-ATRA MP that enables joint-localized, sustained release of ATRA. Using the SKG mouse model of RA, we show that ATRA enhances differentiation of naïve mouse into T_{reg}, an effect that was recapitulated with human T cells. ATRA persistently stabilizes SKG T_{reg} in conditions that otherwise favor trans-differentiation into inflammatory Th17 cells. ATRA increases chromatin accessibility at T_{reg} associated loci and decreases accessibility at Th17 associated loci in a manner that coincides with differences in H3K4me3 histone methylation at the *Foxp3* locus and T_{reg} function associated loci. In SKG mice with established arthritis, PLGA-ATRA MP reside in an arthritic joint for several weeks after a single intra-articular (IA) injection. Bioactive ATRA released from IA PLGA-ATRA MP reduces inflammation and enhances immunoregulatory cells including T_{reg} in the injected joint, which correlates with reduced inflammatory markers, bone erosions and cartilage proteoglycan (PG) loss scores in both injected and uninjected joints, without evidence of non-specific suppression of T cell-dependent immune responses. The immunomodulatory effect of IA PLGA-ATRA MP was validated in the collagen-induced arthritis (CIA) mouse model where similar reduction in arthritis severity in injected and uninjected joints with protection against bone erosions and cartilage PG loss were quantified.

4.3 Results

4.3.1 ATRA promotes T_{reg} differentiation and stability in mouse and human T cells ex vivo

To test the effect of ATRA on T cells differentiation, an ex vivo differentiation and stabilization assay in Th17 inflammatory conditions using cytokine supplementation was used (**Figure 4.1)**. Naïve SKG $CD4^+$ T cells were isolated, which were consistently greater than 80% $CD4^+CD44^-CD62L^+$ post-enrichment (**Figure 4.10a**). Subsequently, these cells were stimulated with anti-mouse CD3 (αCD3) and anti-mouse CD28 (αCD28) antibodies along with Th17 polarizing cytokines IL-6, TGF-β1, IL-1β, and IL-23, and ATRA was added to the T cell culture medium, with concentrations ranging from 10 picomolar (pM) to 10 nanomolar (nM). Immunophenotypic analysis after four days showed that ATRA differentially enhanced FoxP3 and suppressed IL-17A expression in a concentration-dependent manner (**Figure 4.10b**). At a concentration greater than 100 pM, ATRA consistently enhanced FoxP3 expression (40.0 ± 3.4 %) while below 100 pM, 11.2 ± 2.3 % of T cells expressed FoxP3 (**Figure 4.1b**). The fraction of $IL\text{-}17A^+CD4^+$ T cells was comparable at 10 pM ATRA relative to control (9.5 ± 1.7% vs 11.3 ± 1.5%). ATRA reduced the expression of IL-17A at concentrations of 100 pM (7.2 ± 1.5 %), 1 nM (5.4 ± 1.9 %), and 10 nM (5.4 ± 2.3 %) (**Figure 4.1c**). In addition to reduced expression of IL-17A, ATRA comparably reduced the fraction of $ROR\gamma t^+CD4^+$ T cells at 1 nM (53.3 ± 7.9%) and 10 nM (47.9 ± 9.9%) relative to cells exposed 0 nM ATRA (73.3 ± 3.9%) (**Figure 4.1d**).

To test the persistence of the effect of ATRA-mediated T_{reg} enhancement, naïve $CD4^+$ T cells were stimulated with αCD3 and αCD28 coated Dynabeads and added 1 nM ATRA for 24- or 48- hours. Subsequently, the cells were thoroughly washed and replated in Th17

polarizing conditions for an additional 72 hours without ATRA (**Figure 4.1a)**. Pre-treatment of naïve $CD4^+$ T cells with ATRA for 24 hours was sufficient to induce T_{reg} differentiation and inhibit Th17 differentiation (**Figure 4.1e, f**). The fraction of naïve $CD4^+$ T cells that differentiate into T_{reg} increased further when the cells were pre-treated with ATRA for 48 hours, compared to untreated cells (**Figure 4.1g, h**). The fraction of IL-$17A^+CD4^+$ T cells was reduced in the cells pre-treated with ATRA in both the 24- and 48- hour pre-treated groups.

To assess the effect of ATRA on Th17 T cells, naïve $CD4^+$ T cells were stimulated in Th17 polarization conditions for five days to achieve strong Th17 polarization. Subsequently cells were treated with either 1 nM ATRA or no ATRA for 48 hours (**Figure 4.10c**). ATRA treatment significantly increased the fraction of $FoxP3^+$ T cells and reduced IL-$17A^+$ T cells (**Figure 4.10d,e**). $CD4^+$ T cell proliferation was comparable between the two groups (**Figure 4.10f**).

To assess if similar ATRA concentrations could be effective in human T cells, a human Th17 polarization assay was conducted (**Figure 4.10g,h**). Naïve human $CD4^+$ T cells were isolated from peripheral healthy human donor blood, consistently obtaining greater than 90% $CD4^+CD45RO^-CD62L^+$ post-enrichment. Subsequently, these cells were stimulated with plate bound anti-human CD3 and anti-human CD28 antibodies along with IL-6, TGF-β1, IL-1β, IL-23, and IL-21. ATRA was added to the human T cell expansion medium at concentrations ranging from 10pM – 1nM. To represent the differential effect of ATRA on human T cells, the $FoxP3^+$:IL-$17A^+$ T cell ratio was compared. At 1 nM ATRA, the ratio of $FoxP3^+$:IL-$17A^+$ cells in one donor was 0.99:1 ± 0.16, compared to 0.32:1 ± 0.05 and 0.36:1 ± 0.03 in no ATRA and 10 pM ATRA, respectively (**Figure 4.10i**).

The effect of ATRA on enhancing T_{reg} stability was assessed following a previously established T_{reg} destabilization assay[22]. SKG splenocytes and lymphocytes were sorted by flow cytometry (TCR-$\beta^+CD4^+eGFP^+$) to obtaining SKG FoxP3^{eGFP+} T_{reg} post-sorting (**Figure 4.10j)**. FoxP3^{eGFP} T_{reg} were stimulated for 72 hours with plate bound αCD3 and αCD28 with IL-6 and 1 nM ATRA added to the cell culture medium (**Figure 4.1i)**. The addition of ATRA enhanced T_{reg} stability, with 70.8 ± 4.7% of cells retaining FoxP3^{eGFP} expression, significantly greater than 56.5 ± 2.2% cells retaining FoxP3^{eGFP} expression in the absence of ATRA (**Figure 4.1j, Figure 4.1k**). The loss of FoxP3 expression correlated with T_{reg} transitioning to a Th17-like ex-T_{reg} phenotype, with 23.0 ± 1.7% and 13.3 ± 0.3% of cells without ATRA expressing RORγt and IL-17A, respectively, compared to 11.6 ± 1.8% and 5.7 ± 1.1% of cells cultured with 1 nM ATRA (**Figure 4.1l, Figure 4.10k,l**). Treatment with ATRA resulted in comparable transcription factor and cytokine expression to T_{reg} not exposed to IL-6 (**Figure 4.11m-o**).

To measure the immunoregulatory effect of ATRA on other RA-associated immune cells, differentiation experiments were conducted with SKG monocyte-derived dendritic cells (DCs) and macrophages. GM-CSF or M-CSF was used to differentiate SKG bone marrow cells into DCs or macrophages respectively (**Figure 4.11a**). After one week of differentiation, DCs were stimulated with LPS, and macrophages were polarized using LPS and IFNγ. ATRA significantly reduced CD80 and CD86 expression by DCs compared to untreated stimulated DCs, at a level that was comparable to unstimulated DCs (**Figure 4.11b-d**). In DCs, MHCII expression was comparable in all conditions (**Figure 4.11e**). ATRA significantly reduced TNF expression by macrophages compared to untreated stimulated macrophages at a level that was comparable to unpolarized macrophages (M0) (**Figure 4.11f,g**). MHCII expression between

ATRA-treated and polarized macrophages was comparable and higher than the unstimulated macrophages not treated with LPS (**Figure 4.11h**).

4.3.2 ATRA promotes a unique chromatin landscape in T cells differentiated in Th17 polarizing conditions

The enhancement of T_{reg} generation in Th17 polarizing conditions were correlated with changes in chromatin accessibility. Naïve SKG $CD4^+$ T cells were used in a Th17 polarization assay, described in **Figure 4.1a**, and the chromatin accessibility profiles of cells treated with 1 nM ATRA (+ATRA) or cells in Th17 polarizing conditions alone (-ATRA) were compared by assay for transposable-accessible chromatin with high-throughput sequencing (ATAC-Seq). Approximately 18,000 differentially accessible regions (DARs) were found, with ~8000 regions more accessible in the +ATRA condition, and ~10,000 regions more accessible in the -ATRA condition (**Figure 4.2a, b**). The accessible chromatin pattern between the two conditions was notably distinct at the *Foxp3*, *Rorc*, *Il17a*, *Il6rRa* and *Il1r1* loci, which are relevant for T_{reg} and Th17 phenotypes. (**Figure 4.2c**). The integrated chromatin accessibility of the *Foxp3* promoter region was enhanced in the +ATRA condition while that of the *Rorc*, *Il17a*, *Il6rRa* and *Il1r1* promoter regions was reduced or nearly absent in the +ATRA relative to the -ATRA condition (**Figure 4.2d**).

Chromatin interactions maintain contact between genes and distal regulatory elements, such as enhancers and promoters. To confirm potential molecular mechanisms of action of ATRA, the above-mentioned chromatin landscape data were interrogated for transcription factor (TF) binding motifs that were differentially accessible between the groups (**Figure 4.2e, f**). A differential motif enrichment analysis showed that DARs enhanced in the +ATRA condition were enriched in Runt family motifs and select ETS family TFs such as Ets1 and

Etv2. Members of the ETS family have been associated with promoting the development of T_{reg} as well as enhancing their stability and function[23,24]. Members of the Runt family of transcription factors have been shown to have pleiotropic effects in T_{reg} differentiation. Differential association of Runx1 with FoxP3 or Rorγt can inhibit or promote Th17 differentiation respectively, and binding of a complex of Runx1 and core-binding factor subunit beta (CBFβ) promotes FoxP3 expression in T_{reg}[25]. The DARs enhanced in the -ATRA condition were enriched in binding motifs for select bZIP family transcription factors including JunB and BATF which are associated with enhanced Th17 differentiation[26,27].

To assess potential factors that affect chromatin and gene accessibility, modifications to histone and CpG methylation patterns were analyzed. The Cleavage Under Targets and Tagmentation (CUT-and-TAG) assay was conducted to assess the degree of trimethylation at histone H3 lysine 4 (H3K4me3), an epigenetic modification often found at promoter sites known for enhancing transcription, in naïve SKG $CD4^+$ T cells differentiated in +ATRA and -ATRA conditions, as above[28,29]. Significant differences in H3K4me3 modifications were found at the *Foxp3* locus with a ~12-fold change in signal in +ATRA cells compared to -ATRA cells, as well as other sites implicated in T_{reg} function and stability, including *Hic1*, *Cd38*, and *Bcl6* [30–33] (**Figure 4.2g, Figure 4.12a**). However, there were no substantial differences in H3K4me3 methylation patterns at Th17-associated gene loci including *Rorc* and *Tnf*. As hypomethylation of the CNS2 region of *Foxp3* is known to be associated with natural T_{reg} (nT_{reg}) stability, the CpG methylation patterns were analyzed for differential methylation of DNA using reduced representation bisulfite sequencing (RRBS). No significant changes to CpG methylation were seen between +ATRA and -ATRA treated cells in the promoter regions of representative T_{reg} and Th17-associated loci (**Figure 4.2h**). Further, only six differentially

methylated regions were observed between samples, and the regions have not been associated with T_{reg} function or stability (**Figure 4.12b**).

4.3.3 Poly-(lactic-co-glycolic) acid microparticles sustain bioactive ATRA release

The aforementioned results suggested that ATRA is well-suited as a potential intra-articular inducer of persistent immunoregulatory changes that could be transferred to other affected joints via systemic recirculation of T cells. To this end, IA injectable microparticles were developed from poly-(lactic-co-glycolic) acid (PLGA) using a single emulsion method to generate PLGA-ATRA MP (**Figure 4.3a**). Scanning electron microscopy of lyophilized PLGA-ATRA MP was used to characterize the surface morphology. In general, the surface of pristine PLGA-ATRA MP was uniformly textured (**Figure 4.3b**). By controlling the homogenization rate, particles with differing size ranges were generated. The volume-averaged particle size across three batches was quantified (**Figure 4.13a, b**). The polydispersity index within each batch was less than 0.30 in all conditions (**Figure 4.3c**). The loading efficiency of ATRA into the microparticles was 62.4 ± 3.2% which resulted in PLGA-ATRA MP with a composition of approximately 1.2 wt% ATRA.

To quantify ATRA release in vitro, 10 mg PLGA-ATRA MP were suspended in 1 ml of 0.1% bovine serum albumin (BSA) in PBS and incubated at 37ºC, collecting release supernatant over 28 days at pre-determined timepoints. Approximately 13% of ATRA released within the first 24 hours (**Figure 4.3d**). From 24-96 hours, 10 ± 0.6%, 15 ± 0.2%, and 22 ± 1.3% of the original ATRA content was released from the 10.6 µm, 6.5 µm and 3.9 µm average diameter PLGA-ATRA MP respectively. Subsequently, ATRA release was sustained from all PLGA-ATRA MP for the next 24 days at a rate of ~0.4% of the initial loaded ATRA per day,

corresponding to a release of ~0.52 ng ATRA per mg of particles per day. To characterize changes in particle morphology during the course of in vitro degradation, PLGA-ATRA MP were periodically collected, washed and imaged. Dynamic morphological changes in the particle structure was observed which included an initial phase of swelling, erosion and final-stage structural decomposition (**Figure 4.13c, d**). At day 21, 10.6 μm particles had eroded but retained morphology while the 6.5 μm particles had undergone evident erosion and structural changes and most 3.9 μm particles had decomposed.

The bioactivity of released ATRA was assayed following the experimental schematic outlined in **Figure 4.1a** with supernatant collected at day 1, 14 and 28 from 6.5 μm particles, diluted to the expected joint concentration based on delivery of 2 μg PLGA-ATRA MP injected in ~20 μL of synovial fluid. In a mouse Th17 polarization assay, released ATRA collected at all three timepoints and freshly prepared 1 nM ATRA, comparably increased FoxP3 expression and reducing IL-17A expression (**Figure 4.3e, f**). Released ATRA also maintained T_{reg} stability comparable to 1 nM ATRA, improving FoxP3 expression while suppressing IL-17A expression (**Figure 4.3g, h**). In a human Th17 polarization assay, released ATRA also retained bioactivity comparable to 1 nM ATRA (**Figure 4.3i**).

To estimate in vivo concentrations of ATRA in the synovial fluid, spleen, and peripheral blood after IA injection, a two-compartment pharmacokinetic model was developed based on the in vitro release profile (**Figure 4.14a**). The biodistribution of ATRA was approximated using first order rate equations and previously reported experimentally measured kinetic parameters for ATRA half-life in the serum and synovium permeability data (**Figure 4.14b**)[34,35]. The model showed that after an initial spike, concentrations in the joint would be maintained at greater than 6 nM for at least 28 days with 6.5 μm PLGA-ATRA MP, while the

concentration in the peripheral blood are below physiologically relevant values (<20 pM) (**Figure 4.14c-e**). Based on the model and degradation profile, the 6.5 μm PLGA-ATRA MP was selected for further evaluation.

4.3.4 PLGA-ATRA MP suppress joint inflammation in SKG arthritis

SKG mice develop spontaneous RA-mimicking polyarthritis, and the onset can be accelerated by injections of fungal component injection[36,37]. To assess the feasibility of modulating established SKG arthritis, PLGA-ATRA MP were IA-injected in the ankle of SKG mice with mid-stage arthritis. Arthritis onset was synchronized using i.p. mannan injection and the treatment was administered after 14 days (**Figure 4.4a**). To measure particle persistence in the joint, cyanine-5 (Cy5) conjugated PLGA was incorporated to generate fluorescently labeled Cy5 PLGA-ATRA MP and PLGA MP without ATRA (PLGA-Blank MP) and quantified the Cy5 signal in live animals using an In Vivo Imaging System (IVIS).

Post-IA injection, the Cy5 signal remained localized in the joint and steadily decreased in intensity over the course of the study (**Figure 4.4b, Figure 4.15a**). As the Cy5 signal from deeper tissues could be attenuated, harvested tissues from additional cohorts of mice were imaged at one- and five-days post-IA injection. No signal above background was detected in the draining lymph nodes, kidneys, liver, or spleen at either timepoint (**Figure 4.15b**). To quantify uptake of particles by immune cells, flow cytometry analysis of the homogenized ankles, draining lymph nodes, and spleen was conducted (**Figure 4.15c**). Cy5 was detected primarily in $CD45^+CD11b^+CD11c^-$ and $CD45^+CD11b^+CD11c^+$ cells isolated from the injected ankle, with minimal uptake in $CD4^+$ cells, and no detection outside the injected ankle (**Figure 4.15d**).

To assess the role of sustained release in suppressing SKG arthritis, IA PLGA-ATRA MP were compared to a dose-matched IA injection of bolus ATRA. Mice received 2 μg PLGA-ATRA MP suspended in 20 μL of sterile PBS in a single hind ankle joint (ipsilateral ankle) via intra-articular (IA) injection. (**Figure 4.16a**). In a separate group of mice, dose matched bolus ATRA in corn oil was injected in the ipsilateral ankle. In both groups, the opposite ankle joint (contralateral ankle) received a sham injection of PLGA MP without ATRA (PLGA-Blank MP). Arthritis progression was compared between the treatment groups using bi-weekly clinical scoring, following a previously established method.[38] The pre-treatment clinical scores of mice were comparable between the groups, which increased rapidly from an initial score of 0 to an average score of 3.5 on day 14 prior to treatment with mild swelling in both wrist and ankle joints, with the majority of the digits swollen (**Figure 4.4c-f**). Post-treatment, arthritis was suppressed in IA PLGA-ATRA MP treated mice with strong reductions in inflammation in all joints, but no clinical benefit was seen in mice treated with a dose-matched IA bolus ATRA.

To determine if the anti-arthritic effect was due to the ATRA from the PLGA-ATRA MP, IA PLGA-ATRA MP were compared with PLGA-Blank MP. Both groups had an average score of 3.5 on day 14 prior to treatment, as above (**Figure 4.4g**). Clinical scores decreased in mice following treatment with a single IA-injection of 2 μg PLGA-ATRA MP, but not PLGA-Blank MP, four days (D18: 1.9 ± 0.4) and one week (D21: 1.4 ± 0.5) post-treatment and remained reduced until the study endpoint (D35: 1.9 ± 0.5). The scores were significantly lower than those in PLGA-Blank MP treated mice measured at the same timepoints (D18: 3.1 ± 0.5, D21: 3.2 ± 0.9, D35: 4.0 ± 1.0). In addition to the 2 μg PLGA-ATRA MP and PLGA-Blank MP treated mice, a subset of mice received a higher dose, either 20 μg or 200 μg of PLGA-

ATRA MP to assess if there was a dose dependent effect in vivo. Clinical scores of all groups treated with PLGA-ATRA MP were comparable (**Figure 4.16b**). Arthritis scores in all mice that received PLGA-ATRA MP decreased and stabilized following treatment for the remainder of the study. In contrast, the clinical scores in PLGA-Blank MP treated mice progressively increased until the study endpoint at day 35. The improvement in clinical score and ankle thickness measurements in PLGA-ATRA MP- treated mice were quantified in both the ipsilateral and contralateral joints (**Figure 4.4h-j, Figure 4.16c-d**). Ankle thickness of the hind paws in 2 µg PLGA-ATRA MP-treated mice remained stable or decreased following treatment. In contrast, clinical scores increased comparably in both the ipsilateral and contralateral ankles in IA bolus ATRA and PLGA-Blank MP-treated mice. To confirm the clinical observations of PLGA-ATRA MP-mediated, inflammatory markers in the ipsilateral and contralateral joint were quantified. Quantitative polymerase chain reaction (qPCR) confirmed that the inflammatory markers *Il6*, *Il1b*, *Tnf*, *Mmp3*, *Mmp13* were reduced in both the ipsilateral and contralateral joints of mice that received PLGA-ATRA MP but not PLGA-Blank MP, while *Tgfb1* was comparable between groups (**Figure 4.17a-g**).

4.3.5 PLGA-ATRA MP decreases synovial infiltrates, cartilage damage and bone erosions

To assess the structure of arthritic SKG joints, ipsilateral and contralateral ankles from PLGA-Blank and PLGA-ATRA MP-treated mice (subject to the analysis as described in **Figure 4.4**) were processed for histology after sacrifice on day 35. Hematoxylin and eosin (H&E)-stained sections of arthritic ankle sections showed reduced inflammation in the joints of PLGA-ATRA MP-treated mice compared to joints from PLGA-Blank MP-treated mice (**Figure 4.5a**). Inspired by the guidelines recently published for Standardized Microscopic Arthritis Scoring

of Histological sections (SMASH), a computer-aided algorithm in the QuPath software was generated using default settings for tissue thresholding and cell detection/classification, to facilitate quantification of cell infiltrates.[39] Ankles from mice treated with 2 μg PLGA-ATRA MP had significantly reduced cellularity compared to mice that received PLGA-Blank MP and bolus ATRA (**Figure 4.5b, Figure 4.18a-c**). The synovial inflammation and infiltration were comparable between the contralateral and ipsilateral hind joints of the same treatment groups (**Figure 4.5c, Figure 4.18d**). Cartilage proteoglycan (PG) loss and bone erosion (BE) scoring was performed on SMASH-recommended safranin-O-stained ankle joint sections from PLGA-Blank MP-, bolus ATRA-, and 2 μg PLGA-ATRA MP-treated mice. The PG loss scores for PLGA-Blank MP-treated ankles (2.8 ± 0.4) and bolus ATRA-treated ankles (2.5 ± 0.5) were both higher than in 2 μg PLGA-ATRA MP-treated ankles (1.4 ± 0.5) while 20 and 200 μg PLGA-ATRA MP treated mice had comparable PG loss scores to the 2 μg PLGA-ATRA MP mice (**Figure 4.5d, e, Figure 4.18e,f**). PG loss scores were comparable between the ipsilateral and contralateral ankles of the PLGA-Blank MP and 2 μg PLGA-ATRA MP treatment groups (**Figure 4.5f**). 2 μg PLGA-ATRA MP-treated ankles had a BE score of 1.0 ± 0.7, while PLGA-Blank MP-treated ankles had a BE score of 2.0 ± 0.6 and bolus ATRA-treated ankles had a BE score of 2.6 ± 0.5 (**Figure 4.5g, Figure 4.18g**). BE scores were comparable between ipsilateral and contralateral ankles of the PLGA-Blank MP and 2 μg PLGA-ATRA MP treatment groups (**Figure 4.5h**).

4.3.6 IA PLGA-ATRA MP suppress Th17 and enhance T_{reg} at local sites of inflammation

We sought to assess whether the IA route of administration uniquely contributed to the systemic anti-arthritic effect of PLGA-ATRA MP. To this end, arthritic SKG mice were treated

with either 2 μg PLGA-ATRA MP, dose-matched bolus ATRA, or 2 μg PLGA-Blank MP administered subcutaneously into the midscapular scruff region. Unlike with IA PLGA-ATRA MP, no significant improvement in clinical scores or ankle thickness measurements were observed in any of the treatment groups (**Figure 4.6a, b**).

To characterize local and systemic immune modulation mediated by IA PLGA-ATRA MP, $CD4^+$ T cell subsets in the ankles, draining lymph nodes and spleen were characterized 3 days and 11 days post-IA-PLGA-ATRA MP treatment (**Figure 4.6c, Figure 4.19a**). 3 days post-treatment, the number of infiltrating Th17 cells modestly decreased at 3 days in the ipsilateral and contralateral ankles of mice that received 2 μg PLGA-ATRA MP compared to mice that received PLGA-Blank MP (**Figure 4.6d**) but not in the draining lymph nodes or spleens (**Figure 4.6e, Figure 4.19b**). 11 days post-treatment, the number of Th17 in both the ipsilateral and contralateral ankles were lower in mice that received PLGA-Blank MP compared to mice that received PLGA-ATRA MP (**Figure 4.6f**). The same trend was observed in the pooled draining lymph nodes (inguinal and popliteal), with higher Th17 cell counts in both the ipsilateral ankle-draining lymph nodes as well as the contralateral ankle-draining lymph nodes of PLGA-Blank MP treated mice relative to PLGA-ATRA MP treated mice (**Figure 4.6g**). No difference was observed in the spleens of mice between treatment groups (**Figure 4.19c**).

We sought to validate the role of ATRA-enhanced T_{reg} in mediating arthritis protection. SKG $CD4^+$ T cells can transfer arthritis to RAG2-KO mice.[40] Following a previously established assay, T_{reg}-depleted SKG T cells ($CD4^+CD25^-$) were isolated and transferred to RAG2-KO mice via retro-orbital injection.[22] Subsequently, these mice were injected with mannan to induce arthritis. Arthritic mice were then treated via mono-articular injection with either T_{reg} differentiated ex vivo from naive $CD4^+$ T cells in media containing IL-2, TGF-β, and

1nM ATRA (+ATRA T_{reg}), or a sham PBS control (**Figure 4.6h**). Mice that received +ATRA T_{reg} had significantly reduced clinical scores relative to mice receiving sham PBS (**Figure 4.6i**). The T_{reg} fraction was higher in the ankles of mice that received +ATRA T_{reg}, while the IL-17A$^+$ fraction of T cells was comparable (**Figure 4.6j,k**). Moreover, ATRA enhanced CCR9 but not CCR6 expression in ex vivo differentiated T_{reg} (**Figure 4.20a,b**).

To assess whether T_{reg} recirculation between joints would phenocopy the systemic control of disease observed after monoarticular injection of PLGA-ATRA MP. SKG FoxP3^{eGFP} T_{reg}, isolated as described above (**Figure 4.1i, Figure 4.20c**), were expanded for 7 days. Subsequently, the cells were labeled with Cell Trace Violet (CTV) and transferred, via monoarticular ankle IA injection, into either non-arthritic BALB/cJ mice or arthritic SKG mice (**Figure 4.7a**). 3 days post-injection, mice were sacrificed and CTV$^+$ T_{reg} were quantified in the spleen, draining lymph nodes, contralateral lymph nodes, and contralateral and distal paws (**Figure 4.20d**) CTV$^+$ T_{reg} were detected in all analyzed tissues with a preferential accumulation in both the ipsilateral and contralateral arthritic joints of SKG mice, whereas the majority of CTV$^+$ T_{reg} were found in the pooled inguinal and popliteal draining lymph nodes or the spleen of BALB/cJ mice (**Figure 4.7b,c, Figure 4.20e**). The number of CTV$^+$ T_{reg} in the contralateral lymph nodes was comparable between arthritic SKG mice and BALB/cJ mice. IA administration of T_{reg} also reduced overall arthritis severity as measured by clinical scores in arthritic SKG mice and decreased the thickness of the contralateral ankles (**Figure 4.20f,g**). Strikingly, the number of CTV$^+$ T_{reg} in the injected joint of the arthritic mice was comparable to that in the pooled distal joints, supporting that recirculation of arthritis relevant T_{reg} from the joint can mediate arthritis protection.

As T_{reg} instability is known to exacerbate disease in SKG mice, we sought to assess whether PLGA-ATRA MP promote the stability of T_{reg} and the differentiation of new T_{reg} in vivo. A previously-established T_{reg} fate-mapping SKG mouse model was used in which cells actively expressing FoxP3 also express enhanced green fluorescent protein (eGFP), and cells that expressed FoxP3 during tamoxifen administration also express tdTomato (tdTom), allowing for the identification of stable T_{reg} ($CD4^+tdTom^+FoxP3^{eGFP+}IL\text{-}17A^-$) and ex-$T_{reg}$ ($CD4^+tdTom^+FoxP3^{eGFP-}IL\text{-}17A^+$) (**Figure 4.7d**).[41] As tamoxifen administration ends one week prior to arthritis induction, the model also allows for the identification of newly induced T_{reg} ($CD4^+tdTom^-FoxP3^{eGFP+}$). To assess the effect of PLGA-ATRA MP on T_{reg} stability, $CD4^+tdTom^+$ T cells after arthritis induction were compared between littermates that received IA PLGA-ATRA MP or PLGA-Blank MP, analyzing the pooled draining lymph nodes (inguinal and popliteal), pooled ankles, and the spleen. The reduced arthritis severity in this model necessitated pooling of the joints and lymph nodes to obtain adequate number of cells for analysis. Littermates that received PLGA-ATRA MP had a reduced fraction of ex-T_{reg} in both joint draining lymph nodes and ankles as compared to littermates that received PLGA-Blank MP, while the fraction of ex-T_{reg} in the spleen was comparable between treatment groups (**Figure 4.7e-g**). To assess the effect of PLGA-ATRA MP on in situ T_{reg} induction, the fraction of $CD4^+tdTom^-FoxP3^{eGFP+}$ T cells in the draining lymph nodes, ankles and spleen was analyzed. The fraction of induced T_{reg} was increased in the ankles of PLGA-ATRA MP treated littermates (**Figure 4.7h**). The fraction of induced T_{reg} in the draining lymph nodes of mice that received PLGA-ATRA MP was modestly increased in five of the seven pairs, but this trend was not statistically significant (**Figure 4.7i**). There was no difference between newly induced T_{reg} in the spleens of PLGA-ATRA MP treated mice and PLGA-Blank MP treated mice (**Figure 4.7j**).

4.3.7 PLGA-ATRA MP treatment is effective without generalized immunosuppression

To assess if the T_{reg} enhancement induced by IA PLGA-ATRA MP results in generalized suppression of T cell-mediated responses, the response of arthritic SKG mice, treated with either PLGA-Blank MP or PLGA-ATRA MP, was measured after prime/boost immunization. The primary immunization consisted of subcutaneous injection of an emulsion of ovalbumin (OVA), an SKG arthritis-irrelevant antigen, in complete Freund's adjuvant three days post-IA injection, followed by a booster immunization ten days later consisting of OVA in incomplete Freund's adjuvant (**Figure 4.8a**). As this route of OVA immunization is known to produce a strong anti-OVA IgG1 antibody response, the post-prime and post-boost anti-OVA IgG1 antibody concentration in the peripheral blood were quantified. Healthy non-immunized SKG mice without arthritis were used to quantify the baseline immune response. Arthritis progression, as assessed by clinical scoring, was not affected by either the prime or boost immunization in both PLGA-Blank MP and PLGA-ATRA MP mice and was similar to non-immunized mice (**Figure 4.8b**). Plasma anti-OVA IgG1 antibody titers were comparable between PLGA-Blank MP and PLGA-ATRA MP-treated mice, and both groups produced high antibody titers (**Figure 4.8c**).

To quantify the effect of IA PLGA-ATRA MP on arthritis-irrelevant T cell suppression OVA-specific tetramers for quantifying antigen-specific T cells in $H2^b$-background mice were used and the aforementioned immunization study in healthy C57BL/6J (B6) mice was conducted (**Figure 4.8d**). Systemically administered ATRA, delivered as a daily intraperitoneal (i.p.) injection, was also used to assess the effect of systemic exposure. The anti-OVA IgG1 titer in IA PLGA-ATRA MP treated mice was comparable to that in immunized mice that

received no treatment and in mice receiving daily ATRA injections (**Figure 4.8e**). OVA-specific $CD4^+$ T cells, as quantified by I-A(b) QAVHAAHAEIN tetramer staining, were significantly lower after daily i.p. administration of ATRA in the spleen, while a single dose of IA injected PLGA-ATRA MP did not impair the antigen specific $CD4^+$ T cell response relative to untreated immunized mice (**Figure 4.8f**).

4.3.8 PLGA-ATRA MP treatment modulates disease in the mouse model of collagen-induced arthritis (CIA)

To further validate the efficacy of PLGA-ATRA MP, the disease modifying effect was assessed in the CIA mouse model. DBA/1 mice were primed with an emulsion of complete Freund's adjuvant and collagen and subsequently treated with either 2 μg of PLGA-ATRA MP or PLGA-Blank MP in both ankles via IA injection (2x total dose used in the SKG mouse model) three days before boost, prior to the manifestation of clinical symptoms (**Figure 4.9a**). Clinical scores in injected (hind) and uninjected (fore) joints of PLGA-ATRA MP-treated mice were significantly diminished for ~6 weeks post-IA injection compared to PLGA-Blank MP-treated mice, prior to a subsequent increase (**Figure 4.9b,c**). Analysis of high resolution microCT images of the metacarpophalangeal and ankle joints confirmed strong protection against bone erosions by PLGA-ATRA MP as assessed by BE scoring and significantly lower bone surface area to volume ratio compared to the PLGA-Blank MP treated mice (**Figure 4.9d-g**). Ankles were subsequently processed for histomorphometry (**Figure 4.9h,i**). Scoring of H&E- and safranin-O-stained sections of the navicular cuneiform joint confirmed reduced synovitis and PG loss respectively in PLGA-ATRA MP treated mice compared to PLGA-Blank MP treatment (**Figure 4.9j,k**).

4.4 Discussion

Here, we demonstrate that a single IA injection of PLGA-ATRA MP systemically reduced inflammation severity in arthritic SKG mice, which correlated with enhancing anti-inflammatory T_{reg} over pro-inflammatory Th17 cells. We confirmed that ATRA promoted the differentiation of mouse and human T_{reg} and inhibited Th17, consistent with prior reports, and prevented mouse T_{reg} destabilization.[42–44] The immunophenotypic modulation was consistent with ATRA-mediated enhanced chromatin accessibility at T_{reg}-relevant loci and reduced that of Th17-associated loci in Th17 polarizing conditions. A single bolus IA injection of ATRA had no effect on arthritis progression and encapsulation of ATRA in PLGA-based microparticles facilitating sustained release of ATRA at therapeutically relevant concentrations was necessary to suppress disease progression for at least 4 weeks post-injection. Importantly, PLGA-ATRA MP, in addition to reducing inflammation, also acts as a systemic disease-modifying agent in the SKG and CIA mouse models of arthritis. The IA-based immunoregulatory approach is distinct conceptually from IA steroid injections which are used in some RA patients but are neither disease modifying nor are known to cause benefit to uninjected joints.[45] The therapeutic efficacy of PLGA-ATRA MP also compares favorably to systemically administered DMARDs in SKG and CIA mice. The improvement in arthritis scores by IA PLGA-ATRA MP is superior to the reported efficacy of methotrexate in SKG mice, a first line DMARD, even though it is administered at a dose (1mg/kg daily) which is ~20-fold greater than the typical clinically used dose of methotrexate in humans.[46] The efficacy of IA PLGA-ATRA MP was comparable to weekly systemic administration of 100 µg anti-IL-17A antibody treatment in SKG mice or weekly systemic administration of 200 µg anti-IL-6R[22].

Although no mouse model of RA entirely recapitulates the human disease, pre-arthritic and arthritic SKG mice are good models for understanding key pathophysiological features of human RA.[38] Importantly, the SKG mouse model of RA recapitulates well the insufficient T_{reg} function and stability described in many patients with RA.[47,48] We had previously demonstrated that SKG T_{reg} can downregulate FoxP3 and convert to pathogenic IL-17A$^+$ ex-T_{reg} in arthritic joints and draining lymph nodes.[22,41] Inspired by these findings, here we demonstrated that ATRA enhanced differentiation of naïve CD4$^+$ T cells into T_{reg} over Th17 in Th17 polarizing conditions and enhanced stability of pre-existing T_{reg}, which is consistent with prior observations of ATRA on T_{reg}.[49–56] Using ATAC-Seq analysis, we correlated the immunophenotypic modulation to differential changes mediated by ATRA in the chromatin landscape which correlated with differences in H3K4me3 methylation at the *Foxp3* locus. These observations are consistent with the known effect of ATRA on enhancing accessibility of transcription machinery to the *Foxp3* promoter via histone methylation.[52,57] Even though ATAC-Seq analysis supported that Th17-associated loci were differentially accessible, the similarity in H3K4me3 methylation at Th17-associated loci suggests that this ATRA-mediated epigenetic modification did not directly contribute to changes in chromatin accessibility at these sites. Here, the observation that Runt family transcription factors are enhanced by ATRA is notable as it has been previously shown that these factors are important in facilitating the heritable maintenance of the active state of the *Foxp3* locus.[30,42] Moreover, the finding that ATRA stabilizes pre-existing natural (n)T_{reg} is consistent with prior work that has demonstrated that ATRA can directly inhibit the methylation of the *Foxp3* gene and maintains accessibility in the presence of inflammatory cytokines.[58,59] The composition, size and stability of nT_{reg} are controlled by non-coding DNA sequence (CNS) elements at the *Foxp3* locus. ATRA has also

been demonstrated to contribute to nT_{reg} stability by preventing demethylation of the FoxP3 enhancer CNS2.[59] However, demethylation at the CNS2 locus of induced T_{reg} (iT_{reg}) has been demonstrated to be unaffected, regardless of ATRA treatment.[52] Consistent with this observation, T_{reg} and Th17 associated loci did not exhibit differential CpG methylation patterns between cells treated with and without ATRA. Taken together, the data supports that ATRA distinctly promotes iT_{reg} induction and nT_{reg} stability.

In addition to enhancing T_{reg}, we show that ATRA modulates the phenotypes of DCs and macrophages, which are myeloid cell subsets. ATRA reduced the expression of the DC costimulatory markers CD80 and CD86 and TNF expression in stimulated macrophages. DCs have been shown to process and present self-antigens to prime autoimmune responses in lymphoid organs, such as the draining lymph node, which leads to inflammation in the joint.[60–64] In vivo, PLGA-ATRA MP were taken up by myeloid cells in the injected but not uninjected joint. Thus, local immunomodulation of DCs could reduce local joint inflammation and may also facilitate the induction of disease protective T_{reg} that recirculate. The effect of ATRA-mediated reduction in the inflammatory macrophages is consistent with prior reports.[55,65,66] However, macrophages have limited capacity for recirculation, though some subsets could act as antigen presenting cells in the draining lymph node.[67] As PLGA-ATRA MP uptake is restricted to myeloid cells is the injected joint, the resulting immunomodulatory effect is unlikely to directly contribute to systemic disease modulation through recirculation of DCs and macrophages.

IA PLGA-ATRA MP are distinct from other preclinical immunoregulatory strategies in autoimmune inflammatory arthritis that are being explored as alternatives to generalized immunosuppression such as localized delivery of engineered DMARDs, antigen-specific

immunomodulation using tolerogenic vaccines in CIA mice, ex vivo generation and infusion of tolerogenic T_{reg}-inducing dendritic cells by incubation with a mixture of RA autoantigens (Rheumavax), ex vivo generation and infusion of a chimeric antigen receptor (CAR)-T_{reg} against one or multiple RA autoantigens.[68–73] While all these strategies are effective and translatable to the clinic, the efficacy of Rheumavax and CAR-T_{reg} approaches could be limited by the paucity of known autoantigens that can be targeted as substantial antigenic spread is known to occur in RA. A localized immunosuppression approach has also been explored through IA administration of anti-TNF Ab, modified with an extracellular matrix-binding peptide. While the IA agent suppressed arthritis in treated joints, it did not display systemic efficacy.[72] PLGA-ATRA MP have the advantage of acting locally at the site of inflammation to promote disease specific immunomodulation without a priori knowledge of participating epitopes. Other methods using biomaterial depots to expand T_{reg} have used PLGA microparticles encapsulating multiple immunoregulatory agents, such as rapamycin, IL-2 and TGF-β that, when injected near hind paw draining lymph nodes, modulated disease but also resulted in a systemic immunosuppression and non-specific expansion of T_{reg}.[74,75] Moreover, PLGA-ATRA MP can be lyophilized and stored for extended periods and potentially used off-the-shelf and similar to other IA injected agents, if needed, PLGA-ATRA MP injections could be performed under fluoroscopic and ultrasound guidance techniques. Importantly, systemically delivered ATRA is not associated with musculoskeletal symptoms, further supporting the idea that ATRA will be well-tolerated and safe for IA delivery.[53,76]

PLGA-ATRA MP equally protected injected ipsilaterial and uninjected contralateral joints, and systemic disease modulation was not associated with generalized suppression of T cell-dependent immune responses. The ex vivo ability to induce and stabilize T_{reg}, combined

with the reduction of Th17 cells in the ankles and draining lymph nodes of PLGA-ATRA MP treated SKG mice and the similar findings obtained by single IA injection of T_{reg} in the same model supports that local differentiation/stabilization of T_{reg} followed by T_{reg} systemic recirculation underlies the systemic improvement in arthritis progression observed after a single IA injection of PLGA-ATRA.[77] An enhanced fraction of newly induced T_{reg} in the joints of mice treated with PLGA-ATRA MP, distinct from the subset that are stabilized, may also contribute to improved control of inflammation, which is consistent with prior work that has demonstrated the role of induced T_{reg}, which have been show to retain their phenotype and function in cytokine-driven autoimmune arthritis.[78]

In inflamed RA joints, capillary permeability increases to allow cell migration, an effect that also enhances the exit of molecules, especially low molecular weight compounds, from the joint space. Therefore, although bolus IA injection of ATRA can localize the effect of ATRA, it cannot avoid rapid clearance. As IA injections can only be administered with limited frequency, rapid clearance cannot be overcome simply by increasing the frequency of drug administration. For this reason, amounts well above the therapeutically relevant concentration must be introduced in the joint which could cause local toxicity as well as lead to undesired side effects if taken up by off-target tissues after exit from the joint. In contrast, PLGA-ATRA MP enables release of local concentrations of ATRA which are at the same time sustained and effective locally but insufficient to cause systemic ATRA exposure above the immunosuppressive threshold. PLGA-ATRA MP were effective at suppressing disease progression after a single IA injection and well-tolerated at a dose ranging from 2 – 200 micrograms. The systemic exposure at these doses is predicted to be significantly lower than frequent systemically administered ATRA ranging from 0.5-25 mg/kg per dose, which have

been used in other autoimmune disease mouse models modulating inflammation in uveitis, experimental autoimmune encephalomyelitis, and inflammatory autoimmune arthritis.[53–55,79,80] The calculated maximum systemic exposure to ATRA in vivo after a single IA PLGA-ATRA MP injection (C_{max}) is 40 pM, well below the concentrations reached with doses that have been associated with toxicity in rodents (> 14 mg/kg).[81,82] These results are consistent with prior work that evaluated sustained release and systemic concentration of ATRA following a subcutaneous dose.[83] Moreover, our pharmacokinetic model shows that a therapeutically relevant concentration of ATRA is maintained in the synovial fluid of the treated joint and the immunization experiment demonstrate that IA released ATRA avoids generalized immune suppression.

Following IA injection of PLGA-ATRA MP, Th17 cells were reduced in the ipsilateral ankle within 3 days. 11 days post-treatment, reduced Th17 were observed in the ipsilateral, and contralateral ankles and corresponding draining lymph nodes. These results are consistent with prior findings that have correlated disease severity with Th17 cells in SKG mice.[22] Our results from fate mapping SKG mice further support that the enhancement in T_{reg} stability in the ankles and joint-draining lymph nodes following IA injection of PLGA-ATRA MP contribute in part to the observed reduction in Th17. Systemic recirculation of IA injected T_{reg} and preferential accumulation in arthritic joints over non-arthritic joints, accompanied by a corresponding decrease in clinical score support the notion that T_{reg} have the capacity to modulate arthritis severity. Furthermore, treatment of T_{reg} with ATRA enhanced the migratory marker CCR9, which has previously been associated with T cell chemotaxis occurring in a CCL25 dependent manner, a chemokine which is also commonly found in the RA joint synovial fluid.[84–86] While we cannot rule out the contribution of other recirculating cells and soluble factors in mediating

arthritis protection, the results from the in vitro enhancement of T_{reg} function and migratory markers mediated by ATRA, the efficacy of ATRA-treated T_{reg} after transfer into RAG mice, the enhancement in newly induced T_{reg} in vivo by PLGA-ATRA MP and the lack of efficacy of subcutaneously administered PLGA-ATRA MP all support that disease-specific immunomodulation may be attributed, at least in part, to recirculation of T_{reg} from the treated joint.

SKG arthritis symmetrically affects joints and is associated with the elevation of key RA cytokines including IL-6, IL-1β and TNF. Moreover, joint damage manifests as cartilage and bone erosion.[36] Here, we observed that PLGA-ATRA MP treated mice had lower immune cell infiltration, and lower scores for BE and PG loss, in both injected and untreated joints. We also found that treatment with PLGA-ATRA MP resulted in reductions in *Il6*, *Il1b*, *Tnf, Mmp13,* and *Mmp1* expression in both the injected and uninjected joints compared to sham injected controls, but not in *Tgfb1*. PLGA-Blank MP alone modestly reduce these inflammatory markers in the injected ankle, but this reduction was not statistically significant. To further validate these findings of joint protection, we tested PLGA-ATRA MP in the CIA mouse model, widely used in research and preclinical studies. As in SKG mice, T_{reg} in CIA mice have been shown to lose FoxP3 expression and undergo IL-6-mediated trans-differentiation into exT_{reg} that accumulate in inflamed joints.[87] CIA is characterized by synovial hyperplasia, immune cell infiltration and significant bone erosions. Arthritis presentation in CIA mice is well-known to be asymmetric and therefore both ankle joints were treated. Despite the increased dose, the model predicted that the expected systemic concentration of ATRA was well below immunosuppressive concentrations. Upon treatment, PLGA-ATRA MP but not PLGA-Blank MP, significantly reduced clinical scores in both the injected and uninjected joints. Treatment-blinded analysis of

high resolution microCT images of the metacarpophalangeal joints and the bone proximal to the tibio-tarsal junction confirmed strong protection against bone erosions by PLGA-ATRA MP as assessed by BE scoring and a significantly lower bone surface area to volume ratio compared to the PLGA-Blank MP treated mice. Treatment-blinded histomorphometry analysis of H&E- and safranin-O-stained sections of the navicular cuneiform joint confirmed reduced synovitis and PG loss respectively in PLGA-ATRA MP treated mice. These results further validate PLGA-ATRA MP as an immunoregulatory agent in autoimmune arthritis.

Uncontrolled inflammatory arthritides lead to chronic pain and disability. While DMARDs have transformed disease management, a large fraction of patients face difficulty in achieving and remaining in remission. As joint damage and time to remission bear direct proportionality, clinical protocols seek to rapidly minimize disease activity. However, several patients do not respond to multiple DMARDs and in patients who are only partially responsive to specific DMARDs, deepening immunosuppression – for example by combining a second DMARD – increases the risk of infections and cancer. The ability to modulate pathogenic immune cells to delay clinical disease progression, coupled with preservation of cartilage PG and reduced BE, supports the utility of IA PLGA-ATRA MP as a locally delivered agent that provides a systemic disease-specific clinical benefit. If PLGA-ATRA MP-mediated immunomodulation performs similarly in the human context, then its application – especially if administered in early RA – might work as a monotherapy to stem progression of disease. More likely, one or more injections of PLGA-ATRA MP could serve as an immunoregulatory adjuvant to treat those that are inadequately responsive or intolerant to DMARDs, or in combination with DMARDs to enhance control of disease without further impairing the immune response.

4.5 Materials and Methods

4.5.1 Study Design

The objective of this study was to develop an IA-deliverable immunomodulatory agent to promote systemic disease remission in inflammatory arthritis. To this end, PLGA-ATRA MP were formulated and characterized. The single-emulsion method was used to generate PLGA-ATRA MP by consistently generating at least three batches for each particle size. Subsequently, all in vitro material characterization studies were conducted at least three times. All in vitro mouse cell culture studies were performed with a minimum of three technical replicates, and three experimental replicates. Three biological replicates were used for ATAC-seq sample preparation and subsequent analysis. All in vivo studies were conducted following an approved IACUC protocol. Outcomes were generally determined by assessing clinical scores, ankle thickness, flow cytometry assessments and histological appearances, unless otherwise noted. For in vivo arthritis studies, littermate mice were injected with mannan to synchronize disease onset. The criteria for omission were (i) onset of severe arthritis in one or more paws prior to treatment, (ii) signs of arthritis on day 0, and (iii) failure to develop arthritis by day 14 post-mannan injection. All other animals were included in the data analysis. Pre-determined endpoints for data collection were based on changes in and progression of clinical scores in the treatment groups. Prior to treatment, littermate mice were randomly placed into treatment groups after ensuring that the mean clinical score of each group was the same. All arthritis studies were conducted in at least two litters of mice. For fate mapping studies, littermate mice were randomly placed into treatment groups prior to mannan injection. For ovalbumin immunization studies, cages that received treatment prior to ovalbumin immunization were

randomly chosen. In general, statistical power for arthritis studies was based on prior reports. Sample numbers for each individual experiment are provided in the figure legends. Alphanumeric coding was used to blind treatment groups for flow cytometry and histomorphometry analysis. Scoring was performed by two independent operators.

4.5.2 Materials

Poly (lactic-co-glycolic) acid (50:50 PLGA, AP041, lot: 200825RAI-B, MW 10-15 kDa) and Cy5-labeled poly (lactic-co-glycolic) acid (50:50 PLGA-Cy5, AV034, lot: 201215RAI-A, MW 10-15 kDa) were purchased from Akina. All-trans retinoic acid (BML-GR100-0500, lot: 06011830) was purchased from Enzo. DMSO (D128-500, lot:194474) and dichloromethane (DCM, D143-1, lot:194105) were purchased from Fischer Chemical. Poly-vinyl alcohol (363146-500G, lot:MKCF9787, MW 85-124 kDa), corn oil (C8267-500ML, lot:MKCM9808), and mannan (M7504-5G, lot:SLCF4977) were purchased from Sigma-Aldrich. RPMI powder was purchased from (Gibco, lot:2344357). Mannan was purchased from Sigma-Aldrich. Incomplete Freund's Adjuvant + Ovalbumin (EK-0311, lots: 105, 111) and Complete Freund's Adjuvant + Ovalbumin (EK-0301, lots:105, 111) were purchased from Hooke Labs.

4.5.3 In Vitro Mouse T cell Differentiation Assays

Naïve SKG mouse $CD4^+$ T cells were isolated via magnetic depletion using the Naïve $CD4^+$ T cell Isolation kit (Miltenyi Biotech) according to the manufacturer's instructions. Isolated naïve $CD4^+$ T cells were plated in 96 well plates at 100,000 cells/well in RPMI 1640 supplemented with non-essential amino acids (NEAA), sodium pyruvate, and beta-

mercaptoethanol (Complete RPMI). To induce Th17 differentiation, IL-6 (50 ng/mL) (200-06, lot: 031916-1 B2321), TGF-β1 (5 ng/mL) (100-21, lot: 1218209 H1919), IL-23 (5 ng/mL) (200-23, lot: 0712S227 K1119) and IL-1β (20 ng/mL) (200-01B, lot: 0606B95 B2421) were added at the time of plating, with various concentrations of ATRA. All cytokines were recombinant human cytokines purchased from Peprotech. Cells were stimulated with PMA-ionomycin (Cell Stimulation Cocktail, Invitrogen, Cat. No. 00-4970-03, lot: 2430454) and brefeldin A (Invitrogen, Cat. No. 00-4506-51) for 5 hours prior to staining and analysis.

For the ATRA pre-treatment Th17 differentiation assay, the same isolation procedure was followed. Immediately following isolation, cells were plated at 100,000 cells/well in complete RPMI with Dynabeads to provide stimulation at a concentration according to the manufacturer's instructions. Media was supplemented with or without 1 nM ATRA. Following either 24 or 48 hours of incubation at 37 C, the cells were washed four times using a 1:10 dilution to ensure ATRA concentration in the media was below 1 pM. The cells were then resuspended and transferred to a new plate and RPMI with Th17 inducing cytokines as detailed previously were added, and cells were incubated for an additional 72 hours before being stimulated with PMA-ionomycin and brefeldin A for 5 hours prior to staining and analysis.

For the ATRA post-treatment following Th17 polarization assay, the same isolation procedure was followed. Isolated naïve $CD4^+$ T cells were plated in 96 well plates at 100,000 cells/well in complete RPMI with Th17 differentiating factors as described above. After five days, cells were analyzed and split into a group that received 1 nM ATRA and a control group that did not receive 1 nM ATRA for 48 hours. Cells were then stimulated with PMA-ionomycin and brefeldin A for 5 hours prior to staining and analysis.

For the generation of +ATRA T_{reg} for transfer, cells were isolated as previously described. Naïve $CD4^+$ T cells were then plated at 100,000 cells/well in 200 µL of complete RPMI with Dynabeads to provide stimulation according to manufacturer's instructions. Complete RPMI media was supplemented with 1 nM ATRA, 5 ng/mL IL-2 and 5 ng/mL TGF-β. Cells were cultured for 7 days, with 300 µL of media addition and transfer to a 24 well plate on day 3 and 500 µL media addition on day 5. Added media contained all factors listed.

4.5.4 In Vitro Mouse T_{reg} Destabilization Assay

Total $FoxP3^{eGFP+}TCR\beta^+CD4^+$ T cells were sorted using Fluorescence-Activated Cell Sorting (FACS) using a Sony SH800S Cell Sorter (SH800S) from the spleens and lymph nodes of 8–12-week-old female BALB/c $FoxP3^{eGFP}$ SKG mice or 8–12-week-old C57BL/6J $FoxP3^{eGFP}$ SKG fate-mapping mice. After sorting, $FoxP3^+$ T_{reg} were stimulated using plate-bound αCD3 and αCD28 (adsorbed at 5 µg/mL in PBS at 37ºC for 3 hours) with or without IL-6 (Peprotech) at 50 ng/mL in the presence of varying concentrations of DMSO-solubilized ATRA or PLGA-ATRA MP. After 72 hours, cells were removed, washed, and stimulated with PMA-ionomycin and brefeldin A for 5 hours and analyzed for expression of FoxP3, IL-17A, and RORγt via flow cytometry. Results from assays that yielded an overall cell viability of less than 50% at the endpoint were excluded.

4.5.5 In Vitro Human Th17 Differentiation Assay

Fresh whole blood was purchased from the La Jolla Institute for Allergy and Immunology (LJI) and used fresh on the day of the draw. PBMCs were isolated using a Ficoll density gradient (Lymphopure). Isolated PBMCs were then sorted using a Human Naïve CD4

T cell Isolation kit (Miltenyi Biotech) according to the manufacturer's instructions. Isolated naïve CD4 T cells were plated in 96 well plates at 100,000 cells/well in RPMI 1640 supplemented with NEAA, sodium pyruvate, and beta-mercaptoethanol. To induce Th17 differentiation, IL-6 (50 ng/mL), TGF-β1 (5 ng/mL), IL-23 (5 ng/mL) and IL-1β (20 ng/mL), and IL-21 (25 ng/mL) were added at the time of plating, with various concentrations of ATRA. All cytokines were recombinant human cytokines purchased from Peprotech.

4.5.6 In Vitro Dendritic Cell Differentiation and Stimulation Assays

Bone marrow cells (BMCs) were harvested from the tibia and femurs of SKG mice. Following red blood cell lysis, cells were resuspended in complete DMEM (cDMEM) which contains DMEM prepared according to manufacturer's instructions (12100-046, Gibco) as well as 1% non-essential amino acids, 1% penicillin-streptomycin, beta-mercaptoethanol and 10% FBS. For DC differentiation, 50 ng/mL GM-CSF was added to the media and BMCs were plated in 6 well plates with 2 mLs of media at 1 million cells /mL. Media was added on day 3, and whole media was refreshed on day 5. To assess the effect of ATRA on DC differentiation, 10 nM ATRA was added to select wells on day 0 and the concentration was kept constant when adding and replacing media. To stimulate DCs 10 ng/mL LPS was added on day 7. Brefeldin A was added on day 8 for 4 hours prior to harvesting cells via trypsinization for staining and flow cytometry.

4.5.7 In vitro macrophage differentiation and stimulation assays

Bone marrow cells were harvested from the tibia and femurs of SKG mice. Following red blood cell lysis, cells were resuspended in cDMEM. For macrophage differentiation, 25

ng/mL M-CSF was added to the media and BMCs were plated in 6 well plates with 2 mLs of media at 1 million cells /mL. Media was added on day 3, and whole media was refreshed on day 5. To assess the effect of ATRA on macrophage differentiation, 10 nM ATRA was added to select wells on day 0 and the concentration was kept constant when adding and replacing media. To stimulate and polarize macrophages, 10 ng/mL LPS and 50 ng/mL IFNγ were added on day 7. Brefeldin A was added on day 8 for 4 hours prior to harvesting cells via trypsinization for staining and flow cytometry.

4.5.8 ATAC-Seq library preparation and sequencing

Cells used in ATAC-Seq experiments were subject to the same procedure as described in the "In vitro mouse Th17 differentiation assay" above. On day 3, 10^5 cells were removed from media and prepared for ATAC-Seq using the Active Motif ATAC-Seq kit (Active Motif, Cat No. 53150) according to manufacturer instructions. Briefly, isolated cells were washed once with ice-cold PBS and subsequently resuspended in ATAC Lysis Buffer on ice to isolate the nuclei. The lysis buffer was removed, cells were washed, and nuclei were incubated with tagmentation mix at 37ºC for 30 minutes, after which DNA was isolated and purified. DNA was then amplified via PCR using the provided indexed primers according to manufacturer's instructions. SPRI cleanup beads were then used to purify the amplified DNA prior to sequencing. Samples were sequenced at the La Jolla Institute for Allergy and Immunology using an Illumina NovaSeq sequencer (NovaSeq 6000).

4.5.9 ATAC-Seq Analysis

Analysis of raw reads from sequencing of ATAC-seq prepared libraries went as follows: FASTQ files were aligned to mm10 reference genome using bowtie2 with parameters "-k 4 -X 2000".[88] Reads corresponding to Encyclopedia of DNA Elements (ENCODE) blacklisted regions, mitochondrial genome, and chrY were removed.[89] Reads were then filtered for uniquely mappable reads with mapping quality >= 30 using SAMtools, and duplicate reads were removed using MarkDuplicates from Picard tools (https://broadinstitute.github.io/picard).[90] Reads aligning to the (+) strand were shifted by +4 bp and reads aligning to the (-) strand were shifted by -5 bp using deepTools alignmentSieve.[91] Peaks were then called using MACS2 with the parameters (*-g mm -q 0.05 –nomodel –nolambda –keep-dup all –call-summits –shift -100 –extsize 200*).[92] Summits of all peaks were then extended to regions of 500 bp, and the 500 bp peaks from +ATRA group and -ATRA group were merged to get consensus peaks via bedtools slop and merge routines. Shifted BAM files were then converted to beds and the reads for each region of the consensus peaks were counted using bedtools coverage.[93] Count normalization and differential ATAC-seq analysis was then performed using DESeq2.[94] Differentially accessible regions (DARs) were filtered using FDR-adjusted p-values <= 0.05 and fold-change >=2. Normalized coverage tracks were created from shifted BAM filesusing deepTools bamCoverage with parameters "-bs 10 –effectiveGenomeSize 2652783500 –normalizeUsing RPKM -e 200".[91] Motif enrichment analysis was performed by clustering the DARs into 2 clusters using k-means. Hypergeometric Optimization of Motif EnRichment (HOMER) was then used to identify known motifs for transcription factor binding sites enriched in the different clusters of peaks.[95]

4.5.10 CUT-and-TAG library preparation and sequencing

Cells used in CUT-and-TAG experiments were subject to the same procedure as described in the "In vitro mouse Th17 differentiation assay" above. On day 3, 10^5 cells were removed from media and cryopreserved. Cryopreserved mouse primary $CD4^+$ T cells were sent to Active Motif for the CUT&Tag assay. Cells were incubated overnight with Concanavalin A beads and 1 µl of the primary anti-H3K4me3 antibody per reaction (Active Motif, catalog number 39159). After incubation with the secondary anti-rabbit antibody (1:100), cells were washed and tagmentation was performed at 37°C using protein-A-Tn5. Tagmentation was halted by the addition of EDTA, SDS and proteinase K at 55°C, after which DNA extraction and ethanol purification was performed, followed by PCR amplification and barcoding (see Active Motif CUT&Tag kit, catalog number 53160 for recommended conditions and indexes). Following SPRI bead cleanup (Beckman Coulter), the resulting DNA libraries were quantified and sequenced on Illumina's NextSeq 550 (8 million reads, 38 paired end).

4.5.11 RRBS preparation and sequencing

Cells used in RRBS experiments were subject to the same procedure as described in the "In vitro mouse Th17 differentiation assay" above. On day 3, 10^5 cells were removed from media and cryopreserved. Cryopreserved mouse primary $CD4^+$ T cells were sent to Active Motif for RRBS sequencing. Genomic DNA was extracted using the Quick-gDNA MiniPrep kit (Zymo Research D3024) following manufacturer's instructions for cell suspensions and proteinase K digested samples. 100ng of gDNA was digested with TaqaI (NEB R0149) at 65ºC for 2h followed by MspI (NEB R0106) at 37ºC overnight. Following enzymatic digestion, samples were used for library generation using the Ovation RRBS Methyl-Seq System (Tecan 0353-32) following manufacturer's instructions. In brief, digested DNA was randomly ligated,

and, following fragment end repair, bisulfite converted using the EpiTect Fast DNA Bisulfite Kit (Qiagen 59824) following the Qiagen protocol. After conversion and clean-up, samples were amplified resuming the Ovation RRBS Methyl-Seq System protocol for library amplification and purification.

RRBS libraries were measured using Agilent 2200 TapeStation System and quantified using the KAPA Library Quant Kit ABI Prism qPCR Mix (Roche KK4835). Libraries were sequenced on a NovaSeq 6000 at SE75.

4.5.12 RRBS and CUT-and-TAG analysis

Reads were aligned using the BWA algorithm (mem mode; default settings). Duplicate reads were removed, and only reads that mapped uniquely (mapping quality >= 1) and as matched pairs were used for further analysis. Alignments were extended in silico at their 3'-ends to a length of 200 bp and assigned to 32-nt bins along the genome. The resulting histograms (genomic "signal maps") were stored in bigWig files. Peaks were identified using the MACS 2.1.0 algorithm at a cutoff of p-value 1e-7, without control file, and with the –nomodel option. Peaks that were on the ENCODE blacklist of known false ChIP-Seq peaks were removed. Signal maps and peak locations were used as input data to Active Motifs proprietary analysis program, which creates Excel tables containing detailed information on sample comparison, peak metrics, peak locations and gene annotations. For differential analysis, reads were counted in all merged peak regions (using Subread), and the replicates for each condition were compared using DESeq2. Fold change between +ATRA and -ATRA samples was then calculated and compared, and the list of genes with an absolute value of

log_2(fold change) greater than one was generated and compared to differentially accessible regions observed in ATAC-Seq.

4.5.13 Microparticle Synthesis

PLGA and PLGA-ATRA MP were synthesized via an oil-in-water emulsion. PLGA was dissolved at 50 mg/mL in DCM. For fluorescence, 1 mg/mL of PLGA-Cy5 was included. For preparing PLGA-ATRA MP, 100 μL of 20 mg/mL ATRA dissolved in DMSO was added to the PLGA solution and vortexed until fully mixed. The resulting solution was slowly dropped into 20 mL of a 2 w/v% PVA solution that was continuously homogenized for one minute using a handheld homogenizer (Benchmark Scientific D1000 Handheld Homogenizer) to create the emulsion. PLGA-Blank MP and PLGA-ATRA MP were prepared at homogenization speeds of 8500, 17100 and 30000 rpm with a 0.007 m impeller. The primary emulsion was then added to 60 mL of 1 wt% PVA stirring at 400 rpm and left stirring for 4 hours at room temperature. The resulting mixture was then centrifuged at 1000g and washed using sterile DI water 4 times before it was frozen and lyophilized. The resulting size distribution was analyzed using scanning electron micrographs (SEM).

4.5.14 Scanning Electron Micrographs

Samples of lyophilized microparticles were prepared as follows: lyophilized microparticles stored at -20ºC were mechanically agitated until the product was freely moving powder. A small amount of power was placed on carbon tape affixed to an SEM stub, and excess powder was removed by blowing compressed air over the surface. Prepared stubs were sputter coated in an Emitech K575X Sputter Coater under argon at $4x10^{-3}$ mbar using iridium

deposited using 85 mA of current for 8 seconds. Coated samples were then loaded into the SEM (FEI Quanta FEG 250) and imaged using a 3 kV beam in high vacuum. Images were taken after repeated rounds of focusing and direct adjustments were performed to ensure image quality.

4.5.15 Microparticle Size Distribution Analysis

The size distribution of PLGA MP were analyzed as outlined graphically in **Figure 2a**. Briefly, SEM images of PLGA-ATRA MP and PLGA-Blank MP were loaded into the FIJI distribution of ImageJ. The scales of images were set using the "Set Scale" function in conjunction with the SEM scale bar, which was subsequently cropped out. Particle edges were detected using the "Find Edges" function, and the image was converted to a binary mask using the "Convert to Mask" function. The holes in the image were filled using the "Fill Holes" function, and then the particle edges were eroded to allow for detection of distinct particles using the "Erode" function. This decreased the particle size by a set diameter, which was measured and accounted for in subsequent analysis. The particle sizes were then analyzed using the "Analyze Particles" function, and the resulting areas were converted to diameters, the diameters were adjusted to account for loss during the erosion function, and the volume-averaged size distribution was calculated. The results of this technique were validated by comparison to hand measurement results using select images and were found to be in close agreement.

4.5.16 In Vitro Release and Degradation Assay

To quantify the rate of ATRA release from PLGA-ATRA MP, particles were suspended at 10 mg/mL in PBS with 0.1 wt% bovine serum albumin and placed suspended particles in an

incubator at 37ºC. To collect the supernatant to measure ATRA release, PLGA-ATRA MP were spun down at 1000x g for 5 minutes, and the supernatant was carefully collected and refreshed without disrupting the particle pellet. After the supernatant was exchanged, particles were resuspended via vigorous vortexing, and the particles were placed back into the 37 C incubator. The concentration of ATRA in the collected supernatant was determined using a Nanodrop UV-vis spectrophotometer via comparison to a standard curve. The release buffer was replaced every day for the first four days and subsequently on days 7, 14, 21, 28.

4.5.17 PK Modeling

Theoretical in vivo pharmacokinetics were determined using a two-compartment model as illustrated in Figure 3. A concise explanation of two compartment pharmacokinetic models is available elsewhere.[96] Here, the two-compartment model was used to represent the synovial compartment and the peripheral blood. The governing equation was modified for the synovial compartment to include a term to account for the release of ATRA from the IA injected PLGA-ATRA MP. The rate of ATRA release from PLGA-ATRA MP was determined using the vitro release profile. The rate of exchange between the periphery and the synovium was an order of magnitude approximation based on prior reports. The rate of elimination of ATRA from the peripheral blood was based on reported half-life of ATRA in the serum. The model was programmed and implemented in Python using the Anaconda 3 distribution and is publicly available at https://github.com/Shah-Lab-UCSD/PLGA-ATRA-PK

4.5.18 Arthritis Models

All animal work was approved by the University of California, San Diego (UCSD) Institutional Animal Care and Use Committee (IACUC) under protocol # S17160. C57BL/6J (B6, Jax # 000664), BALB/cJ (BALB/cJ, Jax # 000651), DBA/1 (Taconic # DBA1BO-F) and BALB/c RAG2-KO (Taconic # 601) were purchased, BALB/c SKG mice were obtained through a Materials Transfer Agreement between UC San Diego and Kyoto University and colonies are maintained at UCSD. B6.H2d.FoxP3$^{EGFP.ERT2\text{-}Cre}$. R26$^{tdTomfl/fl}$.SKG mice have been previously described [47] and colonies are maintained at UCSD. BALB/c SKG, BALB/cJ, DBA/1 and RAG2-KO mice used were female. B6.H2d.FoxP3$^{EGFP.ERT2\text{-}Cre}$. R26$^{tdTomfl/fl}$.SKG mice were both male and female. All mice were housed under specific pathogen–free conditions. Arthritis onset was induced in 8–12-week-old mice via mannan injection as described elsewhere [47]. Mice were injected intraperitoneally with 20 mg of mannan (Millipore-Sigma, M7504-5G, lot:SLCJ9322) dissolved in 200 µL of sterile PBS. Mice were anesthetized using isoflurane and disease severity was determined twice weekly using clinical scoring and measurement of hind paw swelling using calipers in accordance with a standardized protocol. Briefly, fore and hind paws were assessed independently in each mouse and were assigned scores according to the following criterion: No visible swelling (0), mild to moderate swelling (0.5), severely swollen (1.0), as well as an additional for 0.1 for each swollen digit. Clinical scores reported are the aggregate of all paws (maximum of 5.8) from a single mouse unless otherwise noted. A score of 5.5 was considered the clinical endpoint and mice who attained this score before the end of the study were sacrificed according to IACUC guidelines.

To assess the efficacy of PLGA-ATRA MP, arthritis was induced as described above. On day 14 after arthritis induction, littermate mice received an injection of either 2, 20 or 200 µg PLGA-ATRA MP, 200 µg Blank MP suspended in 20 µL sterile PBS, or dose-matched

bolus ATRA suspended in 20 µL sterile corn oil, injected intra-articular into a single hind ankle. The contralateral hind ankle was injected with PBS or Cy5-labeled PLGA-Blank MPs as a sham control. Clinical scores and ankle thickness of mice were tracked biweekly for an additional 3-21 days after treatment to an endpoint of 35 days after mannan injection. To examine immunological changes after injection of the PLGA-ATRA MP, some cohorts of mice were sacrificed on day 17 after mannan injection (3 days after treatment) and some were sacrificed on day 25 after mannan injection (11 days after treatment). To ensure that all mice were at the same stage of arthritis onset, mice that developed severe arthritis (clinical score of 4.0 or greater or a minimum of 1 paw severely swollen) prior to day 14 were excluded from the study. Mice that did not manifest arthritis were excluded from the study.

For inducing arthritis in RAG2-KO mice, $CD4^+CD25^-$ T cells were sorted from SKG lymph nodes and spleens and transferred to RAG2-KO mice via retro-orbital injection. Seven days after the transfer of the $CD4^+CD25^-$ T cells, RAG2-KO mice were injected with 200 µg of mannan to initiate arthritis onset. Eleven days after mannan injection, mice were treated via intra-articular sham injection of PBS or three hundred thousand ex vivo generated T_{reg} treated with ATRA, as described above. Clinical scores and ankle thickness were tracked following the initial cell transfer, and mice were scored bi-weekly using the same scoring system as SKG mice.

For the collagen induced arthritis (CIA) model, 8-week-old female DBA/1 mice were injected with 50 µL of a complete Freund's adjuvant/bovine collagen emulsion (EK-0220, lot 124, Hooke Laboratories). On day 18, mice received intra-articular injection of 2 µg of either PLGA-ATRA MP or PLGA-Blank MP in both hind ankles. On day 21, all mice received 50 µL of incomplete Freund's adjuvant/bovine collagen emulsion (EK-0221, lot 124, Hooke

Laboratories). Forepaws and hind paws were assessed for clinical signs of arthritis according to the following criteria: No swelling or erythema (0), mild localized swelling or erythema (1), moderate localized swelling or erythema (2), moderate whole paw swelling or erythema (3), severe whole paw swelling or erythema (4). Criteria for euthanasia was a clinical score of 14 or higher.

4.5.19 In Vivo Particle Uptake, Tracking and Degradation Assays

Cy5 labeled PLGA was incorporated into PLGA-ATRA MP and Blank MP as described under synthesis to create fluorescently labeled MP. For degradation studies, arthritic mice were IA injected with 200 μg fluo-MP and fluorescent signal was tracked bi-weekly using an In Vivo Imaging System (IVIS) (Xenogen). Mice were anesthetized and imaged in a prone position with the site of injection oriented upwards. The radiant efficiency was measured and normalized to the highest radiant efficiency value measured in the first three days. For particle uptake and biodistribution studies, arthritic mice were injected IA with 20 μg fluo-MP and sacrificed one and five days after injection. The kidney from the side of injection, liver, spleen, injected and uninjected ankles and both popliteal lymph nodes were removed and fluorescent signal was quantified using IVIS. Ankles, draining lymph nodes, and spleens were dissociated and analyzed using flow cytometry.

4.5.20 qPCR Preparation and Analysis

Arthritis was induced in SKG mice and was treated after 14 days with PLGA-Blank MP and PLGA-ATRA MP as previously described. Ankles were harvested seven days after treatment and were flash frozen in liquid nitrogen and stored. Whole mouse joint homogenate

samples were first cut and homogenized with a handheld homogenizer in TRIzol on ice (cat# 15596018 Invitrogen). RNA was purified from the chloroform phase using RNAeasy Plus Micro kit (cat# 74034 Qiagen) according to manufacturer's protocols. Sample RNA concentration was normalized, and cDNA was synthesized using the SuperScript III First-Strand Synthesis SuperMix for real-time quantitative reverse transcription PCR (qRT-PCR) (cat# 11752250 Life Technologies) according to manufacturer's protocols. qPCR was performed on a Bio-Rad CFX384 Real-Time PCR Detection System, with Kicqstart primer assays for *Mmp13, Tgfb1, Il6, Il1b, Tnf, Mmp3* and *Gapdh* (KSPQ12012G, Sigma) in a final concentration of 10µM and SYBR Green qPCR Master Mix (cat# 330513 Qiagen). Primer assay efficiencies were guaranteed by the manufacturer to be greater than 90%. Each reaction was measured using technical triplicates, and data were normalized to the expression levels of the housekeeping gene *Gapdh.* Results are presented as a fold-change compared to the average expression level in the sham treated ankles of PLGA-Blank treated mice using the ΔΔCq method.

4.5.21 T_{reg} Transfer and Tracking Assay

Live TCRβ^{+}CD4^{+}FoxP3^{eGFP+} T_{reg} were isolated from SKG.FoxP3^{eGFP} mice using a Sony SH800S Cell Sorter. Sorted T_{reg} were expanded on Dynabeads (Invitrogen, 11452D, lot:00911146) in complete RPMI supplemented with 10 ng/mL IL-2 for five days according to manufacturer's instructions for Dynabead use. After 5 days, T_{reg} were washed with PBS and stained for 30 minutes at 37ºC with CellTracker Violet BMQC dye (ThermoFisher, Cat No. C10094, lot:2451243). For staining, cells were washed with sterile PBS and resuspended at a concentration of 10^6 cells/mL in a solution of PBS supplemented with CellTracker Violet

BMQC dye, prepared by adding 2 μL of stock dye per 1 mL of PBS. Cells were then washed twice to remove residual dye and injected into a single ankle of either healthy BALB/cJ or SKG mice with established arthritis at $5x10^5$ T_{reg} suspended in 20 μL of PBS per mouse. Mice were sacrificed three days post-injection and the spleens, draining lymph nodes (inguinal and popliteal), contralateral lymph nodes (inguinal and popliteal), injected ankle and uninjected ankle were all harvested and analyzed using flow cytometry. Mice that did not receive any injection were used as a negative control for analysis.

4.5.22 Fate-Mapping Assays

A previously reported inducible T_{reg} fate-mapping SKG mice (B6.SKG.H2d/d FoxP3$^{eGFP\text{-}ERT2\text{-}Cre+/+}$ tdTomato$^{fl/fl}$) [41] was used. In these mice, FoxP3^{eGFP+} T_{reg} carry an inducible Cre-ERT2 fusion protein that can be activated by administration of tamoxifen, allowing for generation of T_{reg}-specific fate mapping. To induce Cre expression, 8–12-week-old male and female inducible T_{reg} fate-mapping mice were administered 100 μL tamoxifen (T5648, MilliporeSigma, 20 mg/mL dissolved in corn oil) via oral gavage for five consecutive days. One week after the last treatment, mice were injected intraperitoneally with 20 mg of mannan dissolved in 200 μL of sterile PBS. 14 days after mannan injection, littermate pairs of mice were treated via intra-articular injection of PLGA-ATRA MP or PLGA-Blank MP. 11 days following treatment, mice were sacrificed, and spleens, ankles, and ankle-draining lymph nodes (popliteal and inguinal) were harvested and analyzed for expression of FoxP3, tdTomato and IL-17A.

4.5.23 Micro–Computed Tomography (microCT) Analysis

Mouse ankles were placed in 4% paraformaldehyde (PFA) for 48 hours for fixation. After fixation, samples were transferred to 70% ethanol. Treatment-blinded scanning and analysis was performed at the University of Gothenburg. Before scanning, bones were transferred to PBS for 24 hours. Scanning was performed on a Skyscan1176 Micro-CT (Bruker) with a voxel size of 9 μm, at 55 kV/467 mA, with a 0.2-mm aluminum filter. Exposure time was 880 ms. The x-ray projections were obtained at 0.4° intervals with a scanning angular rotation of 180° and a combination of four average frames. The projection images were reconstructed into three-dimensional images using Nrecon software (version 1.6.9.8, Bruker) and aligned for further analysis in DataViewer (version 1.5.0.9, Bruker). Data were processed using CT-Analyzer software (version 1.14.4.1 Bruker), and images were generated using CTVox software (version 2.7, Bruker). Bone erosion was quantified as previously described.[97]

4.5.24 Histological Processing

After sacrifice, mouse hind limbs were excised below the knee joint. Histology is from mice represented in clinical scoring in Figure 4.4 and Figure 4.16. Muscle and skin was removed to the degree possible without damaging internal structures, and the limbs were fixed in 4% PFA for 48 hours. The fixed limbs were then transferred to a 70% ethanol solution. Samples were then sent to the Tissues Technology Shared Resource Core at Moores Cancer Center (histology in Figure 5 and Figure 4.18, except bolus ATRA), the University of Gothenburg (histology in Figure 9), or Inotiv (bolus ATRA histology in Figure 4.19), where they were decalcified and embedded in paraffin. Paraffin embedded limbs were sectioned to an appropriate depth according to SMASH guidelines and stained with either hematoxylin and eosin or safranin-O using standard tissue processing techniques. Stained slides were digitized

using an Aperio AT2 Automated Digital Whole Slide Scanner or a Zeiss Axioscan 7 Slide Scanner.

4.5.25 Histomorphometry Analysis

To quantify immune cell infiltration in histological sections, H&E sections were loaded into the QuPath software (Figure 4c). Representative histological sections were used to train the software using built-in classification tools to broadly classify immune cells, muscle and tendon, and bone. Once trained, the software was then used to detect and classify types in sections from the metatarsals to part way up the tibia. Skin was excluded from the analysis to prevent misidentification of dermal cells as immune cells. For proteoglycan loss scoring and bone erosion scoring, SMASH guidelines were followed (30). Briefly, histological sections were examined and proteoglycan loss was scored as follows: 0 – healthy intact cartilage consisting of fully stained cartilage layer with a smooth surface; 1 – Mild loss of staining in ~ 1/3 of the superficial cartilage zone, still predominantly red when stained with Safranin O; 2 – Moderate loss of Safranin O staining in up to 2/3 of the superficial cartilage zone; 3 – Complete loss of Safranin O staining in the superficial cartilage zone. Bone erosion was scored as follows: 0 – Healthy, intact bone surface; 1 – Small, superficial bone erosion at the outer surface of the bone, no breakage into marrow; 2 – Enhanced local bone erosions into subchondral space, partial or complete penetration of cortical bone; 3 – Massive enlarged subchondral bone erosion, extended synovial pannus invasion causing near-complete breakthrough of cortical bone to the marrow. Scoring was performed by two independent treatment-blinded operators.

4.5.26 Flow Cytometry Analysis

Anti-mouse antibodies against IFN-γ (clone: XMG1.2, lot:2289505), IL-4 (clone: BVD6-24G2, lot:2284161), IL-17A (clone:eBio17B7, lot:2142931), RORγt (clone:B2D, lot:2304447), FoxP3 (clone:FJK-16s, lot:2199652) were purchased from Invitrogen. Anti-mouse antibodies against CD8a (clone:53-6.7, lot:B313471) were purchased from Biolegend. Anti-mouse antibodies against CD4 (cat:1540-26, lot:F2212-T406C) were purchased from Southern Biotech. Anti-human antibodies against FoxP3 (clone:236A/E7, lot:4336544) and RORγt (clone:AFKJS-9, lot:2123761) were purchased from Invitrogen. Anti-human antibodies against IL-17A (clone:BL168, lot:B252098), CD45 (clone:HI30, lot:B256106) and CD4 (clone:SK3, lot:B256770) were purchased from Biolegend. All cells were gated based on forward and side scatter characteristics to limit debris, including dead cells. The Zombie Aqua Fixable Viability Kit (Biolegend, lot:B333785) stain was used to separate live and dead cells. Antibodies were diluted according to the manufacturer's suggestions. Gates were drawn based on fluorescence-minus-one controls, and the frequencies of positively stained cells for each marker were recorded. Intracellular/intranuclear stains were performed by first staining for surface markers according to manufacturer's protocols, then fixing and permeabilizing cells using the FoxP3 Fixation/Permeabilization Buffer Set (Invitrogen, 00-5523-00 , lots:2333698, 2220750, 2203535). To quantify immune cell subsets in mouse ankles, ankles were harvested after sacrificing mice, skin was removed, and ankles were harvested and incubated at 37ºC in a solution of Complete RPMI, 0.1 mg/mL Type VIII collagenase (Millipore-Sigma, C2139-100MG, lot:0000090030) and 0.01 mg/mL DNAase (Millipore-Sigma, 10104159001, lot:60852700) for 60 minutes with intermittent gentle shaking. The supernatant was filtered through a 70 μm cell strainer and tissue was removed from the ankles and pressed through the screen and subsequently simulated with PMA/ionomycin (Biolegend, 00-4970-93,

lot:2430454) and Brefeldin A (Biolegend, 00-4506-51, lot:2229153) for 5 hours, after which cells were stained. To quantify immune cell subsets in the spleen, spleens were mashed and filtered through 70 μm cell strainers using Complete RPMI. Red blood cells were then lysed for 5 minutes, after which samples were washed with Complete RPMI and stimulated with PMA/ionomycin and Brefeldin A for 5 hours. To quantify immune cells in lymph nodes, lymph nodes were mashed and filtered through 70 μm cell strainers using Complete RPMI, and were concentrated via centrifugation, and subsequently stimulated with PMA/ionomycin and Brefeldin A for 5 hours. Cell counts and frequencies were calculated using flow cytometry. A portion of the spleen and lymph nodes were stained, and all cells from processed ankles were stained, unless otherwise noted. Flow cytometry was performed using an Attune® NxT Acoustic Focusing cytometer analyzer (A24858) and data analyzed using FlowJo software.

For tetramer staining of C57BL/6J OVA reactive T cells, cells were incubated with the class II MHC IA-(b) OVA tetramer QAVHAAHAEIN ($OVA_{325-335}$, NIH Tetramer Core Facility, Task Order 57395) for one hour at 37°C, after which cells were stimulated with PMA/ionomycin and Brefeldin A without washing out tetramer for four hours. Cells were subsequently washed and stained, fixed, and permeabilized according to manufacturer's instructions for the FoxP3 Fixation/Permeabilization Buffer Set (Invitrogen 00-5523-00, lot:2333698).

4.5.27 Ovalbumin Immunization Assays

In SKG mice, arthritis was induced via mannan injection as previously described. Arthritis treatments were administered IA on day 14, and mice were vaccinated on day 17 after with two 50 μL of an ovalbumin/complete Freund's adjuvant emulsion at two distinct sites

subcutaneously on the back. Mice were bled 10 days after priming, and subsequently received booster immunizations of a single 100 μL injection of an ovalbumin/incomplete Freund's adjuvant subcutaneously. Mice were then bled and sacrificed 11 days after the booster injection.

In C57BL/6J mice, treatments were administered on day 0. A single IA dose of PLGA-ATRA MP was administered IA. Intraperitoneal ATRA was administered daily for the duration of the experiment at 0.5 mg/kg. On day 3, mice received a priming shot of 100 μL of an ovalbumin/complete Freund's adjuvant emulsion at one site on the back, administered subcutaneously. Mice were bled 13 days after priming, and subsequently received booster immunizations of a single 100 μL injection of an ovalbumin/incomplete Freund's adjuvant subcutaneously. Mice were then bled and sacrificed 11 days after the booster injection and stained as detailed in the flow cytometry section.

4.5.28 Anti-OVA Antibody Titer Analysis

Blood collected from the ovalbumin immunization assays were thawed and diluted in PBS at 1:3 peripheral blood to PBS ratios. Sera was extracted by spinning down at 800 g for 8 minutes and extracting the supernatant. Sera were then analyzed for IgG1 and IgG2a antibodies against ovalbumin using ELISA (Biolegend 406603, lot:B270353 and Biolegend 407104, lot:B268019, respectively). High affinity plates were coated using OVA (Invivogen vac-stova, lot:5823-43-01) and anti-OVA titers were defined as the highest serum dilution factor at which the ELISA optical density reading was ≥ 0.3.

4.5.29 Statistical Analysis

Sample sizes for animal studies were based on our prior work. The Biostatistics Unit of the Clinical and Translational Research Institute at UC San Diego was consulted on statistical analysis. Data outside three SD from the mean were excluded. Data is presented as either mean ± SD or mean ± SEM, as indicated for each experiment in figure legends. Results were analyzed where indicated using unpaired Student's one tailed t-test, paired and unpaired Student's two tailed t-test, one-way ANOVA with post hoc multiple comparison test, repeated measures two-way ANOVA with post hoc multiple comparison test (for clinical time course data with $n < 5$ per group), linear mixed effects model (for clinical time course data with $n \geq 5$ per group), Mann-Whitney rank test, Wilcoxon match-paired signed rank, and Kruskal-Wallis with post hoc multiple comparison test and identified for each individual experiment in the figure legends. p-values are reported in figures. Statistical analysis of clinical scoring and ankle thickness data. Data were analyzed using Graphpad Prism software for all except the linear mixed effects model analysis, which was analyzed in SPSS v28.

4.6 Chapter 4 Acknowledgements

Chapter 4, in full, is adapted with modifications from "Immunomodulatory Microparticles Epigenetically Modulate T Cells and Systemically Ameliorate Autoimmune Arthritis", Advanced Science 2023, 10(11), 2202720 with authors David A. McBride, Matthew D. Kerr, Wade T. Johnson, Anders Nguyen, Martina Zoccheddu, Mina Yao, Edward B. Prideaux, Nicholas C. Dorn, Wei Wang, Mattias N.D. Svensson, Nunzio Bottini, and Nisarg J. Shah.

4.7 Chapter 4 Appendix

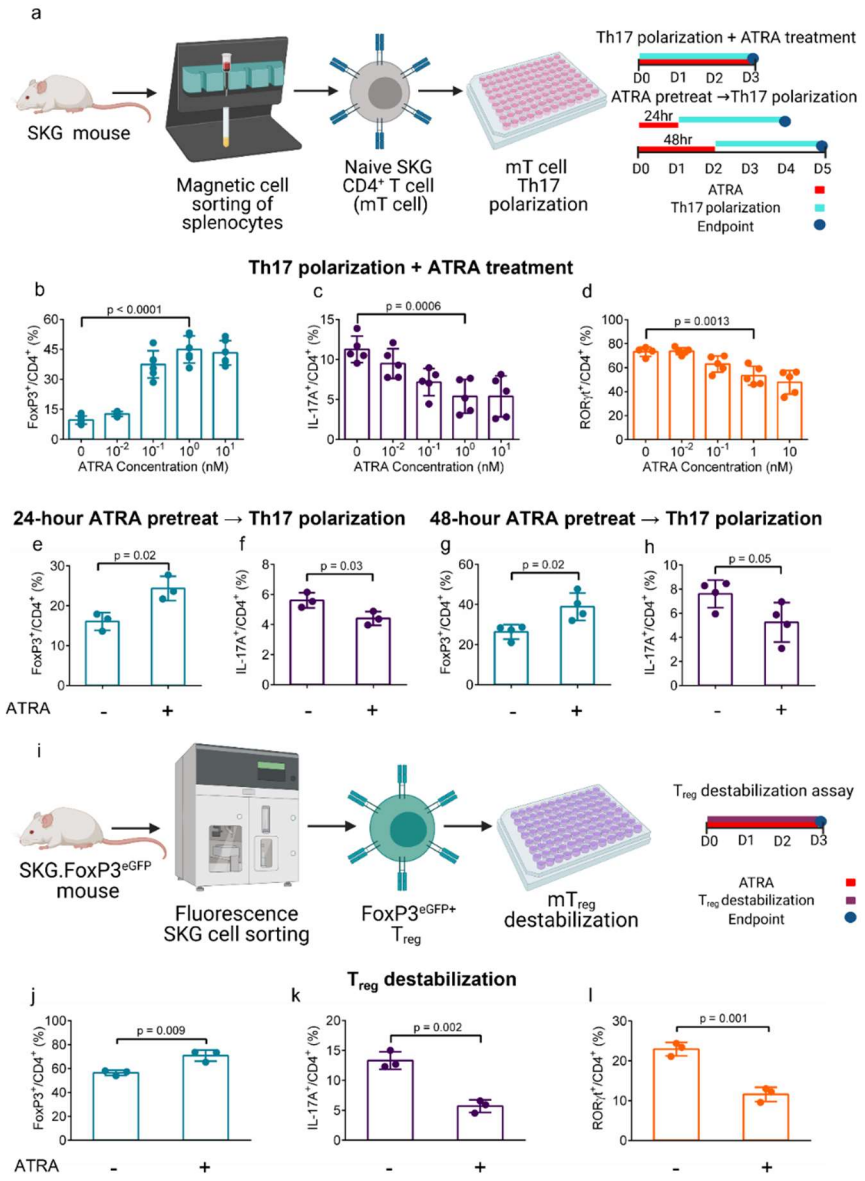

Figure 21 All-trans retinoic acid differentially promotes Treg enhancement and Th17 suppression in a concentration dependent manner.

(a) Experimental schematic and timeline for assessing the effect of all-trans retinoic acid (ATRA) on Th17 and Treg differentiation from naïve CD4+ SKG T (mT) cells. (b-d) Quantification of (b) FoxP3, (c) IL-17A and (d) RORγt expression in CD4+ mT cells differentiated in Th17 inducing conditions with ATRA added at the depicted concentrations. (e-h) Quantification of FoxP3 and IL-17A expression in CD4+ T cells pretreated with or without 1 nM ATRA for either (e, f) 24 or (g, h) 48 hours prior to Th17 induction for an additional 72 hours. (i) Experimental schematic for assessing SKG Treg (mTreg) destabilization. (j-l) Quantification of (j) FoxP3 expression, (k) IL-17A expression and (l) RORγt expression in Treg following an IL-6 mediated destabilization assay with or without 1 nM ATRA. Data in b-h and j-l are the means ± SD of technical replicates from representative experiments; Data in b-d and j-l are representative of three experimental replicates, e-h are data representative of three experimental replicates. Statistical analyses in b-d were performed using one-way ANOVA with post-hoc Dunnett's test; statistical analysis in e-h and j-l were performed using unpaired Student's two tailed t-tests.

Figure 22 ATRA differentially modulates chromatin accessibility at Th17 and Treg associated loci in Th17 polarizing conditions.
(a) Scatterplots of ATAC-Seq counts per peak comparing cells exposed to Th17 polarizing conditions treated with 1 nM ATRA (+ATRA, n = 3) or without ATRA (-ATRA, n = 3). Experimental timeline was the same as that depicted in Fig. 1a). Red corresponds to differentially accessible regions (DARs) enriched in the +ATRA condition, blue corresponds to DARs enriched in the -ATRA condition, and grey corresponds to common regions that are accessible in both conditions, but not significantly different. (b) Boxplots of ATAC-Seq counts per peak from +ATRA and -ATRA conditions at common (grey) or differentially accessible regions enriched in either the +ATRA (red) or the -ATRA group (blue) from the comparison in Fig. 2a. Boxes indicate interquartile range with whiskers ± 1.5 times this range and outlier points. (c) Normalized ATAC-Seq coverage at the Foxp3, Rorc, Il17a, Il17f, Il1r1, Il6ra and Tnf loci in average representations of the +ATRA and -ATRA conditions. (d) Heatmap of select Th17 and Treg associated genes visualized in c for -ATRA and +ATRA conditions with dendrograms showing relatedness of samples (columns) and individual genes (rows). (e) Heatmap of all DARs quantified by z-score. DARs enriched in the +ATRA condition correspond to the red dots in Fig. 2a, while DARs enriched in the -ATRA condition correspond to the blue dots in Fig. 2a. (f) Motif enrichment analysis for the grouped DARs in Fig. 2e quantified by enrichment of motif across clusters shown in (e) with enrichment quantified as the negative of the log(P) value. (g,h) (g) H3 Histone lysine 4 trimethylation (H3K4me3) coverage analyzed using CUT-and-TAG and (h) CpG methylation patterns determined via RRBS-seq at the same loci as in c in representative samples from the +ATRA and -ATRA conditions. All representative RRBS regions of interest are zoomed in to improve clarity in promoter regions except Tnf. Scales in c: Foxp3 [0-150], Rorc [0-380], Il17a [0-130], Il17f [0-260], Il1r1 [0-700], Il6ra [0-920], Tnf [0-900]; boxes in c highlight regions of apparent signal differences between +ATRA and -ATRA cells at respective gene loci; data in d represent the integrated ATAC signal in normalized reads across each known gene promoter region ranked as z-scores using data across each row; data in e represent DAR z-scores calculated using the average of all samples, i.e. across each row; data in f represent motifs with an enrichment log(P) value less than -35 found in 10% or more regions with coverage showing a fold increase of at least 1.5 over background coverage in at least one cluster; scales in g: Foxp3 [0-31], Rorc [0-123], Il17a [0-2.5], Il17f [0-5], Il1r1 [0-5], Il6ra [0-72], Tnf [0-45]; scales in h: Foxp3 [0-70], Rorc [0-26], Il17a [0-26], Il17f [0-12], Il1r1 [0-26], Il6ra [0-76], Tnf [0-79]

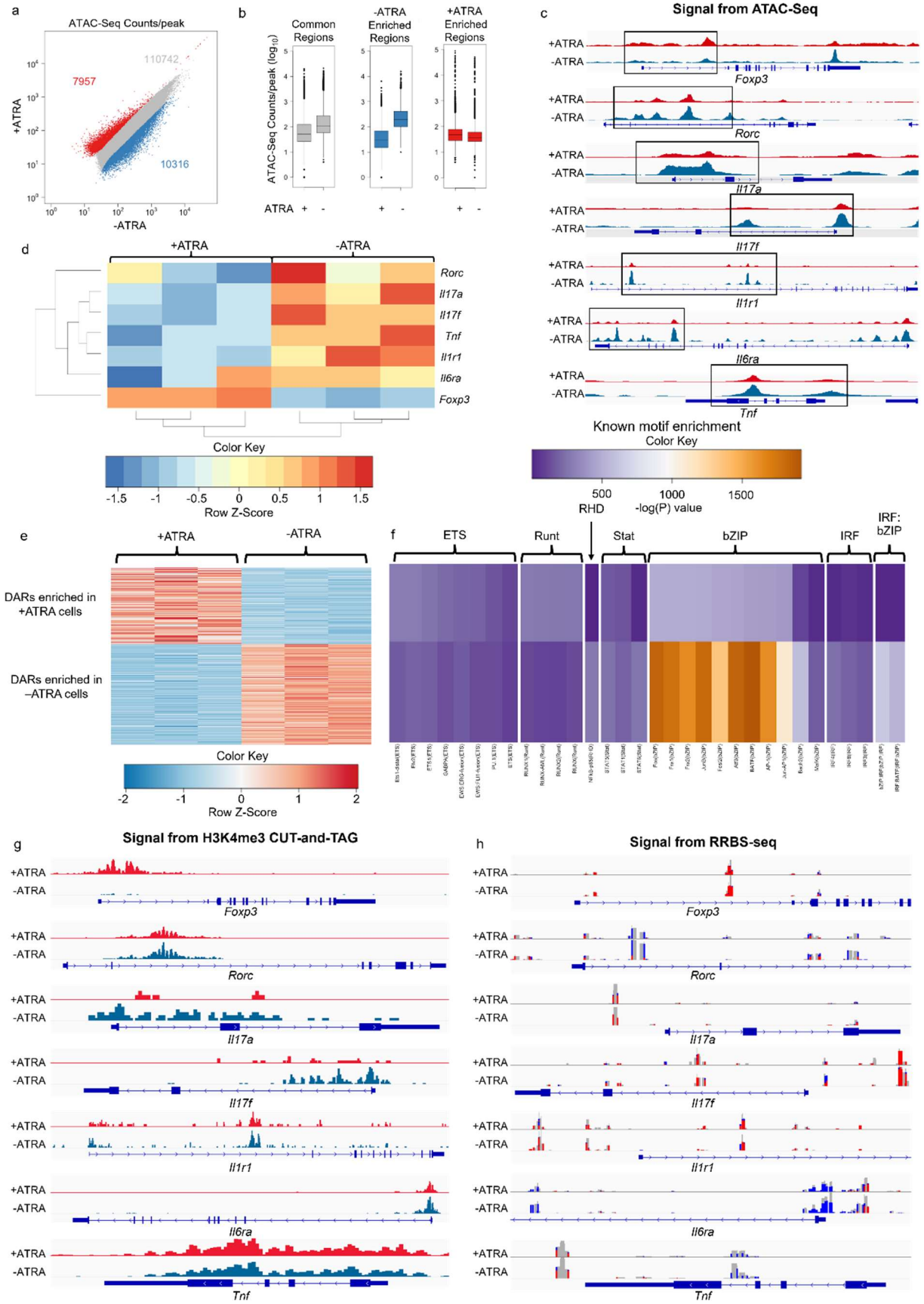
a
ATAC-Seq Counts/peak
110742
7957
10316
+ATRA
-ATRA
b
Common Regions
-ATRA Enriched Regions
+ATRA Enriched Regions
ATAC-Seq Counts/peak (log10)
ATRA + - + - + -
c
Signal from ATAC-Seq
+ATRA
-ATRA
Foxp3
Rorc
Il17a
Il17f
Il1r1
Il6ra
Tnf
d
+ATRA
-ATRA
Rorc
Il17a
Il17f
Tnf
Il1r1
Il6ra
Foxp3
Color Key
-1.5 -1 -0.5 0 0.5 1 1.5
Row Z-Score
Known motif enrichment
Color Key
500 1000 1500
-log(P) value
e
+ATRA
-ATRA
DARs enriched in +ATRA cells
DARs enriched in –ATRA cells
Color Key
-2 -1 0 1 2
Row Z-Score
f
ETS
Runt
RHD
Stat
bZIP
IRF
IRF: bZIP
g
Signal from H3K4me3 CUT-and-TAG
+ATRA
-ATRA
Foxp3
Rorc
Il17a
Il17f
Il1r1
Il6ra
Tnf
h
Signal from RRBS-seq
+ATRA
-ATRA
Foxp3
Rorc
Il17a
Il17f
Il1r1
Il6ra
Tnf

Figure 23 Sustained release of bioactive ATRA from poly-(lactic-co-glycolic) acid (PLGA) microparticles (MP).

(a) Experimental schematic for formulating poly-(lactic-co-glycolic) (PLGA) ATRA microparticles (PLGA-ATRA MP). (b) Scanning electron micrographs (SEMs) of PLGA-ATRA MP (c) spanning varying size distributions. Measurements are based on image analysis outlined in Fig. 4.13. (d) Release of ATRA from 10 mg of 10.6 µm, 6.5 µm, or 3.9 µm PLGA-ATRA MP over 28 days. (e, f) Bioactivity of post-release ATRA measured collected at different time intervals on CD4+ mT cell differentiation as measured by effect (e) IL-17A expression and (f) FoxP3 expression. (g, h) Bioactivity of ATRA released from PLGA-ATRA MP formulations in mTreg destabilization as measured by (g) IL-17A expression and (h) FoxP3 expression. (i) PLGA-ATRA MP release supernatant tested in healthy human (h)T cell differentiation assays described in Fig. 4.10. Averages in c are based on averaging the analysis of three batches per size; data in c are distributions and diameter averages from a single batch for each size, compiled from analysis of three different image sections per size; size distribution analysis represented in c was performed for two additional batches for each size and similar results were obtained (Fig. 4.13b); data in d-i are the means ± SD of technical replicates from representative experiments; Data in d are representative of three technical replicates performed using a single batch of particles for each size; e-h were performed twice; data in i are representative of two donors using three technical replicates per donor. Statistical analysis in d was performed by comparing the area under the curve for each replicate using a one-way ANOVA with post-hoc Tukey test, **** $p < 0.0001$; analyses in e-i were performed using ANOVA with Tukey's multiple comparison test. Schematic in a was composed using BioRender and ChemDraw.

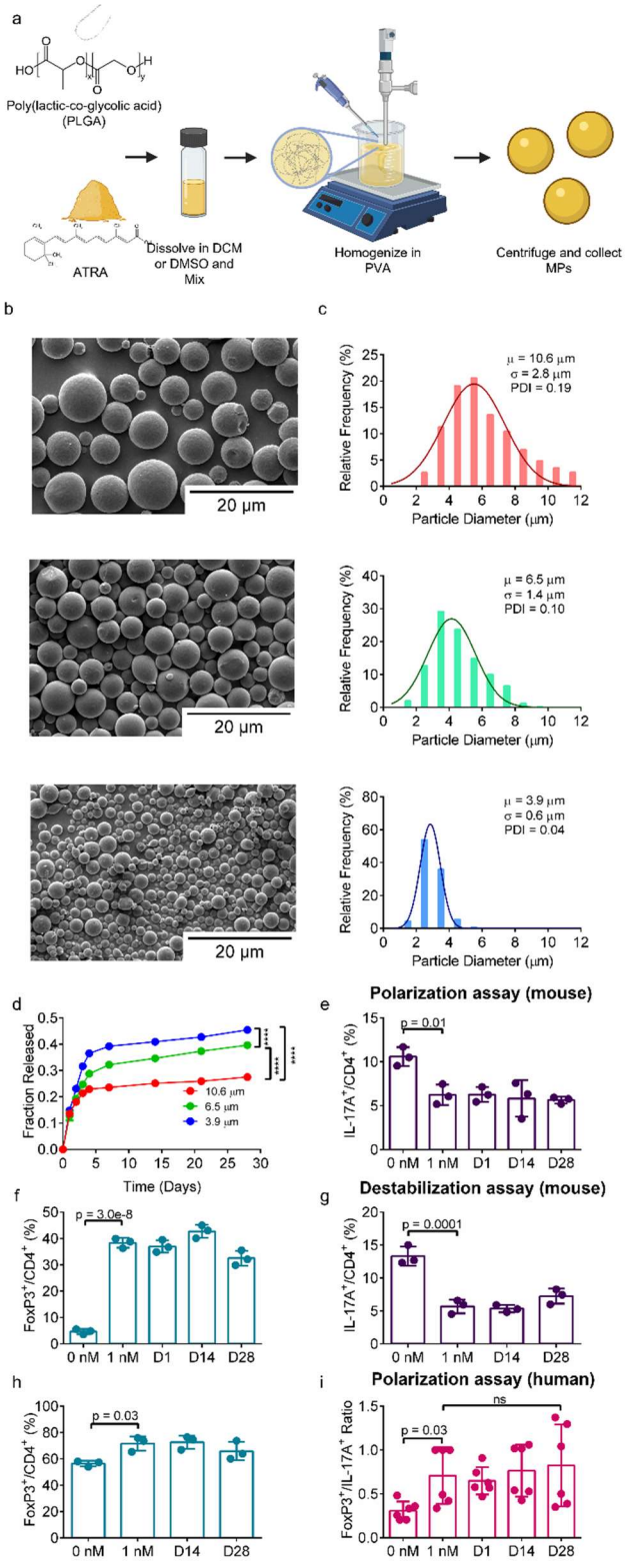
a
Poly(lactic-co-glycolic acid)
(PLGA)
ATRA
Dissolve in DCM
or DMSO and
Mix
Homogenize in
PVA
Centrifuge and collect
MPs
b
c
20 µm
20 µm
20 µm
Relative Frequency (%)
Particle Diameter (µm)
µ = 10.6 µm
σ = 2.8 µm
PDI = 0.19
µ = 6.5 µm
σ = 1.4 µm
PDI = 0.10
µ = 3.9 µm
σ = 0.6 µm
PDI = 0.04
d
Fraction Released
Time (Days)
10.6 µm
6.5 µm
3.9 µm
e
Polarization assay (mouse)
IL-17A+/CD4+ (%)
p = 0.01
0 nM 1 nM D1 D14 D28
f
FoxP3+/CD4+ (%)
p = 3.0e-8
0 nM 1 nM D1 D14 D28
g
Destabilization assay (mouse)
IL-17A+/CD4+ (%)
p = 0.0001
0 nM 1 nM D14 D28
h
FoxP3+/CD4+ (%)
p = 0.03
0 nM 1 nM D14 D28
i
Polarization assay (human)
FoxP3+/IL-17A+ Ratio
p = 0.03
ns
0 nM 1 nM D1 D14 D28

Figure 24 PLGA-ATRA MP modulates autoimmune arthritis in SKG mice.
(a) Experimental schematic for assessing the efficacy of PLGA-ATRA MP in treating established arthritis. (b) Normalized fluorescence signal from intra-articular (IA) injected Cy5-tagged PLGA-Blank MP, quantified using an in vivo imaging system (IVIS). (c-f) Clinical arthritis scores in mice treated with either IA PLGA-ATRA MP or dose-matched bolus IA ATRA presented as (c) aggregated clinical scores, (d) disaggregated ipsilateral (Ipsi) and contralateral (Contra) hind paws, (e) aggregated ankle thickness measurements of hind paws and (f) disaggregated ankle thickness measurements of ipsilateral and contralateral hind paws. (g-j) Clinical arthritis scores in mice treated with either IA PLGA-ATRA MP or unloaded PLGA-Blank MP presented as (g) aggregated clinical scores, (h) disaggregated ipsilateral and sham PBS-injected contralateral hind paws, (i) aggregated ankle thickness of hind paws and (j) disaggregated ankle thickness measurements of ipsilateral and contralateral hind paws. Data in b are means ± SD of normalized radiant efficiency of Cy5-tagged PLGA-Blank MP in n=9 mice; data in c-j are the means ± SEM; data in c, e share a legend, data in d, f share a legend, data in g, i share a legend, data in h, j share a legend; c-f (n = 9 mice for PLGA-ATRA MP, n = 9 mice for bolus IA ATRA) represent data from two independent experiments and g-j (n = 9 mice for PLGA-ATRA MP, n = 11 mice for PLGA-Blank MP) represent data from four independent experiments. Statistical analyses in b were performed using a repeated measures one-way ANOVA with post hoc Sidak's test for multiple comparisons; statistical analyses in c-j were performed using a linear mixed-effects model; Schematic in a was composed using BioRender.

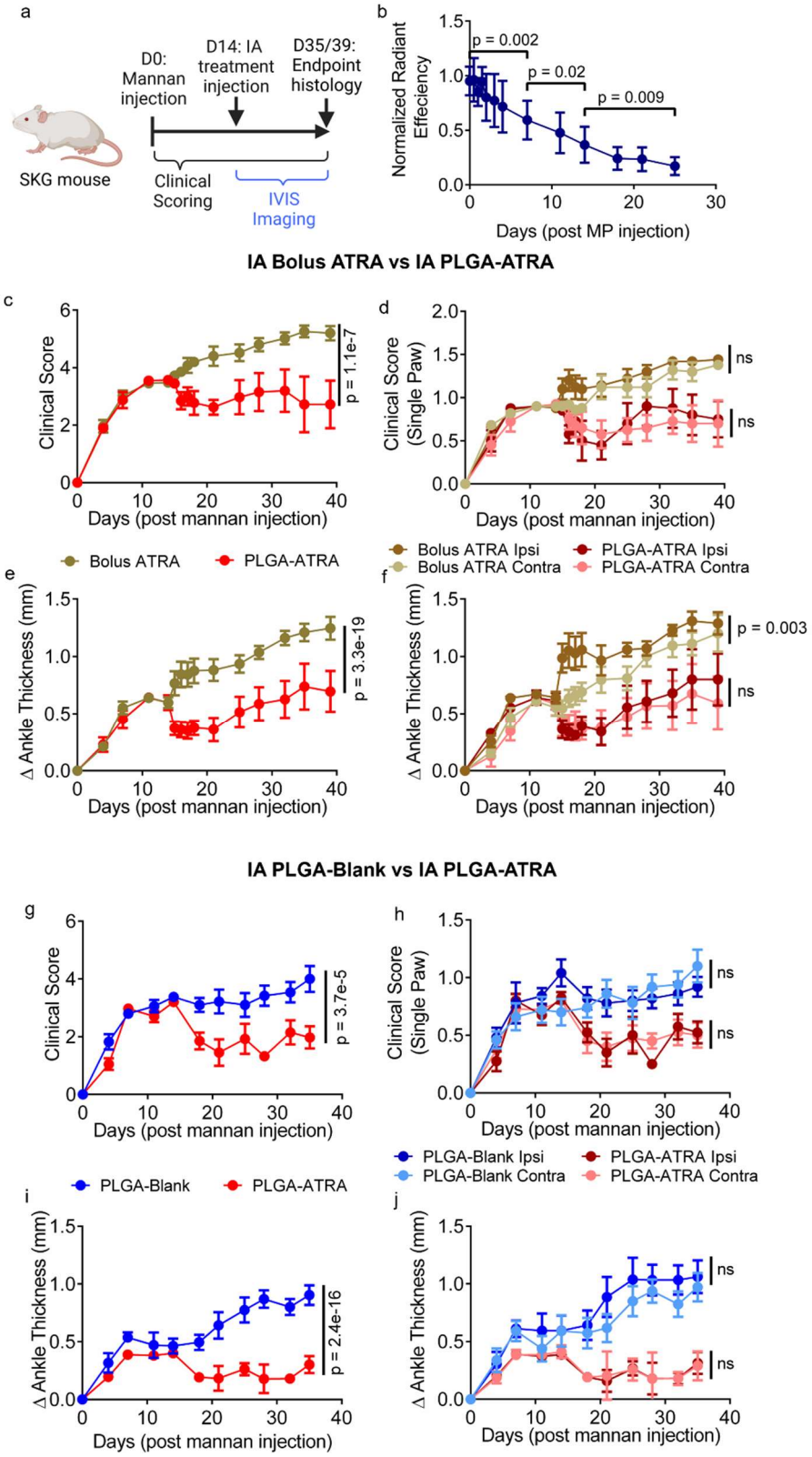
a
D0: Mannan injection
D14: IA treatment injection
D35/39: Endpoint histology
SKG mouse
Clinical Scoring
IVIS Imaging
b
Normalized Radiant Effeciency
p = 0.002
p = 0.02
p = 0.009
Days (post MP injection)
IA Bolus ATRA vs IA PLGA-ATRA
c
Clinical Score
p = 1.1e-7
Days (post mannan injection)
Bolus ATRA
PLGA-ATRA
d
Clinical Score (Single Paw)
ns
ns
Days (post mannan injection)
Bolus ATRA Ipsi
Bolus ATRA Contra
PLGA-ATRA Ipsi
PLGA-ATRA Contra
e
Δ Ankle Thickness (mm)
p = 3.3e-19
Days (post mannan injection)
f
Δ Ankle Thickness (mm)
p = 0.003
ns
Days (post mannan injection)
IA PLGA-Blank vs IA PLGA-ATRA
g
Clinical Score
p = 3.7e-5
Days (post mannan injection)
PLGA-Blank
PLGA-ATRA
h
Clinical Score (Single Paw)
ns
ns
Days (post mannan injection)
PLGA-Blank Ipsi
PLGA-Blank Contra
PLGA-ATRA Ipsi
PLGA-ATRA Contra
i
Δ Ankle Thickness (mm)
p = 2.4e-16
Days (post mannan injection)
j
Δ Ankle Thickness (mm)
ns
ns
Days (post mannan injection)

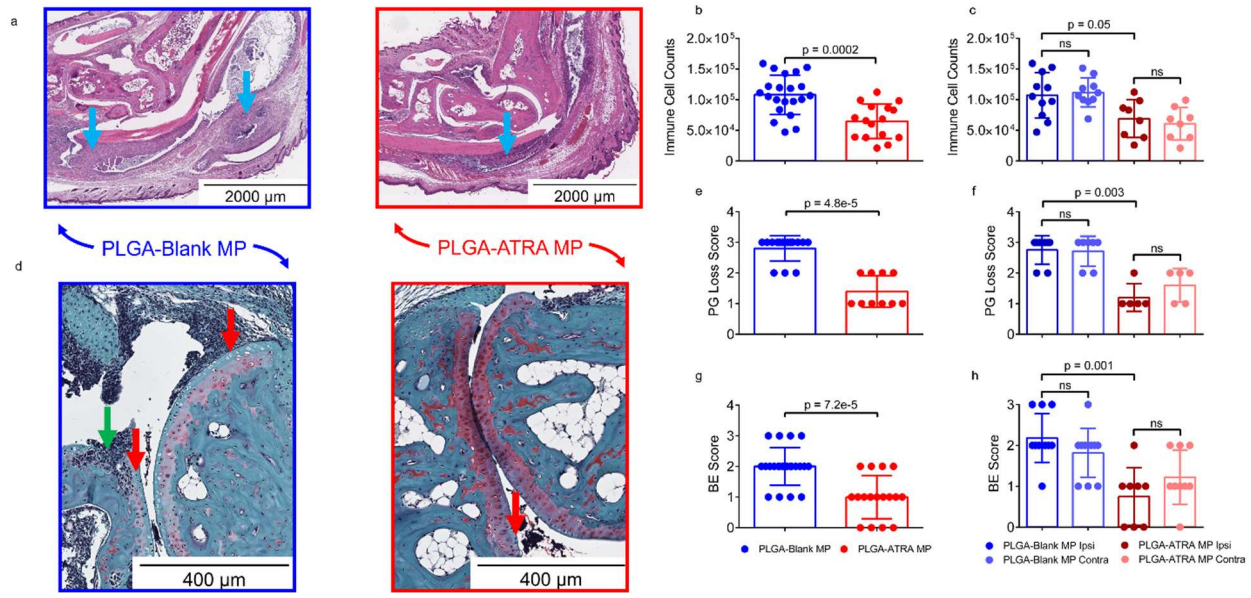

Figure 25 PLGA-ATRA MP reduce immune cell infiltration, cartilage damage and bone erosions in treated mice.

(a) Representative H&E-stained histology sections of ankles from arthritic SKG mice, treated as depicted in Fig. 4a with either PLGA-ATRA MP or PLGA-Blank MP. Immune cells (blue arrows) were quantified and is reported as (b) aggregated infiltration in ankle joints and (c) disaggregated infiltration in ipsilateral (Ipsi) and contralateral (Contra) ankles. (d) Representative safranin-O-stained histological sections showing bone erosion (green arrow) and proteoglycan loss (red arrows) at the talus/tibia junction. (e,f) Quantification of proteoglycan (PG) loss reported as (e) aggregated scores from both ankles and (f) disaggregated scores in ipsilateral and contralateral ankles. (g,h) Quantification of bone erosion reported as (g) aggregated scores from both ankles and (h) disaggregated scores in ipsilateral and contralateral ankles. Data in b, c and e-h represent the mean ± SD Aggregated data for bone erosion scoring and immune cell counts is from n = 21 sections from 11 mice for the PLGA-Blank MP group and n = 16 sections from 9 mice for the PLGA-ATRA MP group. Data for proteoglycan loss is from n = 14 sections from 7 mice for the PLGA-Blank MP group and n = 10 sections from 5 mice for the PLGA-ATRA MP group. Data for bone erosion is from n = 22 sections from 11 mice for the PLGA-Blank MP group and n = 16 sections from 9 mice for the PLGA-ATRA MP group. Statistical analysis in b was performed using unpaired Student's t-test; analysis in c was performed using a one-way ANOVA with post-hoc Tukey test for multiple comparisons; statistical analysis in e and g was performed using a Mann-Whitney test; statistical analyses in f and h were performed using Kruskal-Wallis test with a post-hoc Dunn's multiple comparison test.

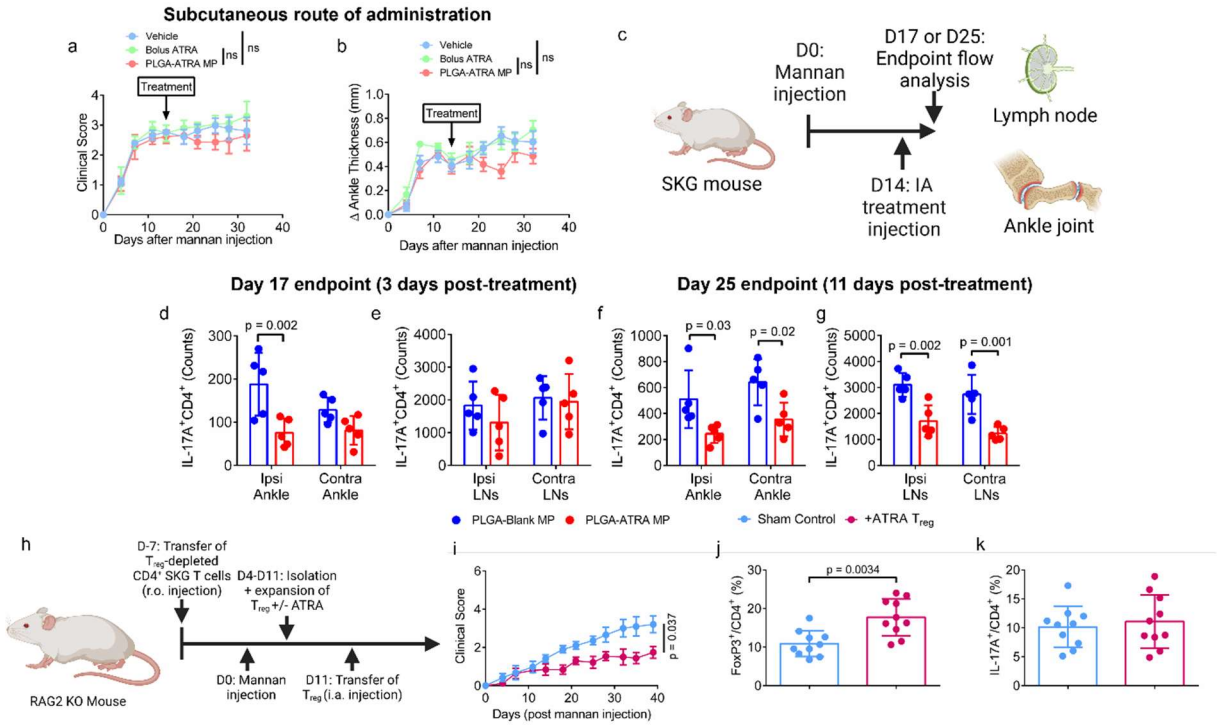

Figure 26 IA PLGA-ATRA MP modulate T cells in joints and draining lymph nodes to promote systemic disease modulation.

(a, b) Quantification of arthritis progression using (a) clinical scores and (b) ankle thickness measurements in mice treated subcutaneously (SubQ) with PLGA-ATRA MP (n = 6), single dose-matched bolus ATRA (n = 5) or vehicle (n = 6). (c) Experimental schematic for immunophenotyping T cells in SKG mice after IA treatment. (d,e) IL-17A+CD4+ T cells in the ipsilateral (Ipsi) and contralateral (Contra) (d) ankles and (e) draining lymph nodes 3 days post- IA PLGA-ATRA MP or IA PLGA-Blank MP. (f, g) IL-17A+CD4+ cells in the (f) ipsilateral (Ipsi) and contralateral (Contra) ankles and (g) draining lymph nodes 11 days post- IA PLGA-ATRA MP or IA PLGA-Blank MP. (h) Experimental schematic for transfer of arthritogenic and regulatory T cells in RAG2-KO mice. (i) Quantification of arthritis progression using clinical scores. Endpoint ankle-isolated (j) FoxP3+CD4+ T cells and (k) IL-17A+CD4+ T cells. Data in a, b (Vehicle n = 6, dose-matched bolus ATRA n = 5, PLGA-ATRA MP n = 6) represent mean ± SEM; data in d-g (n = 5/group) represent mean ± SD; data in i represent mean ± SEM (n = 5/group); data in j, k represent the mean ± SD. Statistical analyses in a, b, i were performed using a linear mixed effects model analysis. Statistical analyses in d-g were performed using a one-way ANOVA with post-hoc Sidak's test. Statistical analyses in j, k were performed using a Student's two tailed t-test.

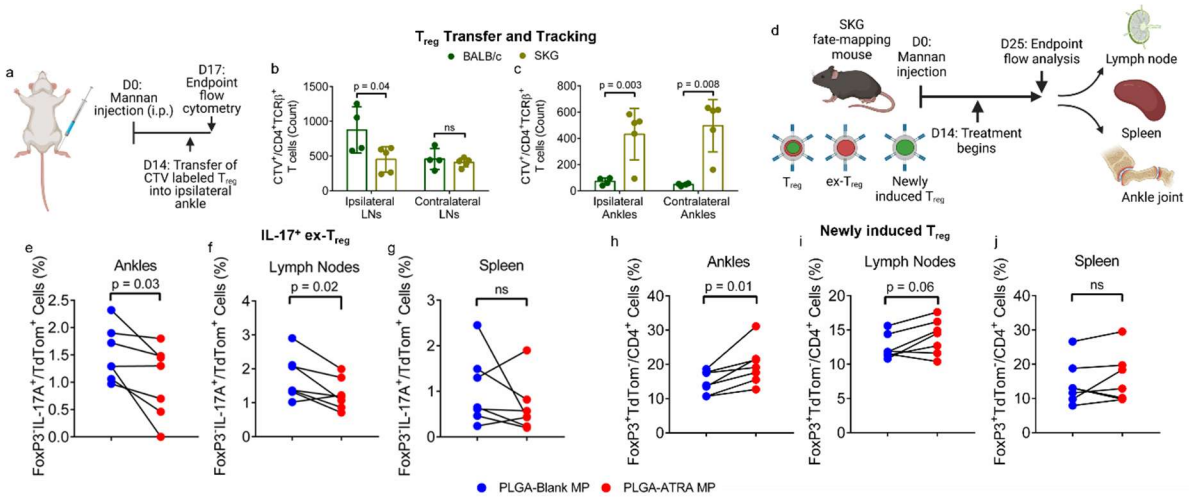

Figure 27 IA PLGA-ATRA MP promote Treg stability and differentiation in vivo.
(a) Experimental schematic for tracking IA injected Treg (b, c) Quantification of CellTracker Violet+ (CTV+) CD4+TCR-β+ T cells in the (b) lymph nodes and (c) ankles three days post IA injection. (d) Experimental schematic for measuring Treg stability and differentiation in SKG fate-mapping mice. (e-g) Percent of destabilized Treg (FoxP3eGFP-IL-17A+/TdTom+) in the (e) ankles, (f) draining lymph nodes, and (g) spleens of littermate paired fate-mapping SKG mice. (h-j) Percent of newly induced Treg (FoxP3eGFP+tdTom-) in the (h) ankles, (i) draining lymph nodes, and (j) spleen 32 days after cessation of tamoxifen administration in paired littermates that are treated with either IA PLGA-Blank MP or PLGA-ATRA MP. Data in b, c (BALB/cJ n = 4, SKG n = 5) are the means ± SD of representative experiments; data points in e-j represent individual mice, with paired littermates treated with either PLGA-Blank MP (n = 7) or PLGA-ATRA MP (n = 7) compared. Statistical analysis in b, c were performed using one-way ANOVA with post-hoc Tukey test. Statistical analyses in e-j were performed using a paired Student's two-tailed t-test.

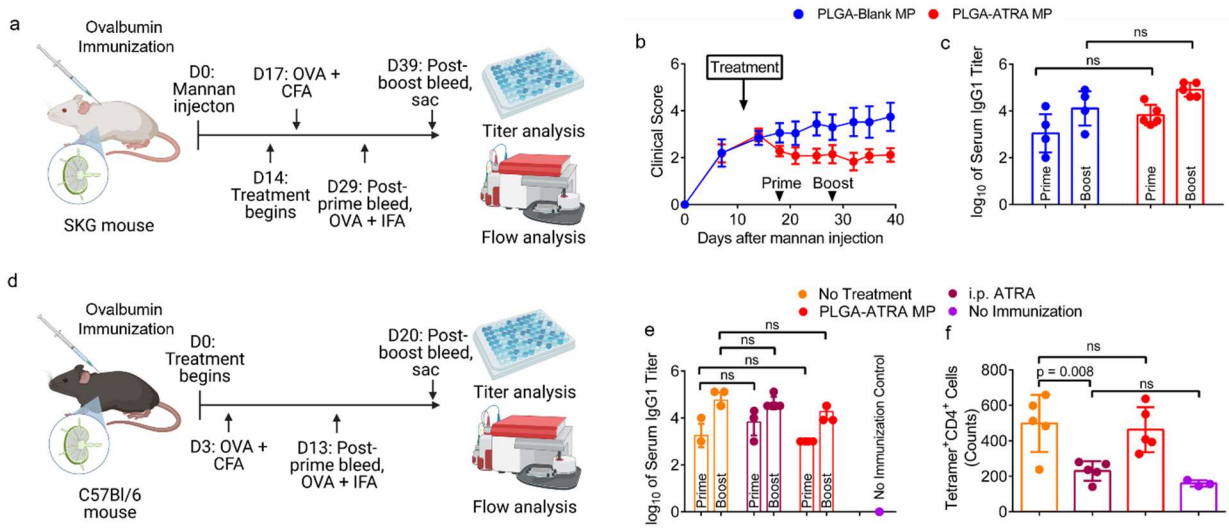

Figure 28 IA PLGA-ATRA MP do not impair systemic immune response against an arthritis-irrelevant antigen.

(a) Experimental schematic for ovalbumin (OVA) immunization in arthritic SKG mice. (b) Clinical scores of SKG mice treated with either IA PLGA-Blank MP (n = 5) or PLGA-ATRA MP (n = 6). (c) anti-OVA serum IgG1 titers before a booster immunization and 10 days after booster immunization. (d) Experimental schematic for OVA immunization in non-arthritic B6 mice. (e) anti-OVA serum IgG1 titers and (f) QAVHAAHAEIN Tetramer+CD4+ T cell counts from mouse splenocytes 20 days after initial immunization with OVA. Data in b represents mean ± SEM for the PLGA-Blank MP (n = 5) and PLGA-ATRA MP (n = 6) groups; data in c, e, f, represents mean ± SD of n = 5/group. Statistical analysis in b was performed by linear mixed effects model analysis; statistical analyses in c, e, f were performed using one-way ANOVA with post-hoc Tukey test.

Figure 29 IA PLGA-ATRA MP reduce synovitis, cartilage degradation and bone erosions in the collagen-induced arthritis (CIA) mouse model.
(a) Experimental timeline for CIA induction and treatment. (b) Aggregated clinical scores and (c) disaggregated by injected vs uninjected joints of CIA mice treated with a 2 µg of either IA PLGA-Blank MP (n = 6) or IA PLGA-ATRA MP (n = 5) in both hind paws (total dose 4 µg). (d) Representative microCT images of hind paws from PLGA-Blank MP and PLGA-ATRA MP treated joints. Magnified images were used for treatment-blinded (e) bone erosion and (f, g) bone surface area to volume quantification for the (f) metacarpophalangeal and (g) ankle joints. Representative (h) H&E- and (i) safranin O-stained histological ankle sections from mice that received either PLGA-Blank MP or PLGA-ATRA MP depicting synovitis (green arrows) and proteoglycan loss (red arrows). Treatment-blinded (j) synovitis and (k) proteoglycan loss scores from H&E and safranin O histological sections, respectively. Data represent mean ± SEM (b, c) or mean ± SD (e-g, j, k). Statistical analysis was performed using linear mixed effects model analysis (b, c), Mann-Whitney test (e, j, k), or Student's t-test (f,g), scale bar: 100µm (h, i).

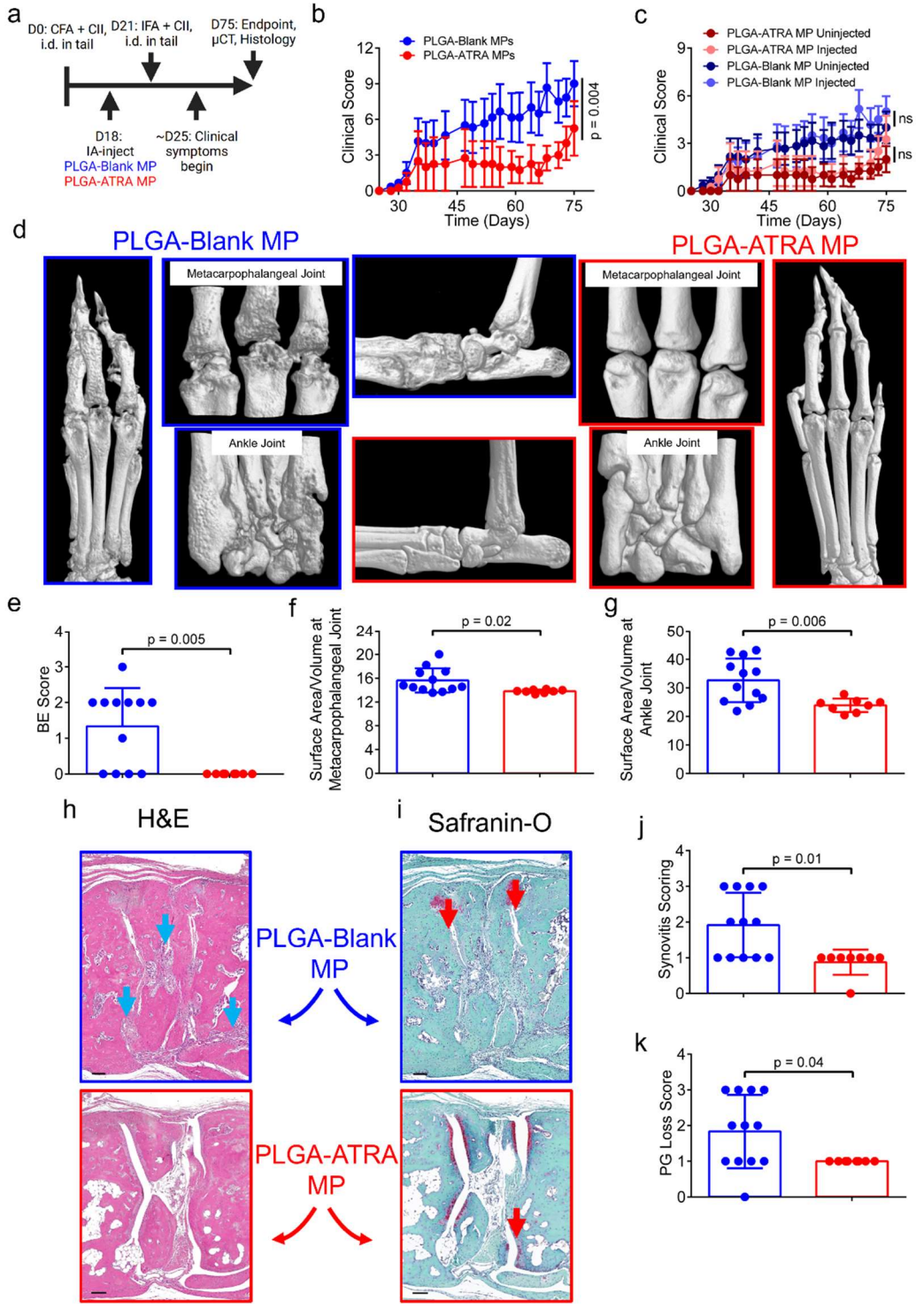
a
D0: CFA + CII, i.d. in tail
D21: IFA + CII, i.d. in tail
D75: Endpoint, µCT, Histology
D18: IA-inject PLGA-Blank MP PLGA-ATRA MP
~D25: Clinical symptoms begin
b
PLGA-Blank MPs
PLGA-ATRA MPs
Clinical Score
Time (Days)
p = 0.004
c
PLGA-ATRA MP Uninjected
PLGA-ATRA MP Injected
PLGA-Blank MP Uninjected
PLGA-Blank MP Injected
Clinical Score
Time (Days)
ns
ns
d
PLGA-Blank MP
PLGA-ATRA MP
Metacarpophalangeal Joint
Ankle Joint
e
BE Score
p = 0.005
f
Surface Area/Volume at Metacarpophalangeal Joint
p = 0.02
g
Surface Area/Volume at Ankle Joint
p = 0.006
h
H&E
i
Safranin-O
PLGA-Blank MP
PLGA-ATRA MP
j
Synovitis Scoring
p = 0.01
k
PG Loss Score
p = 0.04

Figure 30 Extended characterization of ATRA-mediated immunophenotypic modulation of T cells.
(a) Representative flow cytometry-based characterization of naïve CD4+ SKG T cells post-isolation. (b) Representative flow cytometry-based characterization to assess the concentration dependent effect of ATRA on Th17 and Treg differentiation from naïve CD4+ SKG T cells. (c) Timeline and representative flow cytometry of five days of pre-polarization in Th17 polarization conditions and day seven with or without the addition of 1 nM ATRA on day five. (d-f) Quantification of (d) FoxP3 expression, (e) IL-17 expression, (f) and total CD4+ T cell counts from day seven after post-polarization, with or without ATRA added on day five. (g) Experimental schematic for assessing the effect of ATRA on Th17 and Treg differentiation from naïve CD4+ human T (hT) cells. (h) Representative flow cytometry-based characterization of human naïve CD4+ human T cells post-isolation. (i) Ratio of FoxP3+ to IL-17A+ human T cells at different concentrations of ATRA between 0-1 nM. (j) Representative flow cytometry gating for sorting of TCRβ+CD4+FoxP3eGFP+ Treg. (k,l) Representative flow cytometry plots for (k) FoxP3, IL-17A, and (l) RORγt expression in Treg after a destabilization assay. (m-o) Quantification of (m) FoxP3 expression, (n) IL-17A expression and (o) RORγt expression in Treg following an IL-6 mediated destabilization assay with or without 1 nM ATRA, and compared with Treg stimulated without IL-6. Plots in a, b, c, h, j-l, are representative flow cytometry plots of at least three experiments with at least three technical replicates each. Data in d-f are representative of the mean ± SD of four technical replicates. Data in i are representative of the mean ± SD of three technical replicates for a single donor. Data in m-o are representative of the mean ± SD of three technical replicates. Statistical analysis in d-f was performed using a Student's unpaired t-test. Statistical analysis in i, m-o was performed using one-way ANOVA with post hoc Tukey test. Schematic in c was composed in BioRender.

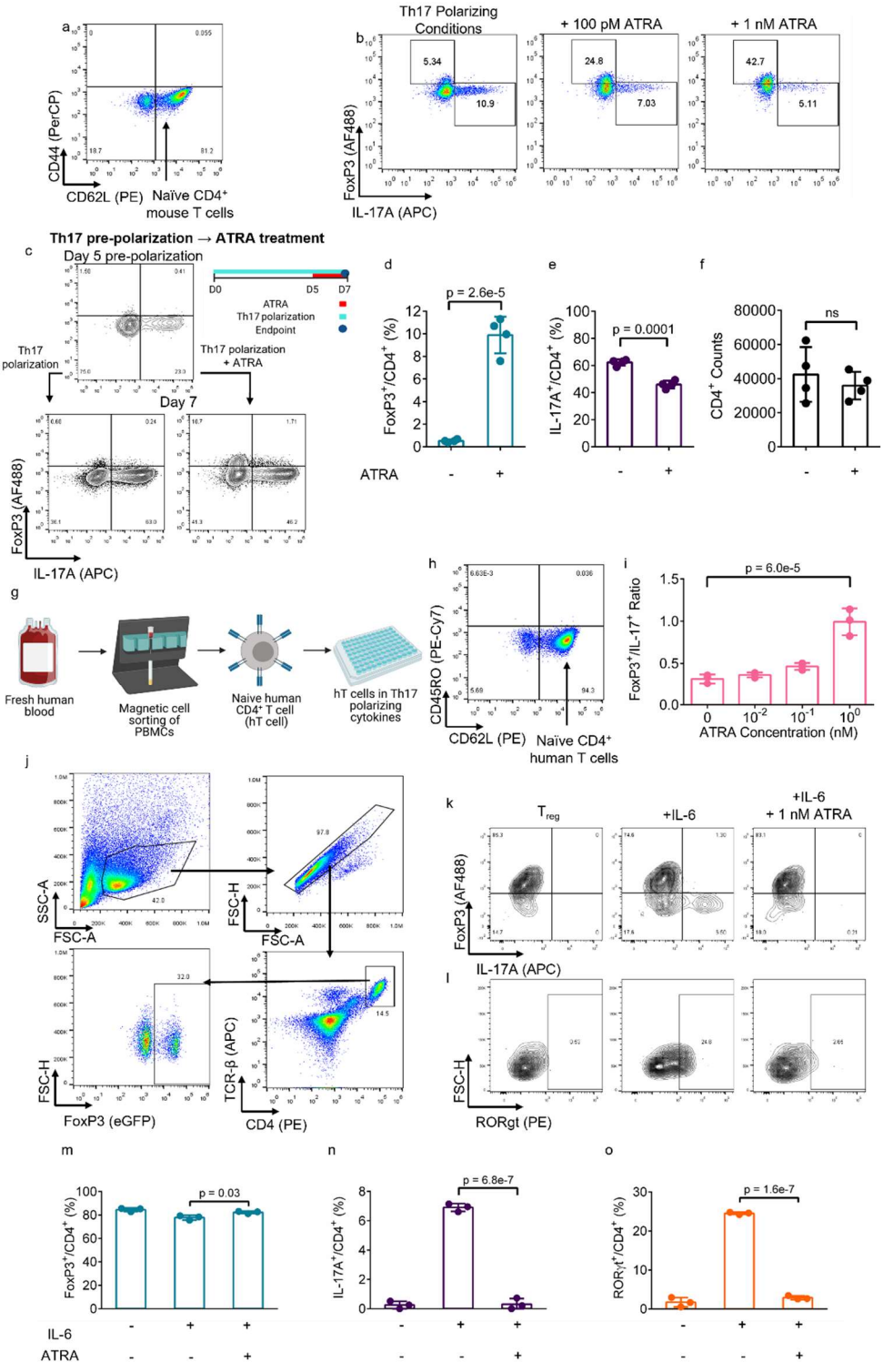
a
CD44 (PerCP)
CD62L (PE)
Naïve CD4+ mouse T cells
b
Th17 Polarizing Conditions
+ 100 pM ATRA
+ 1 nM ATRA
FoxP3 (AF488)
IL-17A (APC)
c
Th17 pre-polarization → ATRA treatment
Day 5 pre-polarization
D0
D5
D7
ATRA
Th17 polarization
Endpoint
Th17 polarization
Th17 polarization + ATRA
Day 7
d
p = 2.6e-5
FoxP3+/CD4+ (%)
ATRA
e
p = 0.0001
IL-17A+/CD4+ (%)
f
ns
CD4+ Counts
g
Fresh human blood
Magnetic cell sorting of PBMCs
Naive human CD4+ T cell (hT cell)
hT cells in Th17 polarizing cytokines
h
CD45RO (PE-Cy7)
CD62L (PE)
Naïve CD4+ human T cells
i
p = 6.0e-5
FoxP3+/IL-17+ Ratio
ATRA Concentration (nM)
j
SSC-A
FSC-A
FSC-H
FoxP3 (eGFP)
TCR-β (APC)
CD4 (PE)
k
Treg
+IL-6
+IL-6 + 1 nM ATRA
FoxP3 (AF488)
IL-17A (APC)
l
FSC-H
RORgt (PE)
m
p = 0.03
FoxP3+/CD4+ (%)
IL-6
ATRA
n
p = 6.8e-7
IL-17A+/CD4+ (%)
o
p = 1.6e-7
RORγt+/CD4+ (%)

Figure 31 Extended characterization of ATRA-mediated immunophenotypic modulation of dendritic cells (DCs) and macrophages.
a) Experimental schematic and timeline for testing ATRA-mediated modulation of DCs and macrophages. (b) Representative flow cytometry of activation markers in unstimulated, stimulated, and stimulated + ATRA treated DCs. (c) CD80+CD11c+ dendritic cells, (d) CD86+CD11c+ dendritic cells and (e) MHCII+CD11c+ dendritic cells. (f) Representative flow cytometry of activation markers in unstimulated, stimulated, and stimulated + ATRA treated F4/80+ macrophages. (g) MHCII+F4/80+ macrophages and (h) TNF+F4/80+ macrophages. Data in c-e, g, h are mean ± SD of technical replicates from a representative experiment. Experiments in a-h were performed twice. Statistical analyses in c-e, g, h were performed using one-way ANOVA with a post hoc Tukey multiple comparison test.

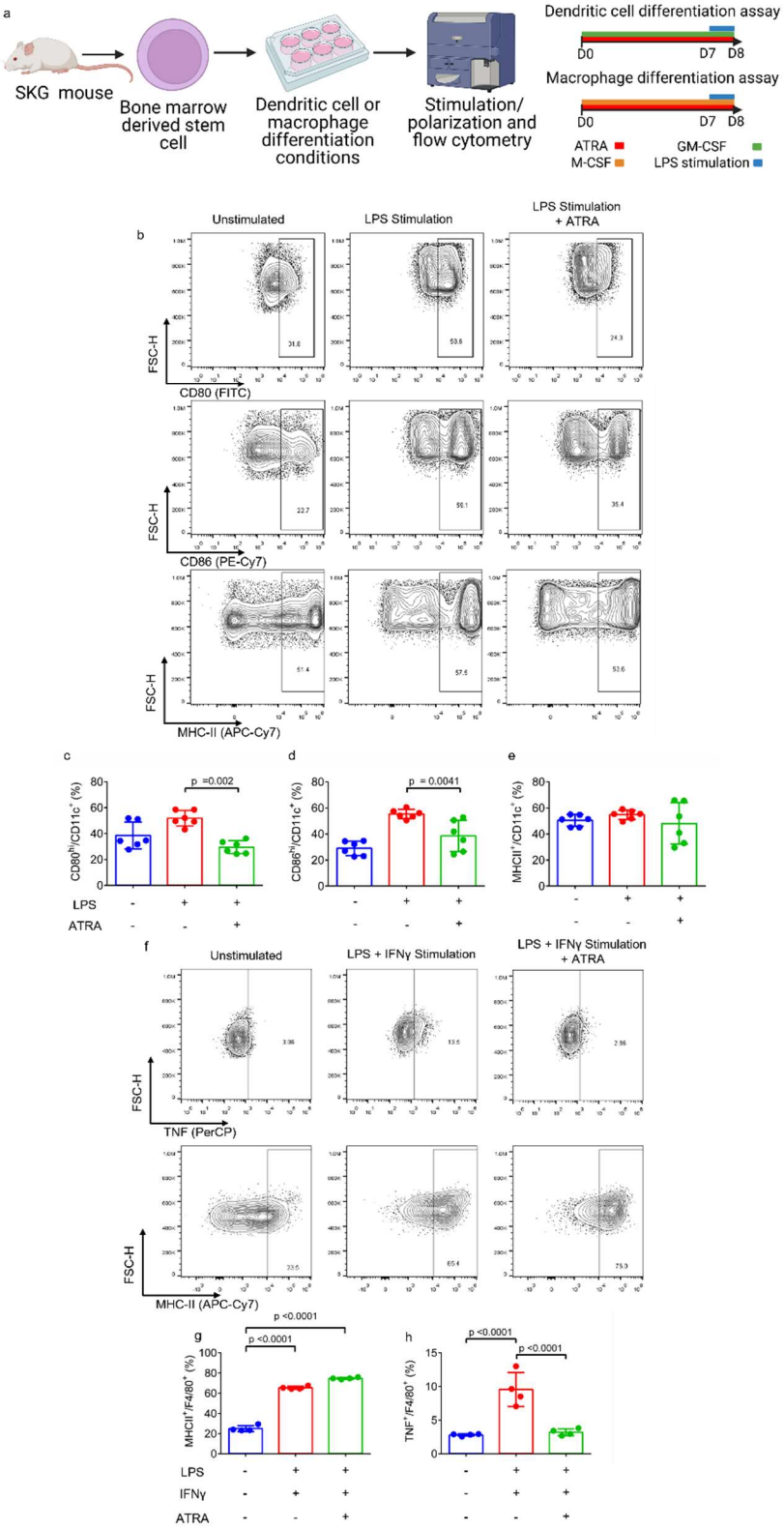
a
SKG mouse
Bone marrow derived stem cell
Dendritic cell or macrophage differentiation conditions
Stimulation/ polarization and flow cytometry
Dendritic cell differentiation assay
D0
D7 D8
Macrophage differentiation assay
D0
D7 D8
ATRA
M-CSF
GM-CSF
LPS stimulation
b
Unstimulated
LPS Stimulation
LPS Stimulation + ATRA
FSC-H
CD80 (FITC)
CD86 (PE-Cy7)
MHC-II (APC-Cy7)
c
d
e
p =0.002
p = 0.0041
LPS
ATRA
f
Unstimulated
LPS + IFNγ Stimulation
LPS + IFNγ Stimulation + ATRA
TNF (PerCP)
MHC-II (APC-Cy7)
g
h
p <0.0001
LPS
IFNγ
ATRA

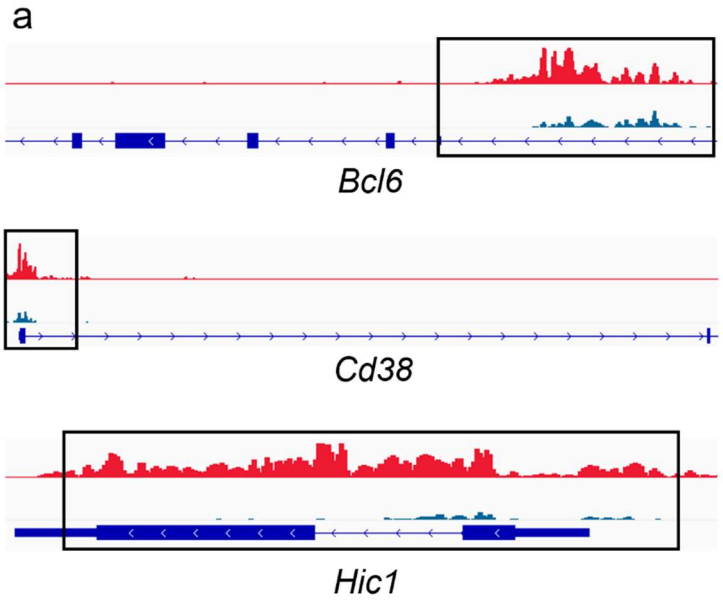

b

List of Differentially Methylated Gene IDs
1700044K03Rik
Tspear
Tspear
Prnd
1700016K19Rik
Gm26578

Figure 32 Extended characterization of ATRA-mediated epigenetic changes in CD4+ SKG T cells.
(a) Visualization of H3K4me3 analysis at additional differentially methylated sites associated with Treg/Th17. (b) List of differentially methylated loci between -ATRA and +ATRA treated CD4+ SKG T cells from RRBS analysis. Scales in a: Hic1 [0-44], Bcl6 [0-24], Cd38 [0-62].

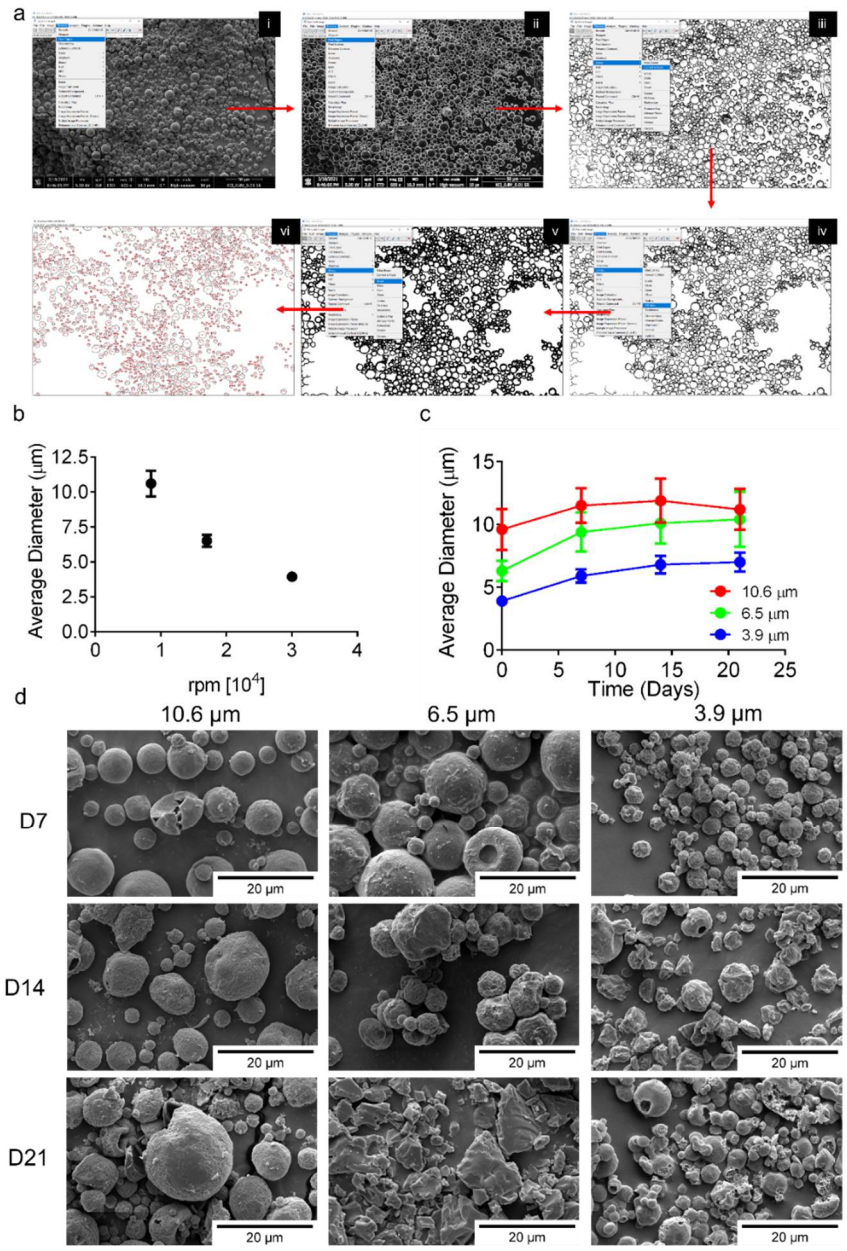

Figure 33 Extended characterization of particle size analysis.
(a) Scanning electron micrograph images were loaded into ImageJ (FIJI distribution) and analyzed in a six step process in which i) the scale of the image was set using the "Set Scale" function, ii) "Find Edges" was applied to find the microparticle edges, iii) image scale bars were cropped out and the image was converted to a black and white binary mask using the "Convert to Mask" function, iv) as much interior was accounted for as possible using the "Fill Holes" function (Note: this loses some particles, but improves measurement accuracy as long as multiple images from the same sample are analyzed), v) edges were expanded using the "Erode" function to avoid detection of aggregates as a single particle and, vi) the area of the particles was analyzed using the "Analyze Particles" function. A subsequent manual check was performed to ensure that no background was incorrectly counted as particles, and particle areas were converted to diameters. The erode function slightly reduces the calculated particle diameters based on the magnification of the image, which was accounted for in final size distribution analyses. (b) Particle size as a function of homogenization speed. (c) Quantification of particle sizes over the duration of four weeks of incubation in release buffer. (d) Representative SEM images depicting degradation of PLGA-ATRA MP over four weeks of incubation in release buffer. Data in b represents mean ± SD of average particle diameter from three batches; data in c represents the mean ± SD of average particle diameter from three representative images.

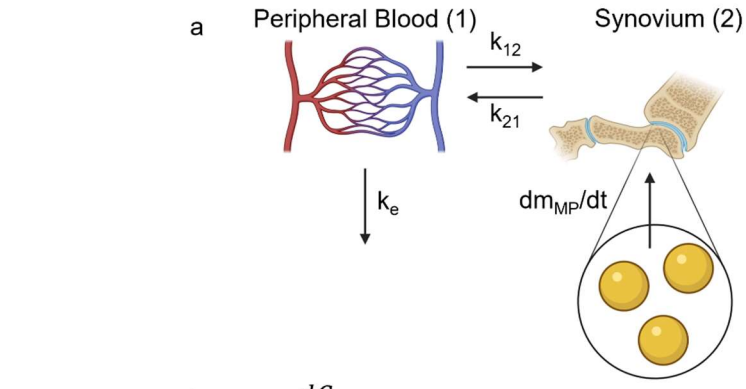

b

$$(1)\ \frac{dC_1}{dt} = -k_{12}C_1 + k_{21}C_2 z - k_e C_1$$

$$(2)\ \frac{dC_2}{dt} = \frac{k_{12}C_1}{z} - k_{21}C_2 + \frac{dm_{MP}(t)}{dt}\frac{1}{V_2}$$

Parameter	k_{12}	k_{21}	k_e	V_2	z
Value	0.2 h^{-1}	0.2 h^{-1}	0.84 h^{-1}	20 µL	0.0013

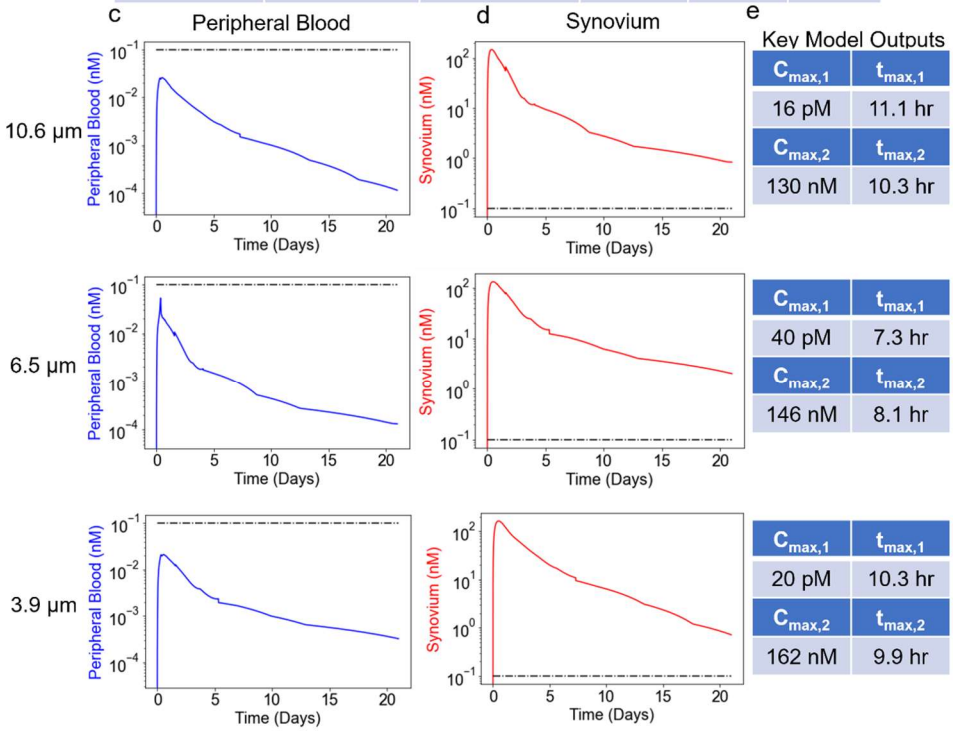

	$C_{max,1}$	$t_{max,1}$	$C_{max,2}$	$t_{max,2}$
10.6 µm	16 pM	11.1 hr	130 nM	10.3 hr
6.5 µm	40 pM	7.3 hr	146 nM	8.1 hr
3.9 µm	20 pM	10.3 hr	162 nM	9.9 hr

Figure 34 Pharmacokinetic modeling of PLGA-ATRA MP.
(a) Schematic of a two-compartment pharmacokinetic (PK) model for the release of ATRA from PLGA-ATRA MP, transfer of ATRA between the synovium and peripheral blood, and elimination of ATRA from the peripheral blood. (b) Governing differential equations for the model compartments and parameter values for first order model coefficients. (c) Model-computed concentration profiles in the peripheral blood based on in vitro release profiles of PLGA-ATRA MP. (d) PK-modeled concentration profiles of ATRA in the synovial fluid. (e) Maximum concentration (Cmax) and the time at which it occurs (tmax) values. Data in c-e represent model outputs using the parameters and the in vitro ATRA release profile from PLGA-ATRA MP. Schematic in a was composed in BioRender.

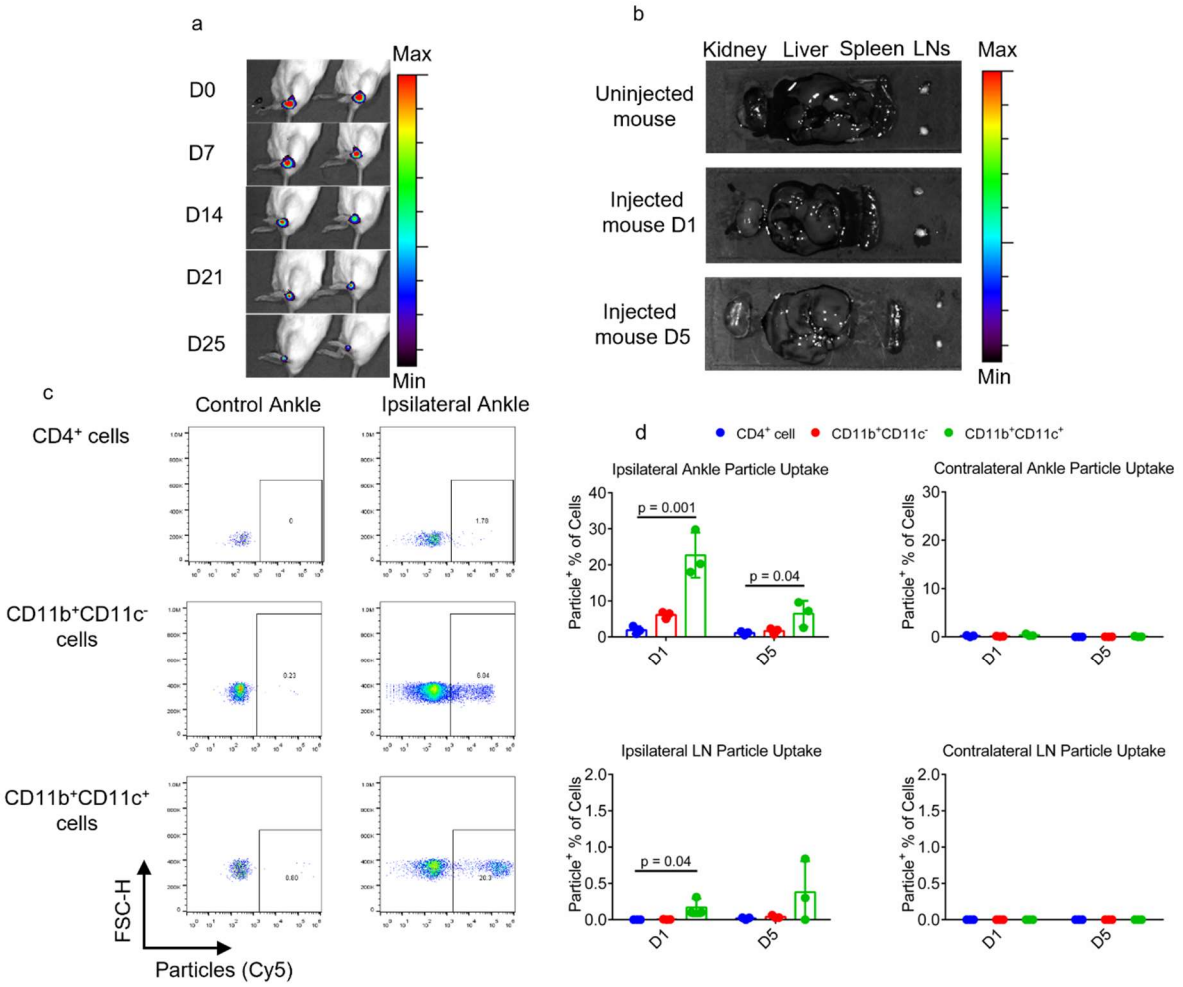

Figure 35 Analysis of PLGA MP retention and uptake in vivo.
(a) Representative IVIS images of data quantified in Fig. 4b showing fluorescence from IA injected Cy5-tagged PLGA-Blank MP. (b) Representative IVIS images depicting Cy5 signal in kidneys, livers, spleens, and popliteal lymph nodes (LNs) (c) Representative flow cytometry-based characterization of particle uptake by CD4+, CD11b+CD11c- and CD11b+CD11c+ cells isolated from ankle joints. (d) Quantification of particle uptake by various cell populations in the ipsilateral and contralateral ankles and the respective draining lymph nodes. Scales in a and b are different. Data in d represent the mean ± SD. Statistical analysis in d was performed using a one-way ANOVA with a post hoc Tukey multiple comparison test.

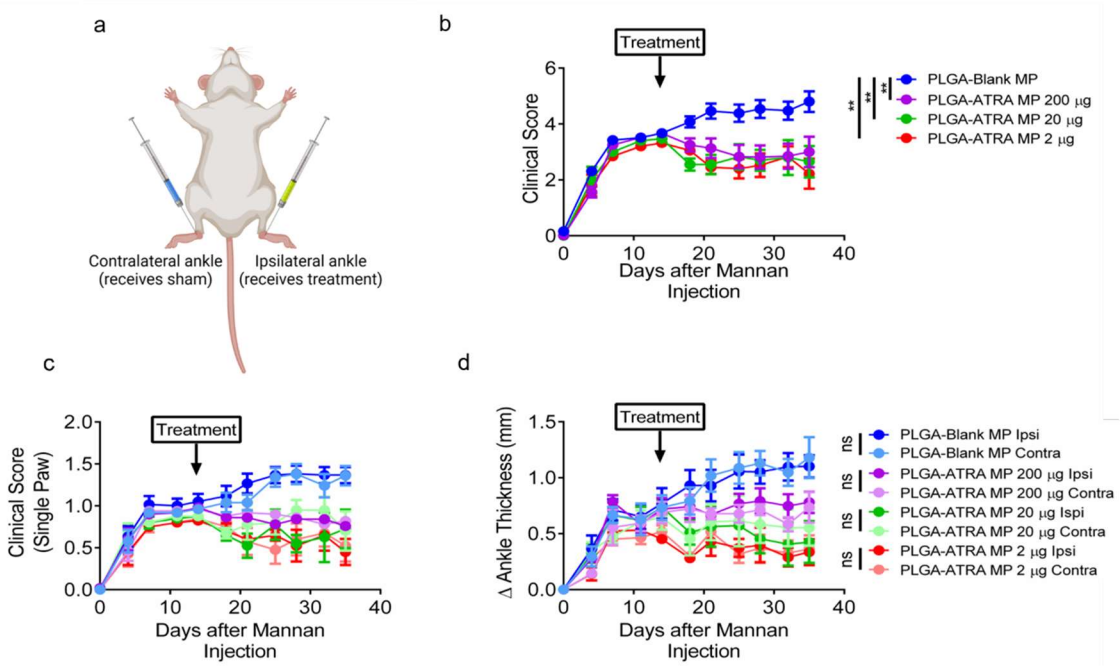

Figure 36 Extended characterization of PLGA-ATRA MP modulating autoimmune arthritis in SKG mice. (a) Schematic depicting IA injections in the ipsilateral and contralateral ankles. (b) Aggregated and (c) disaggregated ipsilateral and contralateral ankle clinical scores and (d) disaggregated ankle thickness measurements in mice treated with either PLGA-Blank MP or PLGA-ATRA MP at 2, 20, or 200 µg doses. Schematic in a generated using Biorender. Data for groups in b-d, were powered as follows: PLGA-Blank MP (n = 8), PLGA-ATRA MP 200 µg (n = 6), PLGA-ATRA MP 20 µg (n= 4), PLGA-ATRA MP 2 µg (n=4). ** $p < 0.01$. Data in b-d represent mean ± SEM. Statistical analyses for b-d were performed using repeated measures two-way ANOVA with post hoc Tukey test. Differences between ipsilateral and contralateral scores in c and d were not significant.

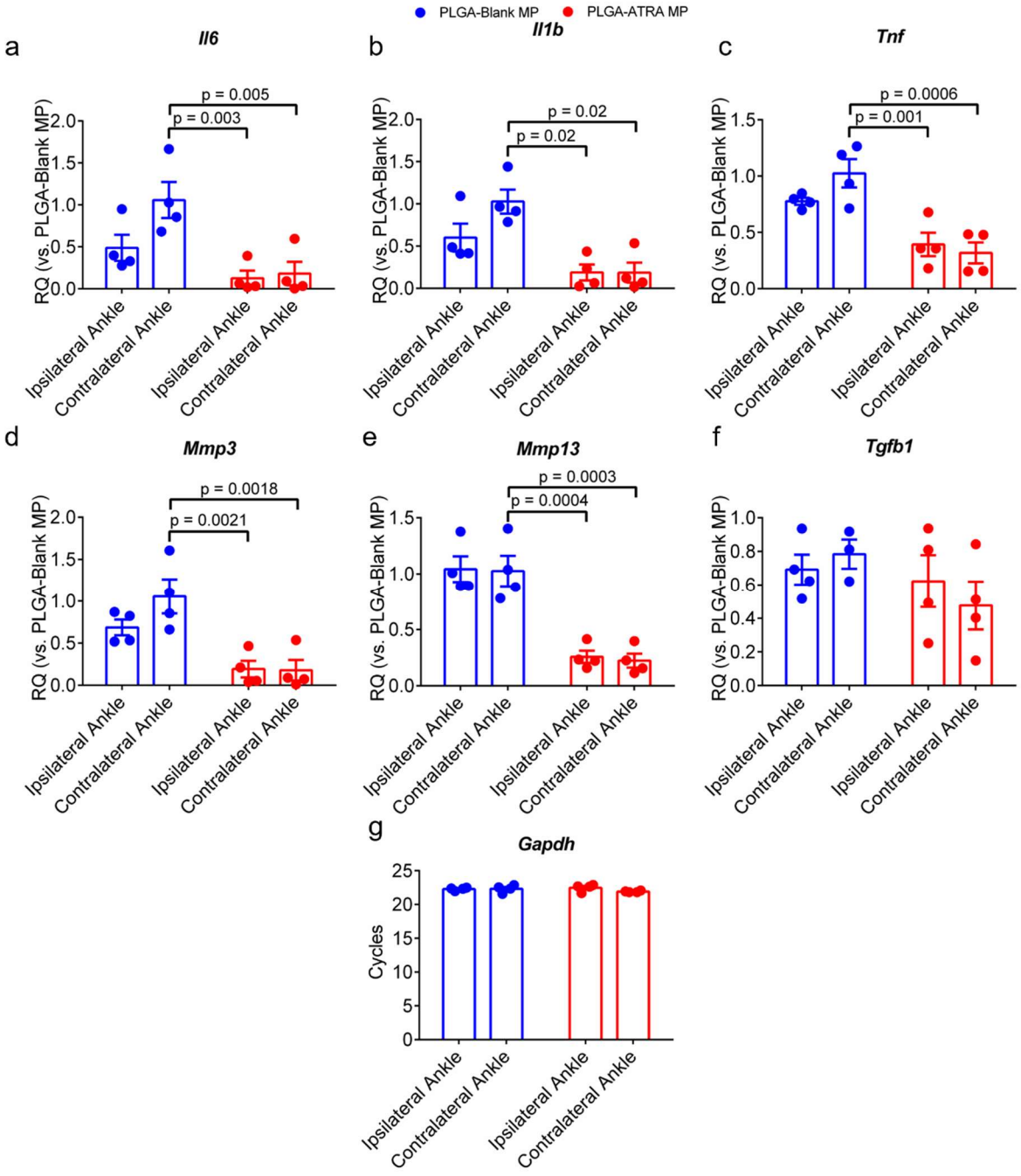

Figure 37 Extended characterization of PLGA-ATRA MP-mediated reduction in joint inflammation in ipsilateral and contralateral ankles.
(a-f) qPCR relative quantification of (a) Il6, (b) Il1b, (c) Tnf (d) Mmp3 (e) Mmp13 and (f) Tgfb. (g) Gapdh cycle counts from qPCR. Data in a-f represent the mean ± SD; data in a-f are normalized first to Gapdh from respective samples then normalized to mRNA expression in PLGA-Blank MP contralateral ankles before comparison between treatment groups. Statistical analysis performed using a one-way ANOVA with a post hoc Dunnett's multiple comparison test.

Figure 38 Extended characterization of IA PLGA-ATRA MP-mediated reduction in immune cell infiltration, cartilage damage and bone erosions in treated mice.
(a) Representative H&E-stained histological sections of ankles from arthritic SKG mice, treated as described in Fig. 4a with indicated treatments. Immune cells (blue arrow) are indicated and (b) quantified using (c) QuPath software-based histomorphometry analysis following the depicted workflow. (d) Representative H&E sections of contralateral ankles from mice treated with either 2 µg PLGA-ATRA MP or PLGA-Blank MP in the ipsilateral ankle. (e) Representative safranin-O-stained histological sections with bone erosion (green arrows) and proteoglycan loss (red arrows) from SKG mice treated as described in Fig. 4a with indicated treatments. (f,g) Quantification of (f) proteoglycan (PG) loss and (g) bone erosion (BE) reported as aggregated scores from both ankles of mice treated as indicated. Data in b, f, g represent mean ± SD. Comparison groups are powered as follows: PLGA-Blank MP (n = 21 sections from 11 mice), bolus ATRA (n = 7 sections from 4 mice), 2 µg PLGA-ATRA MP (n = 16 sections from 9 mice), 20 µg PLGA-ATRA MP (n = 6 sections from 3 mice) and 200 µg PLGA-ATRA MP (n = 8 sections from 5 mice). Images for 2 µg PLGA-ATRA MP and PLGA-Blank MP in a and e are the same images as in Figure 5a, d respectively. Statistical analysis in b was performed using a one-way ANOVA with post-hoc Tukey test; statistical analysis in f, g was performed using a Kruskal-Wallis test with post-hoc Dunn's test. Histology sections included in a are from samples obtained in three separate experiments.

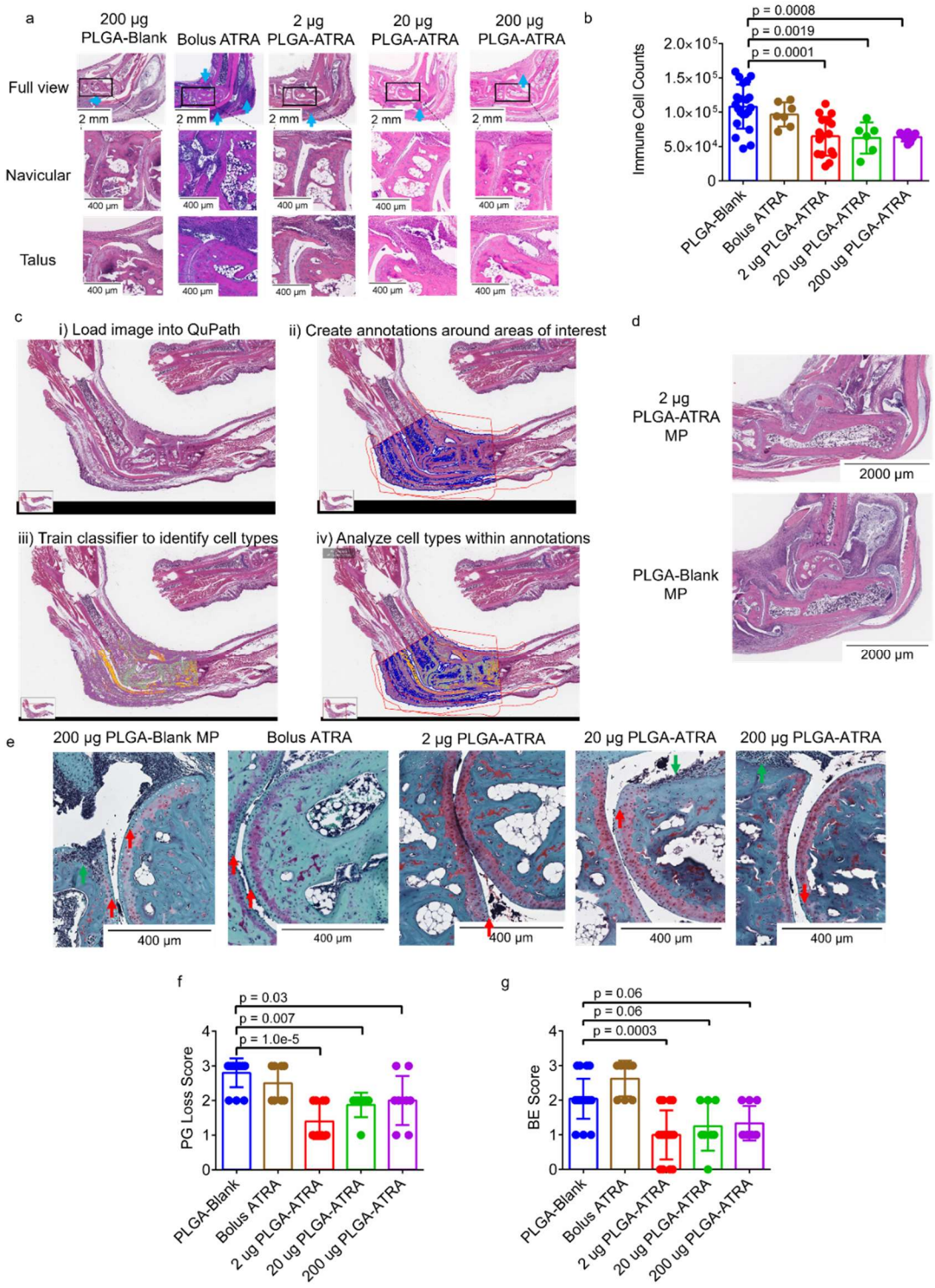
a
200 µg PLGA-Blank
Bolus ATRA
2 µg PLGA-ATRA
20 µg PLGA-ATRA
200 µg PLGA-ATRA
Full view
Navicular
Talus
2 mm
400 µm
b
Immune Cell Counts
p = 0.0008
p = 0.0019
p = 0.0001
PLGA-Blank
Bolus ATRA
2 ug PLGA-ATRA
20 ug PLGA-ATRA
200 ug PLGA-ATRA
c
i) Load image into QuPath
ii) Create annotations around areas of interest
iii) Train classifier to identify cell types
iv) Analyze cell types within annotations
d
2 µg PLGA-ATRA MP
PLGA-Blank MP
2000 µm
e
200 µg PLGA-Blank MP
Bolus ATRA
2 µg PLGA-ATRA
20 µg PLGA-ATRA
200 µg PLGA-ATRA
400 µm
f
PG Loss Score
p = 0.03
p = 0.007
p = 1.0e-5
g
BE Score
p = 0.06
p = 0.06
p = 0.0003

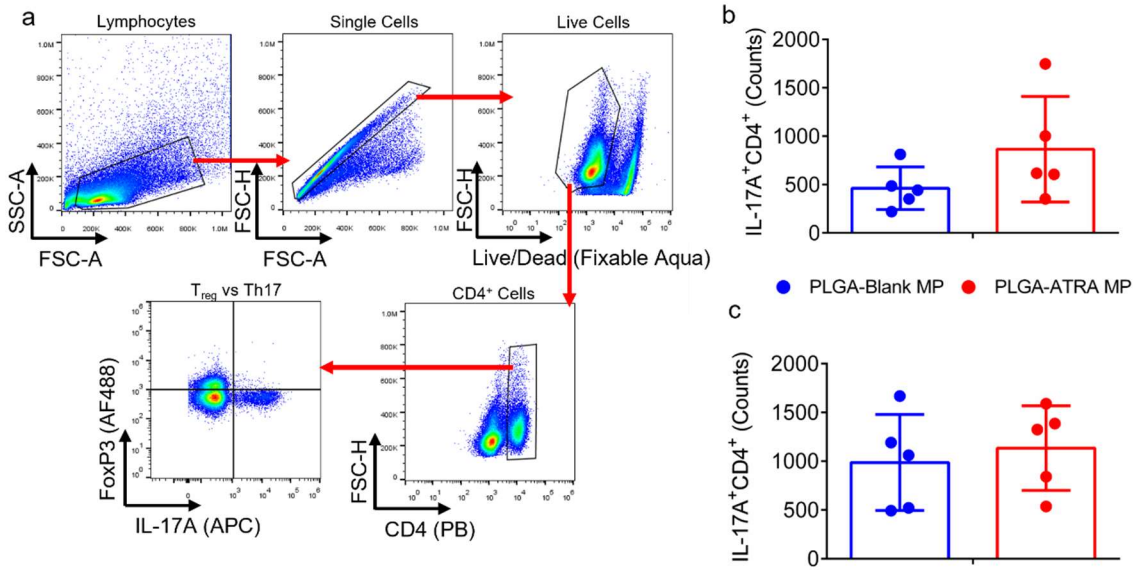

Figure 39 Extended characterization of ATRA-enhanced T_{reg}.
(a) Representative gating strategy for data in Figure 6d-g. (b, c) Quantification of IL-17A+CD4+ T cells in the spleens isolated from mice treated with PLGA-ATRA MP or PLGA-Blank MP on (b) day 17 or (c) day 25 after mannan injection. Data in b, c represent the means ± SD (n = 5/group). Statistical analysis in b, c was performed using Student's unpaired t-test, differences were not significant.

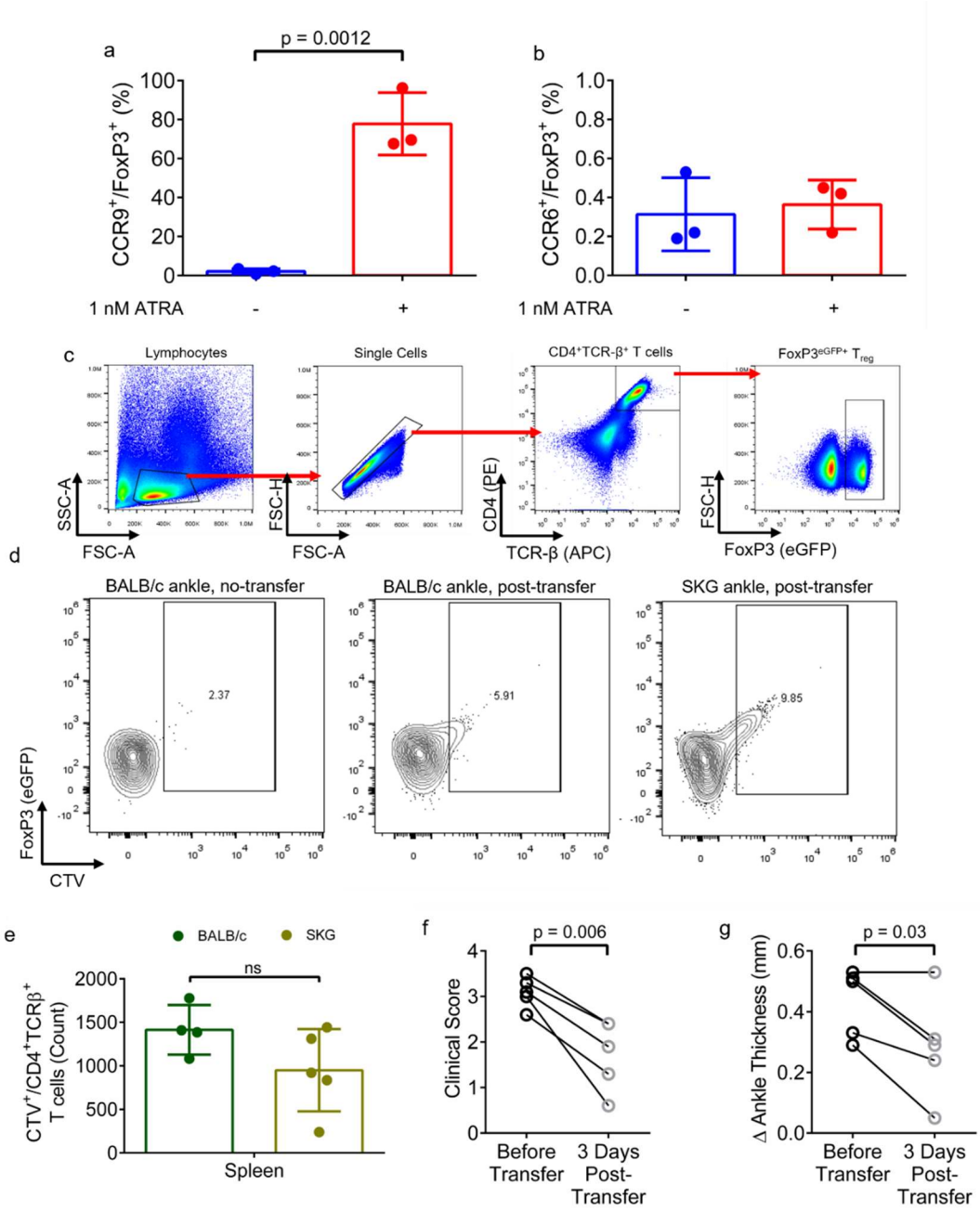

Figure 40 Extended characterization of the immunomodulatory effect of ATRA and PLGA-ATRA MP on T_{reg}.

(a, b) Quantification of (a) CCR9 expression and (b) CCR6 expression in ex vivo differentiated Treg cultured with or without 1 nM ATRA. (c) Representative flow cytometry gating strategy for sorting Treg. (d) Representative flow cytometry plots of CellTracker Violet+ (CTV+) Treg in the ankles. (e) Quantification CTV+CD4+TCR-β+ T cells in the spleen three days after IA injection. (f) Clinical scores of arthritic SKG mice prior to and three days after IA Treg transfer. (g) Change in ankle thickness relative to ankle thickness before arthritis onset in the contralateral ankles of arthritic SKG mice prior to and three days after IA Treg transfer. Data in a, b, e represent the means ± SD (n = 5/group); data in f, g represent clinical scores and change in ankle thicknesses of individual mice (n = 5) respectively prior to and three days after Treg transfer. Data in a, b are technical replicates from a single experiment, which was performed twice. Statistical analyses in a, b, e were performed using an unpaired Student's two tailed t-test. Statistical analyses in f and g were performed using a paired Student's two tailed t-test.

4.8 Chapter 4 References

1. Taylor, P. C.; Moore, A.; Vasilescu, R.; Alvir, J.; Tarallo, M. A Structured Literature Review of the Burden of Illness and Unmet Needs in Patients with Rheumatoid Arthritis: A Current Perspective. Rheumatology International 2016, 36 (5)

2. Aletaha, D.; Smolen, J. S. Diagnosis and Management of Rheumatoid Arthritis: A Review. JAMA - Journal of the American Medical Association 2018, 320 (13).

3. Hinze, C.; Gohar, F.; Foell, D. Management of Juvenile Idiopathic Arthritis: Hitting the Target. Nature Reviews Rheumatology 2015, 11 (5). https://doi.org/10.1038/nrrheum.2014.212.

4. Glück, T.; Müller-Ladner, U. Vaccination in Patients with Chronic Rheumatic or Autoimmune Diseases. Clinical Infectious Diseases 2008, 46 (9), 1459–1465. https://doi.org/10.1086/587063.

5. Ye, H.; Zhang, J.; Wang, J.; Gao, Y.; Du, Y.; Li, C.; Deng, M.; Guo, J.; Li, Z. CD4 T-Cell Transcriptome Analysis Reveals Aberrant Regulation of STAT3 and Wnt Signaling Pathways in Rheumatoid Arthritis: Evidence from a Case–Control Study. Arthritis Res Ther 2015, 17 (1), 76. https://doi.org/10.1186/s13075-015-0590-9.

6. Nakano, K.; Whitaker, J. W.; Boyle, D. L.; Wang, W.; Firestein, G. S. DNA Methylome Signature in Rheumatoid Arthritis. Ann Rheum Dis 2013, 72 (1), 110–117. https://doi.org/10.1136/annrheumdis-2012-201526.

7. Stephenson, W.; Donlin, L. T.; Butler, A.; Rozo, C.; Bracken, B.; Rashidfarrokhi, A.; Goodman, S. M.; Ivashkiv, L. B.; Bykerk, V. P.; Orange, D. E.; Darnell, R. B.; Swerdlow, H. P.; Satija, R. Single-Cell RNA-Seq of Rheumatoid Arthritis Synovial Tissue Using Low-Cost Microfluidic Instrumentation. Nat Commun 2018, 9 (1), 791. https://doi.org/10.1038/s41467-017-02659-x.

8. Ai, R.; Hammaker, D.; Boyle, D. L.; Morgan, R.; Walsh, A. M.; Fan, S.; Firestein, G. S.; Wang, W. Joint-Specific DNA Methylation and Transcriptome Signatures in Rheumatoid Arthritis Identify Distinct Pathogenic Processes. Nat Commun 2016, 7 (1), 11849. https://doi.org/10.1038/ncomms11849.

9. Orange, D. E.; Yao, V.; Sawicka, K.; Fak, J.; Frank, M. O.; Parveen, S.; Blachere, N. E.; Hale, C.; Zhang, F.; Raychaudhuri, S.; Troyanskaya, O. G.; Darnell, R. B. RNA Identification of PRIME Cells Predicting Rheumatoid Arthritis Flares. N Engl J Med 2020, 383 (3), 218–228. https://doi.org/10.1056/NEJMoa2004114.

10. Lu, D. R.; McDavid, A. N.; Kongpachith, S.; Lingampalli, N.; Glanville, J.; Ju, C.-H.; Gottardo, R.; Robinson, W. H. T Cell-Dependent Affinity Maturation and Innate Immune Pathways Differentially Drive Autoreactive B Cell Responses in Rheumatoid Arthritis. Arthritis Rheumatol 2018, 70 (11), 1732–1744. https://doi.org/10.1002/art.40578.

11. Szekanecz, Z.; Koch, A. E. Successes and Failures of Chemokine-Pathway Targeting in Rheumatoid Arthritis. Nat Rev Rheumatol 2016, 12 (1), 5–13. https://doi.org/10.1038/nrrheum.2015.157.

12. Lefèvre, S.; Knedla, A.; Tennie, C.; Kampmann, A.; Wunrau, C.; Dinser, R.; Korb, A.; Schnäker, E.-M.; Tarner, I. H.; Robbins, P. D.; Evans, C. H.; Stürz, H.; Steinmeyer, J.; Gay, S.; Schölmerich, J.; Pap, T.; Müller-Ladner, U.; Neumann, E. Synovial Fibroblasts Spread Rheumatoid Arthritis to Unaffected Joints. Nat Med 2009, 15 (12), 1414–1420. https://doi.org/10.1038/nm.2050.

13. Kinne, R. W.; Stuhlmüller, B.; Burmester, G.-R. Cells of the Synovium in Rheumatoid Arthritis. Macrophages. Arthritis Res Ther 2007, 9 (6), 224. https://doi.org/10.1186/ar2333.

14. Boissier, M.-C.; Semerano, L.; Challal, S.; Saidenberg-Kermanac'h, N.; Falgarone, G. Rheumatoid Arthritis: From Autoimmunity to Synovitis and Joint Destruction. Journal of Autoimmunity 2012, 39 (3), 222–228. https://doi.org/10.1016/j.jaut.2012.05.021.

15. Cope, A. P.; Schulze-Koops, H.; Aringer, M. The Central Role of T Cells in Rheumatoid Arthritis. Clinical and Experimental Rheumatology 2007, 25 (5 SUPPL. 46).

16. Mellado, M. T Cell Migration in Rheumatoid Arthritis. Front. Immunol. 2015, 6. https://doi.org/10.3389/fimmu.2015.00384.

17. FitzGerald, O.; Soden, M.; Yanni, G.; Robinson, R.; Bresnihan, B. Morphometric Analysis of Blood Vessels in Synovial Membranes Obtained from Clinically Affected and Unaffected Knee Joints of Patients with Rheumatoid Arthritis. Annals of the Rheumatic Diseases 1991, 50 (11), 792–796. https://doi.org/10.1136/ard.50.11.792.

18. Iwamoto, T.; Okamoto, H.; Toyama, Y.; Momohara, S. Molecular Aspects of Rheumatoid Arthritis: Chemokines in the Joints of Patients: Chemokines in the Joints of Patients. FEBS Journal 2008, 275 (18), 4448–4455. https://doi.org/10.1111/j.1742-4658.2008.06580.x.

19. Kimura, A.; Kishimoto, T. IL-6: Regulator of Treg/Th17 Balance. European Journal of Immunology 2010, 40 (7). https://doi.org/10.1002/eji.201040391.

20. Pandiyan, P.; Zhu, J. Origin and Functions of Pro-Inflammatory Cytokine Producing Foxp3+ Regulatory T Cells. Cytokine 2015, 76 (1). https://doi.org/10.1016/j.cyto.2015.07.005.

21. Noack, M.; Miossec, P. Th17 and Regulatory T Cell Balance in Autoimmune and Inflammatory Diseases. Autoimmunity Reviews 2014, 13 (6). https://doi.org/10.1016/j.autrev.2013.12.004.

22. Svensson, M. N. D.; Doody, K. M.; Schmiedel, B. J.; Bhattacharyya, S.; Panwar, B.; Wiede, F.; Yang, S.; Santelli, E.; Wu, D. J.; Sacchetti, C.; Gujar, R.; Seumois, G.; Kiosses, W. B.; Aubry, I.; Kim, G.; Mydel, P.; Sakaguchi, S.; Kronenberg, M.; Tiganis, T.; Tremblay, M. L.; Ay, F.; Vijayanand, P.; Bottini, N. Reduced Expression of Phosphatase PTPN2 Promotes Pathogenic Conversion of Tregs in Autoimmunity. The Journal of Clinical Investigation 2019, 129 (3), 1193–1210. https://doi.org/10.1172/JCI123267.

23. Rudra, D.; Deroos, P.; Chaudhry, A.; Niec, R. E.; Arvey, A.; Samstein, R. M.; Leslie, C.; Shaffer, S. A.; Goodlett, D. R.; Rudensky, A. Y. Transcription Factor Foxp3 and Its Protein Partners Form a Complex Regulatory Network. Nature Immunology 2012, 13 (10). https://doi.org/10.1038/ni.2402.

24. Mouly, E.; Chemin, K.; Nguyen, H. V.; Chopin, M.; Mesnard, L.; Leite-de-Moraes, M.; Burlen-defranoux, O.; Bandeira, A.; Bories, J. C. The Ets-1 Transcription Factor Controls the Development and Function of Natural Regulatory T Cells. Journal of Experimental Medicine 2010, 207 (10). https://doi.org/10.1084/jem.20092153.

25. Zhang, F.; Meng, G.; Strober, W. Interactions among the Transcription Factors Runx1, RORγt and Foxp3 Regulate the Differentiation of Interleukin 17-Producing T Cells. Nature Immunology 2008, 9 (11). https://doi.org/10.1038/ni.1663.

26. Schraml, B. U.; Hildner, K.; Ise, W.; Lee, W.-L.; Smith, W. A.-E.; Solomon, B.; Sahota, G.; Sim, J.; Mukasa, R.; Cemerski, S.; Hatton, R. D.; Stormo, G. D.; Weaver, C. T.; Russell, J. H.; Murphy, T. L.; Murphy, K. M. The AP-1 Transcription Factor Batf Controls TH17 Differentiation. Nature 2009, 460 (7253). https://doi.org/10.1038/nature08114.

27. Ciofani, M.; Madar, A.; Galan, C.; Sellars, M.; Mace, K.; Pauli, F.; Agarwal, A.; Huang, W.; Parkhurst, C. N.; Muratet, M.; Newberry, K. M.; Meadows, S.; Greenfield, A.; Yang, Y.; Jain, P.; Kirigin, F. K.; Birchmeier, C.; Wagner, E. F.; Murphy, K. M.; Myers, R. M.; Bonneau, R.; Littman, D. R. A Validated Regulatory Network for Th17 Cell Specification. Cell 2012, 151 (2), 289–303. https://doi.org/10.1016/j.cell.2012.09.016.

28. Wysocka, J.; Swigut, T.; Xiao, H.; Milne, T. A.; Kwon, S. Y.; Landry, J.; Kauer, M.; Tackett, A. J.; Chait, B. T.; Badenhorst, P.; Wu, C.; Allis, C. D. A PHD Finger of NURF Couples Histone H3 Lysine 4 Trimethylation with Chromatin Remodelling. Nature 2006, 442 (7098), 86–90. https://doi.org/10.1038/nature04815.

29. Liang, G.; Lin, J. C. Y.; Wei, V.; Yoo, C.; Cheng, J. C.; Nguyen, C. T.; Weisenberger, D. J.; Egger, G.; Takai, D.; Gonzales, F. A.; Jones, P. A. Distinct Localization of Histone H3 Acetylation and H3-K4 Methylation to the Transcription Start Sites in the Human Genome. Proc. Natl. Acad. Sci. U.S.A. 2004, 101 (19), 7357–7362. https://doi.org/10.1073/pnas.0401866101.

30. Hoeppli, R. E.; MacDonald, K. N.; Leclair, P.; Fung, V. C. W.; Mojibian, M.; Gillies, J.; Rahavi, S. M. R.; Campbell, A. I. M.; Gandhi, S. K.; Pesenacker, A. M.; Reid, G.; Lim, C. J.; Levings, M. K. Tailoring the Homing Capacity of Human Tregs for Directed Migration to Sites of Th1-Inflammation or Intestinal Regions. American Journal of Transplantation 2019, 19 (1), 62–76. https://doi.org/10.1111/ajt.14936.

31. Burrows, K.; Antignano, F.; Bramhall, M.; Chenery, A.; Scheer, S.; Korinek, V.; Underhill, T. M.; Zaph, C. The Transcriptional Repressor HIC1 Regulates Intestinal Immune Homeostasis. Mucosal Immunol 2017, 10 (6), 1518–1528. https://doi.org/10.1038/mi.2017.17.

32. Patton, D. T.; Wilson, M. D.; Rowan, W. C.; Soond, D. R.; Okkenhaug, K. The PI3K P110δ Regulates Expression of CD38 on Regulatory T Cells. PLoS ONE 2011, 6 (3), e17359. https://doi.org/10.1371/journal.pone.0017359.

33. Sawant, D. V.; Wu, H.; Yao, W.; Sehra, S.; Kaplan, M. H.; Dent, A. L. The Transcriptional Repressor Bcl6 Controls the Stability of Regulatory T Cells by Intrinsic and Extrinsic Pathways. Immunology 2015, 145 (1), 11–23. https://doi.org/10.1111/imm.12393.

34. Jing, J.; Nelson, C.; Paik, J.; Shirasaka, Y.; Amory, J. K.; Isoherranen, N. Physiologically Based Pharmacokinetic Model of All-Trans-Retinoic Acid with Application to Cancer Populations and Drug Interactions. The Journal of pharmacology and experimental therapeutics 2017, 361 (2), 246–258. https://doi.org/10.1124/jpet.117.240523.

35. Hurtig, M.; Zaghoul, I.; Sheardown, H.; Schmidt, T. A.; Liu, L.; Zhang, L.; Elsaid, K. A.; Jay, G. D. Two Compartment Pharmacokinetic Model Describes the Intra-Articular Delivery and Retention of Rhprg4 Following ACL Transection in the Yucatan Mini Pig. Journal of Orthopaedic Research 2019, 37 (2). https://doi.org/10.1002/jor.24191.

36. Sakaguchi, S.; Takahashi, T.; Hata, H.; Nomura, T.; Sakaguchi, N. SKG Mice, a New Genetic Model of Rheumatoid Arthritis. Arthritis Res Ther 2003, 5 (3), 10. https://doi.org/10.1186/ar811.

37. Sakaguchi, N.; Takahashi, T.; Hata, H.; Nomura, T.; Tagami, T.; Yamazaki, S.; Sakihama, T.; Matsutani, T.; Negishi, I.; Nakatsuru, S.; Sakaguchi, S. Altered Thymic T-Cell Selection Due to a Mutation of the ZAP-70 Gene Causes Autoimmune Arthritis in Mice. Nature 2003, 426 (6965). https://doi.org/10.1038/nature02119.

38. Firestein, G. S. Rheumatoid Arthritis in a Mouse? Nature Clinical Practice Rheumatology 2009, 5 (1). https://doi.org/10.1038/ncprheum0973.

39. Hayer, S.; Vervoordeldonk, M. J.; Denis, M. C.; Armaka, M.; Hoffmann, M.; Bäcklund, J.; Nandakumar, K. S.; Niederreiter, B.; Geka, C.; Fischer, A.; Woodworth, N.; Blüml, S.; Kollias, G.; Holmdahl, R.; Apparailly, F.; Koenders, M. I. SMASH Recommendations for Standardised Microscopic Arthritis Scoring of Histological Sections from Inflammatory Arthritis Animal Models. Annals of the Rheumatic Diseases 2021, 80 (6). https://doi.org/10.1136/annrheumdis-2020-219247.

40. Hashimoto, M.; Hirota, K.; Yoshitomi, H.; Maeda, S.; Teradaira, S.; Akizuki, S.; Prieto-Martin, P.; Nomura, T.; Sakaguchi, N.; Köhl, J.; Heyman, B.; Takahashi, M.; Fujita, T.; Mimori, T.; Sakaguchi, S. Complement Drives Th17 Cell Differentiation and Triggers Autoimmune Arthritis. Journal of Experimental Medicine 2010, 207 (6), 1135–1143. https://doi.org/10.1084/jem.20092301.

41. Hsieh, W. C.; Svensson, M. N. D.; Zoccheddu, M.; Tremblay, M. L.; Sakaguchi, S.; Stanford, S. M.; Bottini, N. PTPN2 Links Colonic and Joint Inflammation in Experimental Autoimmune Arthritis. JCI Insight 2020, 5 (20). https://doi.org/10.1172/jci.insight.141868.

42. Bai, A.; Lu, N.; Guo, Y.; Liu, Z.; Chen, J.; Peng, Z. All-Trans Retinoic Acid down-Regulates Inflammatory Responses by Shifting the Treg/Th17 Profile in Human Ulcerative and Murine Colitis. Journal of Leukocyte Biology 2009, 86 (4). https://doi.org/10.1189/jlb.0109006.

43. Xiao, S.; Jin, H.; Korn, T.; Liu, S. M.; Oukka, M.; Lim, B.; Kuchroo, V. K. Retinoic Acid Increases Foxp3+ Regulatory T Cells and Inhibits Development of Th17 Cells by Enhancing TGF-β-Driven Smad3 Signaling and Inhibiting IL-6 and IL-23 Receptor Expression. The Journal of Immunology 2008, 181 (4), 2277 LP – 2284.

44. Mucida, D.; Park, Y.; Kim, G.; Turovskaya, O.; Scott, I.; Kronenberg, M.; Cheroutre, H. Reciprocal TH17 and Regulatory T Cell Differentiation Mediated by Retinoic Acid. Science 2007, 317 (5835). https://doi.org/10.1126/science.1145697.

45. Bird, H.; Moll, J.; Rushton, A. Therapeutics in Rheumatology; Springer, 2013.

46. Nagate, T.; Kawai, J.; Nakayama, J. Therapeutic and Preventive Effects of Methotrexate on Zymosan-Induced Arthritis in SKG Mice. J Vet Med Sci 2009, 71 (6), 713–717. https://doi.org/10.1292/jvms.71.713.

47. Sakaguchi, S.; Takahashi, T.; Hata, H.; Yoshitomi, H.; Tanaka, S.; Hirota, K.; Nomura, T.; Sakaguchi, N. SKG Mice, a Monogenic Model of Autoimmune Arthritis Due to Altered Signal Transduction in T-Cells. In The Hereditary Basis of Rheumatic Diseases; 2006. https://doi.org/10.1007/3-7643-7419-5_11.

48. Henderson, L. A.; Hoyt, K. J.; Lee, P. Y.; Rao, D. A.; Helena Jonsson, A.; Nguyen, J. P.; Rutherford, K.; Julé, A. M.; Charbonnier, L. M.; Case, S.; Chang, M. H.; Cohen, E. M.; Dedeoglu, F.; Fuhlbrigge, R. C.; Halyabar, O.; Hazen, M. M.; Janssen, E.; Kim, S.; Lo, J.; Lo, M. S.; Meidan, E.; Son, M. B. F.; Sundel, R. P.; Stoll, M. L.; Nusbaum, C.; Lederer, J. A.; Chatila, T. A.; Nigrovic, P. A. Th17 Reprogramming of T Cells in Systemic Juvenile Idiopathic Arthritis. JCI Insight 2020, 5 (6). https://doi.org/10.1172/jci.insight.132508.

49. Liu, Z. M.; Wang, K. P.; Ma, J.; Guo Zheng, S. The Role of All-Trans Retinoic Acid in the Biology of FOXP3^{+} Regulatory T Cells. Cellular and Molecular Immunology 2015, 12 (5), 553–557. https://doi.org/10.1038/cmi.2014.133.

50. Zaiss, M. M.; Joyce Wu, H. J.; Mauro, D.; Schett, G.; Ciccia, F. The Gut–Joint Axis in Rheumatoid Arthritis. Nature Reviews Rheumatology 2021, 17 (4). https://doi.org/10.1038/s41584-021-00585-3.

51. Sprouse, M. L.; Bates, N. A.; Felix, K. M.; Wu, H. J. J. Impact of Gut Microbiota on Gut-Distal Autoimmunity: A Focus on T Cells. Immunology 2019, 156 (4). https://doi.org/10.1111/imm.13037.

52. Lu, L.; Ma, J.; Li, Z.; Lan, Q.; Chen, M.; Liu, Y.; Xia, Z.; Wang, J.; Han, Y.; Shi, W.; Quesniaux, V.; Ryffel, B.; Brand, D.; Li, B.; Liu, Z.; Zheng, S. G. All-Trans Retinoic Acid Promotes TGF-β-Induced Tregs via Histone Modification but Not DNA Demethylation on Foxp3 Gene Locus. PLoS ONE 2011, 6 (9). https://doi.org/10.1371/journal.pone.0024590.

53. Kwok, S.-K.; Park, M.-K.; Cho, M.-L.; Oh, H.-J.; Park, E.-M.; Lee, D.-G.; Lee, J.; Kim, H.-Y.; Park, S.-H. Retinoic Acid Attenuates Rheumatoid Inflammation in Mice. The Journal of Immunology 2012, 189 (2). https://doi.org/10.4049/jimmunol.1102706.

54. Elias, K. M.; Laurence, A.; Davidson, T. S.; Stephens, G.; Kanno, Y.; Shevach, E. M.; O'Shea, J. J. Retinoic Acid Inhibits Th17 Polarization and Enhances FoxP3 Expression through a Stat-3/Stat-5 Independent Signaling Pathway. Blood 2008, 111 (3). https://doi.org/10.1182/blood-2007-06-096438.

55. Nozaki, Y.; Yamagata, T.; Sugiyama, M.; Ikoma, S.; Kinoshita, K.; Funauchi, M. Anti-Inflammatory Effect of All-Trans-Retinoic Acid in Inflammatory Arthritis. Clinical Immunology 2006, 119 (3). https://doi.org/10.1016/j.clim.2005.11.012.

56. Hill, J. A.; Hall, J. A.; Sun, C.-M.; Cai, Q.; Ghyselinck, N.; Chambon, P.; Belkaid, Y.; Mathis, D.; Benoist, C. Retinoic Acid Enhances Foxp3 Induction Indirectly by Relieving Inhibition from CD4+CD44hi Cells. Immunity 2008, 29 (5), 758–770. https://doi.org/10.1016/j.immuni.2008.09.018.

57. Zheng, Y.; Josefowicz, S.; Chaudhry, A.; Peng, X. P.; Forbush, K.; Rudensky, A. Y. Role of Conserved Non-Coding DNA Elements in the Foxp3 Gene in Regulatory T-Cell Fate. Nature 2010, 463 (7282), 808–812. https://doi.org/10.1038/nature08750.

58. Feng, Y.; Arvey, A.; Chinen, T.; van der Veeken, J.; Gasteiger, G.; Rudensky, A. Y. Control of the Inheritance of Regulatory T Cell Identity by a Cis Element in the Foxp3 Locus. Cell 2014, 158 (4), 749–763. https://doi.org/10.1016/j.cell.2014.07.031.

59. Lu, L.; Lan, Q.; Li, Z.; Zhou, X.; Gu, J.; Li, Q.; Wang, J.; Chen, M.; Liu, Y.; Shen, Y.; Brand, D. D.; Ryffel, B.; Horwitz, D. A.; Quismorio, F. P.; Liu, Z.; Li, B.; Olsen, N. J.; Zheng, S. G. Critical Role of All-Trans Retinoic Acid in Stabilizing Human Natural Regulatory T Cells under Inflammatory Conditions. Proceedings of the National Academy of Sciences of the United States of America 2014, 111 (33). https://doi.org/10.1073/pnas.1408780111.

60. Wehr, P.; Purvis, H.; Law, S.-C.; Thomas, R. Dendritic Cells, T Cells and Their Interaction in Rheumatoid Arthritis. Clinical and Experimental Immunology 2019, 196 (1), 12–27. https://doi.org/10.1111/cei.13256.

61. Ueno, H.; Klechevsky, E.; Morita, R.; Aspord, C.; Cao, T.; Matsui, T.; Di Pucchio, T.; Connolly, J.; Fay, J. W.; Pascual, V.; Palucka, A. K.; Banchereau, J. Dendritic Cell Subsets in Health and Disease. Immunol Rev 2007, 219 (1), 118–142. https://doi.org/10.1111/j.1600-065X.2007.00551.x.

62. Banchereau, J.; Steinman, R. M. Dendritic Cells and the Control of Immunity. Nature 1998, 392 (6673), 245–252. https://doi.org/10.1038/32588.

63. Takemura, S.; Braun, A.; Crowson, C.; Kurtin, P. J.; Cofield, R. H.; O'Fallon, W. M.; Goronzy, J. J.; Weyand, C. M. Lymphoid Neogenesis in Rheumatoid Synovitis. J Immunol 2001, 167 (2), 1072–1080. https://doi.org/10.4049/jimmunol.167.2.1072.

64. Weyand, C. M.; Goronzy, J. J. Ectopic Germinal Center Formation in Rheumatoid Synovitis. Annals of the New York Academy of Sciences 2003, 987 (1), 140–149. https://doi.org/10.1111/j.1749-6632.2003.tb06042.x.

65. Vellozo, N. S.; Pereira-Marques, S. T.; Cabral-Piccin, M. P.; Filardy, A. A.; Ribeiro-Gomes, F. L.; Rigoni, T. S.; DosReis, G. A.; Lopes, M. F. All-Trans Retinoic Acid Promotes an M1- to M2-Phenotype Shift and Inhibits Macrophage-Mediated Immunity to Leishmania Major. Front. Immunol. 2017, 8, 1560. https://doi.org/10.3389/fimmu.2017.01560.

66. Li, S.; Lei, Y.; Lei, J.; Li, H. All-trans Retinoic Acid Promotes Macrophage Phagocytosis and Decreases Inflammation via Inhibiting CD14/TLR4 in Acute Lung Injury. Mol Med Rep 2021, 24 (6), 868. https://doi.org/10.3892/mmr.2021.12508.

67. Randolph, G. J.; Ochando, J.; Partida-Sánchez, S. Migration of Dendritic Cell Subsets and Their Precursors. Annual review of immunology 2008, 26 (1), 293–316.

68. Raffin, C.; Zhou, Y.; Piccoli, L.; Lanzavecchia, A.; Sadelain, M.; Tareen, S. U.; Fontenot, J. D.; Bluestone, J. A. Development of Citrullinated-Vimentin-Specific CAR for Targeting Tregs to Treat Autoimmune Rheumatoid Arthritis. The Journal of Immunology 2018, 200 (1 Supplement).

69. Benham, H.; Nel, H. J.; Law, S. C.; Mehdi, A. M.; Street, S.; Ramnoruth, N.; Pahau, H.; Lee, B. T.; Ng, J.; Brunck, M. E. G.; Hyde, C.; Trouw, L. A.; Dudek, N. L.; Purcell, A. W.; O'Sullivan, B. J.; Connolly, J. E.; Paul, S. K.; Lê Cao, K. A.; Thomas, R. Citrullinated Peptide Dendritic Cell Immunotherapy in HLA Risk Genotype-Positive Rheumatoid Arthritis Patients. Science Translational Medicine 2015, 7 (290). https://doi.org/10.1126/scitranslmed.aaa9301.

70. Allen, R.; Chizari, S.; Ma, J. A.; Raychaudhuri, S.; Lewis, J. S. Combinatorial, Microparticle-Based Delivery of Immune Modulators Reprograms the Dendritic Cell Phenotype and Promotes Remission of Collagen-Induced Arthritis in Mice. ACS Applied Bio Materials 2019, 2 (6). https://doi.org/10.1021/acsabm.9b00092.

71. Hughes, C.; Sette, A.; Seed, M.; D'Acquisto, F.; Manzo, A.; Vincent, T. L.; Lim, N. H.; Nissim, A. Targeting of Viral Interleukin-10 with an Antibody Fragment Specific to Damaged Arthritic Cartilage Improves Its Therapeutic Potency. Arthritis Research and Therapy 2014, 16 (4). https://doi.org/10.1186/ar4613.

72. Yuba, E.; Budina, E.; Katsumata, K.; Ishihara, A.; Mansurov, A.; Alpar, A. T.; Watkins, E. A.; Hosseinchi, P.; Reda, J. W.; Lauterbach, A. L.; Nguyen, M.; Solanki, A.; Kageyama, T.; Swartz, M. A.; Ishihara, J.; Hubbell, J. A. Suppression of Rheumatoid Arthritis by Enhanced Lymph Node Trafficking of Engineered Interleukin-10 in Murine Models. Arthritis and Rheumatology 2021, 73 (5). https://doi.org/10.1002/art.41585.

73. Kim, W. U.; Lee, W. K.; Ryoo, J. W.; Kim, S. H.; Kim, J.; Youn, J.; Min, S. Y.; Bae, E. Y.; Hwang, S. Y.; Park, S. H.; Cho, C. S.; Park, J. S.; Kim, H. Y. Suppression of Collagen-Induced Arthritis by Single Administration of Poly(Lactic-Co-Glycolic Acid) Nanoparticles Entrapping Type II Collagen: A Novel Treatment Strategy for Induction of Oral Tolerance. Arthritis and Rheumatism 2002, 46 (4). https://doi.org/10.1002/art.10198.

74. Bassin, E. J.; Buckley, A. R.; Piganelli, J. D.; Little, S. R. TRI Microparticles Prevent Inflammatory Arthritis in a Collagen-Induced Arthritis Model. PLOS ONE 2020, 15 (9). https://doi.org/10.1371/journal.pone.0239396.

75. Jhunjhunwala, S.; Balmert, S. C.; Raimondi, G.; Dons, E.; Nichols, E. E.; Thomson, A. W.; Little, S. R. Controlled Release Formulations of IL-2, TGF-B1 and Rapamycin for the Induction of Regulatory T Cells. Journal of Controlled Release 2012, 159 (1). https://doi.org/10.1016/j.jconrel.2012.01.013.

76. Zhu, L.; Chanalaris, A.; Lympany, S.; Vincent, T. L. Cartilage Injury Regulates Inflammatory Gene Expression in Part by Suppressing Cellular Retinoic Acid Signaling. Osteoarthritis and Cartilage 2017, 25. https://doi.org/10.1016/j.joca.2017.02.288.

77. Hata, H.; Sakaguchi, N.; Yoshitomi, H.; Iwakura, Y.; Sekikawa, K.; Azuma, Y.; Kanai, C.; Moriizumi, E.; Nomura, T.; Nakamura, T.; Sakaguchi, S. Distinct Contribution of IL-6, TNF-α, IL-1, and IL-10 to T Cell-Mediated Spontaneous Autoimmune Arthritis in Mice. Journal of Clinical Investigation 2004, 114 (4). https://doi.org/10.1172/JCI200421795.

78. Yang, S.; Zhang, X.; Chen, J.; Dang, J.; Liang, R.; Zeng, D.; Zhang, H.; Xue, Y.; Liu, Y.; Wu, W.; Zhao, J.; Wang, J.; Pan, Y.; Xu, H.; Sun, B.; Huang, F.; Lu, Y.; Hsueh, W.; Olsen, N.; Zheng, S. G. Induced, but Not Natural, Regulatory T Cells Retain Phenotype and Function Following Exposure to Inflamed Synovial Fibroblasts. Sci Adv 10AD, 6 (44). https://doi.org/10.1126/sciadv.abb0606.

79. Liang, D.; Zuo, A.; Shao, H.; Born, W. K.; O'Brien, R. L.; Kaplan, H. J.; Sun, D. Retinoic Acid Inhibits CD25+ Dendritic Cell Expansion and Γδ T-Cell Activation in Experimental Autoimmune Uveitis. Invest Ophthalmol Vis Sci 2013, 54 (5), 3493–3503. https://doi.org/10.1167/iovs.12-11432.

80. Abtahi Froushani, S. M.; Delirezh, N.; Hobbenaghi, R.; Mosayebi, G. Synergistic Effects of Atorvastatin and All-Trans Retinoic Acid in Ameliorating Animal Model of Multiple Sclerosis. Immunological Investigations 2014, 43 (1). https://doi.org/10.3109/08820139.2013.825269.

81. Snyder, J. M.; Zhong, G.; Hogarth, C.; Huang, W.; Topping, T.; LaFrance, J.; Palau, L.; Czuba, L. C.; Griswold, M.; Ghiaur, G.; Isoherranen, N. Knockout of Cyp26a1 and Cyp26b1 during Postnatal Life Causes Reduced Lifespan, Dermatitis, Splenomegaly, and Systemic Inflammation in Mice. FASEB Journal 2020, 34 (12). https://doi.org/10.1096/fj.202001734R.

82. Kurtz, P. J.; Emmerling, D. C.; Donofrio, D. J. Subchronic Toxicity of All-Trans-Retinoic Acid and Retinylidene Dimedone in Sprague-Dawley Rats. Toxicology 1984, 30 (2). https://doi.org/10.1016/0300-483X(84)90122-7.

83. Choi, Y.; Lee, C.; Park, K.; Kim, S. Y.; Kim, S. H.; Han, S.; Kim, S. H.; Byun, Y. Subacute Toxicity of All-Trans-Retinoic Acid Loaded Biodegradable Microspheres in Rats. Drug Development Research 2003, 59 (3). https://doi.org/10.1002/ddr.10283.

84. Umar, S.; Palasiewicz, K.; Van Raemdonck, K.; Volin, M. V.; Romay, B.; Ahmad, I.; Tetali, C.; Sweiss, N.; Amin, M. A.; Zomorrodi, R. K.; Shahrara, S. CCL25 and CCR9 Is a Unique Pathway That Potentiates Pannus Formation by Remodeling RA Macrophages into Mature Osteoclasts. Eur J Immunol 2021, 51 (4), 903–914. https://doi.org/10.1002/eji.202048681.

85. Schmutz, C.; Cartwright, A.; Williams, H.; Haworth, O.; Williams, J. H.; Filer, A.; Salmon, M.; Buckley, C. D.; Middleton, J. Monocytes/Macrophages Express Chemokine Receptor CCR9 in Rheumatoid Arthritis and CCL25 Stimulates Their Differentiation. Arthritis Res Ther 2010, 12 (4), R161. https://doi.org/10.1186/ar3120.

86. Manhas, K. R.; Marshall, P. A.; Wagner, C. E.; Jurutka, P. W.; Mancenido, M. V.; Debray, H. Z.; Blattman, J. N. Rexinoids Modulate Effector T Cell Expression of Mucosal Homing Markers CCR9 and A4β7 Integrin and Direct Their Migration In Vitro. Front. Immunol. 2022, 13, 746484. https://doi.org/10.3389/fimmu.2022.746484.

87. Komatsu, N.; Okamoto, K.; Sawa, S.; Nakashima, T.; Oh-hora, M.; Kodama, T.; Tanaka, S.; Bluestone, J. A.; Takayanagi, H. Pathogenic Conversion of Foxp3+ T Cells into TH17 Cells in Autoimmune Arthritis. Nat Med 2014, 20 (1), 62–68. https://doi.org/10.1038/nm.3432.

88. Langmead, B.; Salzberg, S. L. Fast Gapped-Read Alignment with Bowtie 2. Nature Methods 2012, 9 (4), 357–359. https://doi.org/10.1038/nmeth.1923.

89. Amemiya, H. M.; Kundaje, A.; Boyle, A. P. The ENCODE Blacklist: Identification of Problematic Regions of the Genome. Scientific Reports 2019, 9 (1), 9354. https://doi.org/10.1038/s41598-019-45839-z.

90. Li, H.; Handsaker, B.; Wysoker, A.; Fennell, T.; Ruan, J.; Homer, N.; Marth, G.; Abecasis, G.; Durbin, R. The Sequence Alignment/Map Format and SAMtools. Bioinformatics 2009, 25 (16), 2078–2079. https://doi.org/10.1093/bioinformatics/btp352.

91. Ramirez, F.; Ryan, D.; Gruning, B.; Bhardwaj, V.; Kilpert, F.; Richter, A.; Heyne, S.; Dundar, F.; Manke, T. DeepTools2: A next Generation Web Server for Deep-Sequencing Data Analysis. Nucleic Acids Research 2016, 44 (W1), W160–W165. https://doi.org/10.1093/nar/gkw257.

92. Zhang, Y.; Liu, T.; Meyer, C. A.; Eeckhoute, J.; Johnson, D. S.; Bernstein, B. E.; Nusbaum, C.; Myers, R. M.; Brown, M.; Li, W.; Liu, X. S. Model-Based Analysis of ChIP-Seq (MACS). Genome Biology 2008, 9 (9), R137. https://doi.org/10.1186/gb-2008-9-9-r137.

93. Quinlan, A. R.; Hall, I. M. BEDTools: A Flexible Suite of Utilities for Comparing Genomic Features. Bioinformatics 2010, 26 (6), 841–842. https://doi.org/10.1093/bioinformatics/btq033.

94. Love, M. I.; Huber, W.; Anders, S. Moderated Estimation of Fold Change and Dispersion for RNA-Seq Data with DESeq2. Genome Biology 2014, 15 (12). https://doi.org/10.1186/s13059-014-0550-8.

95. Heinz, S.; Benner, C.; Spann, N.; Bertolino, E.; Lin, Y. C.; Laslo, P.; Cheng, J. X.; Murre, C.; Singh, H.; Glass, C. K. Simple Combinations of Lineage-Determining Transcription Factors Prime Cis-Regulatory Elements Required for Macrophage and B Cell Identities. Molecular Cell 2010, 38 (4). https://doi.org/10.1016/j.molcel.2010.05.004.

96. Kanneganti, K.; Simon, L. Two-Compartment Pharmacokinetic Models for Chemical Engineers. Chemical Engineering Education 2011, 45 (2).

97. Andersson, K. M. E.; Svensson, M. N. D.; Erlandsson, M. C.; Jonsson, I.-M.; Bokarewa, M. I. Down-Regulation of Survivin Alleviates Experimental Arthritis. J Leukoc Biol 2015, 97 (1), 135–145. https://doi.org/10.1189/jlb.3A0714-317R.

CONCLUSION

5.1 Summary

This dissertation has focused on the development of biomaterials to promote and enhance T_{reg} for the treatment of autoimmune disease. In Chapter 2 it was demonstrated that cyclodextrins may enhance the solubility of rapamycin in aqueous solution and maintain efficacy for up to one month in solution. The cyclodextrin/rapamycin complexes (CRCs) were able to enrich the fraction of T_{reg} in cell culture and exhibited a synergistic effect on T_{reg} enrichment when combined with TGF-β1. I used my results to generate a mathematical model for how TGF-β1 and CRCs differentially enhance T_{reg} purity, as well as how differences in cell kinetic parameters between species affect T_{reg} enrichment during expansion. The model and methods developed in these studies provide useful tools for establishing and improving quality control of adoptive cell transfer therapies involving T_{reg}.

In Chapter 3, the phenotypic and epigenetic modulation of T cells by short chain fatty acids was examined, and a new liposomal formulation of butyrate was developed to improve delivery to T cells. The capacity for the short chain fatty acids pentanoate and butyrate to promote T_{reg} and inhibit Th17 were examined. It was found that butyrate preferentially promoted a T_{reg} phenotype, and enhanced production of the immunomodulatory cytokine IL-10. However, high concentrations of butyrate were found to be cytotoxic to T cells. To improve the delivery of butyrate and mitigate cytotoxicity issues, butyrate-encapsulating liposomes (BLIPs) were developed which improved the T_{reg} enhancing effect of butyrate while retaining high cell viability. Butyrate is known to promote T_{reg} in part via histone deacetylase (HDAC) inhibition, and it was demonstrated that BLIPs enhanced HDAC inhibition in live cells relative to free butyrate, suggesting that BLIPs enhance butyrate delivery to T cells.

In Chapter 4, injectable microparticles for localized epigenetic modulation of T cells was developed and tested in vivo. First, the capacity for the active pharmaceutical ingredient to mediate T_{reg} enhancing epigenetic changes in inflammatory conditions was confirmed. Next, multiple biomaterial formulations were tested in vitro to compare size and release profiles. Computational pharmacokinetic models were employed to choose a formulation for in vivo testing. The chosen formulation was demonstrated to remain at the site of injection for up to one month and have efficacy in models of established autoimmune arthritis. The immunomodulatory microparticles reduced swelling and enhanced chondroprotection, decreasing bone erosions and cartilage loss. Examination of different routes of injection and bolus injection of the active pharmaceutical ingredient demonstrated that both the route of injection, and the sustained release of the epigenetic modulator were essential for the efficacy of the treatment. Immunological assessments of disease revealed that treatment with the microparticles acted to restore balance between T_{reg} and Th17, both at the site of disease and at distal sites. Experiments with fate-mapping mice revealed that this was due to a combination of reducing T_{reg} destabilization and promoting the differentiation of newly induced T_{reg}. The immunoregulatory effect of the microparticles was shown to be disease-specific as treatment with the microparticles did not inhibit immune response to a disease-irrelevant antigen. This work demonstrates that localized epigenetic modulation of T cell responses at a disease-specific site can generate systemic disease protection without generalized immune suppression.

5.2 Future directions

This work has paved the way for biomaterials to promote immunoregulation in autoimmune disorders. An improved understanding of the mechanisms of action, improved formulations, and examination of efficacy in additional diseases are proposed.

5.2.1 Comprehensive evaluation of immunological changes mediated by T_{reg} enhancement in autoimmune arthritis

The research presented in Chapter 4 focuses on how a localized epigenetic modulating biomaterial mediates changes to the T cell population in autoimmune arthritis. T cells are also responsible for coordinating downstream immune responses. Thus, it would be valuable to characterize other disease-relevant immune cells. Single cell sequencing combined with advanced computational techniques may be used to investigate how and why the immune population shifts after treatment. This will improve understanding of how T_{reg} control autoimmune arthritis from a systems level perspective and will be valuable for further assessing clinical relevance of the treatment.

5.2.2 Local T_{reg} enhancement in additional disease contexts

Here, we have developed a treatment and technique to enhance disease-specific T_{reg} by targeting the site of disease. We focused on autoimmune arthritis because the site of disease is a well-defined compartment that can be readily injected. However, the idea could be applicable to other autoimmune diseases that have significant T cell involvement. Future work may focus on testing the approach in other contexts which may need a distinct route of administration and/or formulations.

5.3 Concluding remarks

The work presented in this dissertation has developed biomaterial-based agents to promote T_{reg} with the ultimate goal of developing immunoregulatory therapies for autoimmune disease. The concept of using biomaterials to enhance the delivery of known agents that could modulate T cell function represents a valuable strategy for durably enhancing T_{reg} and restoring immunoregulatory mechanisms. Furthermore, the demonstration that local enhancement of T_{reg} at a disease site can generate a systemic disease-protective effect is conceptually innovative and represents a powerful strategy to treat autoimmune disorder. This approach could allow for new treatment options for patients that cannot tolerate deepened generalized immune suppression and provide an adjunct option for patients that cannot achieve full disease control with current therapies. Continued development work to translate this approach to the clinic represents an important step towards non-immunosuppressive treatments for autoimmune diseases.